MECHANICAL BEHAVIORS AND RADIATION RESPONSE OF NANOSTRUCTURED MATERIALS

A Dissertation

by

YOUXING CHEN

Submitted to the Office of Graduate and Professional Studies of
Texas A&M University
in partial fulfillment of the requirements for the degree of

DOCTOR OF PHILOSOPHY

Chair of Committee,	Xinghang Zhang
Committee Members,	Karl T. Hartwig
	Haiyan Wang
	Anastasia Muliana
Head of Department,	Miladin Radovic

May 2015

Major Subject: Materials Science and Engineering

Copyright 2015 Youxing Chen

ABSTRACT

Material performance in irradiation environments is central to the design of advanced nuclear reactors, which call for advanced materials that can sustain hundreds of displacements-per-atom (dpa) at elevated temperatures. Conventional coarse-grained materials cannot survive in such a challenging radiation environment. Nanostructured materials have gained increasing attention as they possess abundant boundaries/interfaces that may act as sinks for radiation-induced defects. The goal of this thesis is to investigate certain nanostructured materials to aggressively mitigate radiation damage, and achieve superior radiation tolerance. In particular we applied two strategies to alleviate radiation damage in Cu, which is often severely damaged under radiation environments, including the selection of Cu/Fe and Cu/Co multilayers with coherent immiscible layer interfaces and nanotwinned Cu with nanovoids.

Recent studies on metallic multilayers have shown that chemical immiscibility is important to achieve enhanced radiation tolerance. However the influence of coherency on radiation resistance of immiscible systems remains poorly understood. He ion irradiaton studies on Cu/Fe and Cu/Co multilayers suggest that coherent immiscible interfaces are also effective to alleviate radiaiton damage, and a prominent size effect is observed. *In situ* Cu ion irradiation study on Cu/Fe validates, for the first time, interface affected zone, that is defect density vary as a function of distance to the layer interface. Meanwhile we show, in He ion irradiated Cu/Co multilayers, a surprising size dependent strengthening behavior, that is films with smaller h have greater radiation hardening.

Such unusual size dependent strengthening could be explained via a transition from partial dislocation transmission (before radiation) to full dislocation transmission (after radiation) dictated strengthening mechanisms due to formation of He bubbles at layer interface.

The second strategy involves the selection of nanotwinned Cu with nanovoids. In general radiation induced voids in irradiated materials grow continuously, manifested as void swelling. This study, however, describes a counterintuitive yet significant concept: deliberate introduction of nanovoids in conjunction with nanotwins enables unprecedented damage tolerance. *In situ* irradiation studies and atomistic simulations reveal that such remarkable self-healing capability in nanovoid-nanotwinned Cu stems from high density of twin boundaries that rapidly capture and transport defects to nanovoids, which store and eliminate defects.

DEDICATION

This dissertation is dedicated to:

My wife, Qian Cao

ACKNOWLEDGEMENTS

First and foremost I would like to thank my advisor Prof. Xinghang Zhang. He recruited me five years ago and brought me into this exciting research field. His encouragement, wisdom, patience and support through the entire Ph.D. life have helped me become an independent researcher. In particular, his trust and respect encourage me to do my best all the time. That means a lot to me!

I also would like to acknowledge Dr. Jian Wang at Los Alamos National Laboratory (LANL) for his guidance on molecular simulation. During the 10-month period at LANL, he improved my thinking skills on research as well as life. His working attitude is very respectable.

I am also grateful to my defense committee members, Prof. Haiyan Wang, Prof. Karl T. Hartwig, Prof. Anastasia Muliana, and Prof. Partha Mukherjee for their guidance and precious suggestions that improved the quality of this thesis.

I greatly appreciate the Materials Science and Engineering program coordinator, Jan Gerston, who guided me through my graduate studies.

I express my gratitude to Dr. Nan Li for his help on my research and life at LANL, Drs. Engang Fu and Yongqiang Wang at LANL for their help on He ion irradiation, Drs. Mark A. Kirk and Meimei Li at Argonne National Laboratory (ANL) for their collaboration on *in situ* Kr irradiation, Prof. Lin Shao and Dr. Di Chen at Texas A&M University for their help on heavy ion irradiation and Prof. Yong Yang and

Yuedong Wu at University of Florida for their help on focused ion beam experiments. Dr. Khalid Hattar, Michael Marshall and Daniel Buller are acknowledged for their help on *in situ* radiation experiments at Sandia National Laboratory (SNL). I thank Peter M. Baldo and Edward A. Ryan at ANL for their assistance on *in situ* radiation experiments. In particular for the ANL trip in March 2013, I am touched when they helped us do the *in situ* radiation experiments in the mid-nights.

Many thanks to my colleagues and friends Kaiyuan Yu, Yue Liu, Cheng Sun, Miao Song, Daniel Bufford, Steven Rios, Byoungsoo Ham, David Foley, Zhe Fan, Jin Li, Sichuang Xue, Qiang Li, Liang Jiao, Fauzia Khatkhatay, Aiping Chen, Yuanyuan Zhu, Joonhwan Lee who have helped my experiments and provided useful suggestions.

I am greatly indebted to my parents and wife for their complete, continued, and undoubted support. Without their understanding, I would never have the courage to keep going.

TABLE OF CONTENTS

LIST OF FIGURES

Page

LIST OF TABLES

Page

LIST OF EQUATIONS

CHAPTER I

INTRODUCTION AND LITERATURE REVIEW

1.1 Materials challenges in nuclear energy

Nuclear power currently provides ~ 13% of electrical power worldwide(*1*). Considering that energy generation currently accounts for 66% of worldwide greenhouse gas emissions, nuclear energy is an important energy resource in managing atmospheric greenhouse gases and associated climate change. Currently the vast majority of nuclear reactors are classified as Generation II reactors, completed in the 1970s and 1980s. These reactors are approaching their designed lifetime (~ 40 years) and seeking for an extension of another 20 years despite the risks associated with materials aging(*2*). Access to reliable, sustainable and affordable energy remains a worldwide challenge and advanced fission reactors (Generation IV) and fusion reactors are still under development. One of the challenges for the design of these new-generation nuclear reactors is the long-term reliability of materials, since reactor materials will be exposed to very high temperatures, intense neutron radiation, and corrosive environments and are likely to degrade over the years. As shown in Fig. 1, the advanced nuclear reactors demand materials capable of satisfactory operation up to neutron damage levels approaching 200 atomic displacements per atom (dpa) (*3*). These challenges must be resolved in pursuit of reliable, safe and economical nuclear energy.

These increased demands of materials for future nuclear reactors cannot be satisfied by conventional materials. Recently, nanostructured materials have gained

intensive attention to serve as nuclear materials in new-generation nuclear reactors. It is well known that grain boundaries, interfaces and surfaces are sinks for radiation-induced point defects. For example, dispersion-strengthened (ODS) alloys with dispersed nanoscale oxide particles have been considered to use as cladding and structural materials in Generation IV reactors, as the oxide/matrix interfaces are defect sinks(*4*). However, the detailed mechanisms for these defect sinks (grain boundaries, interface and surface) at the level of the atomic structure are not well understood. Therefore, amounts of efforts are devoting to designing appropriate materials as future nuclear materials.

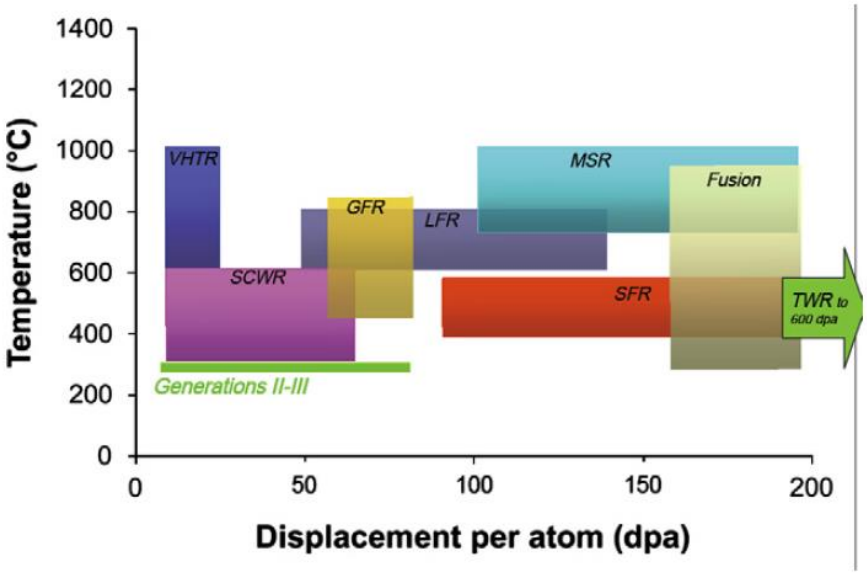

Figure 1 Temperature and dose requirements for in-core structural materials for the operation of the six proposed Generation IV advanced reactor concepts, the traveling wave reactor and fusion reactor concepts. The dimensions of the colored rectangles represent the ranges of temperature and displacement damage for each reactor concept(*5*).

1.2 Introduction of nanostructured materials

Nanostructured materials in general refer to materials with internal microstructural dimension of the order of 100 nm or less (*6*, *7*). Various nanostructured metals have been fabricated in the form of nanograins/nanocrystalline(nc) grains, nanoprecipitates, nanotwins (nt), nanolayers, nanowires, nanoparticles, nanorods, nanotubes and nanoporous (np) structures, as shown in Fig. 2. These nanostructured materials with high-density interfaces have significantly improved properties, including mechanical, magnetic, electrical and chemical behaviors etc.(*8*, *9*), and have been applied in many fields of nanotechnology. For instance, nanolayers with a combination of magnetic and nonmagnetic layers have accomplished giant magnetoresistance (GMR) (*8*), and subsequently drive a series of renovation in data storage device industry. Recently, nanostructured materials have attracted increasing attention for nuclear reactor applications as grain boundaries are defect sinks to absorb radiation induced defects. For instance, nc Ni with grain size of ~ 55 nm shows superior radiation tolerance compared to coarse grained Ni(*10*).

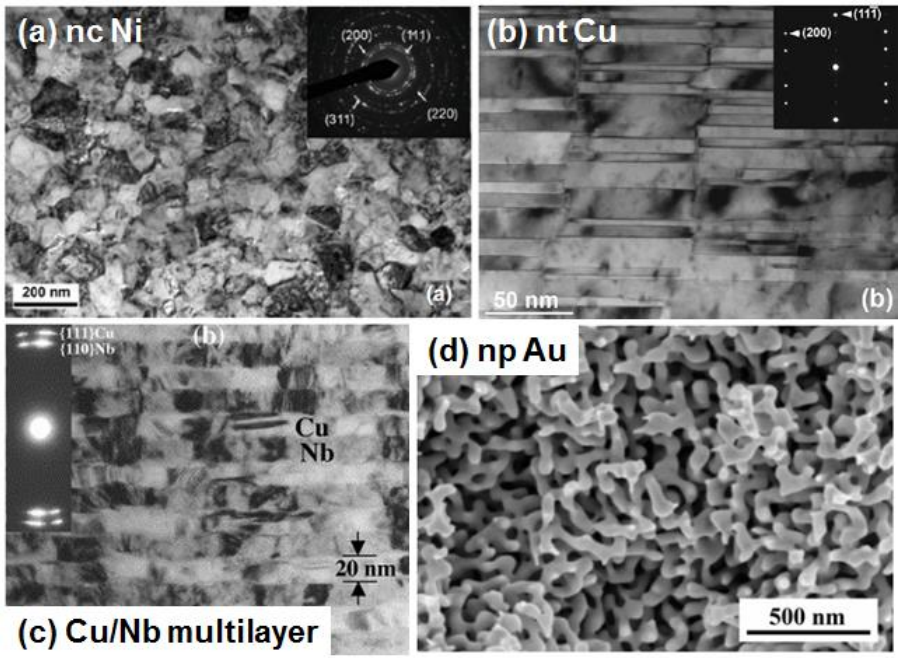

Figure 2 Transmission electron microscopy (TEM) micrographs of (a) nanocrystalline Ni with average grain size of ~ 55 nm(*10*), (b) nanotwinned Cu(*11*), and (c) Cu/Nb multilayers with individual layer thickness of 20 nm(*12*). (d) Scanning electron microscopy (SEM) micrograph of nanoporous (np) Au with sponge-like open-cell foam morphology(*13*).

The unique properties of nanostructured materials are ascribed to the high-density interfaces with large fraction of interface atoms. Fig. 3 schematically illustrates microstructure of nc metals (*6*). Black and whites atoms represent atoms inside grains and at grain boundaries, respectively. The volume fraction of grain boundaries (white atoms) increases along with the decrease of grain size, and can reach as much as 30% for 10 nm grains and 50% for 5 nm grains(*7*).

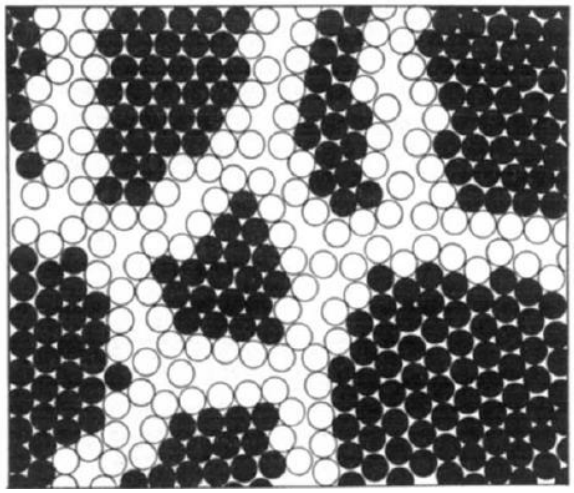

Figure 3 Atomic structure of a two-dimensional nanocrystalline materials, distinguishing between the atoms associated with the individual grains (black particles) and those constituting the grain boundary network (white particles) (*6*).

1.3 Microstructure and mechanical properties of nanostructured metals

1.3.1 Metallic multilayers

Multilayers with well-tailored layer structure have outstanding mechanical properties, as shown in Fig. 4a-b. The strength of the multilayers could approach 1/2-1/3 of the theoretical strength (~ $\mu/30$, where μ is shear modulus). To investigate the novel strengthening behaviors, we need to examine their interfaces in detail.

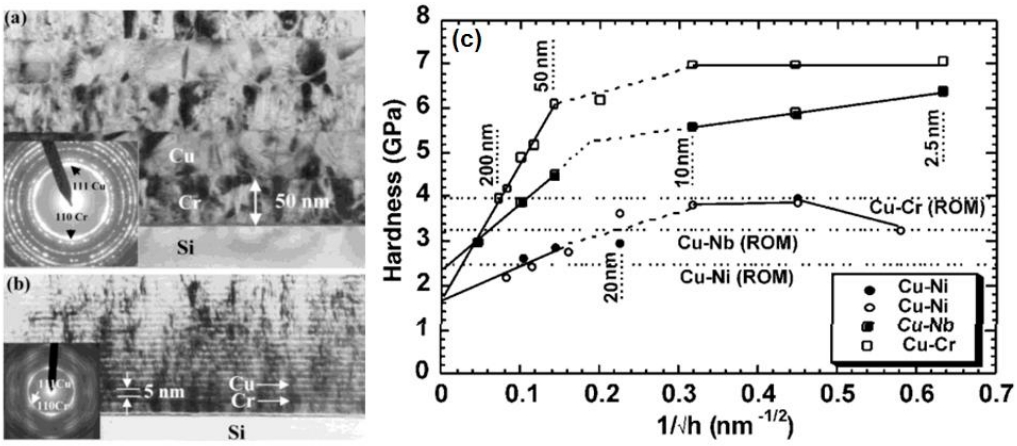

Figure 4 Cross-section TEM micrographs showing Cu/Cr multilayers with (a) h=50 nm and (b) h=2.5 nm. (c) The dependence of hardness on layer thickness (h) (*14*).

The orientation relationship (OR) between two different components in multilayers is of great importance as it directly affects the misfit dislocation network at interfaces. The configuration of dislocation networks, such as density and type of interface dislocations, determines the mechanical behavior of multilayers. Here, we will introduce face-centered cubic (FCC) / body-centered cubic (BCC) interfaces, as they are most widely investigated among all multilayer systems. There are four major types of interfaces: Kurdjumov-Sachs (K-S)(*15*), Nishiyama-Wassermann (N-W)(*16*, *17*), Pitsch(*18*), and Bain(*19*) ORs. The aligned planes and directions are listed as following:

(a) K-S OR: {111} FCC || {110} BCC, <110> FCC || <111> BCC;

(b) N-W OR: {111} FCC || {110} BCC, <110> FCC || <100> BCC;

(c) Pitsch OR: {110} FCC || {110} BCC, <100> FCC || <111> BCC;

(d) Bain OR: {100} FCC || {100} BCC, <100> FCC || <110> BCC.

Interfaces with different ORs have different types of dislocation arrays. Theoretically, misfit dislocations at interface could be identified by atomically informed Frank-Bilby theory (*20-22*). For instance, K-S and N-W interfaces in Cu/Nb have been studied in Fig. 5, and the array of interface dislocations with different ORs demonstrates significant difference.

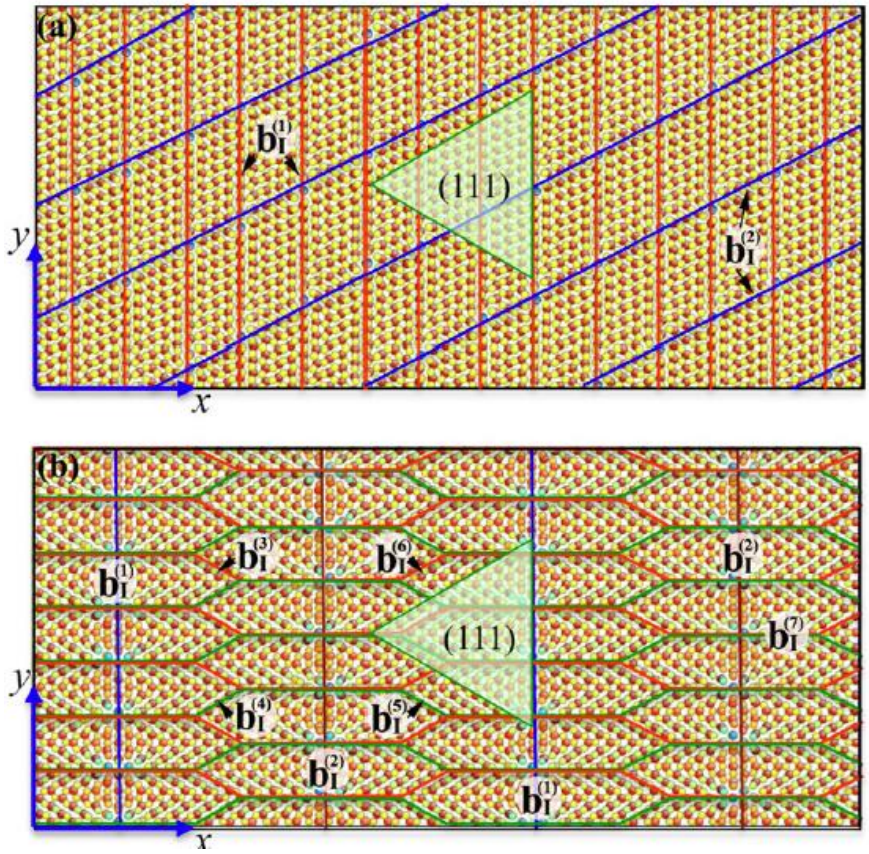

Figure 5 The relaxed atomic structures of the (a) Kurdjumov Sachs (K-S) and (b) Nishiyama Wasserman (N-W) interface. In both figures, the x-direction is <112> Cu and the y-direction is <110> Cu. The solid lines mark interface dislocations where segments of the same color have the same Burgers vector. The three edges of the triangle in the center indicate the traces where the three {111} planes of Cu intersect the interface. (*23*)

Certain metallic multilayers with nanoscale layer thicknesses exhibit high strength close to theoretical values (*14, 24-28*). Deformation mechanisms at different layer thicknesses vary and can be divided into three regimes (Fig. 6), which will be described as follows.

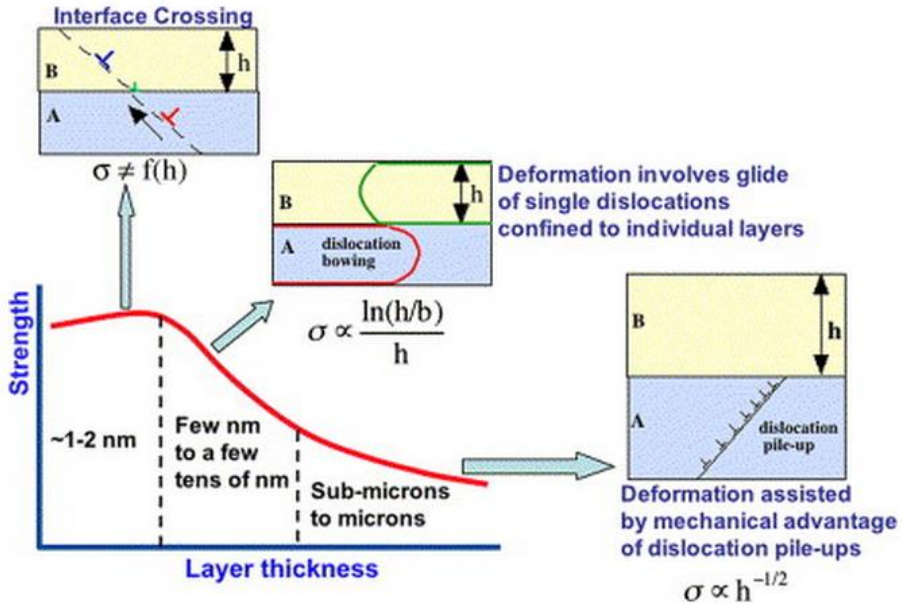

Figure 6 Schematic illustration of the dislocation mechanisms of multilayer strength operative at different length scale(*12*).

Dislocation pile-up: Hall-Petch model (*25, 29*) operates when individual layer thickness, h, is greater than tens of nanometers. Strengthening arises from dislocations pile-up on the glide plane against grain or interphase boundaries. The pile-up process can be described as follows: when the stress applied on dislocations is larger than a critical resolved shear stress (τ_0: friction stress), these dislocations start to glide. The friction stress includes the lattice resistance (Peierls-Nabarro stress), solid solution

effects and precipitation hardening. The number of dislocations at one end of the pile-up is approximated by,

Equation 1 $N = \pi h'(\tau - \tau_o) / G'b$

where τ is the resolved shear stress across the slip plane, b is the unit slip distance provided by a single dislocation, $G' = G/(1-v)$, where G is the shear modulus, and v is Poisson's ratio. The pile-up of dislocations induces stress concentration on the leading dislocation. When the applied stress on the leading dislocation reaches a critical value, just sufficient to promote the dislocation penetration across interface, the stress is termed as barrier stress τ^*,

Equation 2 $\tau^* = N(\tau - \tau_o)$

Therefore, we can get the equation by eliminating N

Equation 3 $\tau = \tau_o + (\frac{G'b\tau^*}{\pi h'})^{1/2}$

which provides the resolved shear stress to push the leading dislocation across the interface. In general, the strengthening equation is written as,

Equation 4 $\tau = \tau_o + Kh^{1/2}$

where K is Hall-Petch slope. From equations (1.3) and (1.4), we have the relationship between τ^* and K. Since Hall-Petch slope K is an experimental value, we can estimated the peak strength (τ^*) of interface directly from the Hall-Petch slope. Thus, physically,

the Hall-Petch slope indicates the resistance of the boundary and is often used to predict the peak strength of multilayers very well (*12, 25, 30*), and an example is shown in Fig. 7.

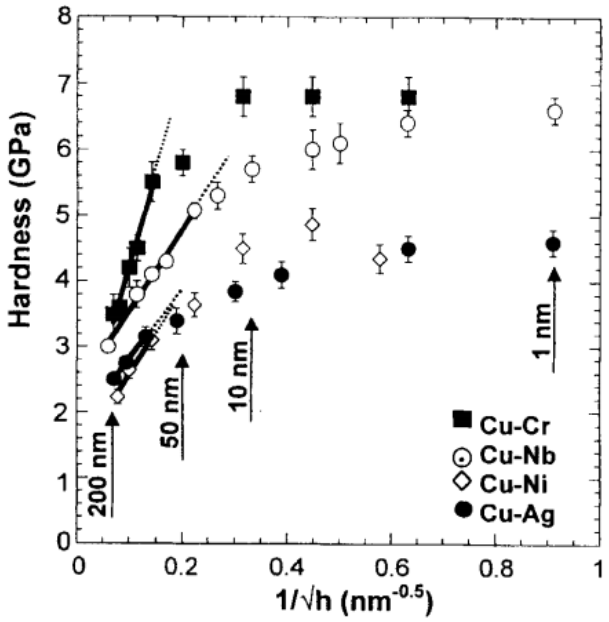

Figure 7 Plot of hardness as a function of inverse square root of layer thickness in several Cu-based multilayers. Linear fit (solid lines) at larger h is consistent with the Hall-Petch model. (*14*)

However, the strength predicted from Hall-Petch slope is sometimes not consistent with the measured peak strength, as there may be nanoscale features within layers, e.g. columnar grains and twins (*31-33*) that have smaller feature size than individual layer thickness. Therefore, certain modifications had to be made accordingly. Misra *et al* (*34*) developed a deformation mechanism map to determine the dominant

feature size for dislocation pile-ups against boundaries by considering grain size inside layers (Fig. 8).

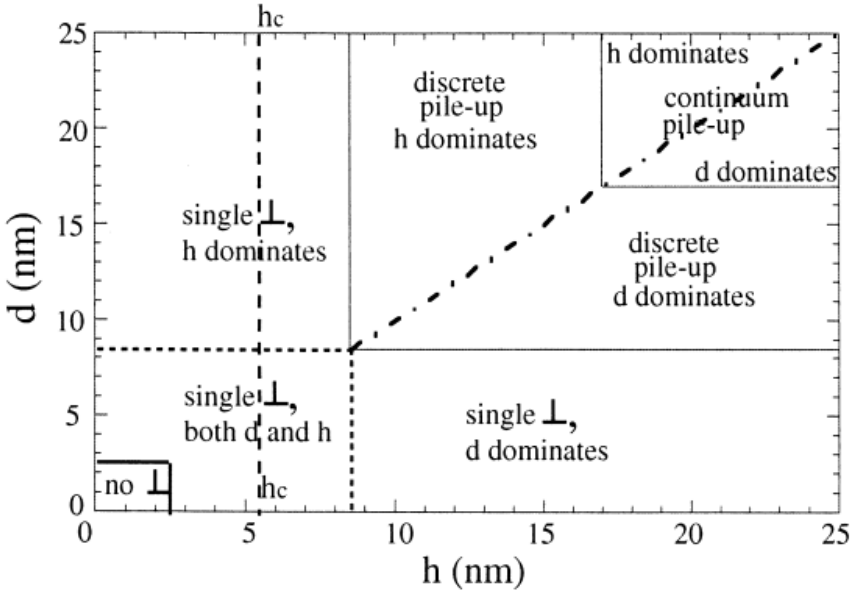

Figure 8 A simple "deformation mechanism map" for Cu-based multilayers with misfit of ~ 2.5%. The second layer is assumed to be harder than Cu (*34*)

Confined layer slip: at smaller h of tens of nm, confined layer slip (CLS) model based on Orowan bowing mechanism (*24*, *35*) is more appropriate,

Equation 5 $$\sigma_{cls} = M\frac{\mu b}{8\pi h}\left(\frac{4-\nu}{1-\nu}\right)\ln(\frac{\alpha h}{b})$$

where M is Tayler factor, u is shear modulus, b is Burgers vector, α represents the core cut-off parameter, h is layer thickness. At this length scale, dislocation pile-up becomes more difficult. Correspondingly dislocations are confined by and glide between layer interfaces, instead of transmitting across the interfaces because the stress required for

bowing of dislocations is less than that for transpassing across interface, as depicted in Fig. 9.

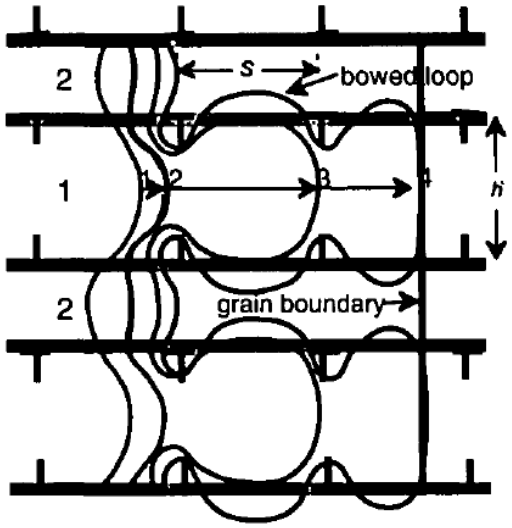

Figure 9 Successive configurations for a threading dislocation as a function of increasing applied stress leading to confined layer propagation (*25*).

However, in some multilayer systems, there is a discrepancy between the calculated stress by CLS model and experimental result. Recently, Misra *et al* (*12*) developed a refined CLS model by considering interface stress and dislocation-dislocation interactions, as

$$\text{Equation 6} \quad \sigma_{cls} = M\frac{\mu b}{8\pi h'}\left(\frac{4-\nu}{1-\nu}\right)\ln\left(\frac{\alpha h'}{b}\right) - \frac{f}{h} + \frac{C}{\lambda}$$

where h' is the distance along the slip plane between adjacent interfaces, f is interface energy in unit of J/m^2, and $C = \mu b/(1-\nu)$. The first term on the right is based on the

normal CLS model, the second term is related to the interface stress and the last term is related to the interaction between interface dislocations and gliding dislocations. Fig. 10 shows a comparison of calculated stress by normal CLS model and refined CLS model (*12*), indicating refined CLS model is more appropriate in some cases to represent the real situation.

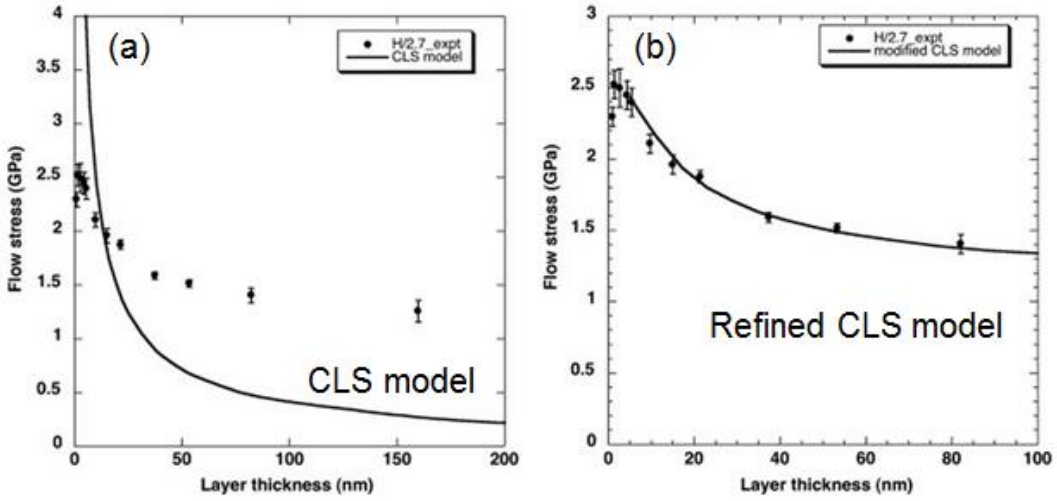

Figure 10 Results of the (a) confined layer slip (CLS) and (b) refined CLS models compared to the experimental data(*12*).

Interface barrier strength: interface barrier strength (IBS) mechanism operates when h is several nm. The strength of multilayer at such length scales is determined by the inherent resistance of layer interface to the transmission of single dislocations. Various factors, including Koehler stress τ_k^* (*36*), coherency stress, chemical stress τ_{ch}^* and misfit dislocations τ_d^* (*37*), etc. are considered to estimate the interface barrier strength, $\tau_{barrier}^*$, as (*38*)

Equation 7 $\tau^*_{barrier} = \tau^*_k + \tau^*_d + \tau^*_{ch}$

Koehler stress τ^*_k arises from a significant repulsive image force for a dislocation to slip from the lower modulus phase to higher modulus counterpart. τ^*_k could be obtained by (*36*),

Equation 8 $\sigma_{\max} \cong R\mu_1 \sin\theta / 8\pi$

where $R = (\mu_2 - \mu_1)/(\mu_2 + \mu_1)$, μ_2 is the modulus of high-elastic-constant material and μ_1 is the modulus of low-elastic-constant material. θ is the angle between the slip plane and the interface.

τ^*_d comes from misfit dislocations and can be expressed by (*37*)

Equation 9 $\tau^*_d = \alpha G^*[(\Delta a / a) - (b/\lambda)]$

where α is Saada's constant, G^* is the mean shear modulus and could be estimated as $G^* = G^*_{Cu} \cdot G^*_{Fe} / (G^*_{Cu} + G^*_{Fe})$. λ is the average spacing of the interface dislocation array. $\Delta a / a$ is the mismatch strain. The term in bracket is the residual elastic strain parallel to the interface plane caused by lattice mismatch.

Meanwhile coherency stresses alternating from tension to compression periodically often exist and lead to resistance to dislocation propagation across interfaces. When the layer thickness is above critical thickness for coherency, misfit dislocation

arrays often appear to accommodate strain between layers. The interaction of misfit and gliding dislocations would also increase the interface strength.

In addition, chemical interaction term τ_{ch}^{*} , should also be considered if stacking fault energy (SFE) difference ($\gamma_2 - \gamma_1$) between layer constituents is prominent,

Equation 10 $$\tau_{ch}^{*} = \frac{\gamma_2 - \gamma_1}{b}$$

In general, interface barrier strength determines the maximum strength of multilayers. Take a model system FCC/FCC Cu/Ni as an example(*27*). The peak hardness can reach as high as 5 GPa at h = 5nm, which fits very well to the calculated data by a sum of Koehler stress τ_k^{*}, coherency stress, chemical stress τ_{ch}^{*} and misfit dislocations τ_d^{*} (*27*).

Moreover, mechanical behavior of certain FCC/BCC multilayers such as Cu/Nb (*39*), Cu/Cr (*40*, *41*), Cu/V (*42*), Ag/V (*43*), with opaque and immiscible layer interfaces have been investigated. The discontinuity of slip systems across interface and the lower shear resistance of layer interface (referred to as weak interface), in e.g. Cu/Nb, promote the dissociation or spread of the core of gliding dislocations at the interface (*44*, *45*). A dislocation once absorbed by a weak layer interface, loses its singularity, making it difficult to be reemitted in the opposite layers. Therefore, the “weak interface” offers a strong barrier to the transmission of dislocations.

1.3.2 Nanotwins

Mechanical behaviors of metals with twin boundaries (TBs) have been intensely investigated since 2004 when nanotwinned (nt) Cu with superior strength and conductivity was discovered by Prof. Lu's group (*46*). Fig. 11 shows nt Cu exhibits obviously higher strength and better ductility than nc Cu. Meanwhile, other nt metals have also shown high strength and ductility (*31, 47-53*), as well as outstanding microstructral stability under both radiation (*54*) and annealing conditions (*55, 56*). Recently, Zhang's group in Texas A&M reported TBs could serve as defect sinks and destruct SFTs in nt metals (*57, 58*).

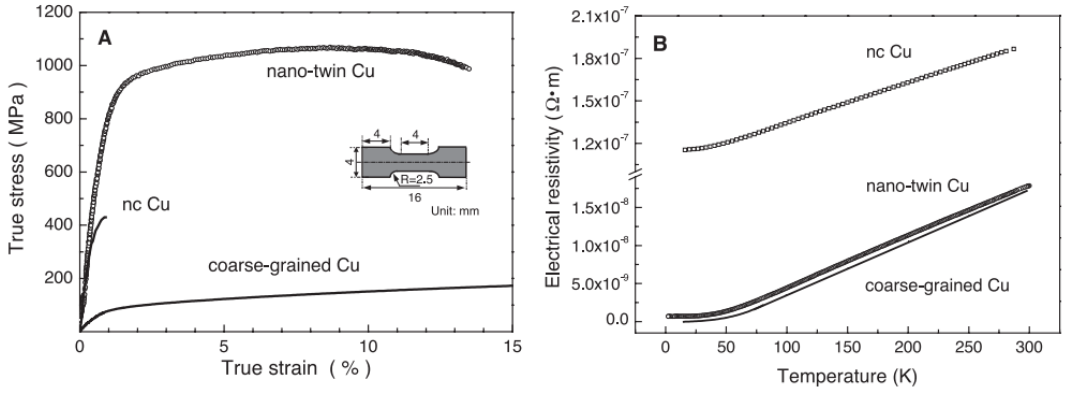

Figure 11 (a) Tensile stress-strain curve for the electro-deposited nanotwinned Cu in comparison with that for a coarse-grained polycrystalline Cu (~100 μm grain size) and a nanocrystalline Cu (~30 nm grain size); (b) electrical resistivity of nanotwinned Cu sample at various temperature in comparison with that of polycrystalline and nanocrystalline Cu. (*46*)

TB is a special class of boundaries with mirror symmetry across the twinning plane. In FCC structure, TBs such as Σ3 (111) coherent twin boundaries (CTBs) and Σ3

(112) incoherent twin boundaries (ITBs) have been significantly investigated. CTBs have a more coherent structure with less free volume and low interface energy (Fig. 12). For instance, CTB energy in Cu is 24-39 mJ/m^2, much lower than high angle grain boundary energies of 625-710 mJ/m^2 (*59-61*), which makes CTBs more stable at elevated temperatures than typical grain boundaries.

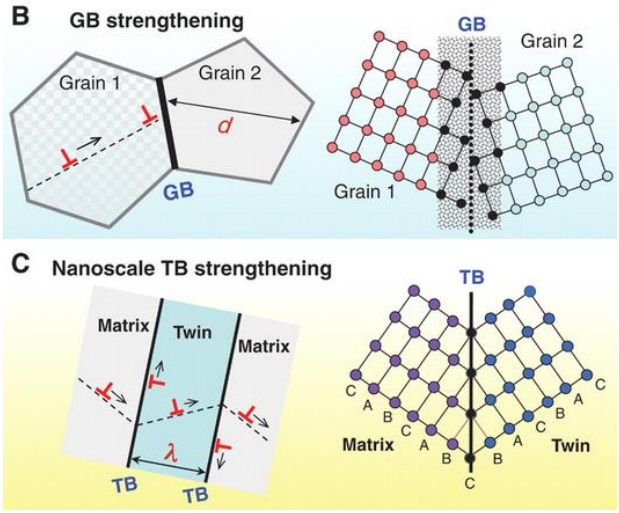

Figure 12 Schematic illustrations of strengthening methods include (B) GB strengthening: a higher stress is needed to deform a polycrystalline metal with a smaller grain size and (C) nanoscale twin boundary (TB) strengthening, based on dislocation-TB interactions from which mobile and/or sessile dislocations could be generated, either in neighboring domains (twin or matrix) or at TBs. Gliding of dislocations along TBs is feasible because of its coherent structure. (*32*)

In general, nanotwins are fabricated in metals with low-to-intermediate stacking fault energy (SFE), such as Cu(*11, 48, 55, 56, 62*), Ag(*51, 63*) and 330 stainless steels(*64*). However, it is challenging to introduce TBs into high SFE metals. Recently, Zhang's group proposed a basic criteria for formation of growth twins in high stacking fault energy metals (*65*) and nanotwins have been successfully fabricated in metals with

high SFE, such as Al(*66*, *67*), Ni in Cu/Ni(*27*, *68*) and Ag/Ni multilayers (*65*, *69*), Al in Ag/Al multilayer and Fe in Cu/Fe multilayers (*70*). The first requirement for twin formation in high SFE metals is the introduction of twin seeds. A low SFE metal can be used as a seed layer to nucleate high-density growth twins. The second criterion is coherency, which permits TBs in low SFE metals to propagate into high SFE metals through coherent interfaces. Fig. 13 shows twins penetrate from low SFE Cu to high SFE Ni(*27*).

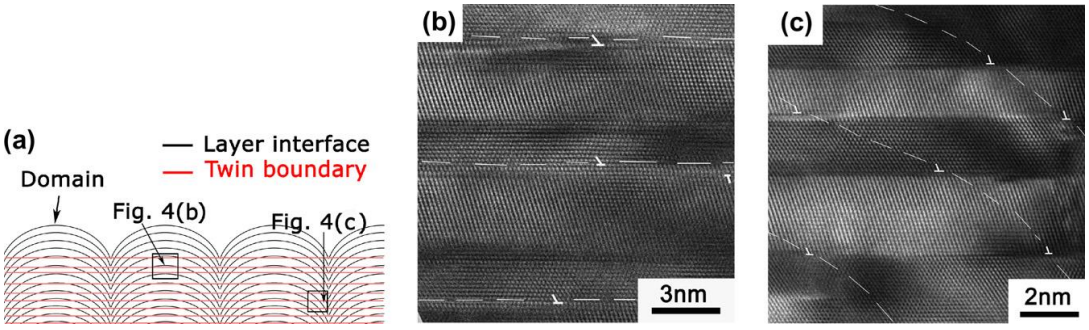

Figure 13 (a) Enlarged schematic of twins that intercept layer interfaces in highly (111) textured 2.5 nm Cu/Ni multilayers. (b) HRTEM micrograph of twins in region b, where twins are nearly parallel to the layer interface. Misfit dislocations can be identified in Ni layers. (c) HRTEM micrograph of region c, where twin interfaces form an angle with the layer interface. Layer interfaces are delineated with interfacial misfit dislocations in Ni(*27*).

Strengthening in nanotwinned structure arises from inherent resistance of TBs to transmission of dislocations. When the twin spacing is relatively large (> 15 nm), TBs resists the pile-up of dislocations. The inherent resistance of TBs against dislocation pile-up is close to that of high-angle grain boundaries(*32*). Pande *et al* (*71*) developed a model to incorporate the influence of twins into grain size effect on Hall-Petch slope.

However, softening was observed in nt Cu when average twin spacing is further reduced to below 15 nm(*47*). With diminishing twin spacing, the density of pre-existing dislocation source increases, requiring lower stress to operate the dislocation source (Fig. 14). Meanwhile, the high-density dislocation sources also increase the ductility of nt Cu.

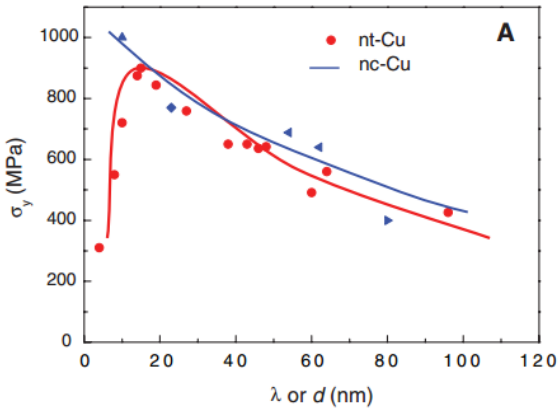

Figure 14 Variation of yield strength as a function of mean twin thickness for the nt Cu samples. A maximum in the yield stress is seen for the nt Cu with d = 15 nm, but this has not been observed for the nc Cu, even when the grain size is as small as 10 nm. (*47*)

1.4 Radiation damage in nanostructured materials

Nuclear energy currently accounts for more than 10% of electricity world wide and the discovery of advanced materials for extreme radiation environments resides at the center of the design of future nuclear reactors (*5*, *72-76*). Certain nc materials has shown promising radiation tolerance. Howerver, nanograins tend to coarsen at elevated temperature and under irradiation (*74*, *77*), compromising their radiation tolerance. Persistant effort was devoted to develop new radiation tolerant materials, such as multilayers and nt metals in this thesis.

1.4.1 Fundamentals of ion-solid interaction

A radiation damage event includes several processes. When an energetic incident particle interacts with a lattice atom, the transferred kinetic energy from incident particle to the lattice atom creates a primary knock-on atom (PKA), which displaces from its original lattice site, leading to the creation of more additional knock-on atoms. When the energy (E) transferred to the PKA is larger than the threshold displacement energy (E_d: the minimum energy transferred to create a displacement), the PKA can continue to knock on other atoms, producing secondary or tertiary knock-on atoms.

The number of displaced atoms in a cascade produced by a PKA of energy E (denoted as $N_d(E)$) can be estimated by Kinchin-Pease model (*78*) based on hard-sphere assumptions as shown in Fig. 15 and can be described as follows.

(1) Elastic collisions occur between atoms, resulting in the cascade. In this process, inelastic collisions are not considered.

(2) When the energy of a PKA (E) is lower than E_d, the atom is not displaced and $N_d=0$.

(3) When the energy of a PKA (E) is greater than E_d but lower than $2E_d$, only one displacement can occur by PKA and $N_d=1$.

(4) When the energy of a PKA (E) is greater than $2E_d$ but lower than the cut-off energy (Ec), more than one atoms are displaced and $N_d(E)= E/2E_d$.

(5) When the energy of a PKA (E) is greater than E_c, no additional displacements occur and $N_d(E)= E_c/2E_d$.

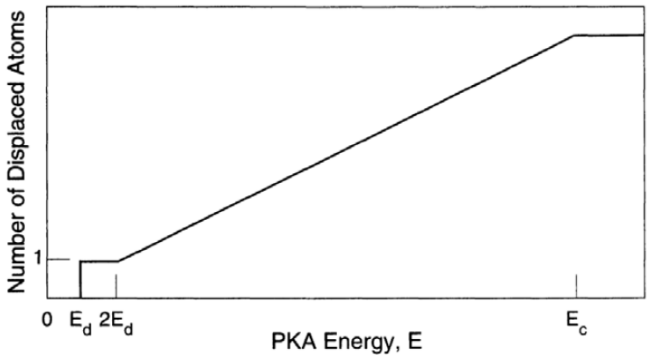

Figure 15 A graphical representation of the number of displaced atoms in the cascade as a function of PKA energy according to Kinchin and Pease model(*78*).

The Kinchin-Pease option for SRIM simulation has recently been adopted by the community as a new routine to reliably estimate radiation damage for irradiated materials (*79*). However, this model does not include the effect of the electronic stopping and crystal structure.

In crystal structure, the energy barrier to displace an atom varies with crystal directions. Taking FCC structure as an example, in Fig. 16a, the struck atom in the corner of FCC unit has several possible low-index flight directions for the recoil, as shown by wavy lines. <100>, <110> and <111> are three crystallographic directions which require the lowest threshold displacement energy. Fig. 16b shows a variation of potential energy along <111> direction.

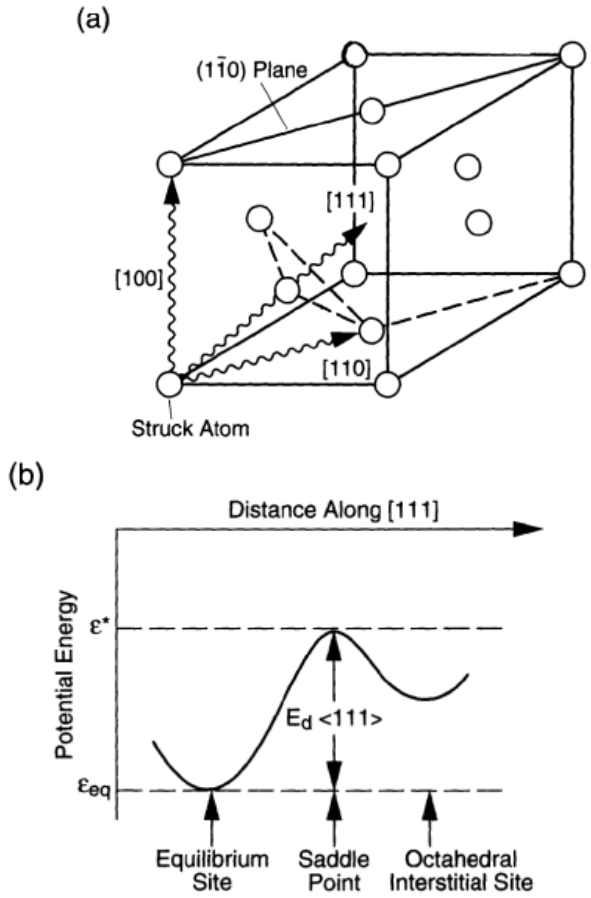

Figure 16 (a) Displacement of a lattice atom recoiling from a collision with an energetic atom; (b) potential energy of the struck atom as it moves along the [111] direction(*80*).

Generally, each crystal direction, [h k l], has its own displacement energy. The threshold displacement energy is lower when the direction of the struck atom is along a line of atoms in the crystal. Fig. 17 shows the threshold orientation dependence in Cu, where the lowest displacement energy is along <100> direction (19 eV).

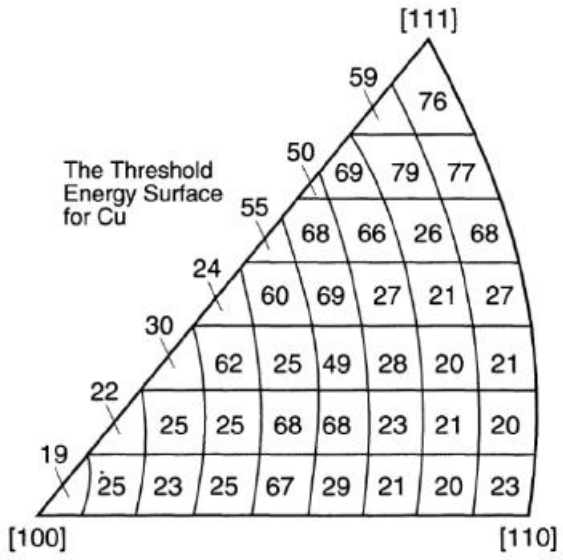

Figure 17 Directional dependence of the displacement threshold for Cu in unit of eV (*81*).

A cascade occurs and terminates with PKA as an interstitial, accompanying with the appearance of a collection of point defects (vacancies and interstitials) and defect clusters. Fig. 18 exhibits one cascade process, in which the displacement leads to a depleted zone, interstitials, and crowdions.

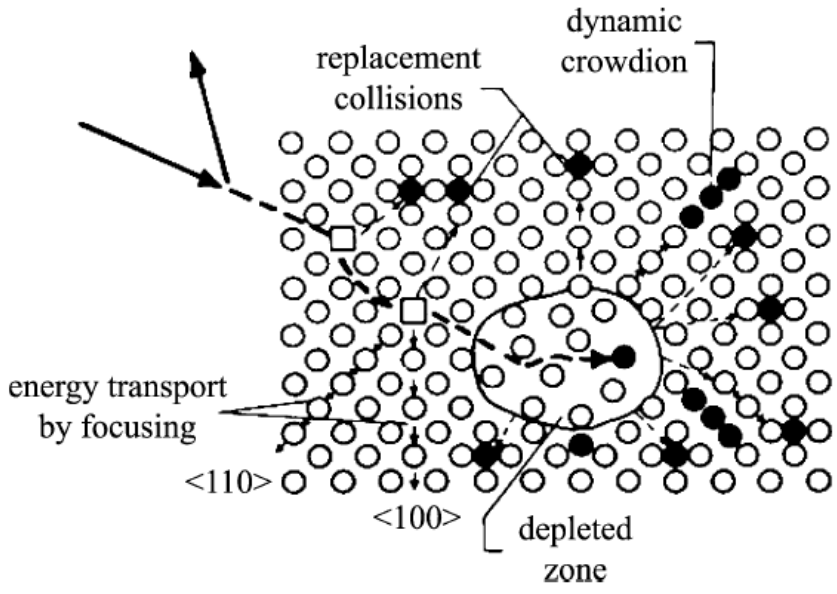

Figure 18 Irradiation induced displacement spike accounting for crystallinity in the damage cascade (*82*).

To better understand this collision/cascade process, we need to investigate the collision/interaction between particles and lattice atoms. There are 3 types of collision processes: neutron-nucleus interaction, ion/atom-atom interaction, ionization collision. Generally, neutron-nucleus collision is understood as both elastic and inelastic scattering. Due to the electrical neutrality of neutrons, elastic collision can be treated as colliding hard spheres, in which the energy is conserved. The penetrating neutrons impart recoil energy to the struck atoms. Meanwhile, another possibility is the neutrons are absorbed by the nucleus, forming a compound nucleus, and subsequently emitting a neutron and a γ-ray.

Collision kinematics is developed to describe the interaction between colliding atoms. Three important classes of ions in ion-atom collisions are studied, including light energetic ions with E_i>1MeV, highly energetic heavy ions with E_i=~100 MeV and lower energy heavy ions with E_i< 1 MeV. An appropriate interatomic potential function is selected, according to ρ/a, the ratio of the distance of closest approach to the screening radius as a function of the recoil energy, T. For example, a pure Coulomb scattering potential is adequate for light energetic ions where ρ<<a, while a hard-sphere potential is appropriate for near head-on elastic collisions. An accurate description of the slowing-down process of an ion/atom over the entire energy requires the consideration of several potential functions together. Fig. 19 shows several potential functions in Cu. Generally, the coulomb potential is used for proton irradiation, hard-sphere potential for neutron irradiation and screened Coulomb for heavy ion irradiation.

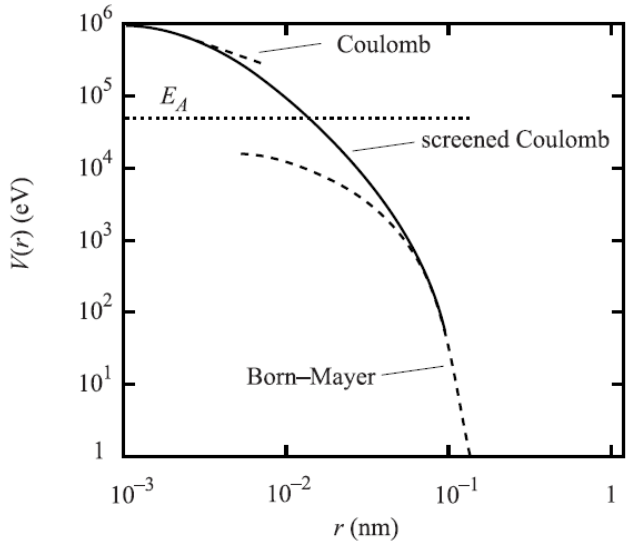

Figure 19 Behavior of various potential functions over a range of separation distances between copper atoms(*82*).

It is worth noting that radiation damage varies significantly by changing different incident particles, as shown in Fig. 20. Light particles, such as electrons and protons, produce isolated Frenkel pairs or small clusters, while neutrons and heavy ions produce large clusters. For instance, half of the recoils for 1MeV proton irradiation in Ni are produced with energies less than ~ 1keV, with an average energy of 60 eV while those for 1MeV Kr are 30keV with an average energy of 5keV.

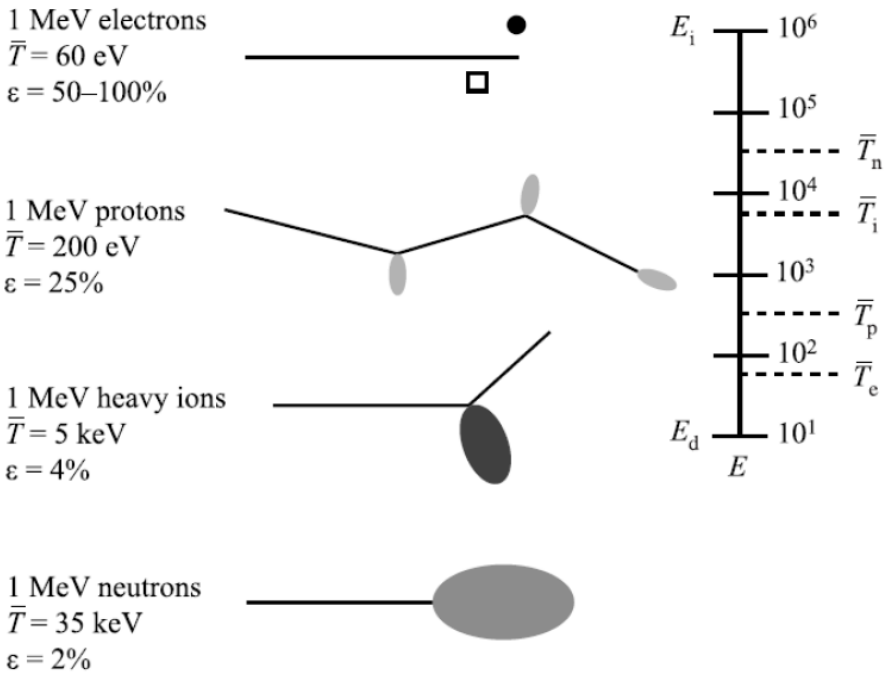

Figure 20 Difference in damage morphology, displacement efficiency and average recoil energy for 1MeV particles of different type incident on nickel(*82*).

In nuclear reactors, radiation damage is induced primarily by neutrons. However, neutron irradiation facilities are limited and it is difficult to achieve high radiation dose with neutrons. Therefore, electrons, heavy ions, and protons are often used to simulate

neutron radiation damage at a much higher dose rate. (1) Electron irradiation is easily performed in a high voltage transmission electron microscope. Two drawbacks should be considered: one is the beam energy is mostly not sufficient to introduce considerable collision cascades; another one is radiation damage is not uniformly distributed across the irradiated region due to the Gaussian profile of the electron beam. (2) Heavy ions can produce high dose rate, sufficient to investigate radiation response of materials in dense cascades. The drawback is the limited penetration depth of implanted ions and large temperature shifts due to high dose rates. (3) Proton irradiation is widely accepted to simulate neutron irradiation as it has obvious advantages over electron and heavy ion irradiation. Smaller recoil energy and more broadly spaced cascades under proton irradiation are closer to that under neutron irradiation. Meanwhile, protons with a few MeV can penetrate tens of microns, much deeper than that under heavy ion irradiation.

1.4.2 Irradiation induced defect clusters in metals

Irradiation of metals by neutrons or heavy ions results in a large number of vacancy and interstitial clusters, which are formed via direct condensation out of collision cascades or aggregation of isolated point defects. Typical defect clusters include Frank loops, perfect loops, voids and stacking faults tetrehedra (SFTs) (*83-85*). Pefect dislocation loops can be understood following the schematic at the top of Fig. 21. AB, CD have edge character and BC and AD have screw character as shown from the orthogonal cross-sectional views. In contrast if an extra disk of atoms is inserted into the materials, a Frank loop is formed. As shown at the bottom half of Fig. 21, every segment

of the loop (from cross-secitonal view) has the edge character. Fig. 22a shows microstructure of neutron irradiated 316 stainless steel (SS) at 580 ℃ subjected to a dose of 1.9 $\times 10^6$ n/m^2. Dislocation lines, dislocation loops and voids were clearly observed. More importantly, radiation induced voids lead to significant dimensional change - swelling, as shown in Fig. 22b.

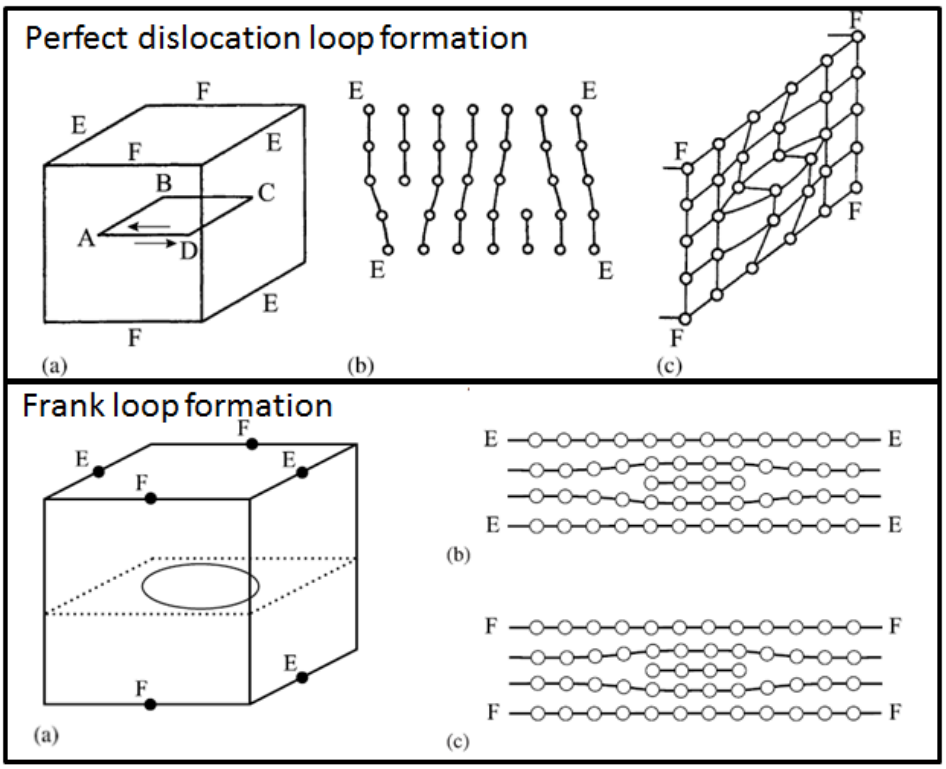

Figure 21 The formation of a perfect dislocation loop and a Frank loop(*82*).

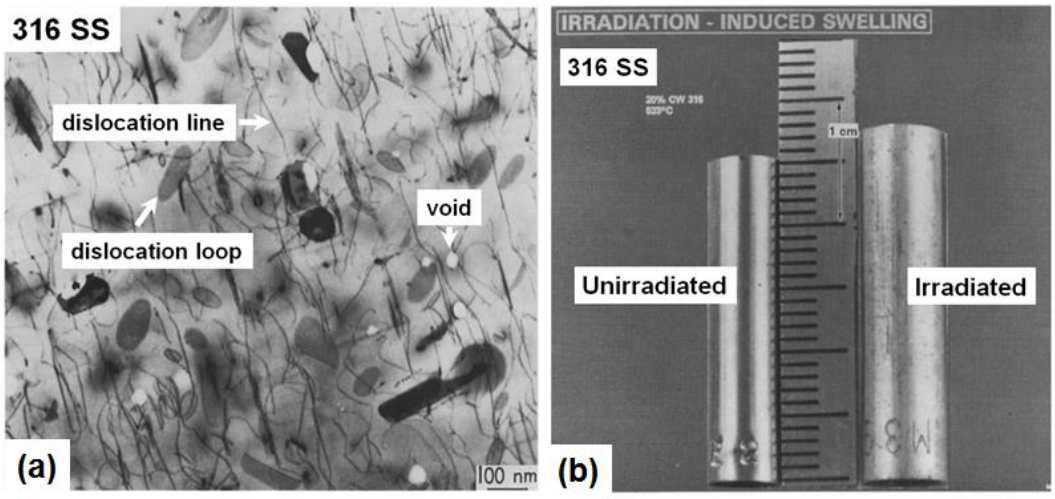

Figure 22 (a) Microstructure of 316 stainless steel neutron irradiated at 580 ℃ to a dose of 1.9 $\times 10^{26}$ n/m^2. (b) Photograph of 316 stainless steel rods before and after irradiation at 533 ℃ to a fluence of 1.5 $\times 10^{23}$ n/m^2 in the EBR-11 reactor(*86*).

SFTs, as another common type of defect clusters, are generally formed in FCC metals with low-to-medium stacking fault energy. An SFT has a three-dimensional stacking fault configuration in the shape of a tetrahedron, and could be formed in two typical conditions. One is the condensation from vacancy clusters in irradiation induced cascades; the other one is the evolution from Frank loops with triangular shape on (111) plane. The [110] edge dislocation with Burgers vector b = a/3 [111] lowers its energy by dissociation into a Shockley partial dislocation with b = a/6 [112] and a stair-rod dislocation with b = a/6 [110]. The Shockley partial glides on another {111} plane, leaving behind the stair-rod dislocation. When the Shockley partial meets another Shockley derived from similar history, they form a stair-rod dislocation. Fig. 23 shows weak beam dark field TEM image of proton irradiated Cu. Most defect clusters are SFTs (*87*). These irradiation induced defect clusters significantly degrade the mechanical

behaviors of nuclear materials in form of irradiation hardening, embrittlement, irradiation creep and cracking (*82*).

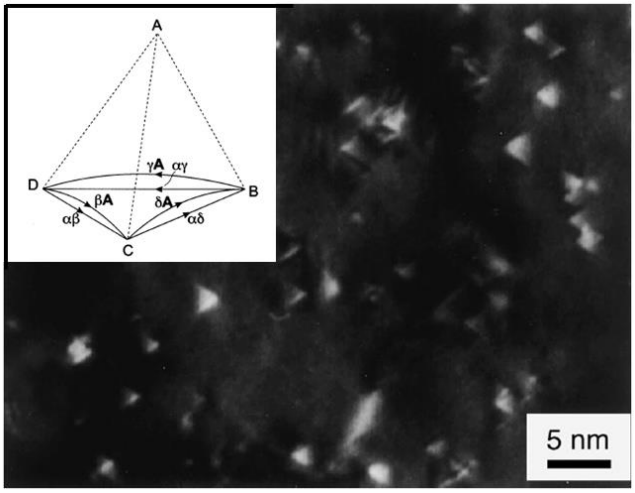

Figure 23 Weak beam dark field TEM image in Proton radiated Cu at a dose of 3.9×10^{-2} dpa(*87*).

1.4.3 Radiation tolerance of nanostructured metals

Grain boundaries: high-angle GBs are considered as defect sinks with excess free volume. Singh and Foreman (*85, 88, 89*) have observed significant grain size dependence of void swelling in stainless steel decades ago. Han *et al*. (*90*) have also found void-denuded zones (VDZs) at GB in Cu irradiated with He ions at elevated temperature, as shown in Fig. 24. The sink efficiency of GBs depend on their GB character, including misorientation and GB habit plane.

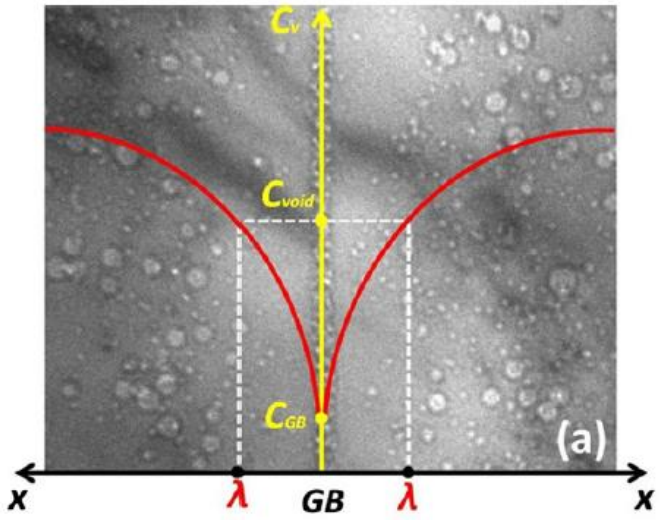

Figure 24 Void-denuded zones on grain boundary in He ion irradiated Cu at 450°C (*90*).

Molecular dynamics (MD) simulations are employed to understand the mechanism of GB enhanced radiation tolerance and studies showed that GBs can emit interstitials into grain interior to annihilate vacancies (*91*). Chen *et al*. (*92*) has also shown that on GBs the interactions are mediated by formation and annealing of chain-like defects. Following the basic idea of introducing abundant defect sinks, significant efforts have been devoted to nanostructured metals which obtain large volume fraction of interfaces. Sun *et al*.(*10*) have reported *in situ* evidence of defect aborption by GBs in nanocrystalline nickel sujected to Kr ion radiation. A reduction of bubble density has also been found in sputter-deposited nanocrystalline Fe film irradiated by He ions (*93*).

Twin boundaries: theretical and experimental evidences show that TBs can serve as defect sinks to radiation induced defects. Theoretically, Serra *et al*. (*94*) have revealed

that **{10$\bar{1}$2}** TBs can act as defect sinks or recombination centers in hcp Zr. Niewczas and Hoagland (*95*) have reported the deconstruction of SFTs by mobile TBs in FCC Cu. As for experimental results, Segall (*96*) has found CTBs are biased sinks for vacancies in quenched Al. King and Smith (*97*) have proposed that CTBs may be sinks for dislocation loops in Al and Cu during *in situ* high-voltage electron radiation. Bailat *et al*. (*98*) have also found a defect denuded zone at the TB in 304 stainless steel. Recently, Yu *et al*.(*99*) have reported *in situ* observation of the removal of SFTs by nanotwins in Kr irradiated Ag, revealing extensive interactions between SFTs and TBs. And the density of defect clusters in Ag has shown a significant dependence on average twin spacing. Fig. 25 shows the reaction of TB with an SFT from its base and apex.

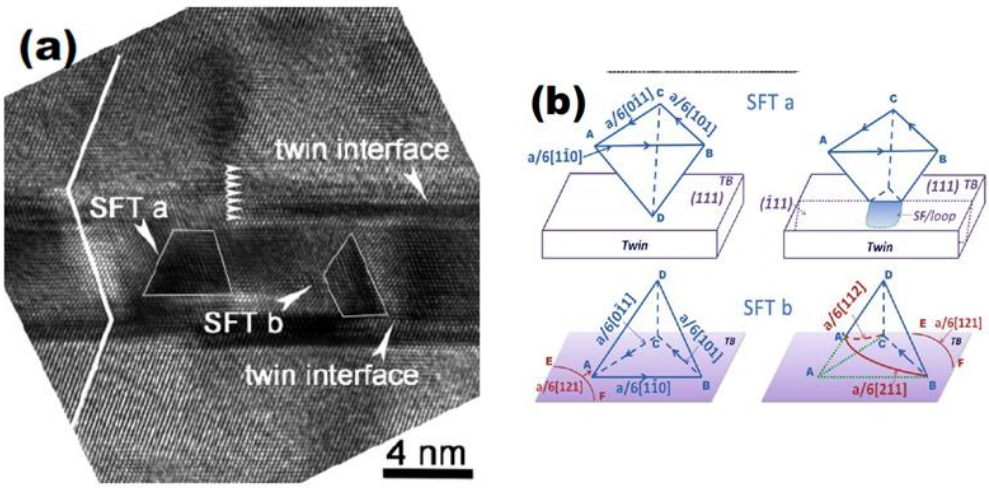

Figure 25 (a) HRTEM image of two truncated SFTs during their interactions with CTBs. SFT-a was truncated from its apex, whereas SFT-b was destructed from its base. Scale bar, 4 nm. (b) Schematics of two types of interactions between SFTs and twin boundaries(*99*).

Current Understanding on Radiation Damage in Metallic Multilayers: layer interfaces have shown significant impact on radiation tolerance of metallic multilayers. We will discribe recent studies on radiation response of multilayers in what follows.

The initial idea to use multilayer interface to mitigate radiation damage was implied in Cu/Ni system by molecular dynamics simulation(*100*). However, no follow-up experiments were reported afterwards mainly due to intermixing among Cu and Ni and degraduation of interface sturcutre. Immiscible FCC/BCC Cu/Nb multialyer system was later chosen as a model system since 2005, to investigate the effectiveness of interfaces in mitigating radiation damage experimently(*101, 102*), followed by a couple of other FCC/BCC multilayer systems (e.g., Cu/V(*103-105*), Cu/Mo(*106*), Cu/W(*107*), Al/Nb(*108*), Ag/V(*109, 110*)). These prelimenary results show that beside superior morphological stability of multilayers, interfaces can (1) serve as defect sinks and mitigate radiation damage and (2) store implanted He atoms to delay bubble nucleation and growth. Meanwhile, a clear size depedence of radiation damage on individual layer thickness was reported.

These observations prompts two fundamental questions to the community (1) How do intefeces act as defect sinks? (2) How do intefaces store He atoms?

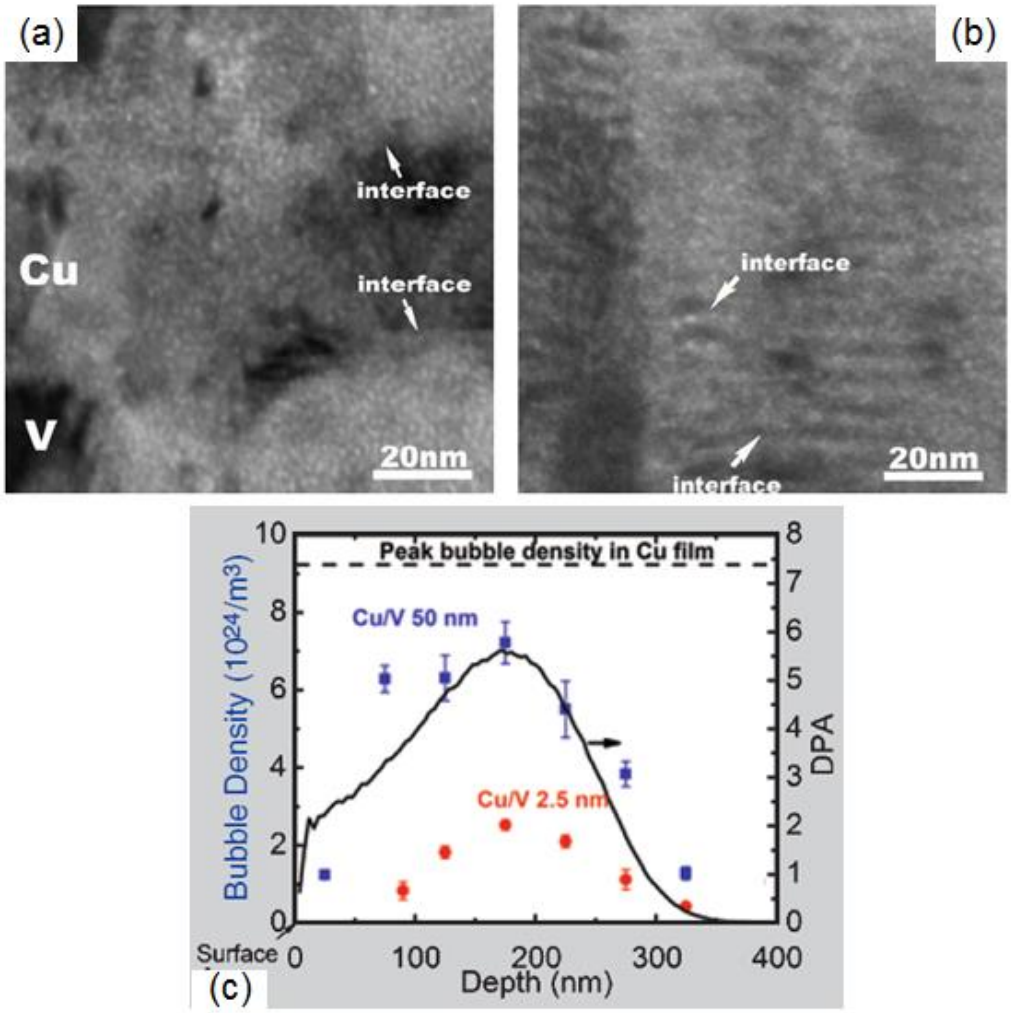

Figure 26 Cross-sectional TEM micrograph of irradiated (a) Cu/V 50 nm and (b) Cu/V 2.5 nm multilayers showing evidence of He bubbles in the peak damage regions. (c) Depth dependent distribution of He bubble density (scattered data points) in irradiated Cu/V 2.5 nm and Cu/V 50 nm multilayers. The bubble density is determined from TEM experiments. The displacement damage in the unit of displacement per atom (dpa) (solid line) predicted by SRIM simulation is also shown in the same chart(*103*, *104*).

Question 1: How do intefeces act as defect sinks? Abundant studies on multilayer systems have shown that layer interfaces can mitigate radiation damage. For instance, He bubble density in He ion irradiated Cu/V 2.5 nm is only half of that in Cu/V 50 nm

multilayer (Fig. 26). MD modeling reveals that that the number of point defects created in collision cascades near Cu-Nb interfaces is 50–70% less than in pure Cu or Nb (*111*). When h decreases to 4 nm, no radiation damage (Frenkel pairs) was observed while radiation damage in terms of Frank pairs is evidented in monolithic Cu and Nb(*112*), as shown in Fig. 27. In a cascade near interface, equal numbers of vacancies and interstitials arrive and recombine at interfaces, removing radiation damage. Further investiagation revealed that the unique characteristics is ascribed to the low formation energy of point defects and excess free volume at interfaces. In addition, layer interfaces can also promote the climb of misfit dislocations by absorbing/emiting interstitials/vacanies(*113, 114*), healing radiation induced damage.

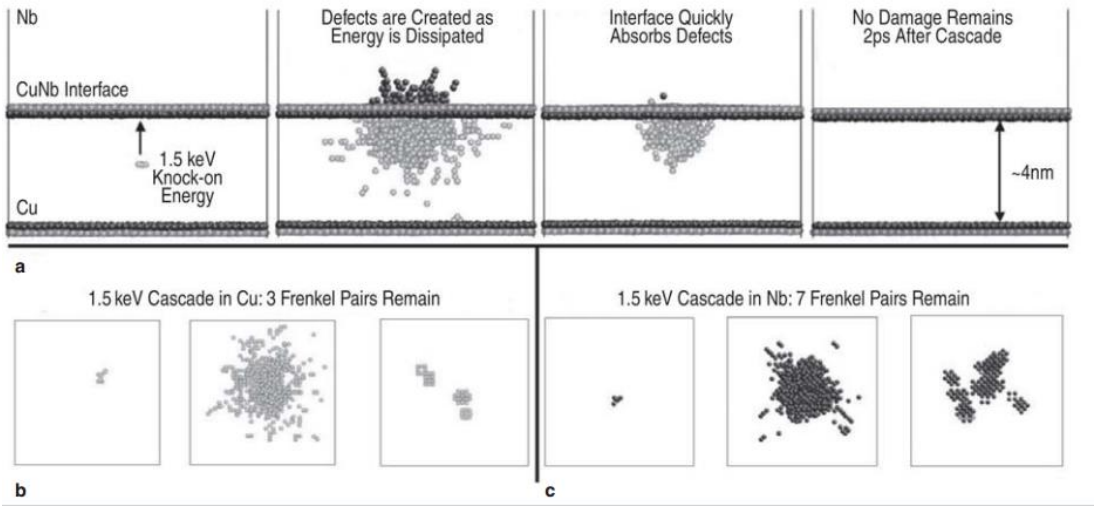

Figure 27 Simulations of 1.5 keV collision cascades in (a) Cu/Nb multilayer composite, (b) perfect crystalline FCC Cu, and (c) perfect crystalline BCC Nb. All atoms whose environments can be described as FCC or BCC have been removed for clarity, leaving behind only defected atomic environments. In (a), interface Cu atoms are dark while interface Nb atoms are light. The CuNb interface quickly absorbs all of the point defects that would have been created by collision cascades occurring at equal energies in perfect crystalline copper or niobium(*112*).

On the other hand, the influence of interface sink strength on the reduction of radiation-induced defect concentrations was also disscussed by using a reaction–diffusion model(*115*). Fig. 28 shows the reduced equilibrium point defect concentration between Cu/Nb interfaces by one-dimensional reaction–diffusion model. This model could be used for future study on defect diffusion in irradiated multilayers over a longer time scale. In general, the performance of interfaces in reducing radiation damage could be comparable to that of high-angle GBs.

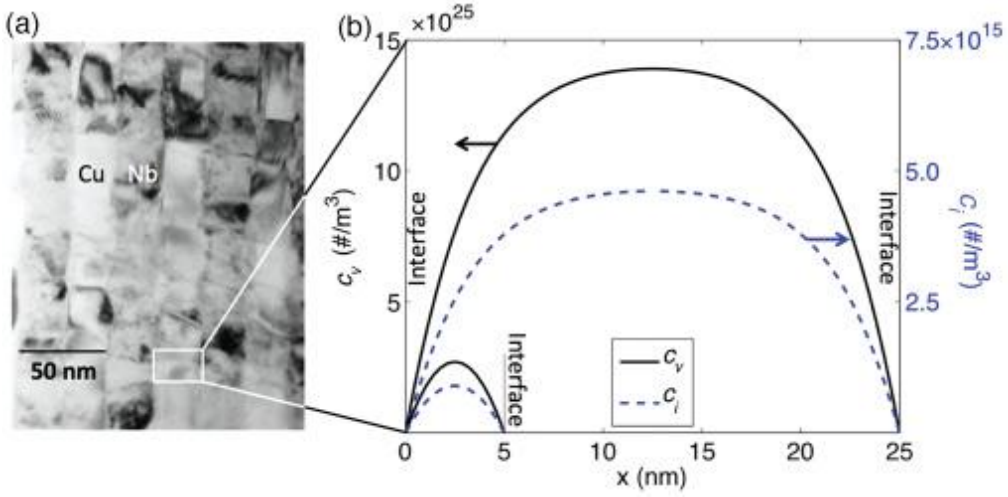

Figure 28 (a) The Cu/Nb multilayer morphology; (b) the concentration of interstitials and vacancies in multilayer, calculeted by the one-dimensional reaction–diffusion model (*115*).

Question 2: How do intefaces store He atoms? In nulcear reactors, transmutation produces He atoms, which are chemically inert and insoluble in most solids. With assistance of vacanies, He atoms could aggregate in forms of He bubbles. It is known that when bubble size is below a critical value, He bubbles are stable under radiation.

Above that value, bubbles evolve into voids by capturing radiation induced vacancies, leading to void swelling and embrittlement. Since He atoms are impurities and cannot be annihilated, after the discovery of bubble-to-void transition(*116, 117*), extensive studies began to focus on how to delay the nucleation of voids by tailoring the formation of He bubble.

Layer interfaces can effectively store He atoms. Surprisingly, He ion irradiated multilayers have shown several orders of magnitude higher He solid solubility compared to bulk metals under irradiation. For instance, Fig. 29 shows that in He ion irradiated Cu/V 50 nm multilayer, He bubbles appear at a threshold He concentration of 0.28 at.%, and in irradiated Cu/V 2.5 nm multilayer, the threshold He concentration could be as high as 1 at.%. This is several orders of magnitude greater than the He solubility in lattices of metals, typically at ppm level. Modeling reveals FCC/BCC interfaces contain high excess atomic volume to trap He atoms and the ability varies to the configuration of misfit dislocations in different multilayer systems. For example, constitutional vacancy concentrations in Cu/Nb and Cu/V interfaces are 5 at. % and 0.8 at. %, respectively(*118*), which is consistant to experimental results in He ion irradiated Cu/V multilayers. Recenly, Demkowicz's group reported that the nucleation and growth of He bubbles at interfaces involves an unexpected new kind of morphological transformation: the ''platelet-to-bubble'' transition (Fig. 30). He atoms can be stored at interfaces in forms of He platelets below a critical He concentration, delaying the nucleation of He bubbles.

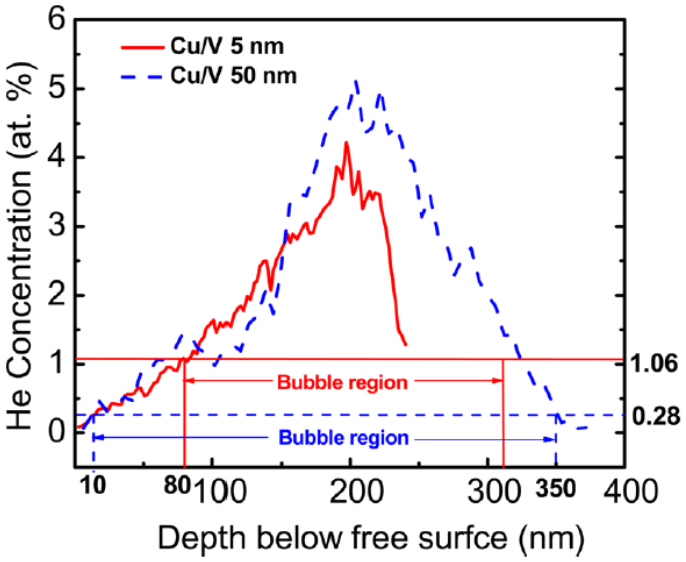

Figure 29 SRIM simulations of depth dependent He concentration in irradiated Cu/V 5 and 50nm multilayer films. The horizontal solid and dashed lines show the threshold He concentration to detect bubbles (obtained from XTEM studies) in irradiated Cu/V 2.5nm and Cu/V 50nm films to be 1 at. % and 0.28 at. %, respectively. SRIM was performed for Cu/V 5 nm instead of Cu/V 2.5nm film due to the depth limitation of the code(*119*).

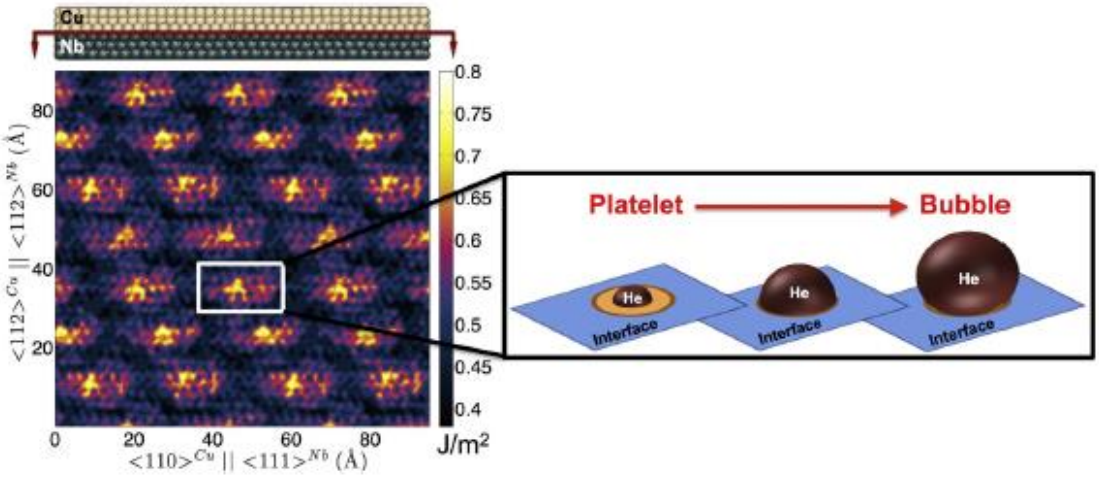

Figure 30 Left: location-dependent energy of Cu–Nb interfaces. The bright, high-energy regions are heliophilic. Right: a He platelet transforms into a bubble once it has grown to occupy the entire heliophilic patch on which it nucleated(*120, 121*).

Beside FCC/BCC interfaces, other multilayer systems have also been studied in parallel, including FCC/FCC interfaces (e.g. Cu/Ni(*100*), Ag/Ni(*122, 123*), Cu/FCC Co(*73*)) and BCC/BCC interfaces (Fe/W(*124*)). In general, immiscible layer interfaces appear to be effective sinks to mitigate radiation induced defect clusters (*125, 126*). It is worth mentioning that *in situ* radiation experiment recently captured the absorption of mobile defect clusters by layer interface in immiscible Ag/Ni multilayers(*123*).

1. 5 Radiation hardening

Irradiation induces an increase in yield strength and degradation of ductility. Obvious radiation hardening and loss of ductility in FCC and BCC steels are shown in Fig. 31, which is ascribed to the radiation induced various defects, including point defects (vacancies and interstitials), impurity atoms, dislocation loops, bubbles/voids and precipitates. Point defects and impurity atoms contribute little to radiation hardening, compared to larger defect clusters, such as dislocation loops and voids. Therefore, here we only take loops, voids/bubbles and precipitates into account as obstacles to dislocation migration.

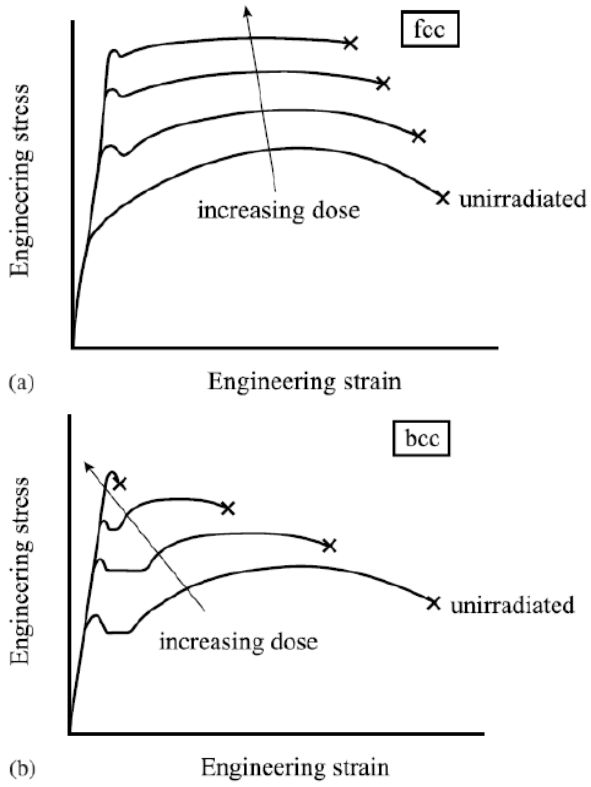

Figure 31 Effect of irradiation on the stress-strain behavior for (a) an austenitic (FCC) stainless steel and (b) a ferritic (BCC) steel(*82*).

Physically, the increase in yield stress $\Delta\sigma_y$ (radiation hardening) arises from the increase in applied stress required for dislocation migration through a field of radiation induced obstacles. When dislocations encounter hard obstacles (Fig. 32a), they undergo Orowan bowing and pinch-off, leaving a ring around the precipitate. When dislocations encounter soft obstacles, such as precipitates (Fig. 32b), they may cut through the obstacle. Based on a dispersed barrier hardening model, the radiation is described as

Equation 11 $\Delta\sigma_y = M\alpha\mu b / l$

where M is Taylor factor, α is the barrier strength, and l is the average spacing between obstacles. Voids and large precipitates act as Orowan (perfectly hard) barriers, with α = 1; for other types of defects, depending on the barrier strength, α varies from 0 to 1.

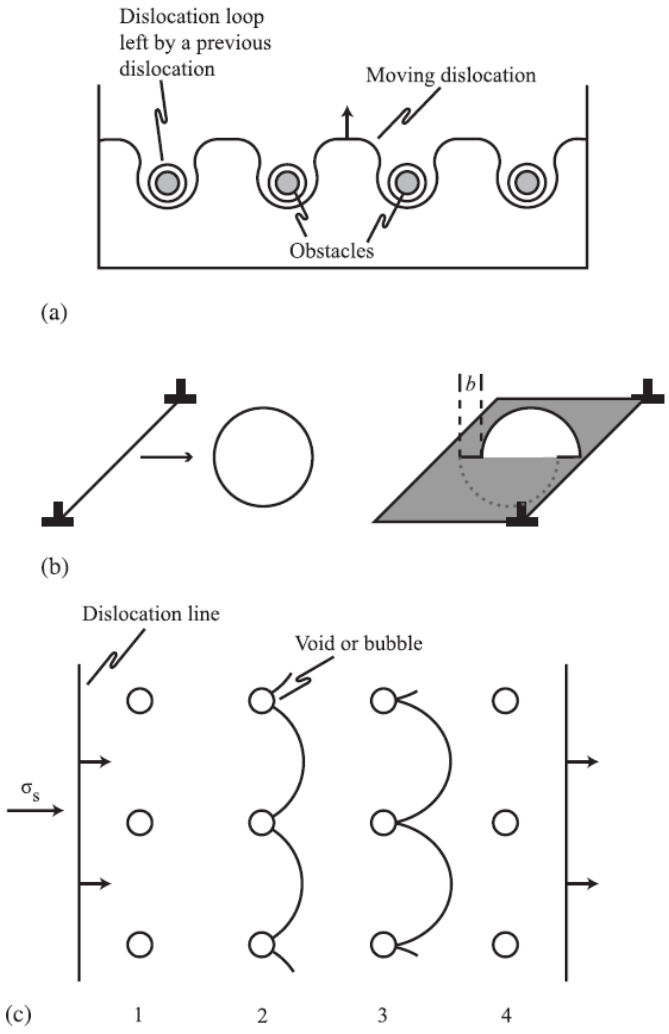

Figure 32 (a) Dislocation bowing around hard obstacles such as large hard precipitates. (b) Dislocation cutting of an obstacle such as a soft precipitate. (c) Dislocation interaction with voids(*82*).

Radiation hardening in multilayers: the study of radiation hardening in multilayer systems is mostly limited to He ion irradiation by nanoindentation technique. In general, He ion irradiation can produce He bubbles at a penetration depth of a few hundred nm, making it possible to probe radiation hardening using nanoindentation.

Size dependent radiation hardening has been quantitatively analyzed in several He ion irradiated metallic multilayer systems, as shown in Fig. 33. The overall trend is the same, that is multilayers with smaller layer thicknesses have less radiation hardening. The models developed by comparing the characteristic dimension (average separation distance between He bubbles) and layer thickness were able to capture the major trend of size dependent strengthening in He ion irradiated nanolayers (*109, 122, 127, 128*). Detailed discussion will be provided as follows.

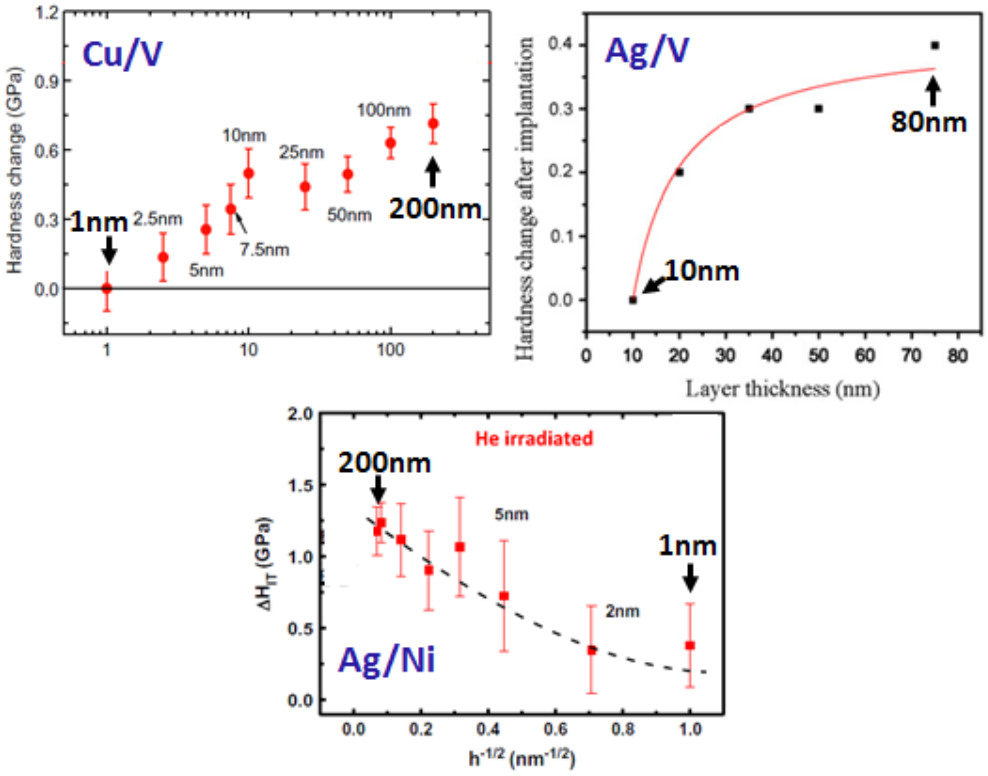

Figure 33 A summary of radiation hardening of He ion irradiated Cu/V(*103, 104*), Ag/V(*109*) and Ag/Ni multilayers(*122*).

Radiation hardening in irradiated multilayer systems depends on strengthening mechanisms before radiation. For large layer thickness h (submicrons to microns), dislocation pile-up mechanism dominates in as-deposited multilayers. After radiation, He bubbles serve as obstacles for dislocation migration. Thus, radiation hardening can be described by equation (1.11), similar to that in coarse-grained metals. Meanwhile, a more specific equation was also developed, considering the stiffness of the bubble in terms of the critical bow-out angle between lines of a dislocation cutting a bubble (*43*),

Equation 12 $$\tau = \frac{\mu b}{2\pi l}\ln\left(\frac{1}{r}\right)(\cos\phi_c)^{1/2}$$

where ϕ_c is half of the critical bow-out angle between dislocation lines cutting through the obstacle (Fig. 34), b is the Burgers vector, μ is the shear modulus, and r is the obstacle radius. This equation can reduce to Orowan formula when ϕ_c is approaching 0.

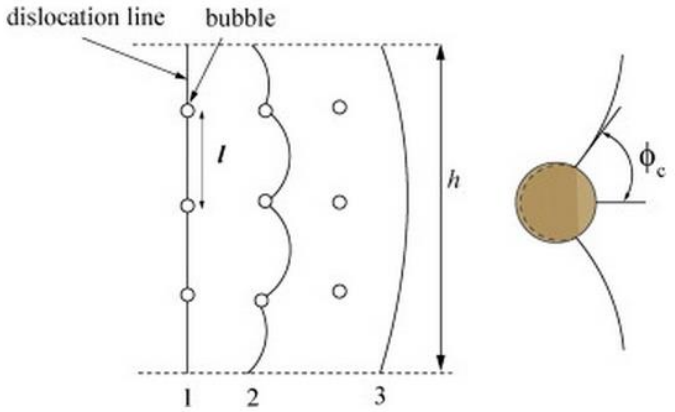

Figure 34 Schematic illustration of glide dislocation interaction with nanometer-scale bubbles of spacing l . Here, *h* refers to the individual layer thickness for multilayers and total film thickness for pure metal films. Numbers 1-3 show the steps of dislocation movement through the bubble distribution. ϕ_c is the semi-critical angle at which the dislocation breaks away from the pinning points(*43*).

When the layer thickness h is a few to a few tens of nm, the model of CLS dominates in as-deposited multilayers; bubbles nucleate and grow at interfaces and inside layers. Bubbles inside layers constitute obstacles that can lead to irradiation-induced hardening, which can be described by (*43*)

Equation 13 $$\Delta\tau = \tau_i \left(1 - \frac{l}{\sqrt{2}h}\right)$$

where τ_i is the average shear strength of obstacles, l is the average obstacle spacing and h is layer thickness.

When the layer thickness h is small (several nanometers), the strength is determined by interface barrier strength. After radiation, the bubble spacing is larger than layer thickness and therefore hardness does not increase after implantation. Similar phenomenon have been discussed in Ag/V(*43*), Cu/Nb(*127*). and Ag/Ni(*122*).

Interestingly Yu *et al.* also noticed that in contrast to size dependent strengthening in He ion irradiated Ag/Ni nanolayers, there is not a strong size dependence in proton irradiated Ag/Ni systems, implying the significance of He bubbles on radiation hardening (*122*).

1.6 Motivation and objective

The goal of this thesis is to investigate the role of interfaces in certain nanostructured materials in mitigating radiation damage, and assist the design of novel nanostructured materials with superior radiation tolerance.

Cu, a metal with low SFE is typically severely damaged under radiation environments. Hence we apply two strategies to alleviate radiation damage in Cu: on the implementation of layer interfaces in Cu/Fe and Cu/Co multilayers, and the introduction of nanovoids in nanotwinned Cu.

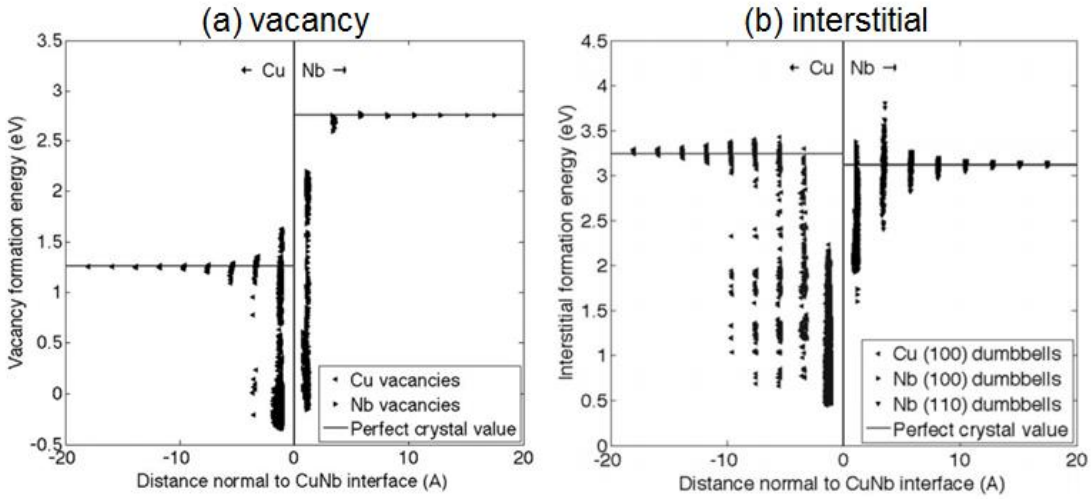

Figure 35 Dependence of (a) vacancy and (b) interstitial formation energies in Cu and Nb as functions of distance normal to the Cu/Nb interface in the KS_1 configuration (*129*).

(1) Cu/Fe multilayers: FCC/BCC interfaces serve as defect sinks for potentially the following reasons: (1) Defect formation energy at interfaces is several times lower than inside crystal lattices (Fig. 35). Point defects are easier to annihilate at interfaces; (2) The range of interaction with other point defects, the so-called core size of trapped defects, is several times larger at interfaces than in crystal lattices; (3) Defect mobility at interfaces is much greater than that in bulk lattices. Thus the probability of recombination of interstitials and vacancies increases significantly at layer interfaces.

Although FCC/BCC multilayers, such as Cu/Nb, Cu/V have been studied, Cu/Fe system is an interesting and unique topic of great importance for the following reasons.

First, previous studies focused on radiation tolerance of incoherent immiscible metallic multilayers, and the influence of coherent immiscible interface on radiation

tolerance remains poorly understood. Fe in Cu/Fe multilayers undergoes a phase transformation from BCC to FCC structure when h is small. Thus an opportunity emerges to investigate the radiation damage in FCC/FCC multilayers with coherent immiscible interfaces. It is unclear if coherent immiscible interfaces are stable during ion beam bombardment such as He ion irradiation, and if stable, can the interfaces also effectively alleviate radiation damage? Second, Fe is the major element in ferritic/martensitic steels (FMS), primary candidates for fuel cladding materials for advanced nuclear reactors (*130-134*). Radiation damage in Fe based multilayer systems may provide insights for the design of radiation tolerant FMS.

(2) Cu/Co multilayers: the motivations of the study on radiation damage in FCC/FCC Cu/Co (100) system include two aspects. First, to date there is only one experimental study on radiation damage in immiscible **FCC/FCC** system, Ag/Ni, which has incoherent interfaces (due to large lattice mismatch between Ag and Ni). In comparison the immiscible Cu/Co has coherent FCC/FCC layer interfaces, permitting us to probe the influence of coherency on radiation tolerance of immiscible FCC/FCC multilayers.

Second, size dependent strengthening mechanism in irradiated Cu/Co multilayers is of significant interest. Recently, we reported that as-deposited immiscible Cu/Co (100) multilayer system has a peculiar size dependent strengthening behavior (*135*). In general we anticipate that Cu/Co (100) (*135*) and Cu/Ni (100) (*27*) multilayer systems should have similar size dependent strengthening. This is because both systems have

comparable Koehler stress (due to the same magnitude of modulus mismatch) and coherency stress (arising from lattice mismatch). However nanoindentation experiment reveals three drastic differences between strengthening behaviors of the two systems (Fig. 36). (1) When individual layer thickness h is several nm, the peak hardness of Cu/Co is significantly lower, by ~ 1 GPa, than that of Cu/Ni. (2) When h is 50-200 nm, the hardness of Cu/Co is greater than that of Cu/Ni nanolayers. (3) Cu/Co (100) system has a much smaller Hall-Petch slope than that of Cu/Ni (100) system. The lower peak strength of Cu/Co is ascribed to the transmission of partial dislocations across the interface, in comparison to full dislocation transmission across Cu/Ni interface, as Cu and Co both have low stacking fault energy (SFE) (γ_{SF}^{Co} = 24 mJ/m^2 , γ_{SF}^{Cu} = 41 mJ/m^2), whereas Ni has inherently high SFE (γ_{SF}^{Ni} = 125 mJ/m^2). At large h, Co has high-density stacking faults, with an average spacing of several nm, and hence contributes significantly to the high strength of Cu/Co nanolayers. He ion irradiation may introduce high-density He bubbles in Cu/Co multilayers, which may block the migration of partials and force partials to constrict. The study will focus on the interaction between dislocations and He bubbles, and corresponding strengthening mechanisms (radiation hardening) of multilayers.

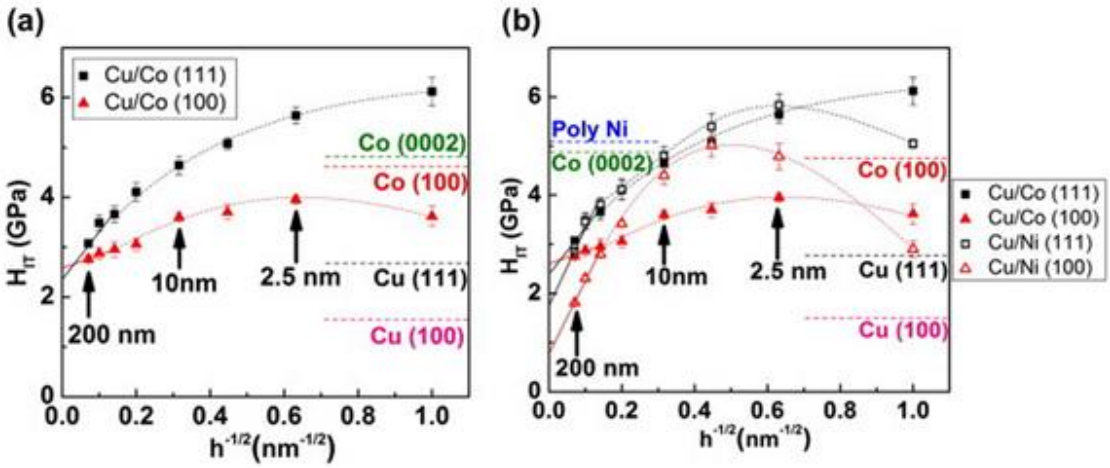

Figure 36 (a) Comparison of indentation hardness of (1 0 0) and (1 1 1) Cu/Co multilayers. (b) Comparison of indentation hardness among (1 0 0) and (1 1 1) Cu/Co and Cu/Ni multilayers. The hardness of (1 1 1) textured Cu/Co and Cu/Ni is comparable, whereas (1 0 0) textured Cu/Co multilayers have a much lower peak hardness than other systems. Softening was absent in the (111) Cu/Co multilayers.

(3) Nanotwinned Cu with nanovoids: in this section, we will introduce a new radiation tolerant nanostructured material with deliberate combination of nanovoids with nanotwins. High-density TBs will provide fast diffusion channels for radiation induced point defects and nanovoids will provide storage sites for the point defects. Nanotwinned structure, instead of nanograins, is chosen due to the fact that TBs have shown outstanding microstructral stability under both radiation (*54*) and annealing conditions (*55, 56*). In contrast, nanograins tend to coarsen at elevated temperature and under irradiation (*74, 77*), compromising radiation tolerance, although nanograins appear to drastically enhance radiation tolerence as shown experimentally (*10, 134*) and theoretically (*91, 136-139*). Fig. 37 shows the ITB structure containing three repetitive partial dislocations (b_1, b_2 and b_3). These dislocations can serve as diffusion channels to

deliver radiation induced defects. The high mobility of interstitials and vacanies enhances the recombination. On the other hand, interstitials migrate faster than vacancies in crystals under radiation, leading to is an imbalance of point defects at TBs. Thus, if we can deliberately introduce nanovoids to store these extra interstitials, the materials may have superior radiation tolerance. This study provides a rejuvenating perspective on the design of metallic materials with extraordinary damage tolerance.

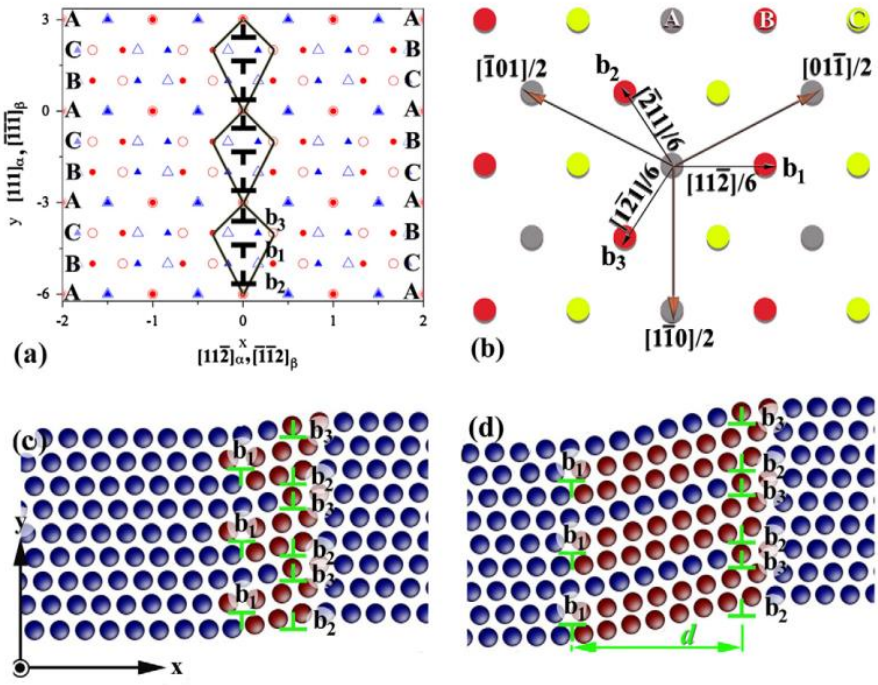

Figure 37 (a) Dichromatic pattern of an incoherent [110] Σ 3{1 1 2}||{1 1 2} twin boundary in FCC lattices. The length units are a/2 [112] for the x-axis and a/2[111] for the y-axis. The solid symbols represent atoms in grain a and the empty symbols represent atoms in grain b. (b) Projection of the (111) plane showing layer-stacking positions for the ...ABCABC... FCC stacking. The plane stacking can be changed by the glide of any of the three Shockley partial dislocations with Burgers vectors a/6<112>. (c and d) Relaxed atomic structures of Σ 3{1 1 2} ITBs under zero applied stress and a shear stress 0.3 GPa. Atoms are colored by common-eighbor analysis. The red atoms represent stacking faults relative to FCC (*140*).

CHAPTER II

EXPERIMENTAL

2.1 Thin film fabrication by magnetron sputtering

Cu/Fe, Cu/Co and Cu thin films were magnetron sputtered at room temperature on HF etched Si (110) and Si (100) substrates (Desert Silicon LLC). The Cu, Co and Fe targets were purchased from Plasmaterials INC. All the targets were 3" in diameter but had different thicknesses. The Cu targets were 1/4" in thickness, with purity of 99.995%; the Fe targets were 1/16" in thickness, with purity of 99.95%, and the Co targets were 1/8" in thickness with purity of 99.98%.

The thin film fabrication was performed by using a custom-built magnetron sputtering system featured with four separate sputtering guns operating with either DC or RF power supplies, as shown in Fig. 38.

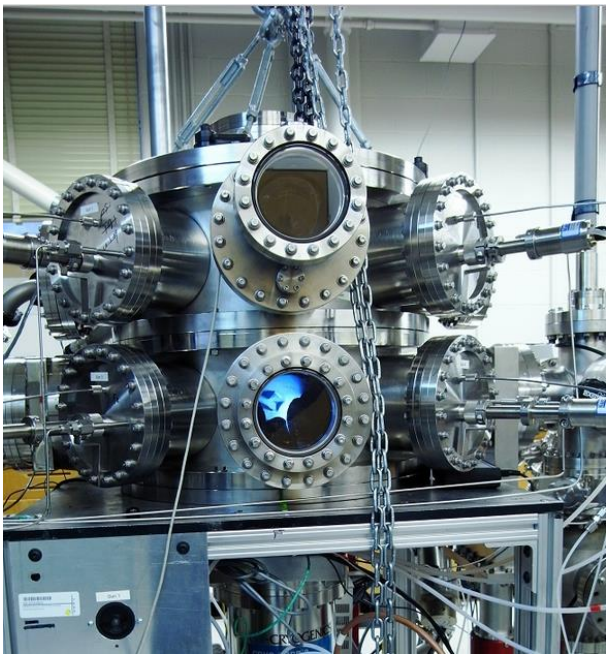

Figure 38 Set-up of four-gun magnetron sputtering system in Texas A&M University.

The basic sputtering process is described as follows: inert Ar gas with partial pressure of 1-3 mtorr is introduced into a vacuum chamber. Under the applied DC voltage between the target (cathode) and substrate (anode), Ar atoms are ionized and become plasma, which containing Ar ions and electrons. The charged and energetic Ar ions fly towards and bombard target atoms, ejecting target atoms into space. These ejected atoms travel to and settle down on the substrate. Fig. 39 schematically demonstrates the process.

We control the deposition rate by varying input power to sputtering guns. Multilayers were deposited by alternatively switching on and off shutters. The whole

sputtering system was controlled by custom-built control system, programmed by LABVIEW.

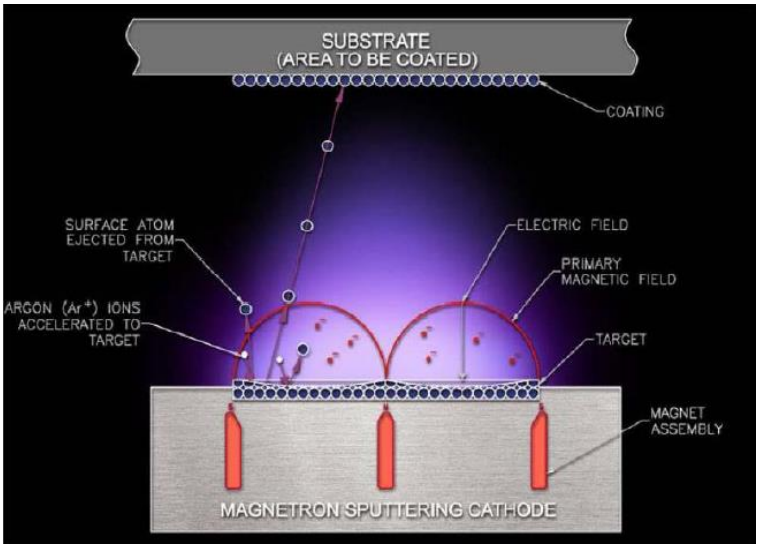

Figure 39 Principles of magnetron sputtering

2.2 Hardness by nanoindentation

The indentation hardness (H_{IT}) was obtained from commercial software, pre-loaded in an instrumented Fisherscope nano/micro hardness tester. Detailed information will be described as follows. The hardness is determined by equation:

Equation 14 $$H_{IT} = \frac{F_{\max}}{A_C}$$

where $F_{\max}$ is the maximum applied force and is the projected area of the contact between the indenter and the test piece determined from the load-displacement curve. A_C cannot be measured directly and is an area function, which describes the shape of the

indenter tip. It can be expressed as a mathematic function relating to the depth of contact of the indenter with the test piece h_c ($A_C = f(h_c)$) (*141*). The selected nanoindentation analysis method is based on elastic contact model developed and refined by Oliver and Pharr in 1992 (*142*), which is commonly used to determine indentation hardness and elastic modulus of thin films. The contact can be modeled using an analytical model for contact between a rigid indenter of defined shape with a homogeneous isotropic elastic half space using equation:

Equation 15 $$S = \frac{2E_r\sqrt{A_C}}{\sqrt{\pi}}$$

where S is the contact stiffness, A_C is the contact area, and E_r is the reduced modulus (*142*). A_C can be obtained by contact depth h_C, which can be expressed by:

Equation 16 $$h_C = h_{\max} - \varepsilon(h_{\max} - h_i)$$

where $h_{\max}$ is the maximum depth, and h_i is the intercept depth, the intercept of the tangent to the load-displacement data at the maximum load (prior to unloading) with the depth axis (*142*). The correction factor ε is a function of the shape of the indenter tip, equal to 3/4 for Vickers indenter in our experiments(*141*). Fig. 40 provides one typical loading-unloading curve for Cu/Co 5 nm multilayer, including all information we need to calculate the indentation hardness. With this information, we obtain the hardness of multilayers at a specific depth.

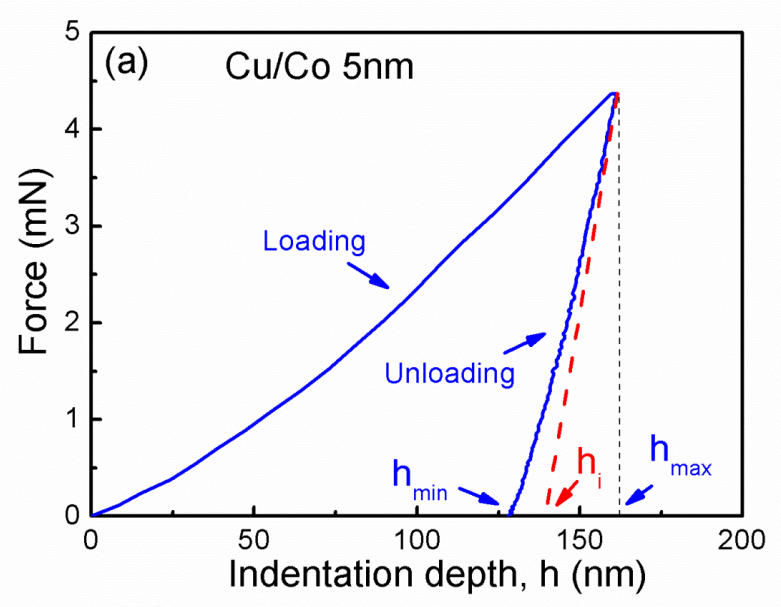

Figure 40 A typical load-displacement curve for Cu/Co 5 nm multilayer.

The indentation hardnesses were then measured and plotted as a function of indentation depth, and the hardness of films is determined by using the hardness plateau value typically obtained over an indentation depth of 10–15% of the total film thickness, where surface and substrate effects are avoided(*143*). A typical example to determine hardness value of Cu/Co multilayers before and after radiation is shown in Fig. 41.

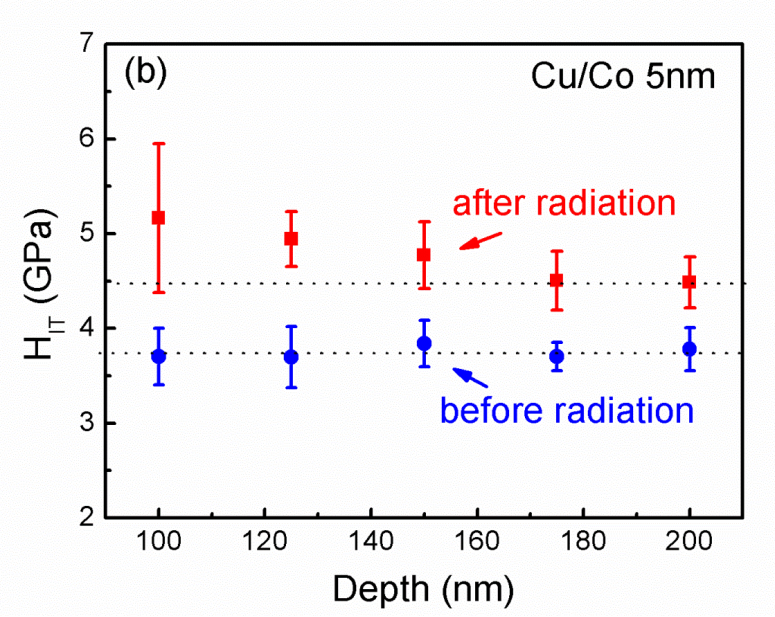

Figure 41 Determination of indentation hardness for Cu/Co 5 nm multilayers before and after He ion irradiation. A hardness plateau is typically observed and the plateau value is considered as the hardness of multilayers (as-deposited or irradiated).

2.3 Structural characterization: X-Ray Diffraction (XRD)

XRD is a non-destructive technique for the structural analyses of materials. When films are exposed to a monochromatic beam of x-rays from a Cu-K_α source, characteristic peaks of the structure arise due to the X-ray wave interference, which follows Bragg's law,

Equation 17 $$2d\sin\theta = n\lambda$$

where n is the order of diffraction, λ is the wavelength for the incident x-ray beam (Cu-K_α), d is the spacing between planes that contribute to diffraction, and θ is the angle between incident beam and the crystallographic plane. The XRD spectrum collected

from the specimen can be compared to standard power diffractions, and thus abundant information will be harvested, e.g. crystal structure, texture, stress, etc. The texture is generally reflected by sharp characteristic peak with high peak density. XRD experiments through this thesis were performed by θ-2θ scanning mode in a Bruker-AXS D8 advanced Bragg-Brentano X-ray powder diffractometer in Department of Chemistry at TAMU. The monochromatic beam of X-ray is generated from a Cu-K_α source, with a wavelength of 1.5406 Å.

2.4 Structural characterization: Transmission Electron Microscopy (TEM)

TEM is a very powerful tool for probing the structure of materials since it can provide morphological information and crystallographic details on a fine scale. Bright field (BF) and dark field (DF) modes are mostly used. In the BF mode, an aperture is placed in the back focal plane of the objective lens and only the direct beam passes the aperture. In this case, the image contrast comes from a weakening of the direct beam due to the interaction between the beam and the sample. Two major aspects need to be considered when analyzing the contrast, including mass-thickness and diffraction contrast. Thicker layers with heavier atoms appear with dark contrast due to stronger scattering for direct beam, while areas aligned in zone also show dark contrast as the diffracted beam are away from direct beam, being block by the aperture.

Selected area diffraction (SAD) is used to determine the crystal structure. The mechanism of SAD is similar to that of XRD, following Bragg's law. The crystal structure can be determined by the spacing of crystallographic planes. For SAD patterns

of polycrystalline or nanocrystalline materials typically contain a couple of rings. Amorphous structure shows diffusive rings.

A scanning transmission electron microscope (STEM) is used to identify the layered structure with Z contrast and perform element mapping. Instead of using spreading beam in regular TEM mode, the electron beam is converged into a nanoscaled spot, scanning over the sample. The contrast in micrographs is sensitive to atomic numbers. With the advantage of the scanning electron beams, STEM is typically accompanied by chemical analysis techniques, such as mapping by energy dispersive X-ray (EDX) spectroscopy and electron energy loss spectroscopy (EELS).

2.5 Irradiation

2.5.1 Estimation of radiation damage

The radiation damage in specimen was designed before radiation experiments. SRIM (Stopping and Range of Ions in Matter) code is widely accepted to estimate radiation damage and incident ion distribution, which can be used to calculate the projectile energy and fluence. SRIM is a program based on Monte Carlo which simulates ion transport and damage production in materials.

We use the Kinchin-Pease option for SRIM calculation (*144*). This method has recently been adopted by the community as a new routine to reliably estimate radiation damage (in unit of dpa) for irradiated materials (*78, 145*). The software provides two output files, including information of displacement and He ion distribution, named

"vacancy.txt" and "ion range.txt", respectively, using which we can calculate the radiation dose in unit of displacements-per-atom (DPA) by

$$\text{Equation 18} \quad DPA = D(1/\text{Å}\cdot ion) \times \frac{Dose(ions/cm^2)}{N(atoms/cm^3)}$$

Where D is displacement obtained from SRIM calculation and N is density. Similarly He ion concentration is calculated by

$$\text{Equation 19} \quad He\% = He(atoms/(cm\cdot ion)) \times \frac{Dose(ions/cm^2)}{N(atoms/cm^3)}$$

These calculation methods are well established to estimate radiation dose and implanted ion distribution.

2.5.2 He ion irradiation

He ion implantation at energy up to 100 keV with a dose of 6×10^{16} ion/cm2 was performed in Los Alamos National Laboratory, collaborated with Dr. Yongqiang Wang's team.

2.5.3 In situ radiation experiments

Researchers have been devoting persistent efforts to understand the microstructural changes as a function of radiation dose. With inserted beamline into microscope, in situ radiation can provide such an opportunity to track the evolution of materials in real time during radiation in a TEM. There are two facilities for *in situ*

radiation experiments in the U.S. out of total10 in the world, one is in Argonne National Laboratory and the other is in Sandia National Laboratory.

In situ radiation experiments on nanotwinned Cu with nanovoids (nv-nt Cu) were performed at the IVEM-TANDEM facility at Argonne National Laboratory (Fig. 42). Available ion sources include hydrogen, the inert gases, and many elements from Al to Au. Kr^{++} with 1 MeV energy is generally preferred by users without specific requirements. A HITACHI H-9000NAR microscope is equipped with the operating voltage of 100-300 keV. The ion beam is ~ 1.5 mm in diameter on the sample centered on the position of the electron beam at the sample.

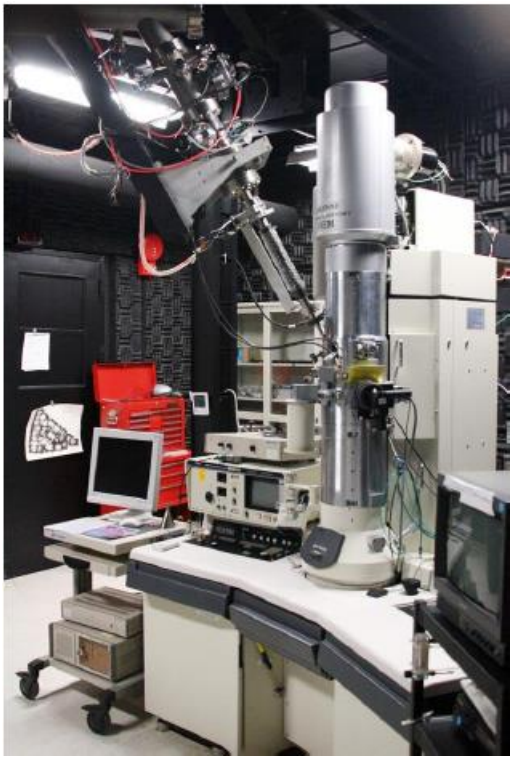

Figure 42 Intermediate Voltage Electron Microscopy (IVEM)-Tandem Facility at Argonne National Laboratory.

In situ radiation experiments on Cu/Fe multilayers were performed Ion Beam Laboratory at Sandia National Laboratory (Fig. 43), collaborated with Dr. Khalid Hattar. A JEOL 2100 microscope is equipped with the operating voltage of 200 keV.

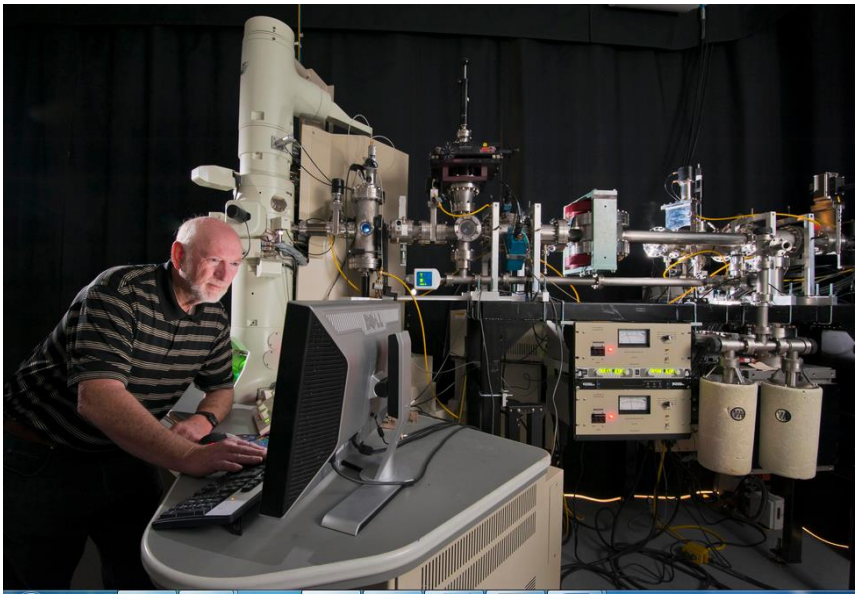

Figure 43 In situ radiation facility in Ion Beam Laboratory at Sandia National Laboratory.

CHAPTER III

MICROSTRUCTURE AND STRENGTHENING MECHANISMS IN CU/FE MULTILAYERS*

3.1 Overview

Nanostructured Cu/Fe multilayers on Si (110) and Si (100) substrates were prepared by magnetron sputtering, with individual layer thickness h, varying from 0.75 to 200 nm. The growth orientation relationship between Cu and Fe at interfaces was determined to be Kurdjumov-Sachs and Nishiyama-Wasserman type. Nanoscale columnar grains in Fe, with an average grain size of 11 - 23 nm, played dominant roles on strengthening mechanism when $h \geq 50$ nm. At smaller h, the hardness of Cu/Fe multilayers with (100) texture approached a peak value, followed by softening due to the formation of fully coherent interfaces. However, abundant twins were observed in Cu/Fe films with (111) texture at h of 0.75 nm, which led to the retention of high hardness in multilayers.

---

*This chapter reprinted with permission from "Microstructure and strengthening mechanisms in Cu/Fe multilayers" by Y. Chen, Y. Liu, C. Sun, K.Y. Yu, M. Song, H. Wang, X. Zhang; Acta Materialia, Volume 60, pages 6312-6321, Copyright 2012 by Elsevier.

3.2 Introduction

Certain metallic multilayers with nanoscale layer thicknesses exhibit high strength close to theoretical values (*14, 24-28*). Deformation mechanisms have been extensively studied in metallic multilayers. Dislocation pile-ups (*29*), moduli mismatch (*36*), misfit dislocations and coherency stress (*37*) are among some of the important factors that contribute to hardening. Some of the models that explain the high strength of multilayers are briefly described as follows.

Hall-Petch model (*25, 29*) operates when individual layer thickness, h, is greater than tens of nanometers. Strengthening arises from dislocations pile-up on the glide plane against grain or interphase boundaries. The hardness increases linearly with $h^{-1/2}$, following the Hall-Petch model. Thus the Hall-Petch slope indicates the resistance of the boundary and is often used to predict the peak strength of multilayers (*12, 25, 30*). However, the strength predicted from slope is sometimes not consist with the measured peak strength, since the multilayers may contain defects, e.g. columnar grains and twins (*31-33*) that have much smaller dimension than individual layer thickness. Certain modifications were made accordingly. Misra *et al* (*34*) developed a deformation mechanism map to determine the dominant feature size for dislocation pile-ups against boundaries. Pande *et al* (*71*) developed a model to incorporate the influence of twins on Hall-Petch slope.

At smaller h, tens of nm, confined layer slip (CLS) model based on Orowan bowing mechanism (*24, 35*) is more appropriate. At this length scale, dislocation pile-up

becomes more difficult. Correspondingly dislocations are confined by and glide between layer interfaces, instead of transmitting across the interfaces because the stress required for bowing of dislocations is less than that for transpassing across interface. Recently Misra *et al* (*12*) developed a refined CLS model by considering interface stress and dislocation-dislocation interactions.

Interface barrier strength (IBS) mechanism operates when h is several nm. The strength of multilayer at such length scales is determined by the inherent resistance of layer interface to the transmission of single dislocations. Various factors, including Koehler stress (*36*), coherency stress and misfit dislocations (*37*), etc. are considered to estimate the interface barrier strength. Koehler stress arises from a significant repulsive image force for a dislocation to slip from the lower modulus phase to higher modulus counterpart. Meanwhile coherency stresses alternating from tension to compression periodically often exist and lead to resistance to dislocation propagation across interfaces. When the layer thickness is above critical thickness for coherency, misfit dislocation arrays often appear to accommodate strain between layers. The interaction of misfit and gliding dislocations would also increase the interface strength.

FCC/BCC multilayers e.g. Cu/Nb (*39*), Cu/Cr (*40, 41*), Cu/V (*42*), Ag/V (*43*), with opaque and immiscible layer interfaces attract significant attention. The discontinuity of slip systems across interface and the lower shear resistance of layer interface (referred to as weak interface), in e.g. Cu/Nb, promote the dissociation or spread of the core of gliding dislocations at the interface (*44, 45*). A dislocation once

absorbed by a weak layer interface, loses its singularity, making it difficult to be reemitted in the opposite layers. Therefore, the "weak interface" offers a strong barrier to the transmission of dislocations. Meanwhile Cu/Fe multilayers were studied in several occasions. Thick Cu/Fe multilayers with h of several microns were fabricated by rolling of alternatively bonded Cu and Fe sheets (*146*). Gao *et al* (*147*) fabricated Cu/Fe multilayers with h over a range of 5 – 40 nm. Their study showed a very high peak hardness, ~ 7.3 GPa, with however little explanation. Shamsutdinov *et al* (*148*) studied Cu/Fe multilayer with fixed Cu sub-layer thickness of 5 nm and varied Fe sub-layer thickness from 13 to 54 nm and found out that grain size and existence of voids in the multilayer determined the stress state in the film. Cu/Fe multilayer was also a popular subject due to its giant magnetoresistance (GMR) effect (*149, 150*).

In spite of these studies, the microstructure of Cu/Fe multilayers were less well understood, and a systematic study of their deformation mechanism is lacking. In this paper, we provide extensive microscopy studies of layer interface and microstructure of Cu/Fe multilayers with two types of textures, and identify the influence of layer interface as well as other defects, such as nanoscale columnar grain boundaries and high density twins, on deformation mechanisms of the system.

3.3 Experimental

Cu/Fe multilayers with equal individual layer thickness (h), varying from 0.75 to 200 nm were magnetron sputtered at room temperature on HF etched Si (110) and Si (100) substrates. The chamber was evacuated to a base pressure less than 8×10^{-8} torr

prior to deposition. Before the deposition of Cu/Fe multilayers, a 100 nm thick Cu seed layer was deposited. The total film thickness was ~ 500 nm when h = 0.75 nm, ~ 1 μm when h = 1 – 5 nm, ~ 1.5 μm when h = 10, 25 nm, ~ 2 μm when h = 50, 100 nm, and ~ 4 μm when h = 200 nm. The total film thickness was designed so that indentation experiment will probe at least one bilayer, but the maximum indentation depth is limited to 10-15% of total films thickness to avoid substrate effect. The deposition rate of Fe is 0.5 nm/s for all layer thicknesses. For Cu, the deposition rate was ~ 0.33 - 1.1 nm/s. X-ray diffraction (XRD) experiments were performed in a Brukers D8 Discover X-ray powder diffractometer at room temperature. Transmission electron microscopy (TEM) experiment was carried out on a JEOL 2010 transmission electron microscope operated at 200 kV. Scanning transmission electron microscopy (STEM) experiments and energy dispersive X-ray (EDX) analyses were performed on an FEI Tecnai G2 F20 microscope operated at 200 kV with a Fischione ultra-high resolution high-angle annular dark field (HAADF) detector (0.23 nm resolution in STEM image mode) and an Oxford Instruments EDX detector with a spatial resolution of ~ 1 nm for chemical analysis. Film hardness and elastic modulus were measured based on an average of 12 - 15 indents at different indentation depths by a Fisherscope HM 2000XYp micro/nanoindentor with a Vickers indenter tip. Several bilayers were typically probed during nanoindentation, while special care was taken to avoid substrate effect. For Cu/Fe film with film thickness ~ 500 nm, the Hysitron Triboindenter was employed to confirm the hardness value. Cross-sectional TEM (XTEM) samples were prepared by dimpling and low energy (3.5 keV) Ar ion milling and subsequent ion polishing.

3.4 Results

3.4.1 Microstructural characterization

XRD patterns of as-deposited Cu/Fe multilayers on Si (110) substrate are shown in Fig. 44. When h ≥ 25 nm, Cu (111) and Fe (110) peaks were observed. At smaller h, the relative intensity of Fe (110) peak diminished rapidly, whereas the Cu (111) peak intensity became much stronger. When h ≤ 10 nm, Fe (110) peak disappeared and Cu (111) became the primary peak. Peaks at 2θ of ~ 42.5^{o} and 45.5^{o} were from substrate.

Fig. 45 compares the selected area diffraction (SAD) patterns of various multilayers on Si (110) substrate. Cu 200 nm/Fe 200 nm (referred to as Cu/Fe 200 nm hereafter) multilayer showed polycrystalline structures while others exhibited increasing intensity of Cu (111) and Fe (110) textures at smaller h. Careful examination showed that Cu (111) and Fe (110) did not overlap until h = 5 nm, below which there is increasing magnitude of coherency. When h = 0.75 nm, single crystal like diffraction pattern was identified. Furthermore the diffraction pattern suggests the formation of both Σ3 (111) type of coherent twin boundary (CTB) and Σ3 (112) incoherent twin boundary (ITB) (*51, 151, 152*).

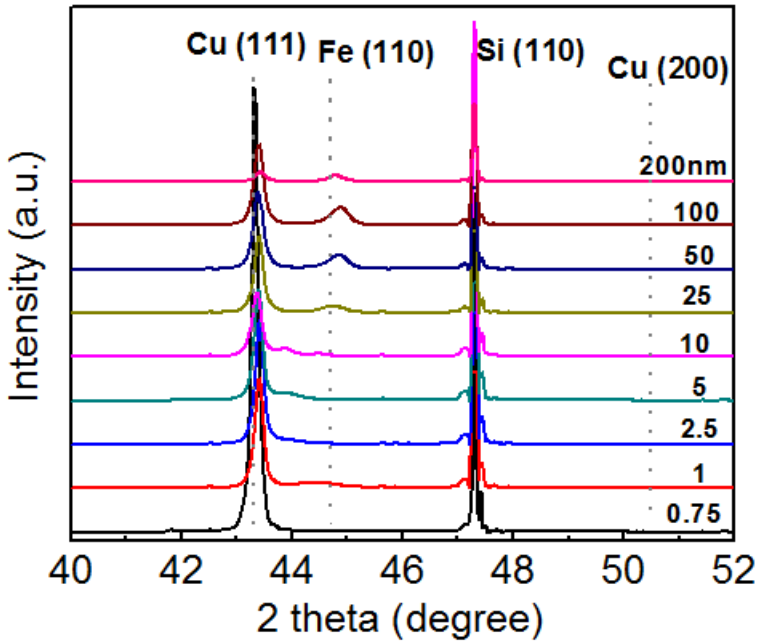

Figure 44 XRD patterns of Cu/Fe multilayers deposited on Si (110) substrates. Only Cu (111) and Fe (110) were observed. At smaller layer thickness, the peak intensity of Fe (110) decreased, whereas that of the Cu (111) increased slightly. The Cu/Fe 0.75nm multilayer exhibits an extremely strong Cu (111) texture. Note that the peak intensity of Cu (111) peaks is partially contributed from 100 nm thick Cu seed layer.

XRD patterns of Cu/Fe multilayers on Si (100) substrate (Fig. 46a) showed that films had polycrystalline nature when $h \geq 5$ nm, very similar to that observed in multilayers on Si (110) substrate. The intensity of Cu (111) and Fe (110) peaks completely diminished only when $h \leq 1$ nm, indicating the formation of fully coherent (100) type of interface. Meanwhile, the Cu (200) peak intensity increased dramatically as h decreased to below 2.5 nm as shown in Fig. 46b.

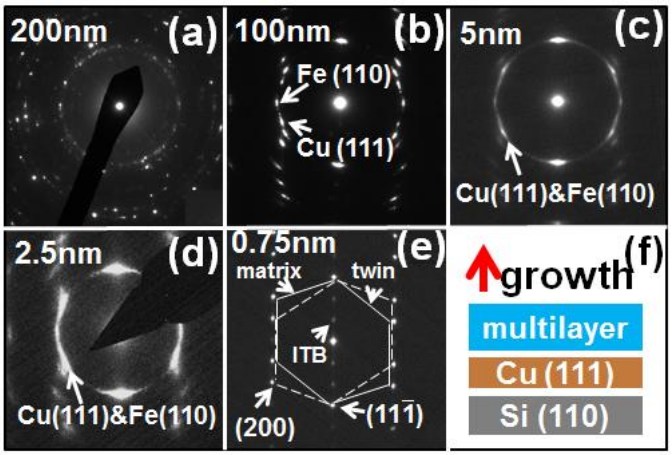

Figure 45 SAD patterns of Cu/Fe multilayers on Si (110) substrates with a 100 nm Cu (111) seed layer: (a) Cu/Fe 200 nm showed polycrystalline structure; (b)-(d) Cu/Fe 100, 5 and 2.5 nm multilayers showed Cu (111) and Fe (110) texture; (e) Cu/Fe 0.75 nm film showed twinned diffraction pattern with single crystal like diffraction spots; (f) schematic exhibition of growth direction and film orientation. When h> 5 nm Cu (111) and Fe (110) diffraction dots were separated.

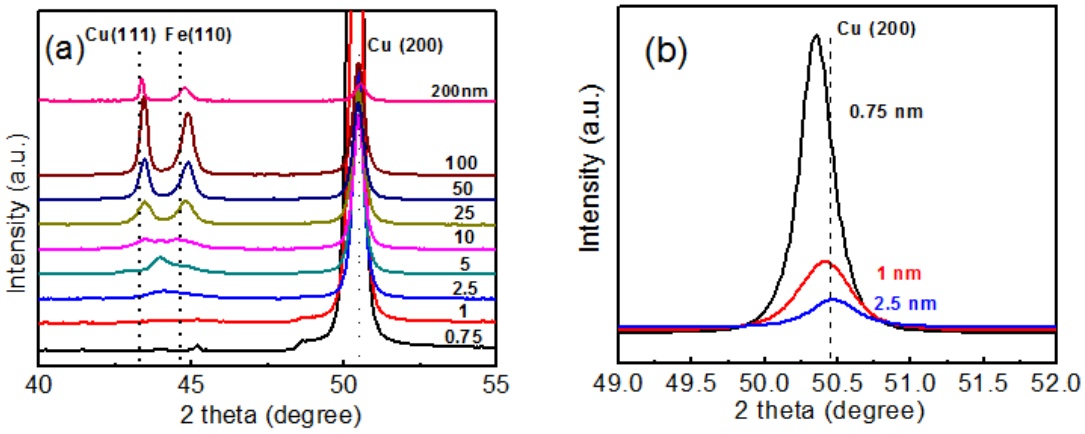

Figure 46 (a) XRD patterns of Cu/Fe multilayers on Si (100) substrates with a 100 nm thick Cu (100) seed layer. Films had polycrystalline nature when h > 5 nm as evidenced by the appearance of Cu (111) and Fe (110) peaks. When h ≤ 2.5 nm, the intensity of the Cu (200) peak increased dramatically. (b) The position of Cu (200) peaks shifted to lower angle at smaller h.

In what follows, we present extensive microscopy studies of the microstructure of multilayers. In Cu/Fe 100 nm multilayer on Si (110) substrate (Fig. 47a-b), twins were occasionally observed in Cu, wherein Fe was composed of nanoscale columnar grains. Statistical analyses in Fig. 47c and d shows that the average columnar grain size of Cu is ~ 47 nm, three times of that in Fe, ~ 16 nm.

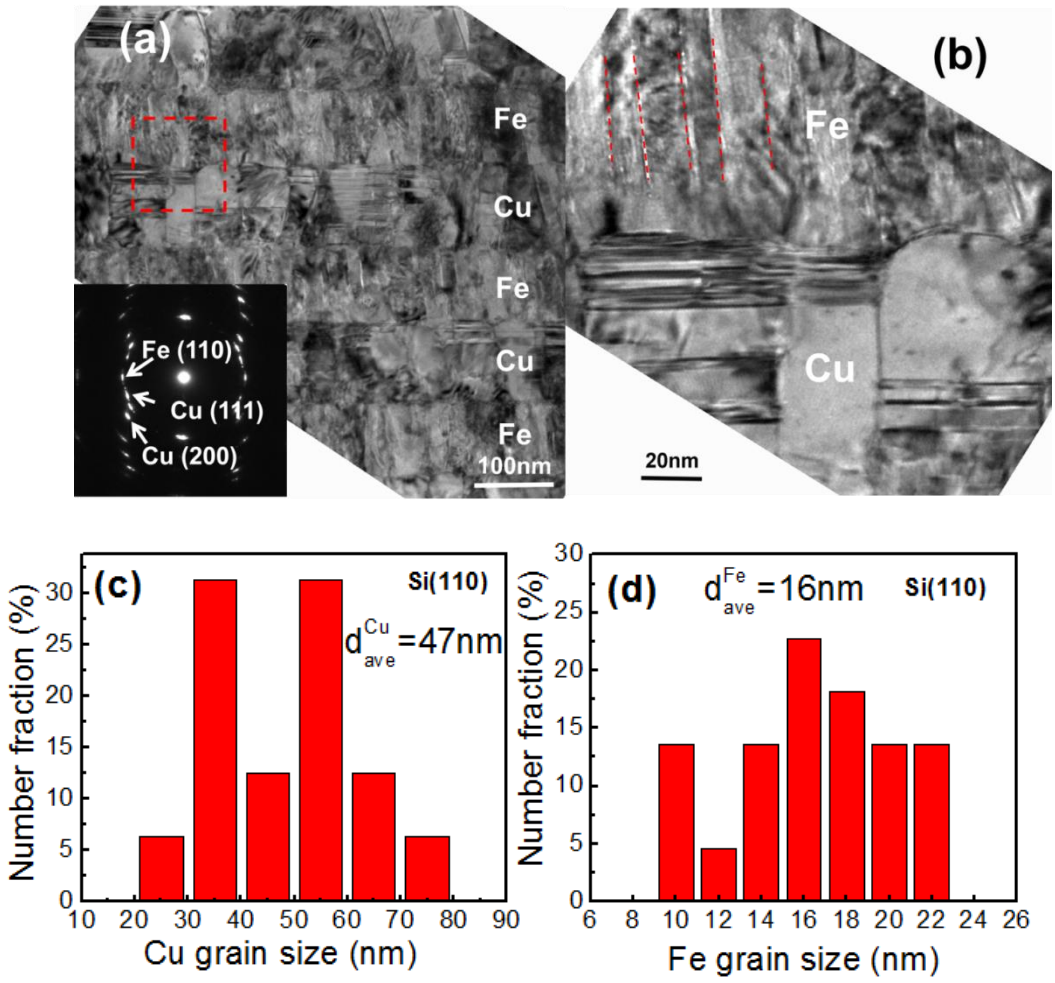

Figure 47 (a) A cross-sectional TEM (XTEM) micrograph of Cu/Fe 100nm on Si (110) substrate shows abundant twins in Cu layers. (b) A magnified view of the box in (a) reveals the formation of nanoscale columnar grains in Fe layers; (c) and (d) display statistical distribution of grain in Cu and Fe, and the average columnar grain sizes of Cu and Fe are ~ 47 and 16 nm, respectively.

Close examination of diffraction pattern of the same specimen (Fig. 48a-b) reveals two types of orientation relationship along interface, one being Kurdjumov-Sachs (K-S) relation - $(\bar{1}1\bar{1})_{Cu}//(110)_{Fe}$, $[011]_{Cu}//[\bar{1}11]_{Fe}$, and the other one being Nishiyama-Wasserman (N-W) relation - $(\bar{1}1\bar{1})_{Cu}//(110)_{Fe}$, $[011]_{Cu}//[001]_{Fe}$, as shown schematically in Fig. 48c. In Fig. 48d, an HRTEM image exhibits the coexistence of the K-S and N-W interfaces. A single grain in Cu (the top layer) formed two types of interface with neighboring Fe grains underneath it. The inserted FFTs confirmed the existence of two different orientations in neighboring Fe grains.

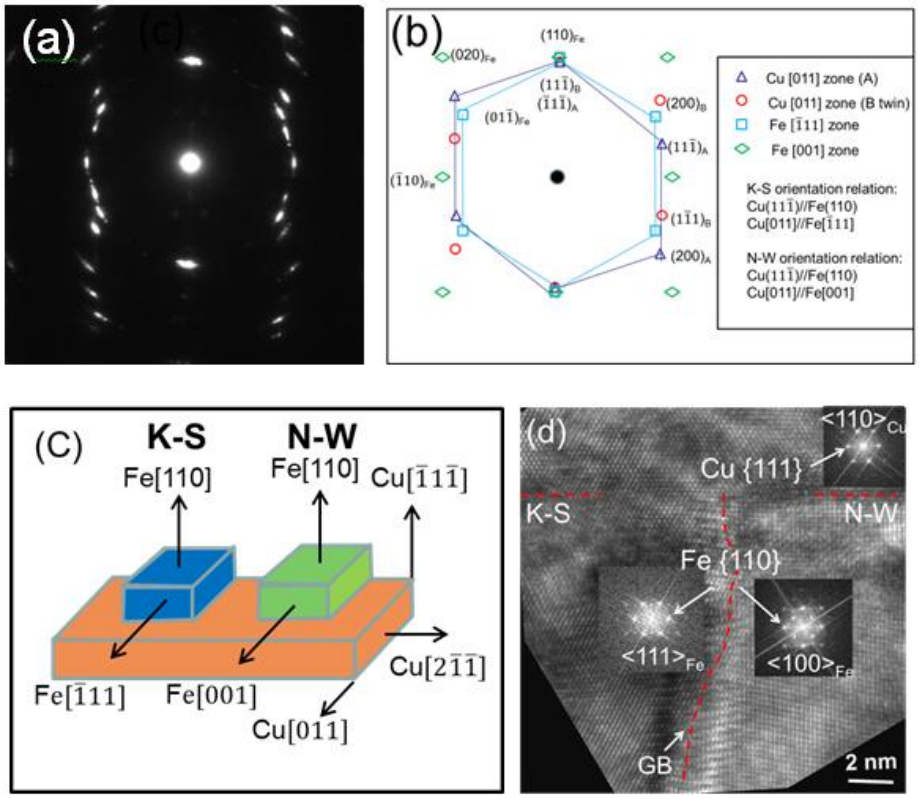

Figure 48 (a) SAD pattern and (b) its corresponding indexes in Cu/Fe 100 nm films on Si (110) substrate illustrate two types of orientation relationship between Cu and Fe, namely K-S and N-W orientation. (c) Schematics illustrate the orientation relationships: K-S ($(\bar{1}1\bar{1})_{Cu}$// $(110)_{Fe}$, $[011]_{Cu}$//$[\bar{1}11]_{Fe}$) and N-W ($(\bar{1}1\bar{1})_{Cu}$//$(110)_{Fe}$, $[011]_{Cu}$//$[001]_{Fe}$). (d) HRTEM micrograph showed the formation of K-S and N-W relationship between Cu and Fe in neighboring grains. Fe was observed along <111> and <100> zone axes, whereas Cu was examined along <110> zone axis as shown by the inserted fast Fourier transforms (FFTs).

In parallel Cu/Fe 100 nm multilayer on Si (100) substrate has much weaker texture (Fig. 49a) and less twins in Cu layer (Fig. 49b). The average columnar grain size in Fe remained small, ~ 15 nm, comparing to ~ 56 nm in Cu as shown in Fig. 49c and d.

As summarized in Table 1, the average columnar grain sizes in Cu and Fe decreased with decreasing h, from 200 to 50 nm, and the grain size of Cu is 3-5 times that of Fe. To see whether the grain size of Fe decreases further at smaller h, we examined Cu/Fe 10 nm multilayer on Si (110). As shown in Fig. 50, the columnar grain size of Fe is comparable or slightly greater than h. The same micrograph also delineates the formation of K-S and N-W type of orientations along interfaces.

Table 1 A summary of grain sizes at different layer thicknesses.

Sample	Cu grain size (nm)	Fe grain size (nm)
Cu/Fe 200 nm // Si(110)	115	23
Cu/Fe 100 nm // Si(110)	47	16
Cu/Fe 50 nm // Si(110)	30	11
Cu/Fe 100 nm // Si(100)	56	15

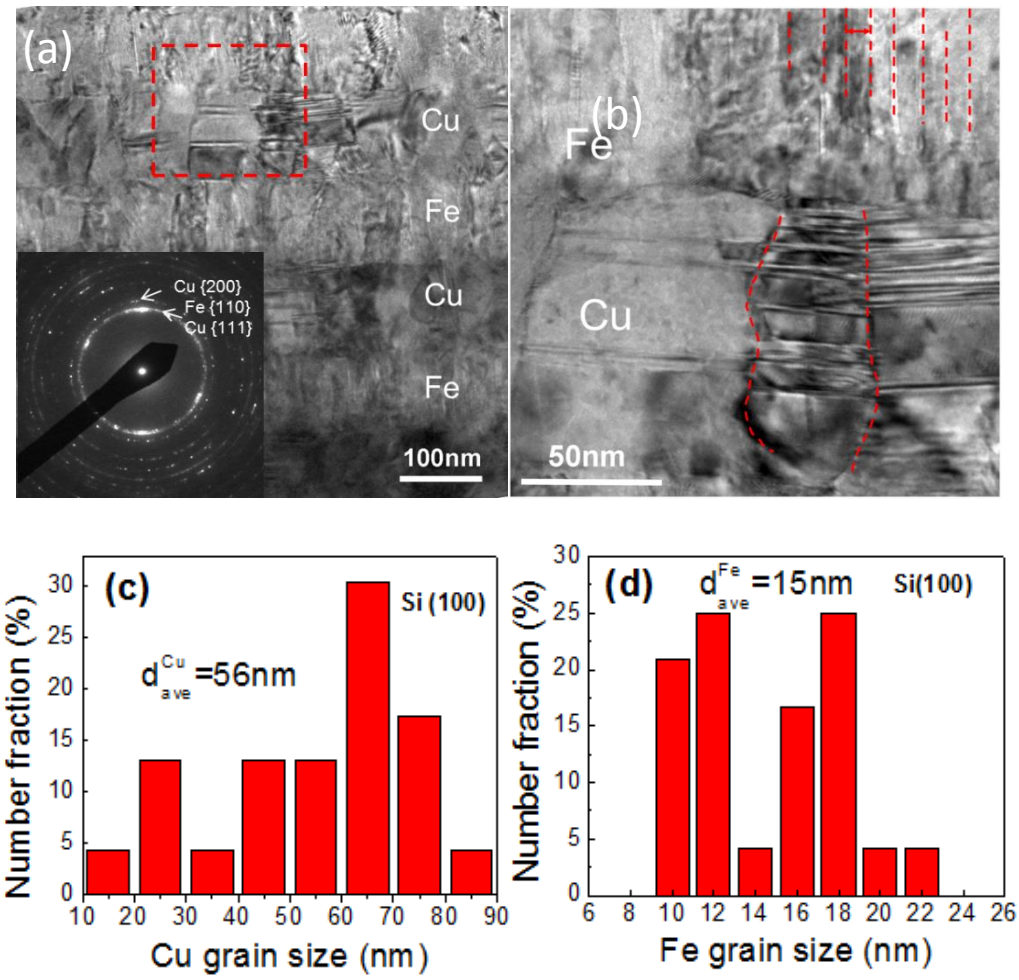

Figure 49 (a) An XTEM micrograph of Cu/Fe 100 nm multilayer on Si (100) substrate shows polycrystalline films as confirmed by the SAD pattern, and some twins were observed in Cu layers. (b) A magnified TEM micrograph shows that Fe layer was again composed of nano-columns. (c) and (d) are statistical distributions that show an average grain size of ~ 56 and 15 nm in Cu and Fe respectively.

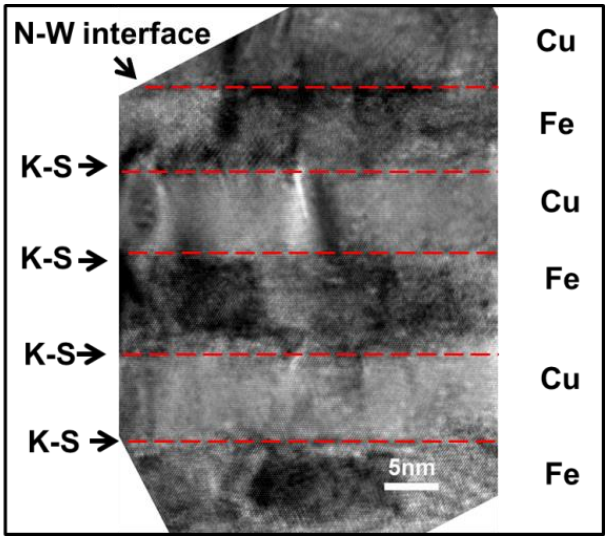

Figure 50 XTEM micrograph of Cu/Fe 10 nm multilayers grown on Si (110) substrate. The grain sizes of Cu and Fe were larger than layer thickness. Both K-S and N-W orientation relationships were observed.

We performed STEM experiments to evaluate the morphology and chemistry of multilayers. Fig. 51 shows a STEM image and compositional line profile of a Cu/Fe 5 nm multilayer. Layer structures are evident in spite of a small difference in atomic number between Cu (Z = 29) and Fe (Z = 26). No significant inter-diffusion occurred as suggested from the compositional profile in Fig. 51b.

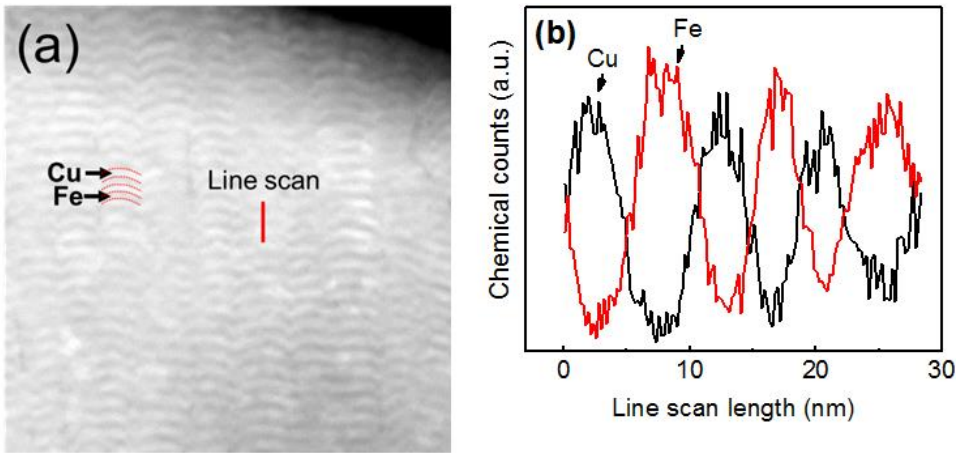

Figure 51 (a) A cross-sectional STEM micrograph of Cu/Fe 5nm film on Si (110) substrate shows discrete layer structure. (b) Compositional line profile displays a chemically modulated layer structure with insignificant intermixing.

Cu/Fe 0.75 nm multilayer deposited on Si (110) had high density twins as shown in Fig. 52a when examined along FCC <110> zone axis (// Si <111>). Along FCC <112> zone axis (// Si <112>), only discrete layer structure could be observed (Fig. 52b), wherein twins were not visible. As shown in Fig. 52c and d, the average twin thickness and columnar grain size are ~ 6 and 40 nm, respectively.

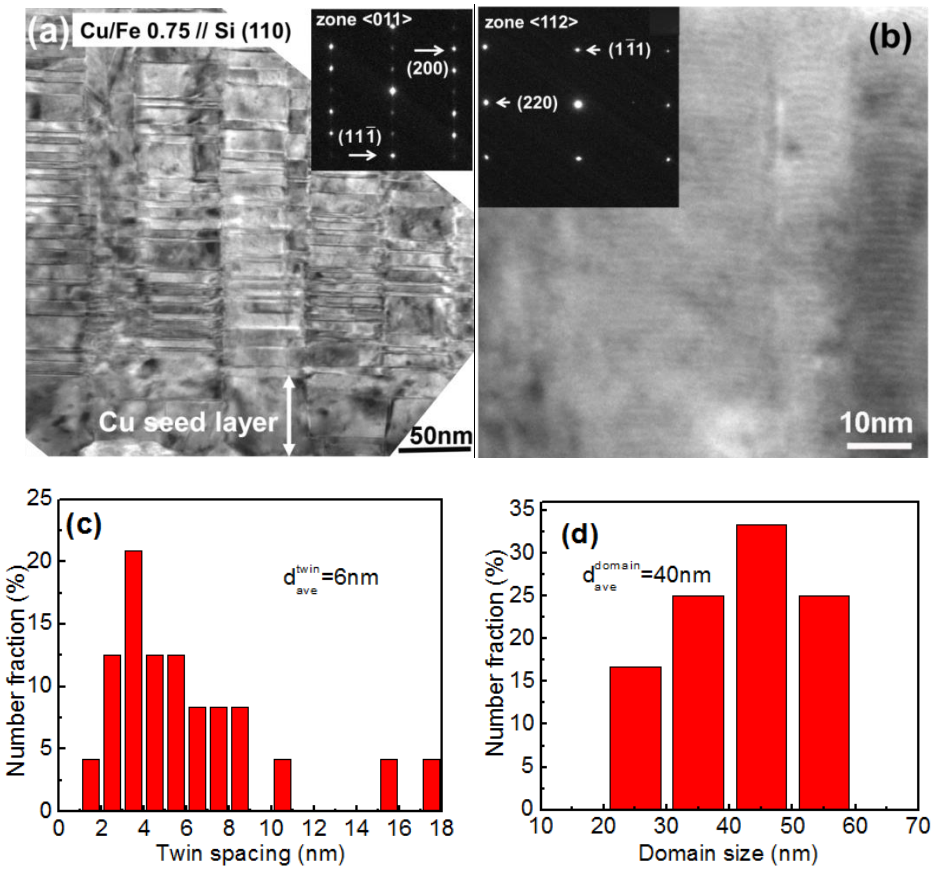

Figure 52 (a) An XTEM micrograph of Cu/Fe 0.75 nm multilayer on Si (110) substrate examined along the FCC <110> zone axis exhibits high density of growth twins. The SAD inset also shows the evidence of incoherent twin boundaries. (b) When the same film was studied along the FCC <112> zone axis, discrete layer structure was observed. (c) and (d): statistical distributions show that the average twin spacing and domain sizes are ~ 6 and 40 nm, respectively.

In comparison in Cu/Fe 0.75 nm multilayers grown on Si (100) substrate, only layer structure was observed and there is no evidence of twins when examined along FCC <001> zone axis (Fig. 53). The SAD pattern indicates the formation of single crystal like structure.

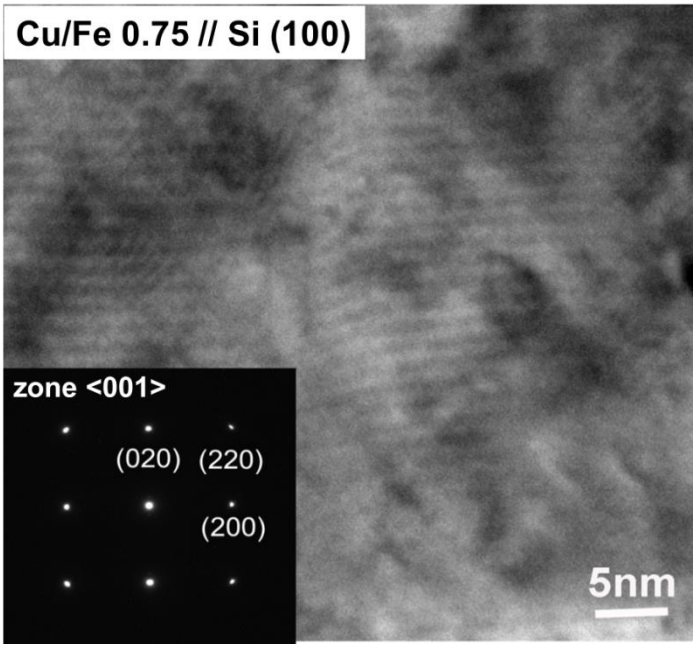

Figure 53 An XTEM micrograph of Cu/Fe 0.75 nm film on Si (100) substrate examined along the FCC <100> zone axis exhibits clear layer structure. The inserted SAD pattern shows single crystal like diffraction pattern.

3.4.2 Multilayer hardness

The hardnesses of Cu/Fe multilayers on Si (110) and (100) substrates are shown as a function of $h^{-1/2}$ in Fig. 54, and are compared to highly textured Cu/Ni (100) multilayers (*27*) and (111) textured Cu/330 stainless steel (SS) multilayers (*30*). Several distinct characteristics are noteworthy.

First, the hardnesses of Cu/Fe multilayers on different substrates overlapped when h > 2.5 nm. At smaller h (< 2.5 nm), softening was observed for the film on Si (100) substrate, which is similar to Cu/Ni on Si (100). However, the hardness of Cu/Fe films on Si (110) retained their high strength at smaller h.

Second, the hardness of two sets of Cu/Fe multilayers reaches a plateau when h = 25 nm, similar to what was observed in Cu/330 SS (*30*). Meanwhile, the maximum strength of the four sets of multilayers is nearly identical.

Third, at large layer thickness (≥ 50 nm), the Hall-Petch slope is ~ 10.3 GPa·nm$^{1/2}$ for Cu/Fe systems, much lower than the slope of Cu/Ni (~ 15 GPa·nm$^{1/2}$) and Cu/330 SS multilayers (~ 19.5 GPa·nm$^{1/2}$).

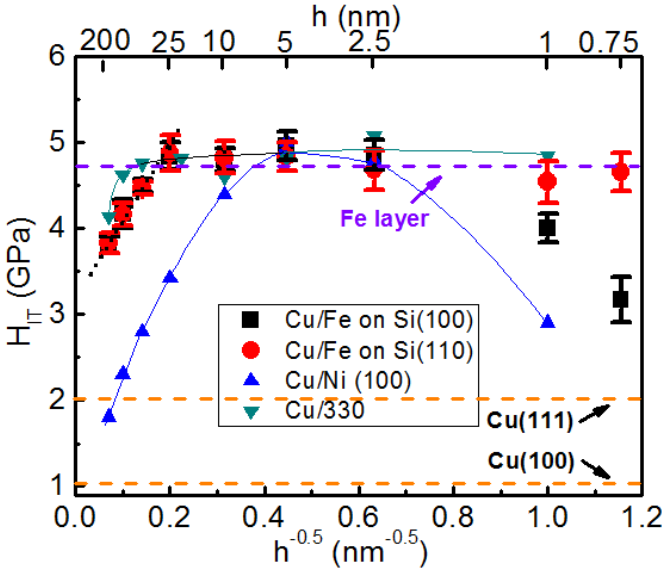

Figure 54 The hardnesses of sputtered Cu/Fe multilayers deposited on Si (100) and Si (110) substrates are plotted as a function of $h^{-0.5}$, and compared to that of Cu/Ni (100) and Cu/330 SS multilayers.

3.5 Discussion

3.5.1 Evolution of microstructure with layer thickness

Columnar grain size clearly evolves with h. When h ≥ 50 nm, the columnar grain size of Cu decreased from 115 to 30 nm at smaller h. Meanwhile the grain size of Fe also decreased from 23 to 11 nm. When h decreased to below 50 nm, the grain size of Fe did not decrease further.

The grain size of Cu is approximately 3 times of that in Fe in Cu/Fe 100 nm multilayer on Si (110) substrate. As the neighboring Fe grains frequently formed both K-S and N-W orientation relationships adjacent to the same Cu grain, thus there must be high angle grain boundaries between Fe grains. The co-existence of K-S and N-W type orientation relationships were also seen in V/Ag system at interfaces with various curvatures (*43*).

Cu/Fe 0.75 nm multilayers on both substrates exhibited single crystal like structure. Fe had face centered cubic (FCC) structure, and hence formed coherent (transparent) interface with Cu. The critical layer thickness for the formation of misfit dislocations can be estimated by (*153*),

$$\text{Equation 20} \quad h_c = \frac{b}{8\pi(1+\nu)\varepsilon_m}\left[\ln\left(\frac{h_c}{b}\right)+1\right]$$

wherein the magnitude of the Burgers vector $\boldsymbol{b}$ is 0.25 nm, the mismatch strain ε_m is 0.83% (the lattice constant of Cu and FCC Fe are 3.615 and 3.585 Å (*154, 155*), respectively),

the Poisson's ratio ν is 0.3. The calculated value for h_c is ~ 3 nm. Thus Cu/Fe 0.75 nm multilayer should be fully coherent. However coherency quickly degraded when h increased to 1 nm in both Cu/Fe (100) and (111) films. This could be related to the fact that FCC Fe is a metastable phase. Hence there is a driving for FCC Fe to transform to stable BCC phase. The energy difference between FCC and BCC Fe was not considered when calculating h_c, and thus leads to its overestimation.

3.5.2 The formation of nanotwins in (111) Cu/Fe multilayers

It is unusual to spot the formation of twins in Cu/Fe multilayers. It is known that twins can relieve stress. Hence it is necessary to compare the mismatch strain energy and the energy required for the formation of twins.

To nucleate a twin interface, one leading partial dislocation is emitted from grain boundary, followed by a twinning partial dislocation of the same Burgers vector on the adjacent slip plane (*156, 157*). Based on the formation of twinned nuclei, subsequent atoms would stack continuously to extend the twin thickness during deposition process. Thus, we assume two partial dislocations are required to nucleate a twin interface. The energy for formation of a twin, E_{twin}, is thus estimated by

$$\text{Equation 21} \quad E_{twin} = E_{dis} + \gamma_{twin}$$

where γ_{twin} is the energy of twin boundaries (~ 24 mJ/m^2 [9]) for Cu, and E_{dis} is the energy of a pair of partial dislocations and can be calculated by

Equation 22 $$E_{disl} = \frac{Gb^2}{2\pi}\ln(\frac{D}{b}+1)$$

where D is the grain size. The energy of a pair of partial dislocation with 40 nm in length (equal to the average grain size) is thus ~ 3.24×10^{-17} J. Meanwhile the energy of twin boundary in a 40 nm grain is ~ 3.84×10^{-17} J. The mismatch strain energy, E_m can be calculated by (*158*)

Equation 23 $$E_m = \varepsilon_m^2 M_{Fe} h_{Fe}$$

where M is biaxial modulus of Fe and ε_m is mismatch strain. As the average twin thickness is ~ 6 nm, indicating that when the thickness of Fe approaches 3 nm, a twin partial forms as shown schematically in Fig. 55. Hence using h_{Fe} = 3 nm, we arrive that the overall mismatch strain energy in a 40 nm grain is ~ 9.9×10^{-17} J, sufficient to trigger the formation of twins and a pair of partial dislocations.

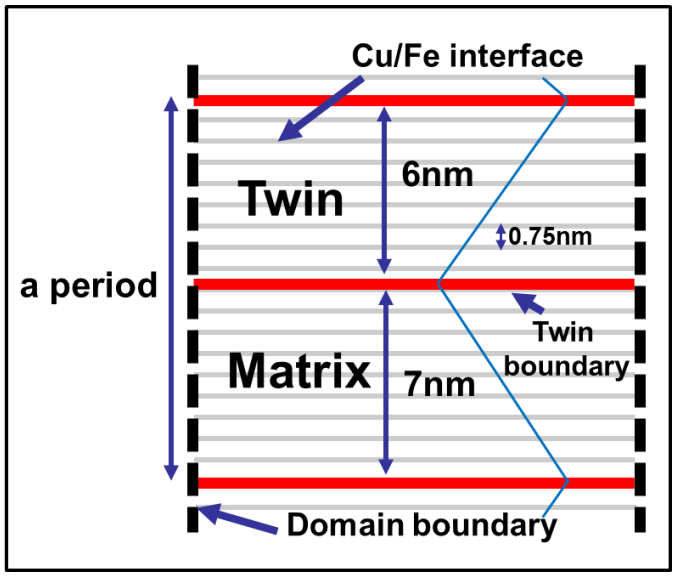

Figure 55 Schematic illustration of a period of (111) Cu/Fe 0.75 nm multilayer with twin structure, including a twin and a matrix.

Next we estimate the shear stress close to the free edge of islands to nucleate a Shockley partial in Cu. At the free surface, there is no stress; while inside the island, the biaxial stress (mismatch stress) increases rapidly to a steady state value. An interfacial shear stress is thus required to transfer the stress (from substrate or seed layer) into films. The shear stress, τ, can be estimated as (*68, 158*)

Equation 24 $$\tau \approx \sigma_m \sqrt{\frac{kh_f}{2\pi x}}$$

where σ_m is the biaxial mismatch stress, x is the distance from the edge of island, k is the biaxial modulus ratio between substrate and films, and can be calculated as

Equation 25 $$k = \left(\frac{E_s}{1-\nu_s}\right) / \left(\frac{E_f}{1-\nu_f}\right)$$

τ is estimated to be ~ 0.7 – 1.0 GPa when *x* is ½ - 1 h_f. It has been shown that the required shear stress to create a Shockley partial in Cu is ~ 540MPa (*68*), thus the shear stress is sufficient to nucleate a Shockley partial in Cu.

3.5.3 Mechanical properties-grain, layer and twin interface induced strengthening

(a) Strengthening at large layer thickness (h = 50 - 200 nm): the following analyses show that an appropriate parameter to determine the size dependent strengthening mechanisms is the average columnar grain size of Fe, rather than h.

Hall-Petch model: dislocation pile-up against layer interface: previous studies show that if layer thickness is deterministic dimension for Hall-Petch type of strengthening in multilayers, then the maximum hardness can be estimated reasonably well by using the Hall-Petch slope (K_{HP}) via (*25*):

Equation 26 $$K_{HP} = \sqrt{\tau^* \mu b / [\pi(1-\nu)]}$$

where τ^* is the interface barrier strength, μ is the shear modulus (μ=48 GPa for Cu), b is the Burgers vector (b=0.25 nm for Cu), and ν is the Poisson's ratio (~ 0.33). Using the measured slope 10.3 GPa·$nm^{1/2}$ for Cu/Fe we obtain τ^* = 0.24 GPa. The peak hardness could be estimated as 8.1τ^* by using the Tabor relation (H = 2.7 σ, where σ is the flow stress) and considering Taylor factor ($\sigma = 3\tau^*$). Thus, the estimated peak hardness is merely 1.9 GPa, much lower than the measured peak hardness, ~ 5 GPa. In

Table 2, we listed the relationship of Hall-Petch slope and peak hardness of Cu/304 SS (*159*), Cu/330 SS(*30*), and Cu/Ni (111) and (100) (*27*). We found that except for Cu/Fe, the difference of measured and calculated peak hardnesses in most other systems is small. Thus Hall-Petch slope cannot be used to predict the peak strength of Cu/Fe multilayers.

Table 2 Comparison among the estimated interface barrier strength, τ* from measured Hall-Petch slopes, peak hardness calculated from estimated interface barrier strength and the measured peak hardness.

Material	Cu/Fe	Cu/304 SS	Cu/330 SS	Cu/Ni(111)	Cu/Ni(100)
Experimental K_{HP} ($GPa \cdot nm^{1/2}$)	10.3	16.9	19.5	17.7	15
Calculated τ* (GPa)[a]	0.24	0.64	0.85	0.84	0.6
Calculated peak hardness (GPa)	1.9	5.2	7	6.8	4.8
Measured peak hardness (GPa)	5	5.5	5.1	5.8	5

[a] $K_{HP} = \sqrt{\tau^* \mu b / [\pi(1-\nu)]}$

Confined layer slip (CLS) model to describe dislocation activity in columnar Fe grains: the break-down of Hall-Petch model at such a large layer thickness and exceptionally high hardness of Cu/Fe (than Cu/Ni with identical h) indicates that strengthening mechanism is no longer determined by h alone. Microscopy studies have shown that when h = 50 - 200 nm, Fe was composed of nanoscale columnar grains with various grain sizes, ~ 11-23 nm. The grain size of Fe is clearly much less than layer

thickness. Fig. 56 shows schematically the deformation mechanism in Cu/Fe with nanocolumns in Fe.

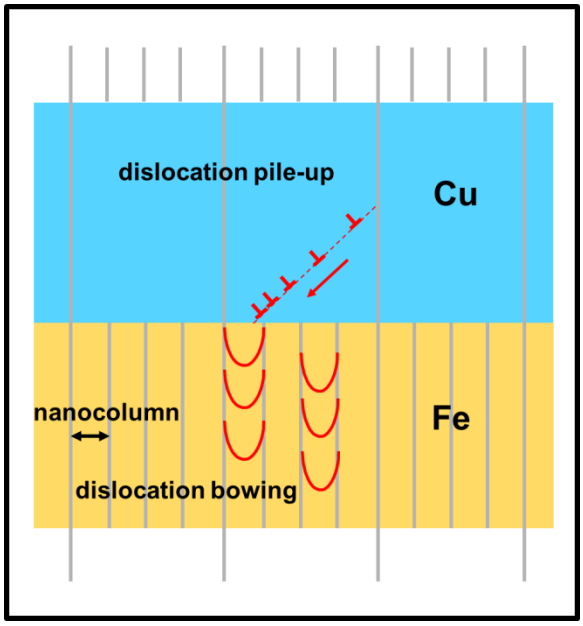

Figure 56 Schematic illustration of deformation mechanism in Cu/Fe multilayer with large layer thickness. In the Cu layer, dislocations pile up against phase interface; in Fe layer, dislocations bow out by confined layer slip mechanism.

Dislocations may pile-up in Cu. But for dislocation to transmit across interface into Fe layer, the dislocation must be able to propagate within narrow columns in Fe. Hence plastic yielding is determined by the stress necessary for single dislocation bowing via the CLS mechanism. The critical resolved shear stress τ_{cls} can thus be calculated by (*12*)

Equation 27 $$\tau_{cls} = \frac{\mu b}{8\pi d}\left(\frac{4-\nu}{1-\nu}\right)\ln\left(\frac{\alpha d}{b}\right)$$

where μ is shear modulus (77.5 GPa for Fe), d is the columnar grain size of Fe, b is Burgers vector (0.248 nm for Fe) and α represents the core cut-off parameter. The calculated results (two dash lines) by using α = 0.11 and α = 0.15 are compared to experimental data in Fig. 57. The estimated hardness fits the experimental data well. Twin density was low in Cu at such a large layer thickness, and hence the contribution of twins may be insignificant over this range of layer thickness.

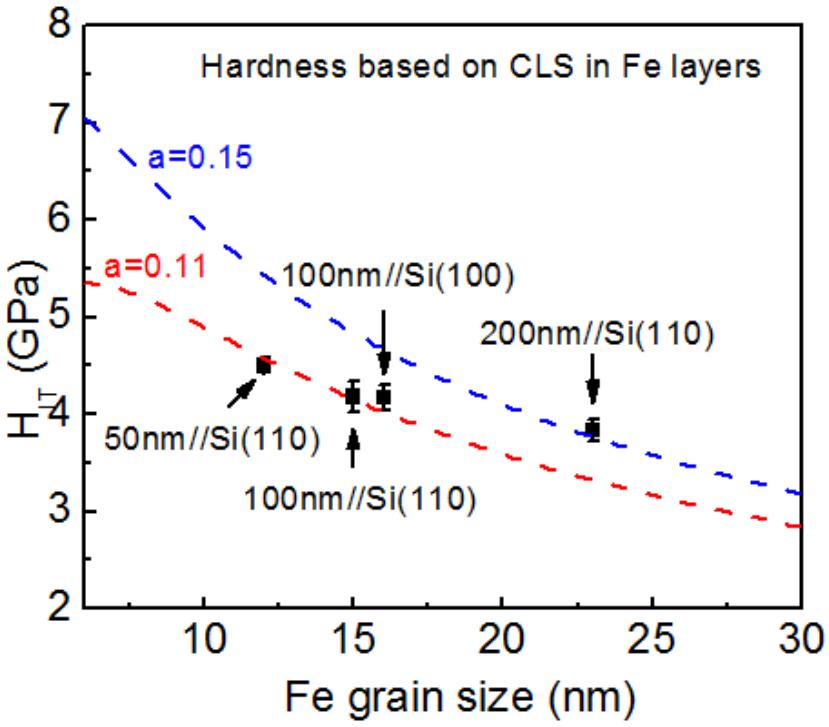

Figure 57 Experimental hardness data of multilayer with respect to Fe grain size at h=50-200 nm. Two dash curves are simulated hardness value based on CLS model of Fe grains.

(b) Strengthening mechanism when h = 2.5 – 25 nm: previous discussion demonstrates that the strengthening mainly arises from confined dislocation propagation in nanocolumns in Fe. However, with continuous decrease of layer thickness, the grain size is eventually greater than h. Hence strengthening is now determined by Cu/Fe interfaces. We now attempt to estimate the interface barrier strength, $\tau^*_{barrier}$, as (*38*)

Equation 28 $\tau^*_{barrier} = \tau^*_d + \tau^*_k$

The first term τ^*_d comes from misfit dislocations and can be expressed by (*37*)

Equation 29 $\tau^*_d = \alpha G^*[(\Delta a / a) - (b / \lambda)]$

where $\alpha \approx 0.41$ is Saada's constant, G^* is the mean shear modulus and could be estimated as $G^* = G^*_{Cu} \cdot G^*_{Fe} / (G^*_{Cu} + G^*_{Fe})$. λ is the average spacing of the interface dislocation array (λ=25 nm). $\Delta a / a$ is the mismatch strain (~ 2.94% for Cu/Fe (BCC Fe) with K-S type of interface). The term in bracket is the residual elastic strain parallel to the interface plane caused by lattice mismatch. Then the estimated hardness by lattice mismatch from Eq.(3.10) is ~ 2 GPa.

The second term, named Koehler stress, τ^*_k comes from the differences in elastic moduli and maximum τ^*_k could be obtained by (*36*),

Equation 30 $\sigma_{\max} \cong R\mu_1 \sin\theta / 8\pi$

where $R=(\mu_2-\mu_1)/(\mu_2+\mu_1)$, μ_2 is the modulus of high-elastic-constant material and μ_1 is the modulus of low-elastic-constant material. θ is the angle between the slip plane and the interface. Assuming $\sin\theta$ =0.81664, we can estimate hardness by modulus difference is ~ 3 GPa. As a result, we can obtain the calculated peak hardness is ~ 5 GPa. This is consistent with the plateau hardness we obtained. The peak hardness is similar between Cu/Ni (100) and Cu/Fe (100) multilayer, since the mismatch strain and modulus difference are very similar in both systems.

(c) Softening and twining induced strengthening (when h < 2.5 nm): at this length scale, the hardnesses of Cu/Fe (111) and (100) have clearly different dependence on layer thickness. Softening was observed in Cu/Fe (100), similar to that in Cu/Ni (100) (*27*). Softening could be explained by the formation of fully coherent interface and diminishing Koehler stress (as the dislocation core radius is comparable to h). The hardness of Cu/Fe 0.75 nm multilayer on Si (100) substrate was ~ the rule-of-mixture hardness of single layer Cu and Fe films. In contrast, the hardness of Cu/Fe 0.75 nm with (111) texture remained high, ~ 4.7 GPa. The retention of high hardness is related to the formation of high density twins which have an average twin spacing of ~ 6 nm. In Eq. (27), assuming α = 0.16, and use the twin thickness (6 nm) and μ=48 GPa (Cu), we obtain a calculated hardness value of ~ 4.6 GPa, similar to experimental observations.

3.6 Conclusion

We studied strengthening mechanisms of Cu/Fe multilayers with various individual layer thicknesses on Si (100) and Si (110) substrates. K-S and N-W orientation relationships were identified along layer interfaces. When h > 25 nm, the nanocolumn grain size in Fe is smaller than h, and is the primary parameter that dominates the strength of multilayers. A plateau of hardness is achieved when h = 2.5 - 25 nm, and can be explained by interface barrier strength model. Fully coherent interfaces were achieved at h of 0.75 nm in both sets of multilayers. The hardness of (111) textured Cu/Fe 0.75 nm multilayer remains high due to the formation of a large amount of nanotwins, wherein (100) textured Cu/Fe, significant softening was observed due to the formation of fully coherent layer interface and diminishing Koehler stress.

3.7 Acknowledgements

We acknowledge financial support by US Army Research Office – Materials Science Division, under contract no. W911NF-09-1-0223. Partial supports by DOE-NEUP under contract no. DE-AC07-05ID14517-00088120 and NSF 1129065 are also acknowledged. We also acknowledge the usage of microscopes at the Microscopy and Imaging Center at Texas A&M University.

CHAPTER IV

ENHANCED RADIATION TOLERANCE IN IMMISCIBLE CU/FE MULTILAYRS WITH COHERENT AND INCOHERENT LAYER INTERFACES*

4.1 Overview

Recent studies have shown that chemical immiscibility is important to achieve enhanced radiation tolerance in metallic multilayers as immiscible layer interfaces are more stable against radiation induced mixing than miscible interfaces. However the influence of coherency on radiation resistance of immiscible systems remains poorly understood. Here we report on radiation response of immiscible Cu/Fe multilayers, with individual layer thickness h varying from 0.75 to 100 nm, subjected to He ion irradiation. When interface is incoherent, the peak bubble density decreases with decreasing h and reaches a minimum when h is 5 nm. At even smaller h when interface is increasingly coherent, the peak bubble density increases again, however void swelling in coherent multilayers with smaller h remains less than those in incoherent multilayers. Our study suggests that the coherent immiscible interface is also effective to alleviate radiaiton induced damage.

---

*This chapter reprinted with permission from "Enhanced radiation tolerance in immiscible Cu/Fe multilayers with coherent and incoherent layer interfaces" by Y. Chen, E.G. Fu, K.Y. Yu, M. Song, Y. Liu, Y.Q. Wang, H. Wang and X. Zhang; Journal of Materials Research, In press, Copyright 2013 by Cambridge University Press.

4.2 Introduction

Neutron radiation creates two major types of radiation damage in structural materials: point defects and their clusters,(*82*) and transmutation induced Helium (He), which can swiftly combine with vacancies to form He bubbles(*160-162*). These radiation induced defects can significantly degrade the mechanical stability of irradiated metallic materials. To alleviate radiation damage in structural materials, various types of defect sinks have been investigated, including grain boundaries (GB)(*88-90, 93, 163*) and interphase boundaries(*112, 125, 128, 164, 165*). Grain boundaries, which are unbiased sinks[12,13], can mitigate radiation damage by absorbing point defects and clusters, and promoting their recombination (*91, 138*). Radiation studies on nanocrystalline (nc) metals show that defect density can be significantly reduced(*93, 166-168*) and *in situ* radiation provides direct evidence on defect cluster absorption by high angle grain boundaries in nc Ni(*10*).

Phase boundaries in ODS alloys with abundant metal/oxide interfaces are critical to allevaite radiation damage and have been extensively studied(*130-134, 169*). Radiation responses of multilayers with well-controlled layer interfaces were increasingly investigated (*112, 125, 126, 128, 170-174*). In metallic multilayers, various types of interfaces have been intensively studied, including FCC/ BCC interfaces (e.g. Cu/Nb(*112, 127, 128, 175*), Cu/V(*103-105*), Cu/Mo(*106*), Cu/W(*107*), Al/Nb(*108*), Ag/V(*109, 110*)), FCC/FCC interfaces (e.g. Cu/Ni(*100*), Ag/Ni(*122, 123*), Cu/FCC Co(*176*)) and BCC/BCC interfaces (Fe/W(*124*)), where FCC and BCC stand for face-

centered cubic and body-centered cubic, respectively. In general, immiscible layer interfaces appear to be effective sinks to mitigate radiation induced defect clusters (*125, 126*). In Cu/V nanolayers, the density of He bubbles and radiation hardening decline prominently with decreasing individual layer thickness h, demonstrating an appealing size effect (*103-105*).

The motivations of the current study on radiation damage in Cu/Fe system include the followings. First, previous studies focused on radiation tolerance of incoherent immiscible metallic multilayers, and the influence of coherent immiscible interface on radiation tolerance remains poorly understood. It is unclear if coherent immiscible interfaces are stable during ion beam bombardment such as He ion irradiation, and if stable, can the interfaces also effectively alleviate radiation damage? Second, we reported recently that Fe in Cu/Fe multilayers undergoes a phase transformation from BCC to FCC structure when h reduces to 2.5 nm or smaller(*177*). Thus an opportunity emerges to investigate the radiation damage in FCC/FCC multilayers with coherent immiscible interfaces. Third, Fe is the major element in ferritic/martensitic steels (FMS), primary candidates for fuel cladding materials for advanced nuclear reactors(*130-134*). Radiation damage in Fe based multilayer systems may provide insights for the design of radiation tolerant FMS.

4.3 Experimental

Cu/Fe multilayers with identical h, varying from 0.75 to 100 nm, were magnetron sputtered at room temperature on HF etched Si (100) and Si (110) substrates. The chamber was evacuated to a base pressure less than 1×10^{-5} Pa prior to deposition. Before the deposition of Cu/Fe multilayers, a 100 nm thick Cu seed layer was deposited. Detailed information was reported elsewhere(*177*). The films with various h were irradiated at room temperature using 100 keV He ions with a total fluence of 6×10^{20} ions/m^2. The temperature rise of the sample was ~ 50^{o}C during implantation. The base pressure in the ion implantation system was 4×10^{-5} Pa. X-ray diffraction (XRD) experiments were performed in a Brukers D8 Discover X-ray powder diffractometer at room temperature. Transmission electron microscopy (TEM) experiments were carried out on a JEOL 2010 transmission electron microscope operated at 200 kV and an FEI Tecnai G2 F20 microscope operated at 200 kV with a Fischione ultra-high resolution high-angle annular dark field (HAADF) detector. Cross-sectional TEM (XTEM) samples were prepared by dimpling, low energy (3.5 keV) Ar ion milling, and subsequent ion polishing. Depth-dependent damage and defect concentration profiles were calculated by the Stopping and Range of Ions in Matter (SRIM)-2008 using the Kinchin-Pease option in the SRIM software (*144*).

4.4 Results

Fig. 58 shows the depth profiles of radiation damage in unit of displacements-per-atom (dpa) and Helium concentration obtained from SRIM simulation of $Cu_{50}Fe_{50}$ compound subjected to He ion irradiation at 100 keV with a total fluence of 6×10^{20} ions/m^2. The default threshold displacement energies in the SRIM were used in the calculation. The peak damage approaches ~ 2.5 dpa at a depth of ~ 300 nm and the projected ion penetration depth is ~ 500 nm. Peak He concentration reaches ~ 3 at. % (or 30,000 appm) at a depth of ~ 350 nm.

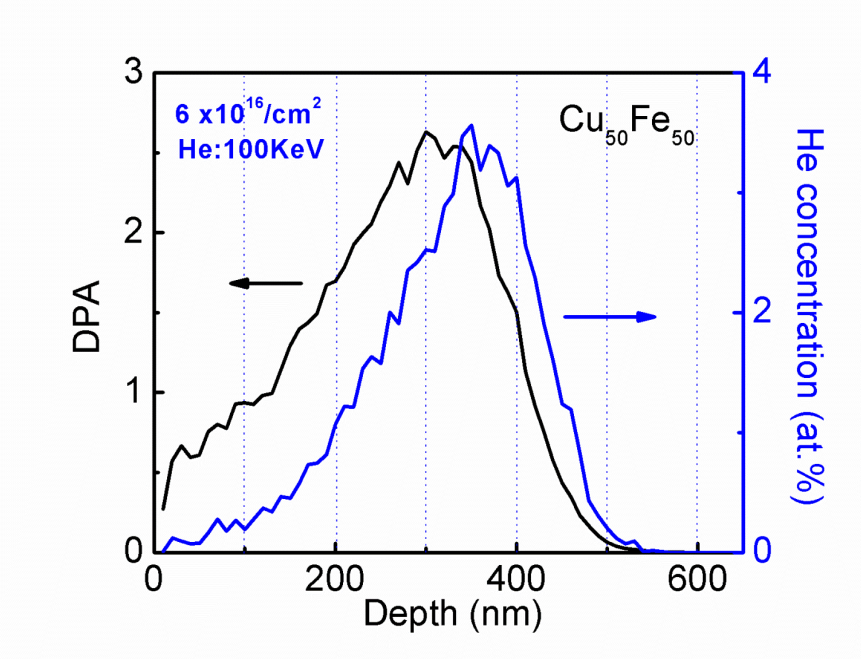

Figure 58 The depth profile of radiation damage in unit of displacements-per-atom (dpa) (left) and He concentration (atomic percent) obtained from SRIM simulation in $Cu_{50}Fe_{50}$ subjected to He ion irradiation at 100 keV with a total dose of 6×10^{16} ions/cm^2 (right). The peak damage and peak He concentration are approximately 2.5 dpa and 3 at. % (or 30000 appm).

Structural evolution of multilayers before and after radiation was characterized by XRD patterns. As-deposited multilayers had incoherent interface when $h \geq 5$ nm as evidenced by the co-existence of Cu (111) and Fe (110) diffraction peaks (Fig. 59a). When $h < 5$ nm coherency became dominant as no Fe (110) peak can be observed. When h decreased to 0.75 nm, interface was fully coherent for Cu/Fe multilayers deposited on both Si (100) and Si (110) substrates (Fig. 59b). Radiation in general led to reduction of peak intensity and insignificant variation of peak positions in multilayers when $h \geq 2.5$ nm as shown in Fig. 59a. In comparison after radiation of Cu/Fe 0.75 nm multilayers, shoulder peaks appeared surrounding the original Cu (111) or Cu (200) peak for the film grown on Si (110) or Si (100) substrates. The deconvolution of each peak in irradiated Cu/Fe 0.75 nm multilayers will be discussed later.

The microstructures of He ion irradiated Cu/Fe nanolayers were examined by TEM. Fig. 60a shows an XTEM micrograph of irradiated incoherent (FCC/BCC) Cu/Fe 100 nm multilayer with superimposed He concentration profile. Two boxes, b and c were selected and magnified in Fig. 60b and 60c to examine defects in Cu and Fe layers in detail. High-density He bubbles were clearly observed in Cu (Fig. 60b) and Fe layers (Fig. 60c), which were in the peak damage area. Fe had small columnar grain size of ~ 17 nm and He bubbles appeared to distribute along columnar grain boundaries.

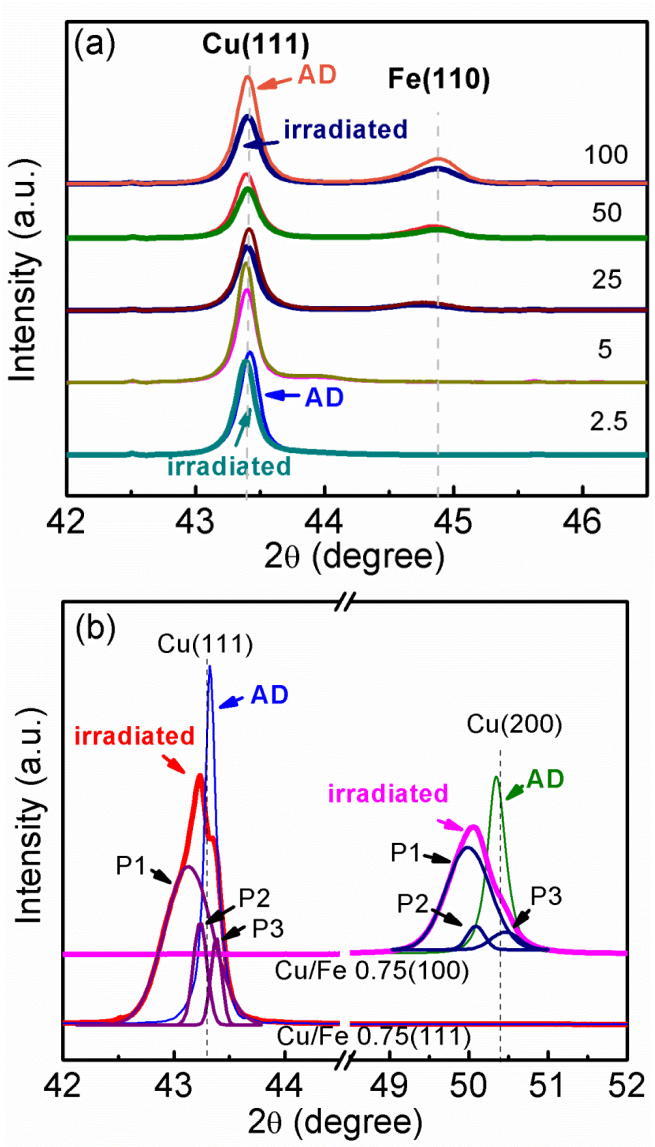

Figure 59 X-ray diffraction (XRD) patterns of as-deposited (AD) and He ion irradiated Cu/Fe multilayers. (a) No significant change in peak positions and intensities was observed after irradiation with layer thicknesses varying from 2.5 to 100 nm on Si (110). Coherency between Cu (111) and Fe (110) began to form when h=5 nm and became dominant when h=2.5 nm as no Fe (110) peak appeared. (b) For h=0.75 nm, fully coherency formed in Cu/Fe multilayers on both Si (100) and Si (110) substrates. After radiation, shoulders appeared in (111) and (200) peaks and the deconvolution of each displays three sub-peaks, P1, P2 and P3.

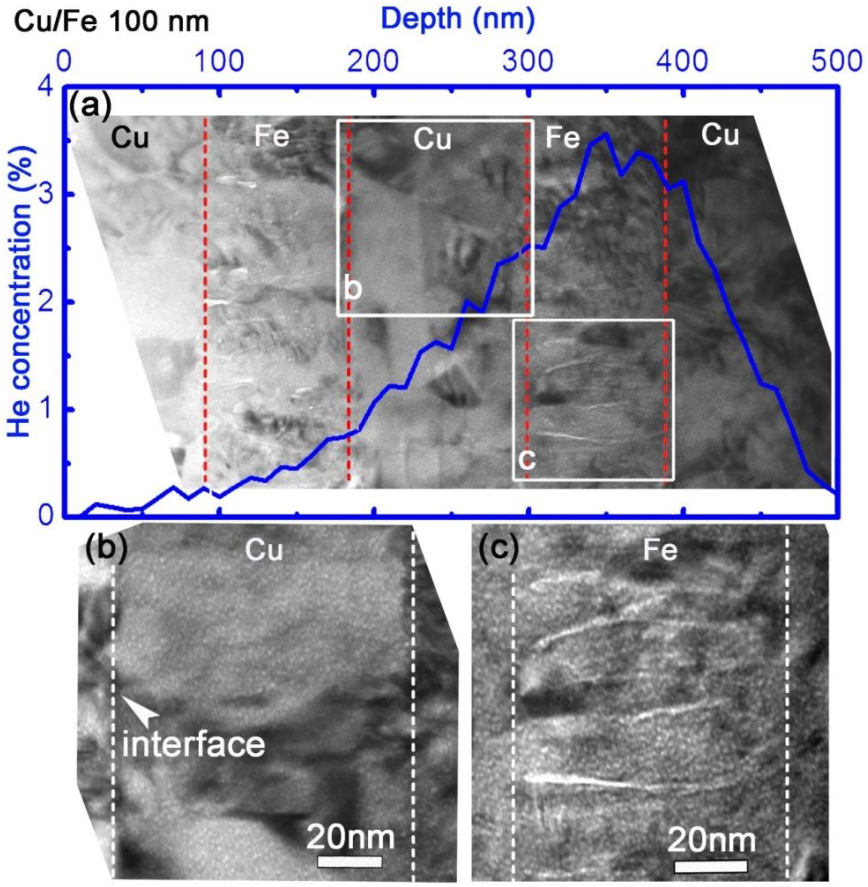

Figure 60 (a) A cross-sectional TEM (XTEM) micrograph of He ion irradiated incoherent (FCC/BCC) Cu/Fe 100 nm multilayer on Si (110) substrate. The blue curve is He concentration calculated by SRIM. (b) and (c) display the microstructure of the 3rd (Cu) and 4th (Fe) layers at higher magnification (labeled as boxes in (a)). High-density He bubbles were clearly observed. The average bubble size is ~ 1.3 nm.

Radiation damage in Cu/Fe 5 nm multilayers was examined in parallel. A panoramic view of irradiated film is shown in Fig. 61a. The depth dependent He concentration profile is embedded in the same figure. He bubbles appeared to distribute along wavy layer interfaces. Magnified images at two locations, close to surface and

peak damage are shown in Figs. 66b-c. It is evident that a large number of He bubbles were aligned along Cu/Fe interfaces.

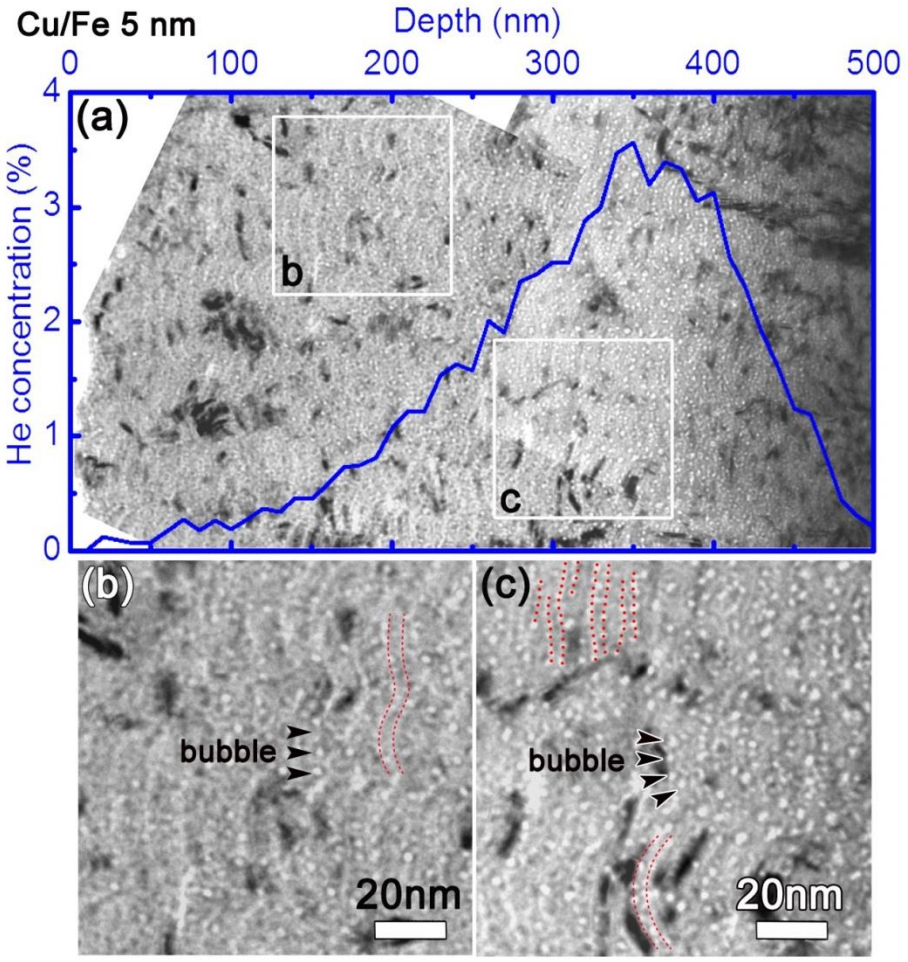

Figure 61 (a) An XTEM micrograph of He ion irradiated Cu/Fe 5 nm on Si (110) substrate. The blue curve is He concentration calculated by SRIM. (b) and (c) display magnified images of the box b and c labeled in (a). (b) Most He bubbles were aligned along interfaces. (c) Bubble density increased and Cu/Fe interfaces became more preferred locations for He bubbles. The average bubble size is ~ 1.8 nm.

Scanning transmission electron microscopy (STEM) experiments were performed to examine irradiated multilayers at various locations, close to surface (Fig.

62a), peak damage (Fig. 62b) and unirradiated region beyond projected ion range (Fig. 62c). Layer interfaces were clearly discernable throughout the entire irradiated multilayer. Comparisons of compositional line profiles between the peak damage (Fig. 62d) and unirradiated area (Fig. 62e) show modulated variation of Cu and Fe compositions across layer interface, implying insignificant intermixing after He ion irradiation.

TEM examinations of irradiated fully coherent Cu/Fe 0.75 nm multilayers on Si (100) (Fig. 64) and Si (110) (Fig. 65) substrates were also conducted to investigate the radiation response of coherent immiscible interfaces. Before radiation, HRSTEM and HRTEM micrographs in Fig. 63 confirms that as-deposited (111) and (100) textured Cu/Fe 0.75 nm multilayers are fully coherent, as Fe in both systems has undergone phase transformation from BCC to FCC Fe.

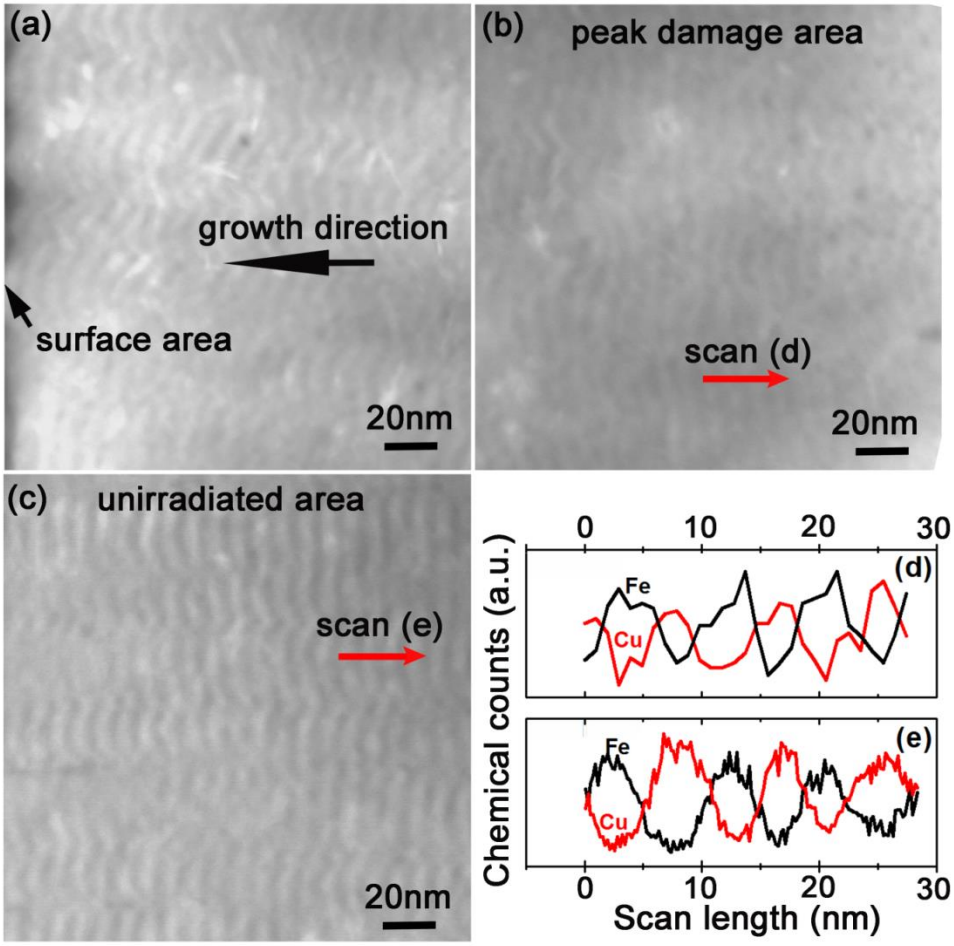

Figure 62 Cross-sectional scanning TEM (STEM) micrographs of irradiated Cu/Fe 5 nm multilayer film on Si (110) substrate showing microstructures at three locations: (a) close to surface, (b) peak damage area, and (c) unirradiated area. Layer interface retained in irradiated multilayers. (d) Comparisons of compositional line profiles obtained from the peak damage area in (b) and unirradiated area in (c) show modulated variation of Cu and Fe compositions across layer interface, implying insignificant intermixing after He ion radiation.

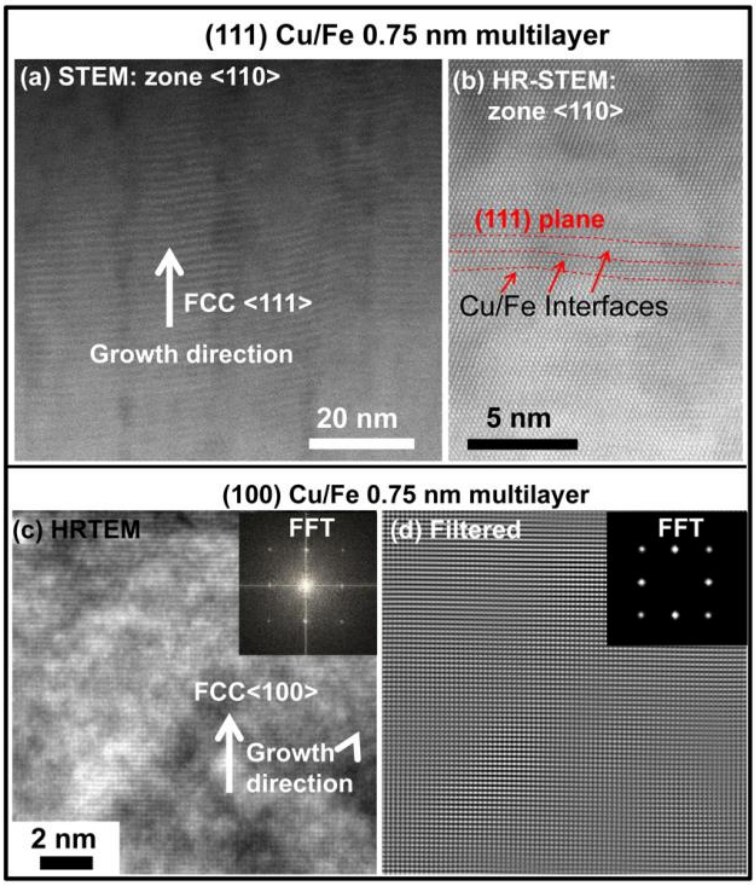

Figure 63 (a) An STEM image of as-deposited (111) Cu/Fe 0.75 nm multilayer. (b) A high-resolution STEM image revealing coherent interfaces between Cu and Fe. (c) A high-resolution TEM image and (d) FFT-filtered image displaying coherent interfaces between Cu and Fe in as-deposited (100) Cu/Fe 0.75 nm multilayer. Fe in both systems has undergone a phase transformation from BCC to FCC Fe.

Fig. 64a displays an XTEM micrograph that overviews the microstructure of He ion irradiated fully coherent (100) Cu/Fe 0.75 nm multilayer accompanied by SRIM simulated He concentration profile. Three boxes, b-d, were magnified to examine radiation damage in detail at higher magnification. Close to surface (Fig. 64b), low-density He bubbles were randomly distributed. High-density He bubbles appeared in the

peak damage area (Fig. 64c). Although no clear interfaces were observed in surface and peak damage areas, the irradiated multilayer retained fully coherent and single-crystal-like microstructure as indicated by the embedded selected area diffraction (SAD) pattern in Fig. 64a. In the region close to the end of He concentration profile (Fig. 64d), layer interface in irradiated Cu/Fe 0.75 nm multilayers retained, and arrays of low-density He bubbles (with diameter of ~ 1 nm or less) with an average separation distance of 1.5 nm were observed. The smaller size of He bubbles (comparing to those in thicker multilayers) appears to be curtailed by the individual layer thickness. Furthermore if bubbles reside at layer interfaces, the average spacing of arrays of He bubbles should be 0.75 nm. Thus we speculate He bubbles may nucleate primarily within the layers.

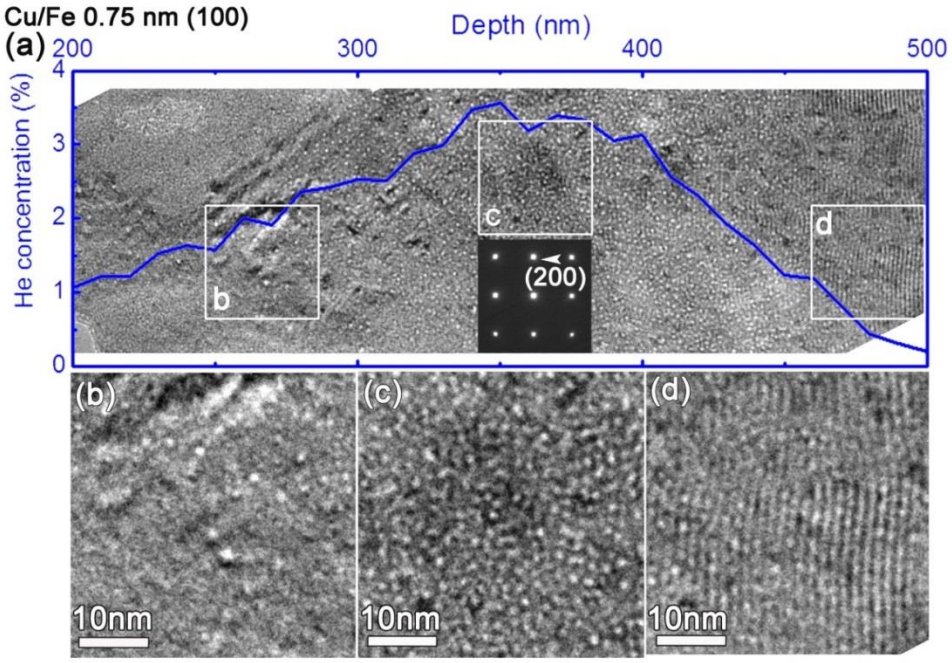

Figure 64 (a) An XTEM micrograph that overviews the microstructure of He ion irradiated fully coherent Cu/Fe 0.75 nm multilayer on Si (100). The evolution of bubble density is consistent to the superimposed He concentration profile (blue curve). (b), (c) and (d) display the respective magnified images of the irradiated films at location b-d shown as boxes in (a). (b) Close to surface, bubbles were randomly distributed with low density. (c) High-density He bubbles appeared in the peak damage area. No clear layer interfaces were observed in both (b) and (c). However, the structure remained fully coherent and single-crystal-like, as shown in the embedded SAD in (a). (d) In less damage location (at the end of He concentration profile), layer interface retained and low density tiny He bubbles were confined primarily in Cu layers. The average bubble size is 1 nm.

In irradiated coherent (111) Cu/Fe 0.75 nm multilayer, high-density growth twins were visible (Fig. 65a), whereas layer interface cannot be easily distinguished along this zone axis. Radiation damage close to the surface (Fig. 65b) and in peak damage zone (Fig. 65c) also revealed abundant He bubbles, similar to those observed in

irradiated (100) Cu/Fe 0.75 nm multilayer. The irradiated (111) Cu/Fe 0.75 nm multilayers remained highly coherent and epitaxial.

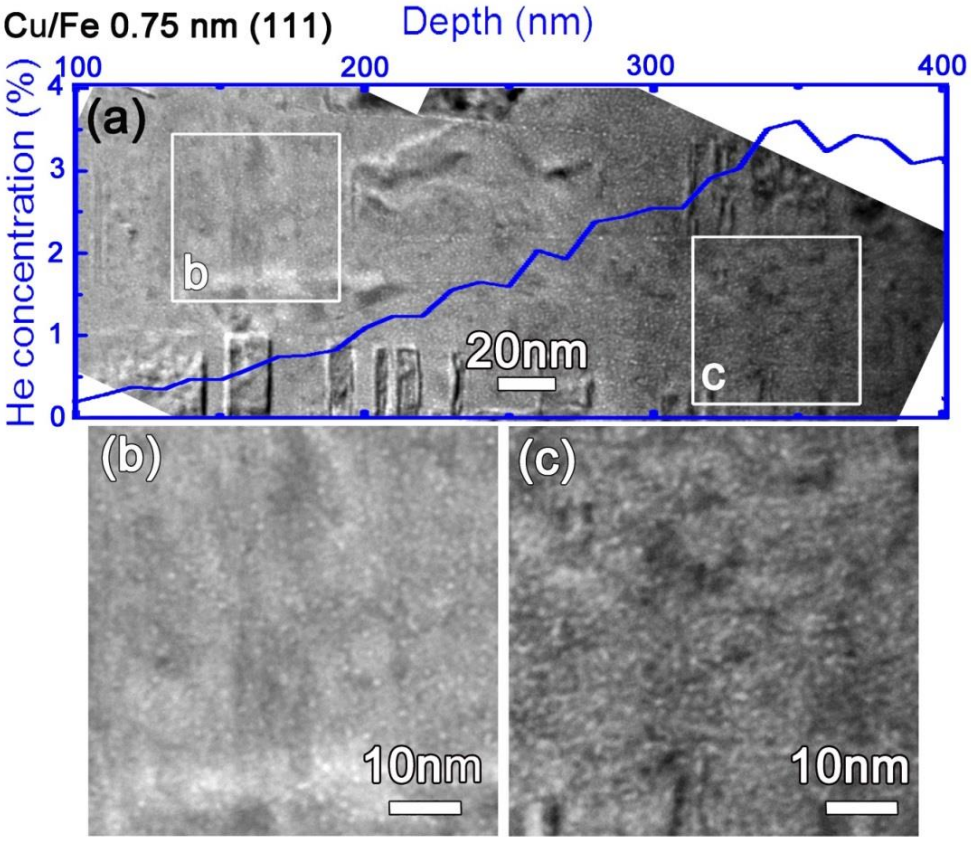

Figure 65 (a) An XTEM micrograph that overviews the microstructure of He ion irradiated fully coherent Cu/Fe 0.75 nm multilayer on Si (110). The evolution of bubble density is consistent to the superimposed He concentration profile (blue curve). (b) and (c) display the respective magnified images of the irradiated films at location b and c shown as boxes in (a). (b) Close to surface, bubbles were randomly distributed with low density. (c) High-density He bubbles formed in the peak damage area. No clear layer interfaces were detected in both (b) and (c).

Statistical distributions of He bubble density versus penetration depth in several irradiated Cu/Fe multilayers are compared in Fig. 66. Overall, the evolution of He

bubble density followed that of He concentration profile (the dash line), that is He bubble density increased with radiation depth and approached maxima where He concentration also achieved a maximum value, and decreased rapidly thereafter. The He bubble concentration profiles of Cu/Fe 0.75nm on two types of Si substrates were similar, and hence only one of them is shown for clarity.

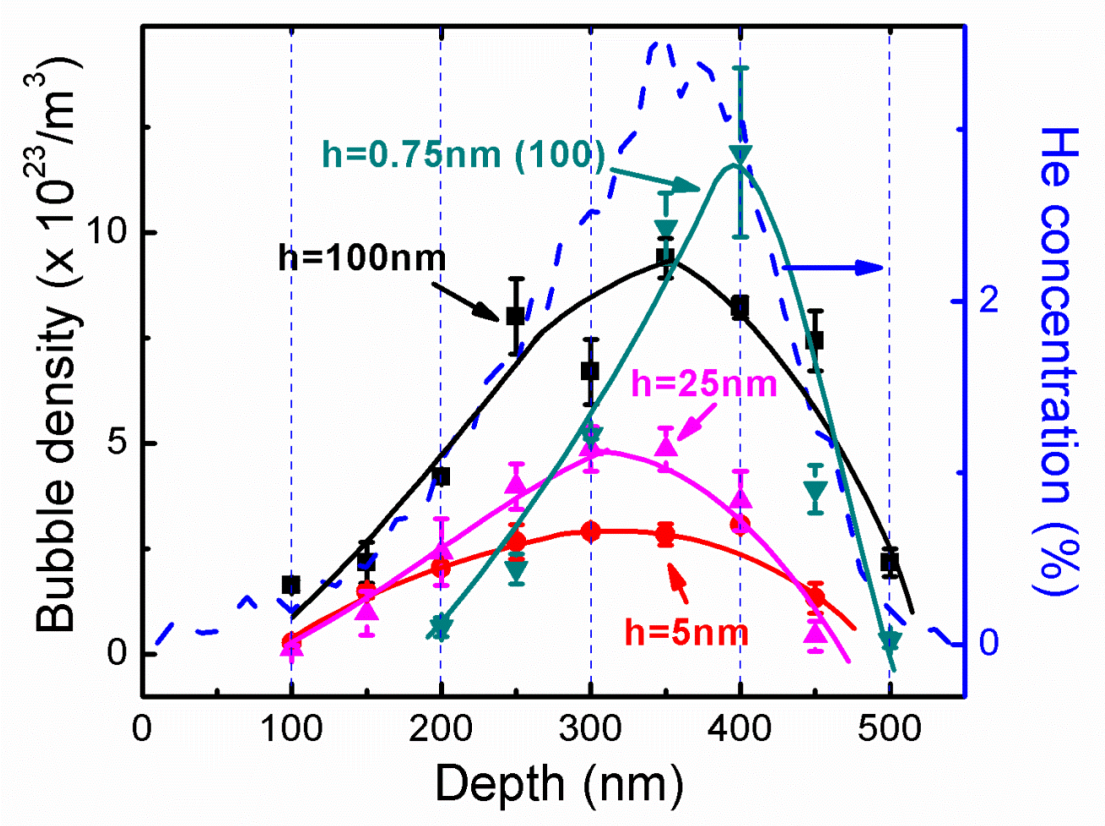

Figure 66 A statistical study of He bubble density distribution versus penetration depth in irradiated Cu/Fe 100, 25, and 5 nm multilayers on Si (110) and Cu/Fe 0.75 nm multilayer on Si (100). The evolution of He bubble density matched closely to that of He concentration profile.

The peak bubble density in multilayers (as shown in Fig. 67a) decreased continuously with decreasing h, reached a minimum value when h = 5 nm, and bounced back up rapidly when h < 5 nm. Meanwhile, the average bubble size (Fig. 67b) and swelling (Fig. 67c) in multilayers were also compared to obtain a comprehensive knowledge of size dependent radiation damage. Careful examination of Fig.67b shows that with decreasing h, the average bubble size increased from 1.2 to a maximum of 1.8 nm when h = 5 nm, and decreased rapidly thereafter to a minimum of ~1 nm when h = 0.75 nm. From measured bubble density and size, we estimated swelling (due to He bubbles) in Fig. 67c. When h is in the range of 5-100 nm, swelling did not vary significantly, but remained lower than that of monolith Cu (shown by the horizontal dash line). Swelling decreased when h = 2.5 nm and increased slightly with further decrease of h to 0.75 nm.

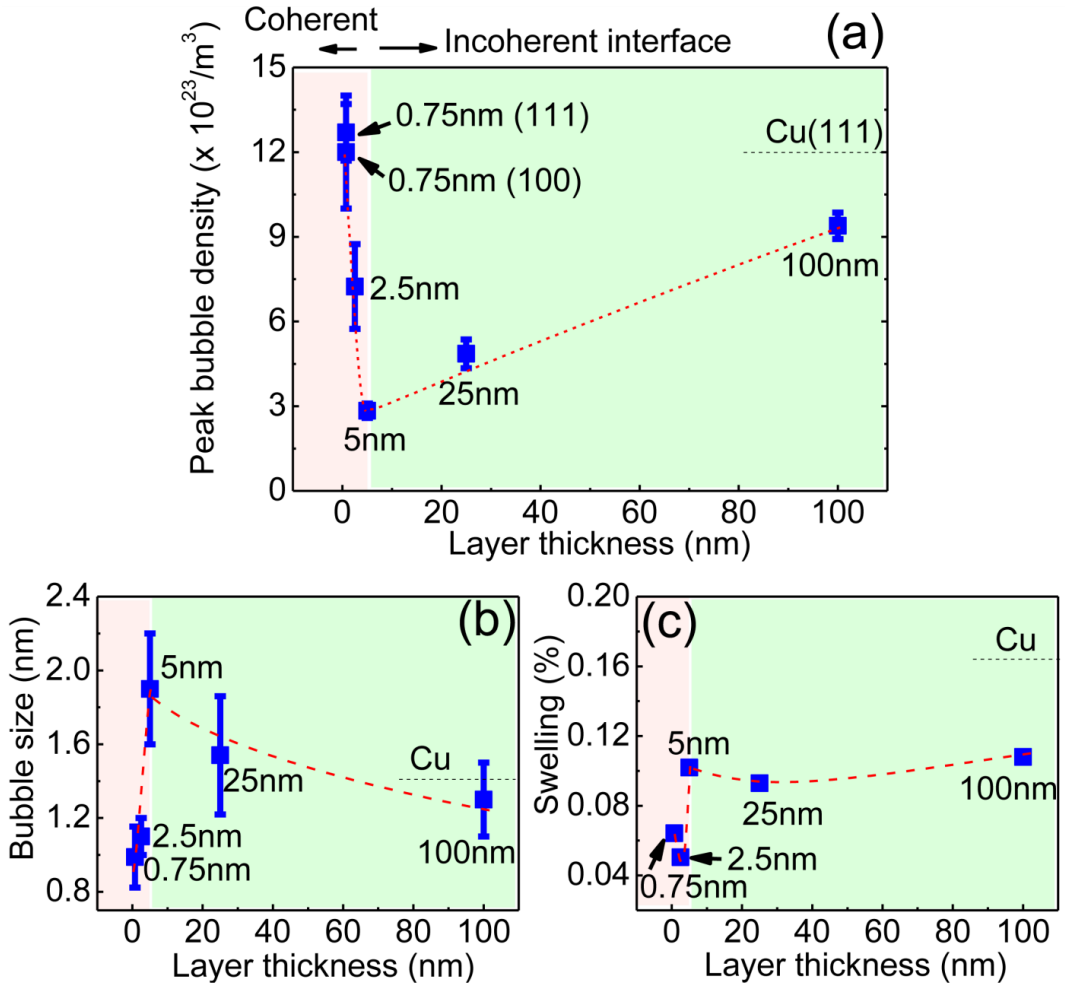

Figure 67 (a) The variation of peak He bubble density with layer thickness h shows that with the decrease in h, the peak bubble density firstly decreases continuously and reaches a minimum value when h = 5 nm, and bounces back rapidly when h < 5 nm. The peak bubble densities in Cu/Fe 0.75 multilayers are comparable to that of pure Cu films. (b) shows the evolution of bubble size has an opposite trend to that of peak bubble density. (c) Swelling is estimated based on the bubble densities and sizes. When h= 100-5 nm, swelling does not change significantly. The optimized swelling reaches at h = 2.5 nm and the swelling bounces back slightly with further decrease of h to 0.75 nm.

4.5 Discussion

4.5.1 Radiation response of incoherent Cu/Fe interfaces at large layer thickness (h⩾5 nm)

Immiscible multilayer systems with FCC/BCC incoherent interfaces have been widely investigated(*112, 125, 126, 128*), as abundant layer interfaces serve as effective defect sinks (*112*) without significant radiation induced intermixing(*104, 108, 124-126*). Examination of microstructures of He ion irradiated Cu/Fe multilayers with h in the range of 5-100 nm, reveals a size dependent reduction of average and peak He bubble density. The average bubble spacing L (estimated by $L = 1/N^{1/3}$ where N is bubble density) escalates from ~ 10 nm in Cu/Fe 100 nm multilayer to 16 nm in irradiated Cu/Fe 5 nm multilayer. Incoherent Cu/Fe interfaces act as defect sinks and provide the recombination/annihilation sites for radiation induced point defects/defect clusters. Similar phenomena have been reported in He ion irradiated FCC/BCC systems, such as Cu/V(*103, 104*), Cu/Nb(*112, 127*) and Cu/Mo (*106*), and FCC/FCC multilayers, such as Ag/Ni(*122, 123*).

As bubble density significantly deceases with decreasing layer thickness, a natural question arises: where are He atoms distributed in multilayers? As the solid solubility of He in crystal lattice is exceptionally low(*160-162*), a majority of He atoms could be located either at layer interfaces or within He bubbles. Atomistic explanation of He storage at multilayer interfaces has been provided in Cu/V and Cu/Nb multilayers by molecular dynamics(*165*). Our previous studies(*177*) identified two types of interfaces in

FCC/BCC Cu/Fe multilayers, a primary Kurdjumov-Sachs (K-S), and secondary Nishiyama-Wasserman (N-W) orientation relationships. He atoms should be stored at these interfaces in form of either nanoscale platelets(*165*) or stable He-vacancy clusters(*178*). It is worth mentioning that the combination of vacancies with trapped He atoms at layer interfaces leads to the nucleation of He bubbles along interfaces.

Another interesting phenomenon is that, in Cu/Fe 5 nm multilayer, average bubble size (Fig. 67b) (~ 1.8 nm) is slightly larger than that in Cu/Fe 100 nm (~ 1.3 nm), which implies that fast diffusion of He atoms and point defects to layer interfaces when h is small promotes the preferred bubble nucleation and growth at interfaces. Since bubbles mostly stay at Cu/Fe 5 nm multilayer interfaces, we will use a simple thermodynamic model to estimate the bubble pressure at interface. Note that bubbles in irradiated Cu/Fe at room temperature have spherical shape (Fig. 61), which is different from the lenticular shape of bubbles at GB or at layer interfaces during high temperature radiation(*179*). For a gas-filled bubble with radius R, embedded in a matrix, the change of free energy of the matrix due to the bubble is given by (*82*),

Equation 31 $$dG = Vdp + \gamma dA$$

Where V is the volume of bubble, p is the outward pressure of gas, γ is the surface tension of bubble, A is the area of bubble surface. If a spherical bubble resides at interface, the growth of the bubble is accompanied by reducing the interface area and as a result, Eq. (31) can be modified as

Equation 32 $$dG = Vdp + \gamma dA - \gamma_{Int} dA'$$

where γ_{Int} is the interface energy, A' is the interface area consumed by the bubble, and it follows that

Equation 33 $$Vdp = d(pV) - pdV$$

For an ideal gas, pV =constant and $V = 4/3\pi R^3$, $A = 4\pi R^2$, $A' = \pi R^2$. Then,

Equation 34 $$\frac{dG}{dR} = -4\pi R(p - \frac{2\gamma}{R} + \frac{\gamma_{Int}}{2R})$$

At equilibrium state ($dG/dR = 0$),

Equation 35 $$p = \frac{2\gamma}{R} - \frac{\gamma_{Int}}{2R}$$

Second term on the right indicates that at equilibrium state, bubble pressure at interfaces is lower than that in matrix. Knowing the surface energy of the bubble in Cu (~ 1.77 J/m^2 (*180*)) and Cu/Fe interface energy (~ 0.44 J/m^2 (*181*)), we can estimate the bubble pressures in Cu/Fe 100 nm multilayer (matrix) and Cu/Fe 5 nm multilayer (most bubbles located at interface) are ~ 5.3 and 3.7 GPa. Thus, we conclude that bubble pressure at interface in multilayers with smaller h (h=5 nm) is lower than that inside multilayers with larger h (h=100 nm).

4.5.2 Radiation response of incoherent Cu/Fe interfaces at small layer thickness (h < 5 nm)

Radiation tolerance of immiscible FCC/FCC metallic multilayer systems was barely studied as few such systems have immiscibility. Prior studies on He ion, proton and Kr ion irradiated Ag/Ni multilayers with large lattice mismatch (~ 14%) show

multilayers with smaller h have lower defect density after radiation(*122, 123*). Foregoing study indicates that immiscibility and incoherency are two important factors to design an interface with superior radiation tolerance. To date, however, little is known on the radiation response of coherent immiscible interfaces as it is a challenge to design coherent immiscible interfaces in metallic materials. Significant solid solubility typically prevails in metallic systems with same crystal structure and nearly identical lattice parameters, , such as Cu/Ni (*27*), Ag/Au(*182*), Ag/Al (*67, 183*), or Fe/Cr (*184*) multilayer, which are vulnerable to prominent intermixing during radiation. Due to epitaxial growth of FCC Fe on Cu in Cu/Fe multilayers, the immiscibility and coherency criteria can both be satisfied, providing a rare opportunity to study the radiation response of coherent immiscible interfaces.

The critical layer thickness for the formation of misfit dislocations in FCC Cu/Fe multilayer can be estimated as ~ 3 nm(*177*), considering the magnitude of the Burgers vector $\boldsymbol{b}$ as 0.25 nm and the mismatch strain ε_m as 0.83%. Coherent Cu/Fe interfaces start to dominate when h = 2.5 nm and complete coherency is achieved when h = 0.75 nm.

He bubble density escalates with decreasing h or increasing coherency when h < 5 nm (Fig. 67a). The bubble density in fully coherent Cu/Fe 0.75 nm multilayer is comparable to that in monolithic Cu. However, the average bubble size in fully coherent Cu/Fe 0.75 nm multilayer is smaller than multilayers with larger h and monolithic Cu (Fig. 67b), indicating that fully coherent interface can still mitigate radiation damage by effectively curtailing the bubble size. It is worth mentioning that the increase of bubble

density with decreasing h could not be attributed solely to the coherency at layer interfaces. At smaller h, bubble size is also curtailed by the layer thickness. Hence a higher bubble density will be necessary to accommodate the same concentration of implanted helium. Furthermore the magnitude of bubble induced swelling is lower in Cu/Fe 2.5 nm multilayer than the multilayers with larger h.

An intriguing phenomenon observed in irradiated Cu/Fe 0.75 nm multilayer is that bubbles reside frequently in Cu layers as shown in Fig. 64d. Such peculiar radiation response may be ascribed to relaxation of coherency strain and modulus difference between Cu and FCC Fe. First, in as-deposited coherent FCC Cu/Fe 0.75 nm multilayer, Cu is under compression and Fe is under tension with a coherency strain of ~ 0.83% (Fig. 68b). As the formation of bubbles introduces tensile strain(*104*), the bubbles may prefer to accumulate in Cu layers that are under compression to release strain energy. XRD results in Fig. 59b reflect the structural evolution of (100) and (111) Cu/Fe 0.75 nm multilayers before and after radiation. After radiation, the fully coherent diffraction peak in Cu/Fe 0.75 nm multilayers can be deconvoluted into three peaks, with respective strain of ~ 0.5% (P1), 0.2% (P2) and -0.1% (P3) near (111) peak in (111) Cu/Fe 0.75 nm multilayer. Similarly the strain in 3 deconvoluted peaks is ~ 0.7% (P1), 0.5% (P2) and -0.2% (P3) in (100) Cu/Fe 0.75 nm multilayer. We suspect that P1, P2, P3 are associated with irradiated Cu layers with confined bubbles, coherency peak between irradiated Cu and Fe, and irradiated FCC Fe layers, respectively. After radiation, the relaxation of coherency strain results in the separation of Cu and Fe peaks. Second, shear modulus of Cu (μ_{Cu} = 48 GPa) is lower than that in Fe (μ_{Fe} = 77.5 GPa). Thus it may be easier to

nucleate bubbles in Cu than in Fe. As the average layer thickness of Cu is 0.75 nm, the average bubble diameter is in the same range, ~ 1 nm, much smaller than those observed in other Cu/Fe multilayers with greater h.

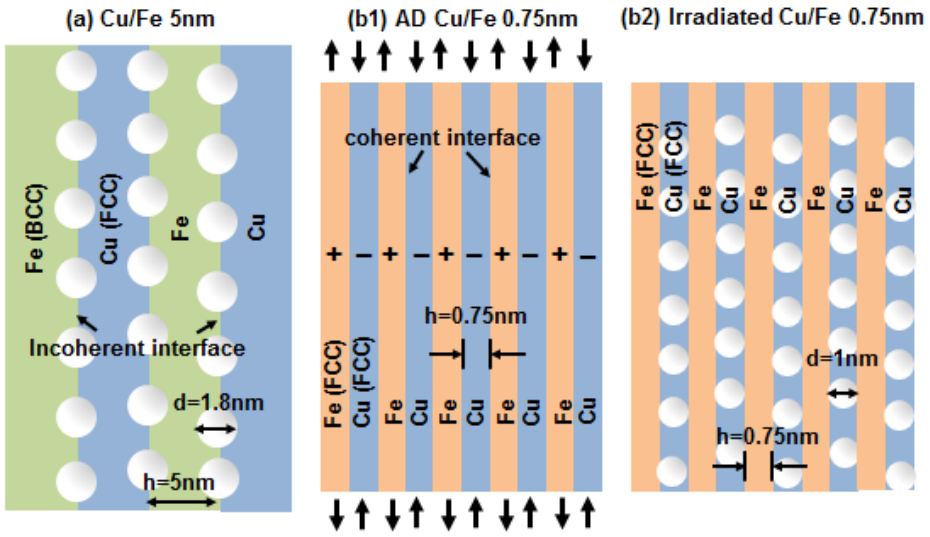

Figure 68 (a) Schematics illustrate that in incoherent Cu/Fe 5 nm multilayer, He bubbles align predominantly along layer interfaces. (b1) Prior to radiation in fully coherent immiscible Cu/Fe 0.75 nm multilayer, Cu is under compression and Fe is under tension. (b2) After radiation, He bubbles prefer to nucleate in Cu layers and are constricted to reside inside Cu layers.

Foregoing discussions suggest that bubble size is effectively curtailed by layer thickness in coherent immiscible multilayers, resulting in a substantial decrease of swelling. Coherent immiscible layer interfaces also play an essential role in mitigating radiation damage.

4.6 Conclusion

A systematic study on radiation response of immiscible Cu/Fe multilayers with incoherent and coherent layer interfaces was performed. At large layer thickness ($h \geq 5$ nm), incoherent Cu/Fe interface is stable and enables significant reduction of He bubble density. At smaller layer thickness ($h \leq 2.5$ nm) when coherency prevails, bubble density increases. However the average bubble size is substantially curtailed by fully coherent immiscible interfaces, leading to reduced swelling. Therefore, this study suggests that coherent immsicible interfaces can also prominently alleviate radiaiton damage.

4.7 Acknowledgements

We acknowledge financial support by NSF DMR-1304101. This work was performed, in part, at the Center for Integrated Nanotechnologies (CINT), a U.S. Department of Energy Nanoscience user facility, jointly operated by Los Alamos and Sandia National Laboratories. Los Alamos National Laboratory, an affirmative action equal opportunity employer, is operated by Los Alamos National Security, LLC, for the National Nuclear Security Administration of the U.S. Department of Energy under contract DE-AC52-06NA25396. HAADF-STEM was performed by Dr. Yuanyuan Zhu at the National Center for Electron Microscopy at Lawrence Berkeley National Laboratory, which is supported by the Office of Science, Office of Basic Energy Sciences of the US Department of Energy (Contract DE-AC02-05CH11231). Access to microscopy and imaging center (MIC) at Texas A&M University is also acknowledged.

CHAPTER V

IN SITU STUDIES OF HEAVY ION IRRADIATION RESPONSE OF IMMISCIBLE CU/FE MULTILAYERS

5.1 Overview

Recent studies show that immiscible incoherent metallic multilayers can effectively reduce defect density in ion irradiated metals. Layer interfaces are active defect sinks that capture and annihilate radiation induced defect clusters. Although there is general anticipation that defect density within the layers should vary as a function of distance to the layer interface, there is, to date, no *in situ* evidence to validate such a hypothesis. In this study monolithic Cu films and Cu/Fe multilayers with individual layer thickness (h) of 100 and 5 nm were subjected to *in situ* Cu ion irradiation at room temperature to 1 displacements-per-atom inside a transmission electron microscope. Rapid formation and propagation of defect clusters were observed in monolithic Cu, whereas fewer defects with smaller dimensions were generated in Cu/Fe multilayers with smaller h. Furthermore *in situ* video shows that the accumulative defect density (acquired over a period of time) in Cu/Fe 100 nm multilayers indeed varies as a function of distance to the layer interfaces, supporting the long postulated hypothesis.

5.2 Introduction

High energy neutrons and heavy ion particles can induce significant density of interstitials, vacancies and defect clusters in irradiated metallic materials, and

correspondingly lead to degradation of their performance in nuclear reactors. For instance neutron irradiation to a dose of several to tens of displacements-per-atom (dpa) may lead to void swelling, radiation embrittlement and radiation creep in a variety of metallic materials with face-centered cubic structures (*86, 185, 186*). Meanwhile the advanced nuclear energy systems call for extraordinary materials that can sustain neutron irradiation damage up to 200 dpa (*72-74, 187, 188*). Such a daunting challenge drives extensive materials research towards the discovery and design of advanced radiation tolerant materials.

In general, there are several approaches to accomplish enhanced radiation tolerance in materials (*187*). First, the inherent radiation tolerance of metallic materials appears to depend on their crystal structures. For instance the visible density of defect clusters is much greater in Cu than in Fe subjected to the same dose of radiation (*189, 190*). MD simulations suggest that the total defect densities in Cu and Fe are very similar at the same dose. However, cluster size in Cu at the same dose is much larger than that in Fe, due to the formation of large vacancy clusters in the cascade core in Cu, and the much larger number of free vacancies in Fe (*79*). Bacon et al also suggested that defect clusters in irradiated BCC Fe are relatively small and more finely dispersed, which enhances recombination during radiation (*191*). In parallel ferritic/martensitic steels with primarily BCC type structures are frequently shown to possess superior void swelling radiation resistance than austenitic stainless steels with FCC type of crystal structures (*185*). Second, an intensively investigated approach is to design materials with high-density defect sinks, including grain boundaries (GBs) (*88-90, 93*), twin boundaries(*163,*

192), and phase boundaries (*112, 125, 128, 164, 165, 175*). A majority of these boundaries, acting as unbiased defect sinks, can absorb point defects and their clusters, and promote their recombination (*91, 138*). For instance nanocrystalline (nc) metals with high volume ratio of GBs showed significantly reduced defect density during radiation(*93, 166-168*) and recently direct evidence on defect cluster absorption by high angle GBs in nc Ni was reported via *in situ* radiation experiments inside a transmission electron microscope (*10*). In nanotwinned Ag with high density twin boundaries, the density of irradiation induced defects decreased at smaller average twin spacing (*163*). Furthermore twin boundaries were shown to be mobile and actively engage and absorb radiation induced defect clusters (*163, 192*). Also the abundant metal/oxide phase boundaries in oxide-dispersion-strengthened (ODS) alloys are critical to alleviate radiation damage (*130-134*).

Meanwhile there are increasing studies on the role of layer interfaces on radiation damage in multilayers. (*112, 125, 126, 128, 174*), There are several studies on systems with metal/ceramic interfaces (e.g. Fe/TiO_2 (*172*), Fe/Y_2O_3 (*173*)) and ceramic/ceramic interfaces (TiN/MgO (*170*), TiN/AlN (*171*)). These studies show that layer interfaces could preserve integrity of layers, such as suppressing crystallization in amorphous Y_2O_3 in Fe/Y_2O_3 and amorphization in AlN in TiN/AlN and TiO_2 in Fe/TiO_2. In comparison, various types of metallic multilayer systems have been investigated, including those with FCC/BCC interfaces (Cu/Nb (*112, 127, 128, 175*), Cu/V(*103-105*), Cu/Mo(*106*), Cu/W(*107*), Al/Nb(*108*), Ag/V(*109, 110*)), FCC/FCC interfaces (e.g. Cu/Ni(*100*), Cu/FCC Co (*193*) Ag/Ni(*122, 123*)), BCC/BCC interfaces (Fe/W(*124*)) and

BCC/amorphous interfaces (Fe/Fe_2Zr), where FCC and BCC stand for face-centered cubic and body-centered cubic, respectively. Alternatively these multilayer systems could be classified into two groups: systems with chemically immiscible and miscible interfaces. In general, layer interfaces in immiscible systems are more effective (than those in miscible counterparts) to mitigate radiation damage as they are not prone to radiation induced intermixing (*125, 126*). Prominent size effect on radiation tolerance has been reported in immiscible Cu/V multilayer system (*103-105*). The magnitude of radiation hardening and density of radiation induced defect clusters (such as He bubbles) decrease with decreasing individual layer thickness h. However a reversal was recently observed in (100) textured Cu/Co systems with FCC/FCC interfaces, that is the magnitude of radiation hardening (due to He ion irradiation) increases with decreasing layer thickness. The reverse size effect arises due to the transition of deformation mechanisms from partial dislocation dominated strengthening in as-deposited multilayer to full dislocation dictated deformation mechanism in He ion irradiated Cu/Co multilayers. He bubbles segregated to layer interface and hence forcing partials to constrict at layer interface (*193*). In spite of the reverse size dependent strengthening in Cu/Co system, the multilayer still has the anticipated mitigation of defect density. As layer interfaces are effective defect sinks, one anticipate that, similar to the existence of GB denuded zones near high angle GBs, interface affected zones should exist near layer interfaces in immiscible multilayers. However, such evidence has not been reported to date. A convincing method to validate such a hypothesis is to use *in situ* technique.

In situ irradiation experiments inside a transmission electron microscope provide a unique opportunity to investigate generation of defects, their migration kinetics, and interactions of radiation induced defects clusters with defect sinks. Although multilayer systems have been extensively studied, direct evidence on size effect on radiation damage in FCC/BCC multilayers remains scarce. Here we use Cu/Fe multilayer as a model system to investigate, via *in situ* radiation technique, size dependent response to radiation damage under heavy ion irradiation. Cu and Fe are selected as both are classical model systems for FCC and BCC crystal structures and they have drastically different response to radiation damage. Our studies show that there is a size dependent variation of defect density in multilayers, and the concentration of defects indeed varies as a function of distance to layer interfaces, manifesting the existence of interface affected zone.

5.3 Experimental

Cu/Fe multilayer films with individual layer thickness h of 100 and 5 nm (referred to as Cu/Fe 100 nm and Cu/Fe 5 nm hereafter) were magnetron sputtered at room temperature on HF etched Si (110) substrates. The chamber was evacuated to a base pressure less than 8×10^{-8} torr prior to deposition. Before the deposition of Cu/Fe multilayers, a 100 nm thick Cu seed layer was deposited. Details on deposition experiments were reported previously (*177*). *In situ* Cu ion irradiation experiments were conducted at room temperature in a JEOL JEM-2100 transmission electron microscope in the Ion Beam Lab at Sandia National Laboratories. A 6 MV EN tandem ion

accelerator was used to generate a 3 MeV Cu^{3+} beam. The ion beam enters the microscope at 90^{o} to the electron beam to radiate a tilted TEM foil. Depth-dependent damage and defect concentration profiles were calculated by the Stopping and Range of Ions in Matter (SRIM)-2008 (*144*). SRIM simulation shows that most Cu ions at 3 MeV penetrate through the thin specimen, leaving behind displacement damage in the irradiated TEM foil. *Ex situ* transmission electron microscopy (TEM) experiments were carried out on an FEI Tecnai G2 F20 microscope operated at 200 kV with a Fischione ultra-high resolution high-angle annular dark field (HAADF) detector. Cross-sectional TEM (XTEM) samples were prepared by dimpling and low energy (3.5 keV) Ar ion milling and subsequent ion polishing. The average thickness of TEM thin foils was determined to be 100 nm, by using convergent beam electron diffraction (CBED) technique.

5.4 Results

Microstructures of monolithic Cu, Cu 100 nm/Fe 100 nm and Cu 5 nm / Fe 5 nm multilayers (referred to as Cu/Fe 100 nm and Cu/Fe 5 nm multilayers hereafter) irradiated by Cu ions at 3 MeV are compared in TEM micrographs in Fig. 69. In monolithic Cu irradiated to a dose of 0.5 dpa, high-density defect clusters were generated (Figs. 69a1-a2). In comparison, radiation to 1 dpa led to a moderate increase in loop density in Cu/Fe 100 nm multilayers (Figs. 69b1-b2). The columnar grains with an average grain size of 16 nm in Fe layers retained after radiation. Few radiation

induced defect clusters were detected in irradiated Cu/Fe 5 nm nanolayers (Figs. 69c1-c2).

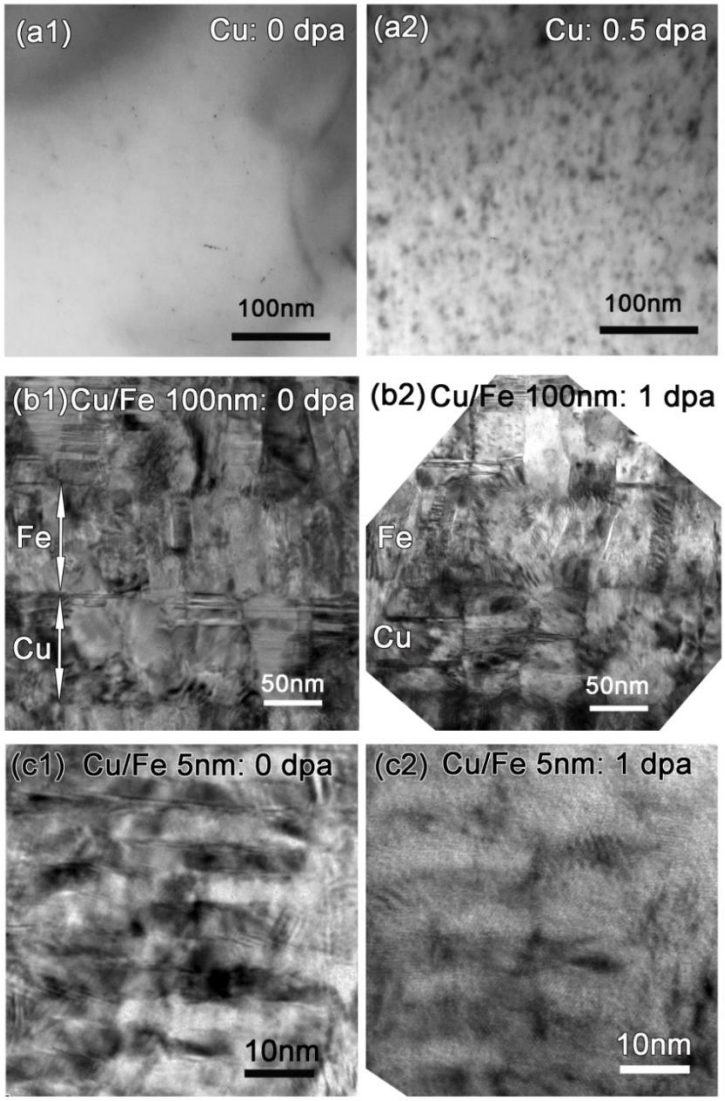

Figure 69 A comparative overview of radiation damage in monolithic Cu film, Cu/Fe 100 nm and Cu/Fe 5 nm multilayers irradiated by Cu ions at 3 MeV to 0.5-1 dpa at room temperature. (a1-a2) In irradiated monolithic Cu subjected to a dose of 0.5 displacements-per-atom (dpa), high-density defect clusters were generated. (b1-b2) Radiation to 1 dpa led to a moderate increase in loop density in Cu/Fe 100 nm multilayers. Nanoscale columnar grains in Fe layers retained after radiation. Defect clusters were sporadically distributed in primarily Cu layers. (c1-c2) Few defect clusters were detected in irradiated Cu/Fe 5 nm nanolayers.

Several TEM micrographs in Fig. 70 recorded during *in situ* radiation (up to 1 dpa) of Cu/Fe 100 nm multilayers revealed microstructural evolutions. As shown in Fig. 70a, the as-deposited multilayer is nearly free from defect clusters. At a radiation dose of 0.1 dpa, a few dislocation loops outlined by red dash lines appeared in Cu layers. While many of these loops have spherical geometry, loops with triangular geometry were frequently identified. With the increase of radiation dose to 0.5 and 1 dpa, the dimension of defect clusters increased monotonically without significant increase in defect density in irradiated Cu layers. Few defect clusters were generated in irradiated Fe layers throughout the entire radiation experiment. Meanwhile, no significant intermixing along layer interfaces was observed in irradiated multilayers.

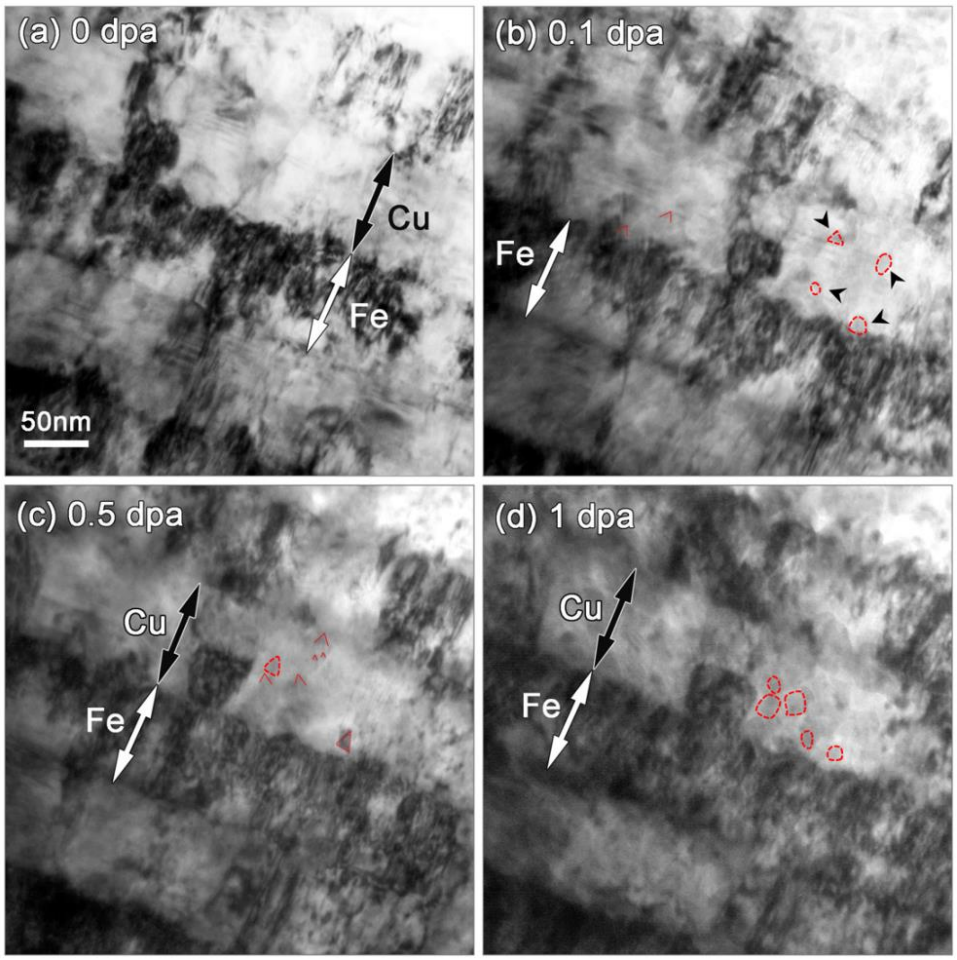

Figure 70 *In situ* observation of radiation induced evolution of microstructure in Cu ion irradiated Cu/Fe 100 nm multilayer up to 1 dpa. (a) The Cu in as-deposited multilayers is nearly free from defect clusters. (b) At 0.1 dpa, dislocation loops appeared in Cu layers as shown by arrows. (c) When the dose increased to 0.5 dpa, the density of defect clusters also increased. (d) No significant increase of defect density was observed up to 1 dpa. Few defects were observed in irradiated Fe layers throughout the entire radiation experiment. There is insignificant morphology change for layer interfaces in irradiated multilayers.

The Cu/Fe 5 nm multilayer shows superior microstructural stability under radiation. As marked in Fig. 71, several pre-existing growth defects (marked as 1-4 in blue arrows) in as-deposited layers were identified as references and these pre-existing

defect clusters barely changed during radiation. The density of newly generated defect clusters (labeled as 5 and 6 by red arrows) during radiation is insignificant compared to that of pre-existing defects.

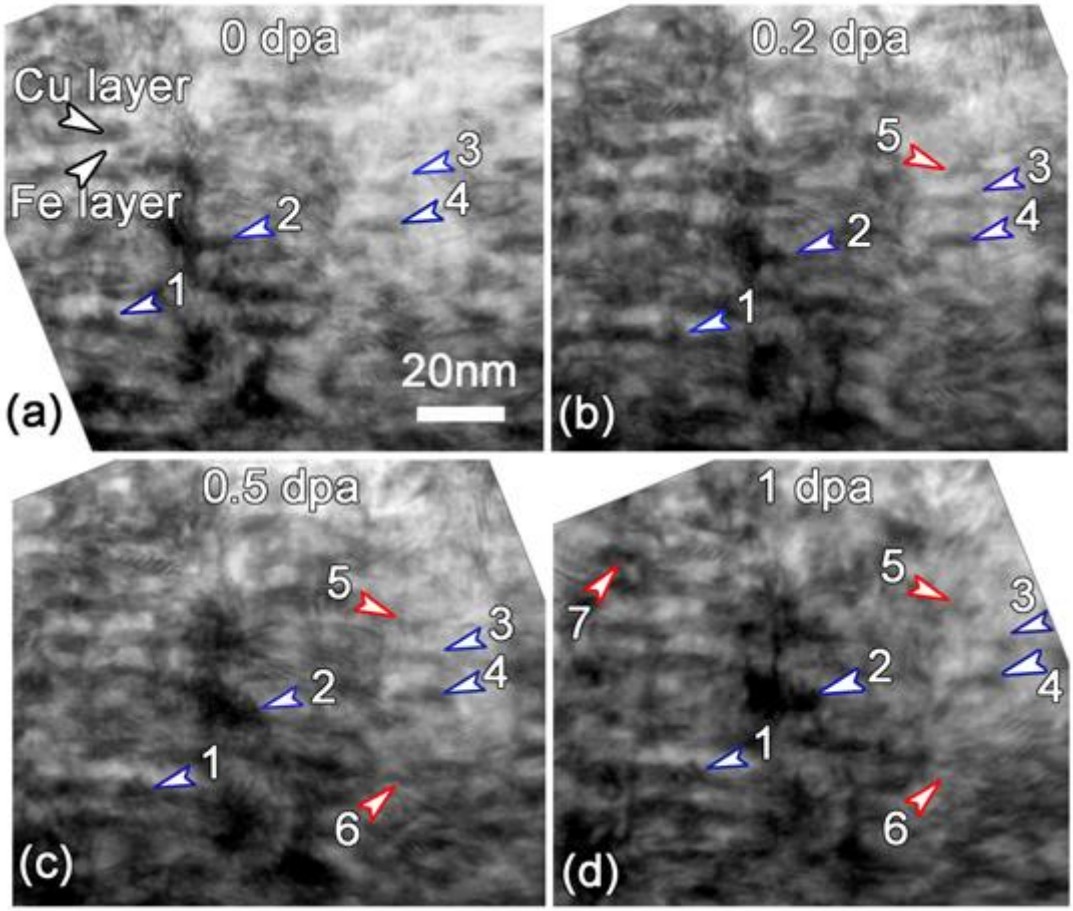

Figure 71 *In situ* observation of defect evolution in Cu/Fe 5 nm multilayer subjected to a dose of 1 dpa. The Cu/Fe layered structure shows superior structural stability under radiation and very few defects (marked as 5-7 with red arrows) were generated in irradiated nanolayers. Several pre-existing growth defects (marked as 1-4 in blue arrows) in as-deposited layers were identified as references and these pre-existing defect clusters only changed slightly during radiation.

Statistical studies on evolution of density and dimension of defect clusters were performed on Cu ion irradiated monolithic Cu, Cu/Fe 100 nm and Cu/Fe 5 nm multilayers. As shown in Fig. 72a, defect density in irradiated Cu increased rapidly with dose and did not reach saturation by 0.5 dpa (*194*). In contrast, defect density in irradiated Cu/Fe 100 nm multilayer increased much more slowly than that in Cu, and by 0.5 dpa, and appeared to reach a saturation at a level ~ 1/5 of that in irradiated Cu. Much fewer defect density was observed in Cu/Fe 5 nm multilayer than that of Cu/Fe 100 nm multilayer. Another interesting observation is the average dimension of defect clusters (defect size) in irradiated monolithic Cu is 7 ± 2 nm, similar to that in Cu layers in irradiated Cu/Fe 100 nm multilayers, 9 ± 3 nm. In contrast the defect size in irradiated Cu/Fe 5 nm multilayer was 3 ± 1 nm), much smaller than the other two specimens.

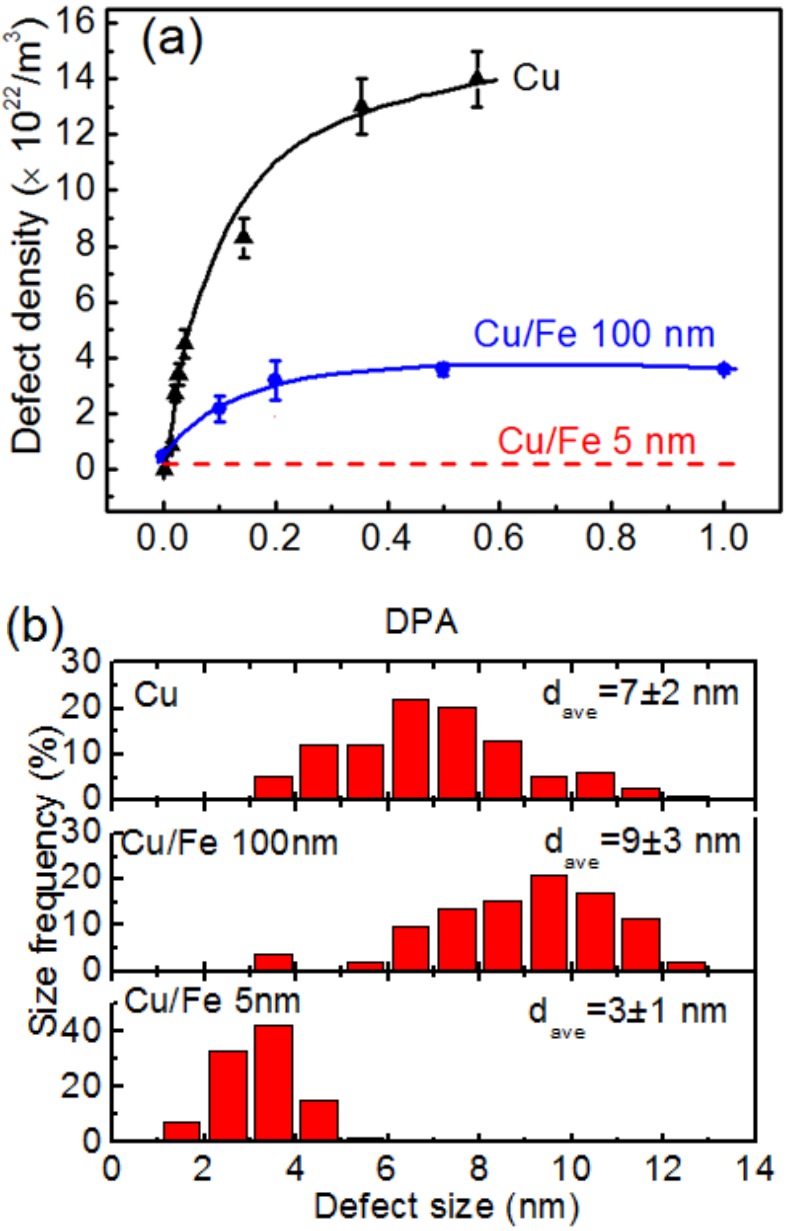

Figure 72 A statistical study of defect cluster density and size in Cu ion irradiated monolithic Cu, Cu/Fe 100 nm and Cu/Fe 5 nm multilayers. (a) In irradiated Cu, defect cluster density increased rapidly with dose. In contrast, defect density in Cu/Fe 100 nm multilayer is ~ 1/5 of that in irradiated Cu. Fewer defects were generated in irradiated Cu/Fe 5 nm multilayer (excluding the density of pre-existing defect clusters before radiation). (b) The average defect size in irradiated monolithic Cu is 7 ± 2 nm, comparing to 9 ± 3 nm for Cu/Fe 100 nm and 3 ± 1 nm for irradiated Cu/Fe 5 nm multilayers.

5.5 **Discussion**

5.5.1 The influence of Cu/Fe layer interfaces on absorption of radiation induced defects

Incoherent layer interfaces in immiscible multilayer systems have been proven as defect sinks in irradiated multilayers (*112, 125, 128*). The Cu/Fe interfaces in irradiated Cu/Fe multilayers also appear effective in alleviation of radiation induced damage. *In situ* irradiation studies show a clear layer thickness dependence of defect density in irradiated Cu/Fe multilayers: multilayers with smaller h show much lower radiation induced defect density than those in irradiated monolithic Cu. Meanwhile, the smaller layer thickness (h=5nm) effectively refrain the growth of defect clusters in Cu layers, evidenced by the fact that the average defect size in irradiated Cu/Fe 5 nm multilayer (~ 3nm) is much smaller than that in monolithic Cu and Cu/Fe 100 nm multilayers (~ 7 and 9 nm respectively).

Size effect on alleviation of radiation induced defect cluster density has been observed in several immiscible metallic multilayer systems. For instance the density of He bubbles in He ion irradiated Cu/V, Cu/Nb, Ag/Ni and Ag/V multilayers decreases monotonically with decreasing h(*103, 109, 122, 126*). However, recently we observed that the density of He bubbles in He ion irradiated Cu/Fe multilayers first decreased with decreasing h to ~ 5 nm, and then increased at smaller h(*195*). When h reduces to less than 5 nm, the Cu/Fe multilayers become increasingly coherent (due to the formation of FCC Fe). Hence at a first sight, such a reversal on size effect appears to suggest that there is optimum layer thickness below which the radiation tolerance of multilayers is

degraded. However, our studies show that the magnitude of swelling still has a positive size effect, that is the void swelling decreases monotonically with decreasing h.

The size effects on layer interface alleviated radiation damage in numerous immiscible metallic multilayers seem to suggest that there shall be a layer interface affected denuded zone, wherein the density of defect clusters is much lower adjacent to the layer interface than those in layer interior. Such a long postulated hypothesis has not been validated to date. There is indeed some *in situ* evidence that captured the absorption of mobile defect clusters by layer interface in immiscible Ag/Ni multilayers(*123*). However the post radiation analysis or comparisons of individual snap shots captured at different doses during radiation do not provide direct support for the existence of layer interface affected zone. To address this question, we performed accumulative time and dose dependent studies in Cu/Fe multilayers.

A statistical study on accumulative defect density in Cu layers in Cu/Fe 100 nm multilayer irradiated over a dose of 0.25 - 0.31 dpa in 160 s is provided in Fig. 73. A parabolic distribution is evident: that is a maximum defect density was identified in the middle of the Cu layer, whereas defect density quickly diminished on both side of the hump. The density of defect clusters in Cu reached a minimum level adjacent to the Cu/Fe layer interfaces. Although there are still defects in the regions immediate to layer interface, such a parabolic distribution of defect density clearly suggest that the prior hypothesis for the existence of layer interface affected zones is at least qualitatively correct.

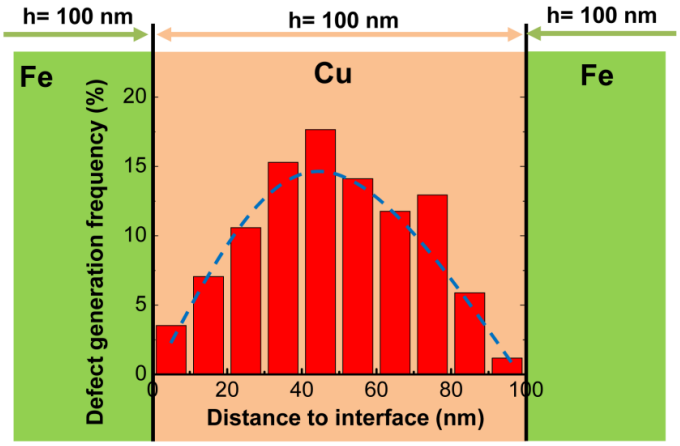

Figure 73 A statistical study on the accumulative number of defect clusters (total number of ~90, normalized in unit of fraction) generated in Cu layers in Cu/Fe 100 nm multilayer over a dose of 0.25-0.31 dpa in 160 seconds. It is evident that near Cu/Fe interfaces, fewer defects were generated; in contrast increasing defect density was observed further away from the layer interfaces.

The existence of layer interface affected zones also implies that it is more difficult for defect clusters to nucleate near layer interface, as point defect density is lower approaching layer interface, consistent to the reaction-diffusion model proposed by Demkowicz *et al.* (*115*). The defect density gradient leads to defect diffusion from grain interiors to layer interfaces. Therefore, the capability of multilayers to mitigate radiation damage by absorbing/eliminating radiation induced defects is enhanced when h is reduced to a dimension comparable to that of the fast diffusion zone. Meanwhile, due to lattice discontinuity across layer interface, cascades are confined when the cascade size and layer thickness are comparable. As a result, the separation distance of vacancies and interstitials is reduced within smaller cascades, leading to an enhanced recombination. Another possibility is defects generated near interfaces are absorbed by

interfaces directly. Either way will produce fewer survived Frenkel pairs and subsequent lower defect density, compared to the case without cascade confinement. The average cascade size can be estimated in irradiated Cu/Fe 5 nm multilayer. The average recoil energy under 1 MeV heavy ion irradiation is ~ 5 keV, although such an estimation has slight dependence on the mass of projectiles (*196*). The individual cascade size under 1 MeV heavy ion irradiation is ~ 5 nm in Cu according to Averback's study (*197, 198*). Therefore, in our experiments, the 3 MeV Cu ions may generate slightly larger cascades, comparable to h in Cu/Fe 5 nm multilayer. Such a crude estimation is consistent with little radiation induced defects and superior stability in irradiated Cu/Fe 5 nm multilayers.

5.5.2 The formation of stacking fault tetrahedron (SFT) in Cu in irradiated Cu/Fe 100 nm multilayers

The formation of defect clusters in irradiated FCC metals is largely associated with their stacking fault energy (SFE). In Cu with a low SFE of ~24 mJ/ cm^2, radiation induced vacancies prefer to aggragate to form SFTs. SFTs are frequently observed in irradaited FCC metals experimentally (*199*) and several theoretical studies have been performed to decribe the formation mechamism of SFT under radiation (*200*). Hoever, little *in situ* evidence on the formation of SFT has been reported to date. During in situ radiation of Cu/Fe 100 nm multilayer at a dose of ~ 0.5 dpa, we captured an event during the formation of an SFT in a Cu layer.. As shown in Fig. 74, a vacancy (Frank) loop emerged in Cu layer next to the Cu/Fe layer interface during radiation at 0 s. The Frank

loop continued to expand within the next 0.6 s. By 1.5 s, a stable SFT formed. SFT is a stable configuration of vacancy clusters, and can retain in FCC metals during radiation.

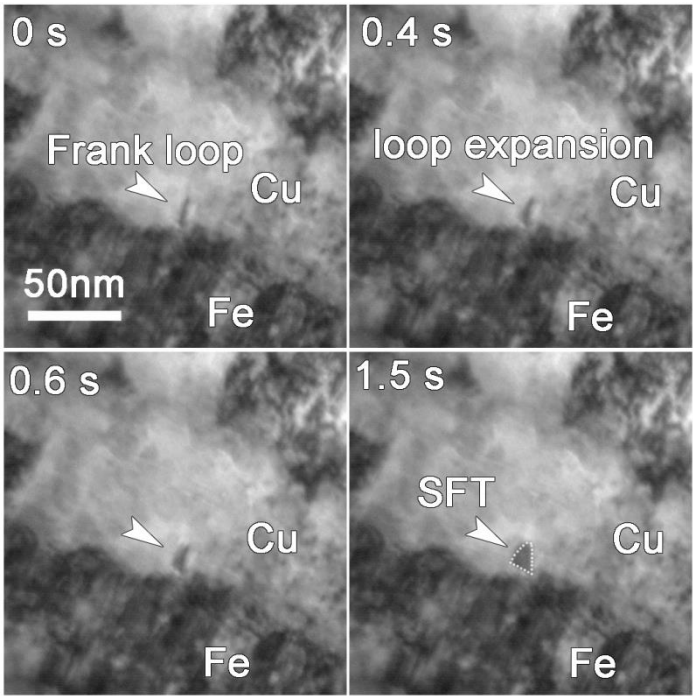

Figure 74 *In situ* video snapshots capturing the formation of a stacking fault tetrahedron (SFT) in Cu layer in irradiated Cu/Fe 100 nm multilayer over a dose of ~ 0.5 dpa. (a) At 0 s, a Frank loop appeared in Cu layer adjacent to the Cu/Fe layer interface. (b-c) The Frank loop continued to grow (evolve) during radiation. (d) A stable SFT formed by 1.5 s.

During *in situ* radiation of Cu/Fe multilayers, we observed apparently greater defect density in Cu layers, and little defects were detected in irradiated Fe layers. This is consistent with prior studies that showed the apparent defect density in irradiated monolithic Cu is much greater than that in BCC Fe at a dose level of 1 dpa or less (*190*). Such a large difference was explained by the preferential clustering of vacancies at the

cascade core in irradiated Cu, whereas most vacancies do not cluster in irradiated Fe. Furthermore the interstitial defect cluster size in Fe is much smaller and more mobile than those in Cu, hence reducing the dimension of defect clusters in Fe(*79, 187*).

5.6 **Conclusion**

We studied monolithic Cu films and Cu/Fe multilayers with individual layer thickness of 100 and 5 nm, subjected to *in situ* Cu ion irradiation at room temperature to 1 displacements-per-atom, where a clear size effect in defect density and size was observed: in monolithic Cu, rapid propagation of defect clusters was observed, whereas fewer defects (less than 1/5 of defects in Cu) were generated in Cu/Fe 100 nm multilayer and radiation induced defects in Cu/Fe 5 nm multilayer were barely observed. A statistical study in 100 nm thick Cu layers via *in situ* video reveals the existence of layer interface affected zone, that is the number of nucleation sites of loops declines when approaching Cu/Fe interfaces. Meanwhile, the defect growth in 5 nm thick Cu layers was suppressed (~ 3 nm) by Cu/Fe interfaces while the defect sizes in monolithic Cu (~ 7 nm) and Cu layers in Cu/Fe (~ 9 nm) 100 nm multilayer are close.

5.7 **Acknowledgements**

We acknowledge financial support by NSF DMR-1304101. Michael Marshall and Daniel Buller are acknowledged for their assistance on the TEM and ion beam at Sandia National Laboratory. Access to microscopy and imaging center (MIC) at Texas A&M University is also acknowledged.

CHAPTER VI

UNUSUAL SIZE DEPENDENT STRENGTHENING MECHANISMS IN HELIUM ION IRRADIATED IMMISCIBLE COHERENT CU/CO NANOLAYERS*

6.1 Overview

He ion irradiation induced damage in several immiscible metallic nanolayer systems with incoherent interfaces has been investigated recently and a prominent size effect on mitigation of radiation damage has been observed. In general the magnitude of radiation hardening and defect cluster density are both less at smaller individual layer thickness (h) than those with larger h, as interfaces can effectively reduce density of radiation induced defect clusters. Here we show, however, an opposite size dependent strengthening behavior in He ion irradiated immiscible coherent Cu/Co multilayers, that is films with smaller h have greater radiation hardening. Such unusual size dependent strengthening could be explained via a transition from partial dislocation transmission (before radiation) to full dislocation transmission (after radiation) dictated strengthening

*This chapter reprinted with permission from "Unusual size dependent strengthening mechanisms in helium ion irradiated immiscible coherent Cu/Co nanolayers" by Y. Chen, Y. Liu, E.G. Fu, C. Sun, K.Y. Yu, M. Song, J. Li, Y.Q. Wang, H. Wang, X. Zhang; Acta Materialia, Volume 84, pages 393-404, Copyright 2015 by Elsevier.

mechanisms due to formation of He bubbles at layer interface. Furthermore we show that, similar to incoherent immiscible systems, coherent interface in immiscible system can also effectively reduce the population of radiation induced defect clusters.

6.2 Introduction

Neutron radiation on structural materials in nuclear reactors creates abundant vacancies and interstitials, which could form defect clusters, primarily in the form of dislocation loops and voids/bubbles (*82*). The nucleation and growth of voids/bubbles are enhanced by Helium (He), a byproduct of (n,α) nuclear transmutation. He can swiftly migrate into and combine with vacancies to accelerate the nucleation of bubbles and stabilize them (*160-162*). Recent study shows that He atoms can be trapped and stored at defect sinks such as grain boundaries (GB) (*90, 93*) and interphase boundaries (*112, 125, 128, 164, 165*). The storage of He at interfaces can delay bubble growth significantly and thus alleviate radiation hardening, void swelling and blistering. GB and interphase boundaries also provide effective annihilation sites for radiation induced interstitials and vacancies (*174, 201*). Increasing efforts have been devoted to investigate the radiation tolerances of nanostructured materials, including ODS alloys with abundant metal/oxide interfaces (*130-134*), nanocrystalline (nc) metals(*10, 93*) and multilayers (*112, 126, 128*). Experimentally, Singh and Foreman (*88, 89*) have observed significant grain size dependence of void swelling in stainless steel decades ago. Sun *et al*.(*10*) have reported the first *in situ* evidence of defect aborption by grain boundaries (GBs) in nanocrystalline nickel sujected to Kr ion radiation. Theoretically, molecular dynamics

(MD) simulations have shown that GBs can emit interstitials into grain interior to annihilate vacancies (*91*). Chen *et al.* (*138*) have also shown defect-GB interactions by formation and annealing of chain-like defects. Yu *et al.* (*163, 192*) reported that twin boundaries can effectively interact with and remove radiation induced defect clusters, such as stacking fault tetrahedra. Besides these internal defect sinks, free surfaces in nanoporous (np) metals were also reported to significantly reduce defect density during irradiation (*202-204*). Furthermore *in situ* radiation studies on np Ag also revealed that both global and instantaneous diffusivity of defect clusters in np Ag is much lower than those in coarse grained Ag, quite different from general perception (*204*).

Radiation damage in metallic multilayer systems with various types of interfaces has been investigated, including face-centered cubic (FCC)/ body-centered cubic (BCC) interfaces (e.g. Cu/Nb (*112, 128*), Cu/V (*103-105*), Cu/Mo (*106*), Cu/W (*107*), Al/Nb (*108*), Ag/V(*109, 110*)), FCC/FCC interfaces (e.g. Cu/Ni (*100*), Ag/Ni (*122, 123*)), BCC/BCC interfaces (Fe/W (*124*)) and FCC/hexagonal close-packed (HCP) interfaces (Al/Ti (*205*)). In general clear size dependent enhancement of radiation tolerance was observed in immiscible systems, that is the density of defect clusters (dislocation loops or He bubbles) declines with decreasing individual layer thickness h. Meanwhile the magnitude of radiation hardening typically decreases at smaller h. The rationale behind these phenomena is that immiscible layer interfaces appear to be effective sinks that absorb and remove radiation induced defect clusters (*125, 126*). Yu *et al*. (*123*) have provided the first *in situ* observation where layer interface in immiscible Ag/Ni nanolayers can effectively capture and annihilate radiation induced defect clusters.

Size dependent radiation hardening has also been quantitatively analyzed in several He ion irradiated metallic multilayer systems. The peak strength of irradiated multilayers is determined by the inherent resistance of layer interfaces to the transmission of single dislocations and the interaction of dislocations with radiation induced obstacles, such as dislocation loops, stacking fault tetrahedra, and He bubbles. The models developed by comparing the characteristic dimension (average separation distance between He bubbles) and layer thickness were able to capture the major trend of size dependent strengthening in He ion irradiated nanolayers (*109, 122, 127, 128*). Interestingly Yu *et al.* also noticed that in contrast to size dependent strengthening in He ion irradiated Ag/Ni nanolayers, there is not a strong size dependence in proton irradiated Ag/Ni systems, implying the significance of He bubbles on radiation hardening (*122*).

Recently, we reported that as-deposited immiscible Cu/Co (FCC) (100) multilayer system has a peculiar size dependent strengthening behavior (*135*). In general we anticipate that Cu/Co (100) (*135*) and Cu/Ni (100) (*27*) multilayer systems should have similar size dependent strengthening. This is because both systems have comparable Koehler stress (due to the same magnitude of modulus mismatch) and coherency stress (arising from lattice mismatch). However nanoindentation experiment reveals three drastic differences between strengthening behaviors of the two systems. (1) When individual layer thickness (h) is several nm, the peak hardness of Cu/Co is significantly lower, by ~ 1 GPa, than that of Cu/Ni. (2) When h is 50-200 nm, the hardness of Cu/Co is greater than that of Cu/Ni nanolayers. (3) Cu/Co (100) system has

a much smaller Hall-Petch slope than that of Cu/Ni (100) system. The lower peak strength of Cu/Co is ascribed to the transmission of partial dislocations across the interface, in comparison to full dislocation transmission across Cu/Ni interface, as Cu and Co both have low stacking fault energy (SFE) (γ_{SF}^{Co} = 24 mJ/m^2 , γ_{SF}^{Cu} = 41 mJ/m^2), whereas Ni has inherently high SFE (γ_{SF}^{Ni} = 125 mJ/m^2). At large h, Co has high-density stacking faults, with an average spacing of several nm, and hence contributes significantly to the high strength of Cu/Co nanolayers.

The motivations of the study on radiation damage in Cu/Co (100) system include the followings. (1) To date there is only one study on radiation damage in immiscible FCC/FCC system, Ag/Ni, which has incoherent interfaces (due to large lattice mismatch between Ag and Ni). In comparison the immiscible Cu/Co has coherent FCC/FCC layer interfaces, permitting us to probe the influence of coherency on radiation tolerance of immiscible FCC/FCC multilayers. (2) Size dependent strengthening mechanisms in irradiated Cu/Co with coherent interface may not be identical to immiscible multilayers with incoherent interface. (3) To examine size dependent variation of defect density in a system with immiscible coherent interfaces. (4) The stability of FCC Co could be varied during radiation.

6.3 Experimental

Cu/Co multilayers with identical h, varying from 1 to 200 nm, were magnetron sputtered at room temperature on HF etched Si (100) substrates. The chamber was evacuated to a base pressure less than 8×10^{-8} torr prior to deposition. Before the deposition of Cu/Co multilayers, a 100 nm thick Cu seed layer was deposited. The total thickness of multilayers was ~ 1 μm when $h \leq 10$ nm, ~ 1.5 μm when $10 \text{ nm} < h < 100$ nm, and ~ 4 μm when $h \geq 100$ nm. The total film thickness was designed so that indentation experiment will probe at least one bilayer, but the maximum indentation depth is limited to 10-20% of total film thickness to avoid substrate effect. The deposition rate of Cu and Co is ~ 0.5 nm/s for all layer thicknesses. The films with various h were irradiated at room temperature using 100 keV He ions with a total fluence of 6×10^{20} ions/m^2. The temperature rise of the sample stage was ~ 50^{o}C during implantation. Calibration studies show that the sample temperature is close to sample stage temperature, within 10^{o}C as there were conducting copper tapes connected between stage and sample. The sample temperature difference among irradiated multilayers of various layer thicknesses is very small, ± 10^{o}C. The base pressure in the ion implantation system was 4×10^{-5} Pa. X-ray diffraction (XRD) experiments were performed on a Brukers D8 Discover X-ray powder diffractometer at room temperature. The plan-view samples were examined by conventional out-of-plane method, in reflection mode, with energy of 20 keV. Transmission electron microscopy (TEM) experiment was carried out on a JEOL 2010 transmission electron microscope operated at 200 kV and an FEI Tecnai G2 F20 microscope operated at 200 kV with a Fischione

ultra-high resolution high-angle annular dark field (HAADF) detector. Film hardness was measured from an average of 12 - 15 indents at different indentation depths by using instrumented nanoindentation technique on a Fisherscope HM 2000XYp micro/nanoindentor with a Vickers diamond indenter tip, using instrumented indentation technique (*73*). One typical load-displacement curve is provided in Fig. 86a, which can be used to calculate indentation hardness at a specific indentation depth. The average indentation hardness is determined when hardness value reaches a plateau, nearly independent of indentation depth (*27*) and one example is displayed in Fig. 86b. Cross-sectional TEM (XTEM) samples were prepared by dimpling and low energy (3.5 keV) Ar ion milling and subsequent ion polishing. The average TEM foil thickness was measured by using convergent beam electron diffraction (CBED) technique. The thickness of TEM foils is measured to be ~ 100 ± 20 nm throughout the irradiated regions in multilayer films. The CBED method can reach an accuracy of ~ 5% in determining foil thickness (*190*). The detailed procedure of thickness measurement is shown in reference (*200*). In addition, this method has been employed in our previous studies (*103-106, 108, 122-124, 163*).

Depth-dependent damage and defect concentration profiles were calculated by the Stopping and Range of Ions (*189*) in Matter (SRIM)-2008 using the Kinchin-Pease option in the SRIM software (*144*). The Kinchin-Pease option for SRIM calculation has recently been adopted by the community as a new routine to reliably estimate radiation damage for irradiated materials (*79*).

6.4 Results

Fig. 75. shows the depth profile of He ion radiation damage in unit of displacements per atom (dpa) and helium concentration obtained from SRIM simulation of $Cu_{50}Co_{50}$ compound subjected to He ion radiation at 100 keV with a total fluence of 6 $\times 10^{20}$ ions/m^2. The peak damage approaches ~ 2.5 dpa at a depth of ~ 300 nm and the projected ion penetration depth is ~ 500 nm. He concentration approaches a maximum of ~ 3% at a depth of ~ 350 nm.

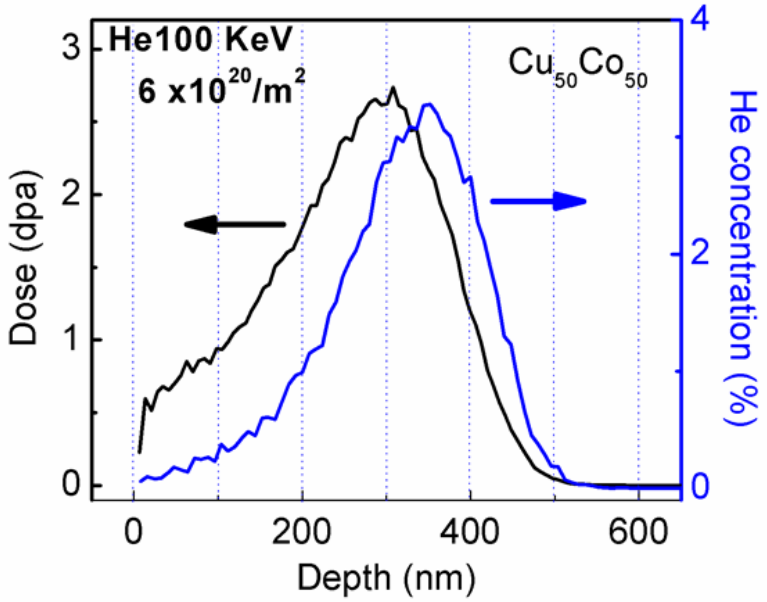

Figure 75 The depth profile of He ion radiation damage in unit of displacements per atom (dpa) and helium concentration obtained from SRIM simulation (using the Kinchin-Pease option) of $Cu_{50}Co_{50}$ compound subjected to He ion irradiation at 100 keV with a total fluence of 6 $\times 10^{20}$ ions/m^2. The peak damage approaches ~ 2.5 dpa at 300 nm from surface, and the projected ion penetration depth is ~ 500 nm.

XRD patterns were collected to investigate radiation induced structural evolution. For as-deposited films, when h ≥ 10 nm (Fig. 76a), only Cu (200) and FCC Co (200) peaks were detected. Superlattice peaks were observed in Cu 10 nm/Co 10 nm (referred to as Cu/Co 10 nm hereafter) nanolayers. Radiation led to diminished peak intensity with insignificant peak shift. Further decrease of h (1-5 nm) led to a fully coherent peak located between Cu (200) and Co (200) in the as-deposited films (Fig. 76b). The position of satellite peaks is consistent with bilayer thickness in these fine nanolayers. After radiation, the intensity of all diffraction peaks decreased, and the central peak became broader. No hexagonal closely packed (HCP) Co peaks were detected after radiation.

Extensive TEM experiments were performed to examine the microstructure of irradiated Cu/Co nanolayers. As-deposited Cu/Co 100 nm multilayer contained high density of stacking faults (SFs) in Co layers. The density of SFs in Co decreased rapidly at smaller h. No bubbles and little dislocation loops were detected in as-deposited Cu/Co multilayers without He ion irradiation, as shown in Fig. 77.

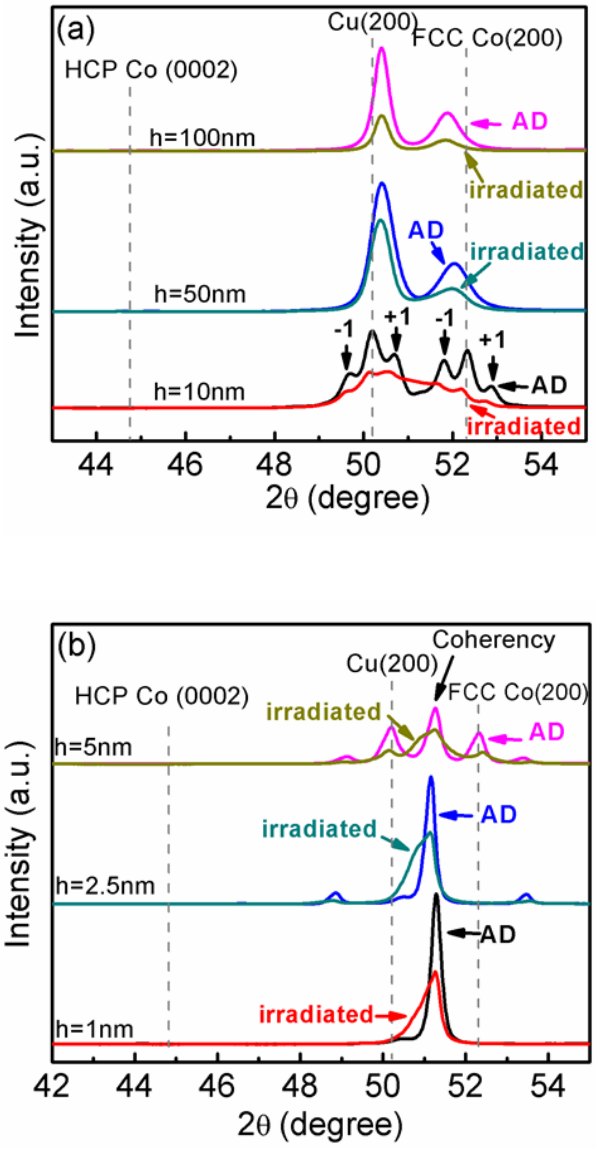

Figure 76 X-ray diffraction (XRD) patterns of as-deposited (AD) and He ion irradiated Cu/Co multilayers with various individual layer thickness h. (a) h= 10 - 100 nm and (b) h = 1- 5 nm. For as-deposited films, when h ≥ 5 nm, only Cu (200) and face-centered cubic (FCC) Co (200) peaks were detected. Further decrease of h led to a fully coherent peak located between Cu (200) and Co (200). Satellite peaks appeared when h ≤ 10 nm. After radiation, the intensity of all diffraction peaks decreased. When h ≤ 5 nm, the coherent peak became broader after radiation. No hexagonal closely packed (HCP) Co peaks were detected both before and after radiation.

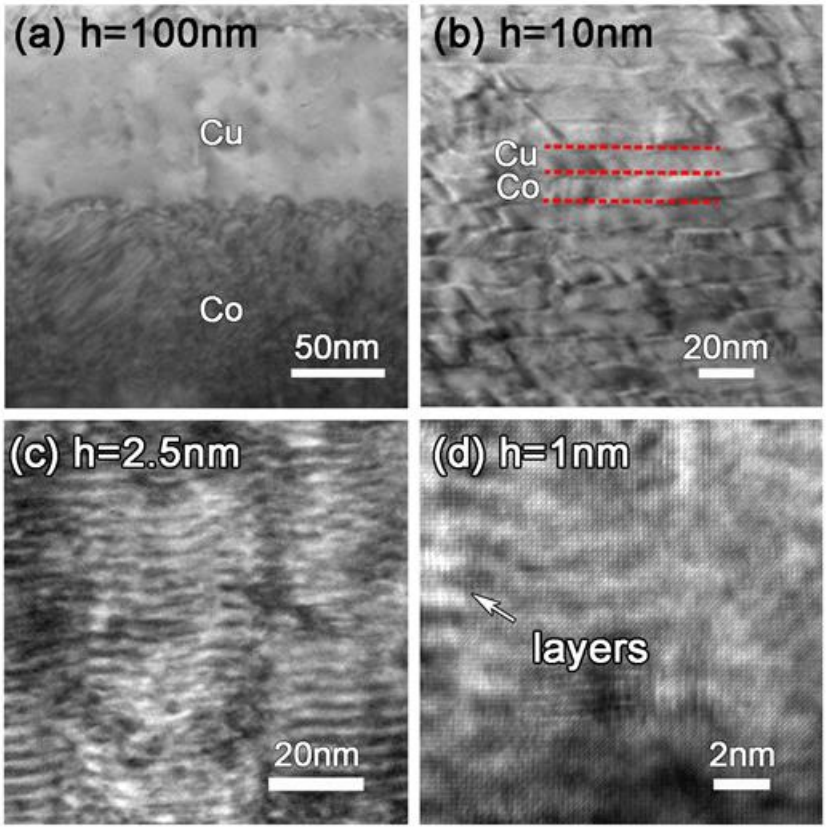

Figure 77 TEM images of as-deposited (100) Cu/Co multilayers. (a) High density of inclined stacking faults (SFs) were observed in Co in Cu/Co 100 nm multilayer. (b) In Cu/Co 10 nm multilayers, SFs were observed occasionally in Co layers. (c-d) No SFs appeared in Cu/Co 2.5 nm and Cu/Co 1 nm multilayer films. No bubbles or little dislocation loops were detected in any as-deposited Cu/Co multilayers.

Fig. 78a shows the cross-section TEM (XTEM) overview of He ion irradiated Cu/Co 100 nm nanolayer along <001> zone axis. The superimposed solid curve shows the depth profile of He concentration calculated by SRIM. The layered structure can be clearly discerned and the embedded selected area diffraction (SAD) pattern of the irradiated region confirms the retention of single-crystal like Cu and FCC Co. Boxes b-e at different penetration depth are shown at higher magnification in succeeding figures. In

the surface region (Fig. 78b), He bubbles were randomly distributed. In the peak damage region, high-density bubbles were observed in both Cu (Fig.78c) and Co (Fig.78d) layers. Fewer He bubbles were observed in Co layer near the end of projected ion range (Fig. 78e).

Fig. 79 displays XTEM images of irradiated Cu/Co 5 nm multilayer. In the peak damage region, 400 nm from surface (Fig. 79a), He bubbles were distributed both within the layers and along layer interfaces as indicated by arrays of dash lines. In a region (600-700 nm from surface) beyond the peak radiation damage (Fig. 79b), we observed clear alignment of bubbles along layer interfaces (indicated by dash lines). The embedded SAD pattern of irradiated Cu/Co multilayer shows the film retained epitaxial structure with fully coherent Cu/FCC Co interface. A typical region captured at underfocus (Fig. 79c1) and overfocus (Fig. 79c2) conditions confirmed the alignment of He bubbles, appearing as white and dark dots, along interfaces.

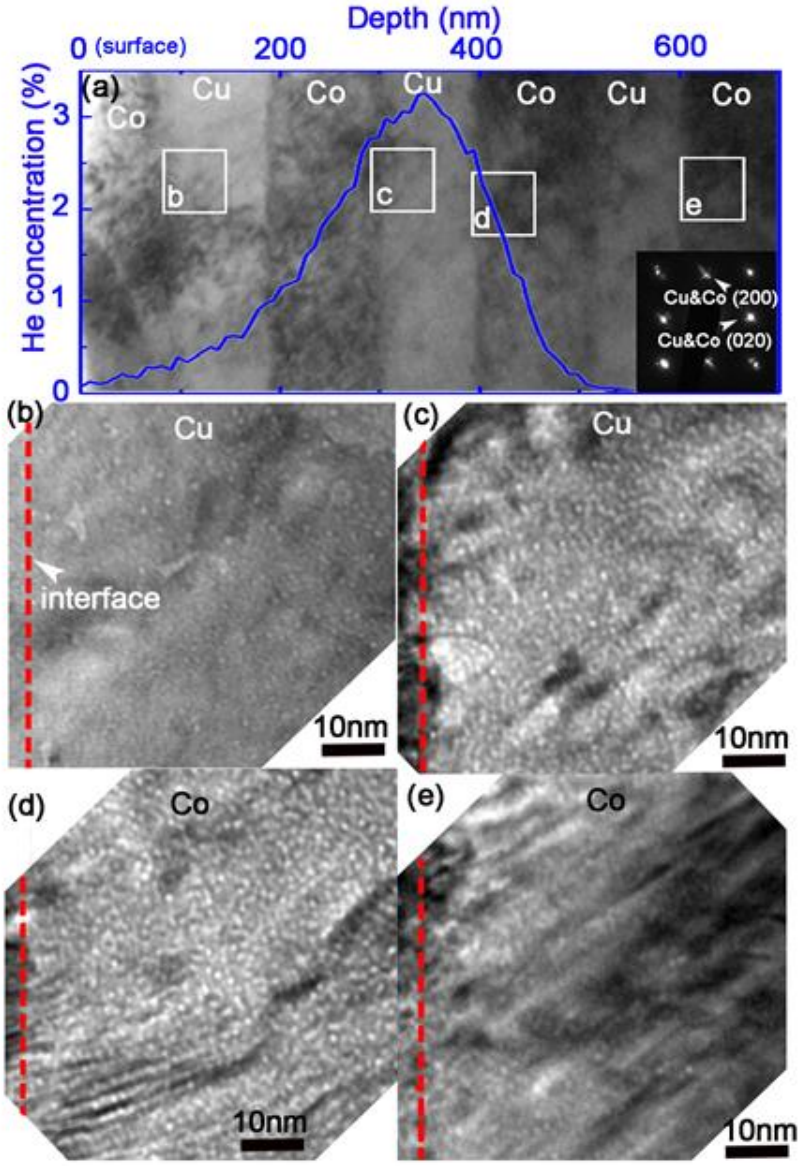

Figure 78 Cross-section TEM (XTEM) images of He ion irradiated Cu/Co 100 nm multilayer. (a) Overview of the irradiated multilayer at low magnification. The superimposed solid curve shows the depth profile of He concentration calculated by SRIM. The embedded selected area diffraction (SAD) pattern of irradiated region confirmed the film retained single-crystal like FCC Cu and Co phase. The boxes b-e at different penetration depths are shown at higher magnification in the succeeding figures. (b) Bubbles were observed with random distribution. (c) and (d) show high-density bubbles observed in Cu and Co layers, respectively. (e) In location e, fewer He bubbles were observed in Co layer.

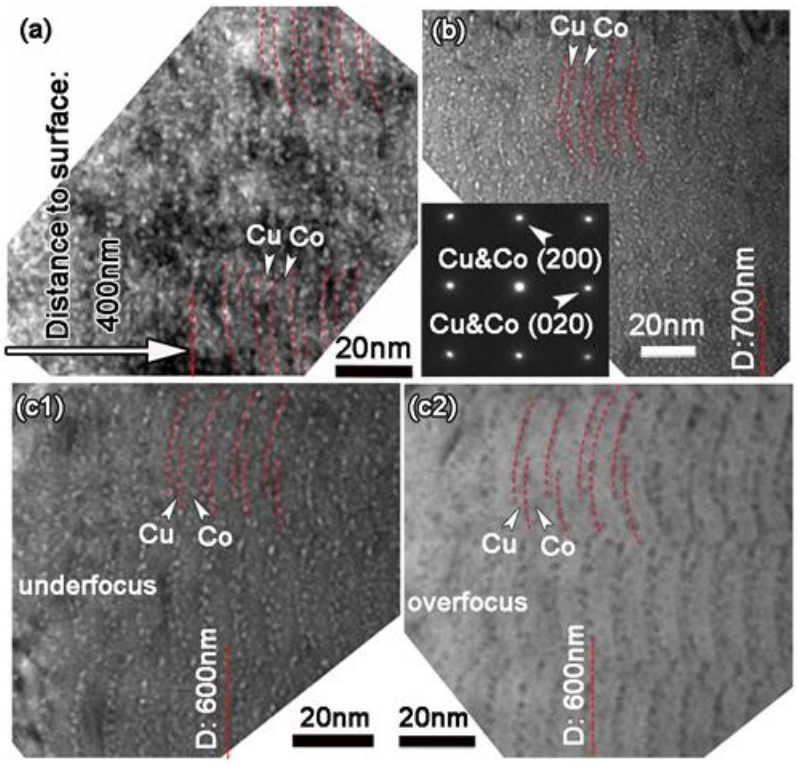

Figure 79 XTEM images of irradiated Cu/Co 5 nm multilayer. (a) In the peak damage region, He bubbles were distributed both within the layers and along layer interfaces. (b) In a region deeper than maximum radiation damage, clear alignment of He bubbles along layer interfaces was observed. The embedded SAD pattern shows the film retained epitaxial structure with fully coherent Cu/FCC Co stacking. (c1-c2) A typical irradiated region captured at underfocus (c1) and overfocus (c2) conditions confirmed the alignment of He bubbles at interfaces. Bubbles appeared as white (dark) dots in underfocus (overfocus) condition.

Similarly the microstructure of He ion irradiated Cu/Co 1 nm multilayer was also examined by XTEM. Fig. 80a exhibits a panoramic view of the irradiated specimen incorporating the SRIM simulated depth dependent profile of He concentration. The

embedded SAD pattern of the irradiated region confirmed the retention of epitaxial FCC Cu/FCC Co structure. Boxes b-d captured at different penetration depth are shown at higher magnifications. The surface region of irradiated specimens (Fig. 80b) contained randomly distributed He bubbles with barely discernable layer interfaces. High-density bubbles were observed (Fig. 80c) around peak damage region in absence of layer structures. However, layered structure can be distinguished with few He bubbles at the end of the irradiated region, as shown in Fig. 80d.

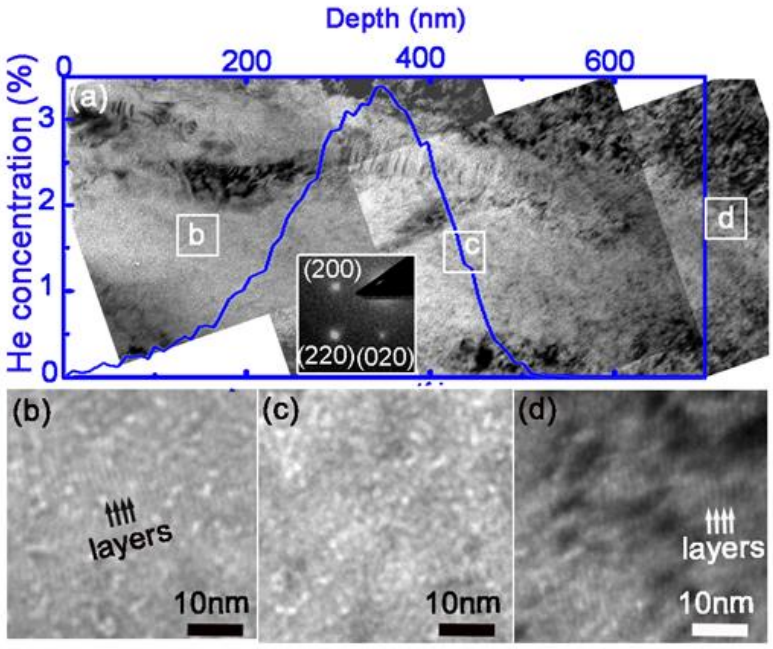

Figure 80 XTEM images of He ion irradiated Cu/Co 1 nm multilayer. (a) A panoramic view of the irradiated specimen incorporating the depth dependent profile of He concentration calculated by SRIM simulation. The embedded SAD pattern of the irradiated region confirmed the retention of epitaxial Cu/Co crystal structure. The boxes b-d at different penetration depths are shown at higher magnifications. (b) Close to the surface of irradiated specimens, He bubbles were randomly distributed with barely discernable layer interfaces. (c) High-density bubbles were observed in box c in peak damage region in absence of layer structures. (d) Layered structure can be distinguished with few He bubbles at the end of the irradiated region.

Comparisons of depth dependent He bubble density in several irradiated Cu/Co multilayers were made in Fig. 81, based on XTEM results. We selected 3 boxes with dimensions of 50 × 50 nm^2 at one specific depth to measure the bubble density at that depth, and analyzed bubble density at various depths along the projected ion path. This method has been successfully applied to investigate depth dependent bubble density distribution in other He ion irradiated nanolayers (*103-106, 108, 122-124, 163*). Several features are noteworthy. First, the peak He bubble density in Cu/Co 5 and 1 nm is similar, ~ 60% of that in Cu/Co 100 and 50 nm counterparts. Second, the locations of peak bubble density in irradiated Cu/Co 100 and 50 nm multilayers coincide with that of the calculated He concentration profile (the dash line), while the positions of peak maxima in irradiated Cu/Co 5 and 1 nm multilayers are slightly deeper. Third, the range of He bubble profiles in irradiated multilayers exceeds that of the calculated He profiles.

The method to determine indentation hardness was discussed in experimental section (Fig. 82a,b). Hardnesses of as-deposited and irradiated Cu/Co multilayers as a function of $h^{-1/2}$ are compared to that of as-deposited Cu/Ni (100) (*27*) in Fig. 82c,d. The comparisons reveal the following characteristics. (1) In general radiation induced hardening in Cu/Co across all h. (2) Compared to as-deposited Cu/Co, the peak hardness of irradiated Cu/Co multilayer increased substantially from ~3.8 to 5 GPa. (3) When h = 2.5 – 10 nm, the hardnesses (including peak hardness) of irradiated Cu/Co overlapped with that of as-deposited Cu/Ni with the same h. (4) When h= 50 - 200 nm, the Hall-Petch slope of irradiated Cu/Co is much greater than that of as-deposited Cu/Co, but close to that of as-deposited Cu/Ni (100).

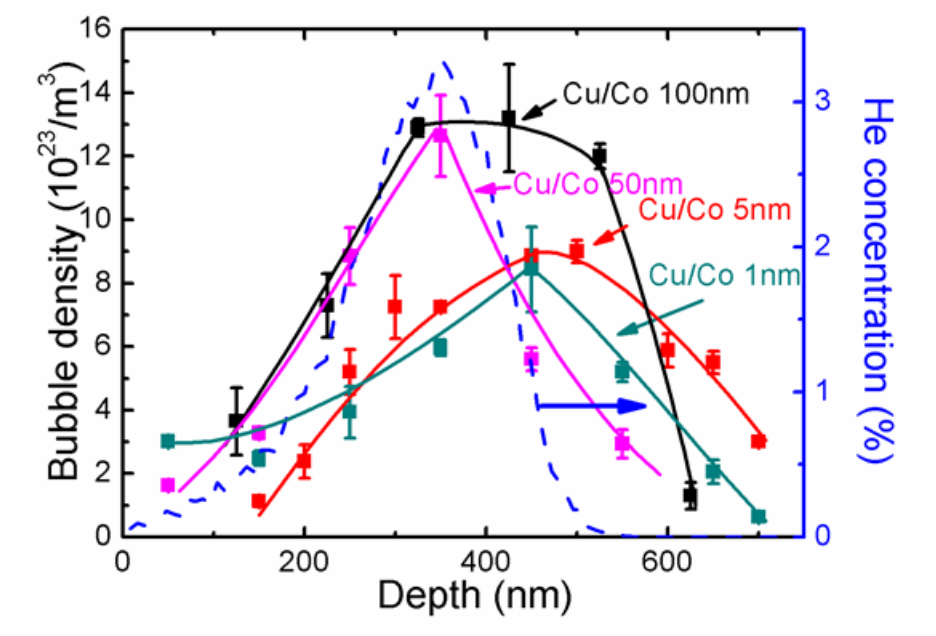

Figure 81 Comparison of the evolution of He bubble density along penetration depth in several Cu/Co multilayers. The peak damage region in irradiated Cu/Co 100 and 50 nm coincides with the calculated peak of He concentration profile (the dash line), while penetration depth is somewhat deeper in irradiated Cu/Co 5 and 1 nm multilayers. The overall penetration depths in all specimens are beyond calculated damage region. The peak He bubble density in Cu/Co 5 and 1 nm is ~ 60% of that in Cu/Co 100 and 50 nm counterparts.

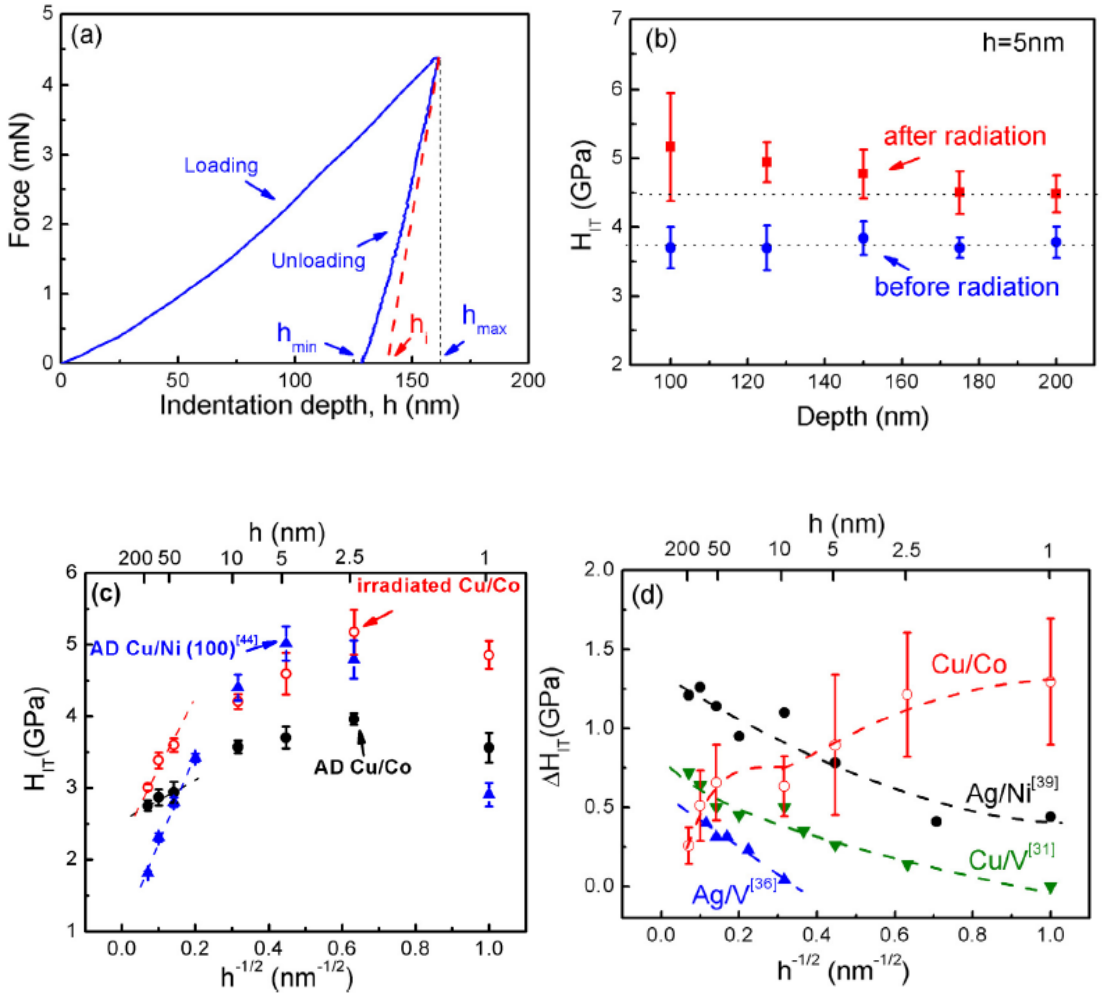

Figure 82 (a) A typical load-displacement curve with the maximum indentation depth of ~ 150 nm for He ion irradiated Cu/Co 5 nm multilayer is displayed, which is adopted to calculate indentation hardness at a specific depth of the film. (b) The average indentation hardness is determined when hardness value reaches a plateau, nearly independent of indentation depth. (c) Comparison of hardnesses of as-deposited and irradiated Cu/Co multilayers as a function of $h^{-1/2}$. The hardness of as-deposited Cu/Ni (100) (*27*) is also provided for comparison. After radiation, radiation hardening is prominent in Cu/Co multilayers, and the Hall-Petch slope (when h= 50 - 200 nm) increases significantly to a value close to that of as-deposited Cu/Ni (100). The peak hardness of Cu/Co increases from ~3.8 to 5 GPa after radiation, comparable to the peak hardness of as-deposited Cu/Ni (100). (d) Inverse size dependent radiation hardening in Cu/Co. The magnitude of radiation hardening is greater at smaller h. In contrast, radiation hardening in irradiated Ag/Ni (*122*), Ag/V (*109*), Cu/V (*104*) with immiscible incoherent interfaces have opposite size dependence, that is the smaller the h, the less the radiation hardening.

6.5 Discussion

6.5.1 Comparisons of radiation induced microstructure evolution in multilayers with immiscible coherent and incoherent layer interfaces

Metallic multilayers are attractive systems to study radiation damage as they possess abundant layer interfaces which could be effective defect sinks (*112*). In general, in comparison to miscible multilayers, immiscible multilayer systems are more effective to alleviate radiation damage as layer interfaces are more stable against radiation induced intermixing (*104*, *108, 124-126*). Among immiscible systems, multilayers with FCC/BCC incoherent interfaces have been extensively investigated (*112, 125, 126, 128*). The driving force behind the frequent selections of incoherent FCC/BCC multilayers for radiation studies may be attributed to the general perception that incoherent interfaces may be more effective in eliminating radiation induced defects than their coherent siblings. Among FCC/FCC metallic multilayer systems, few have immiscibility. Ag/Ni is one such system that has been investigated after He, proton and heavy ion (Kr) irradiations (*122, 123*). Indeed Ag/Ni multilayer with smaller h has lower He bubble density after radiation (*123*). Foregoing discussions focus on systems with immiscibility and incoherency. A question follows naturally: what is the radiation response of a coherent immiscible system?

The challenge in the design of such a system is that coherency typically exists in metallic materials with the same crystal structure and nearly identical lattice parameters, such as Cu/Ni (*27*), Ag/Au(*182*), Ag/Al (*67, 183*), or Fe/Cr (*184*). However metallic

materials with these similarities typically have significant solid solubility, in other words, the immiscibility criterion cannot be satisfied. Interestingly we have recently discovered that Cu/Co (100) multilayers can be fabricated, where Co has FCC phase, stabilized by FCC Cu. Furthermore FCC Co has lattice parameter of 3.709 Å, nearly identical to Cu, 3.615 Å, and is immiscible in Cu. Hence opportunity arises to compare radiation tolerance of a coherent immiscible system to the incoherent immiscible systems.

Examination of microstructures of irradiated Cu/Co reveals several important phenomena. First when reducing h from 200 to 5 nm, there is a prominent reduction of average and peak He bubble density, that is size dependent alleviation of radiation damage is also observed in immiscible FCC/FCC system with coherent layer interfaces. *In situ* radiation of immiscible Ag/Ni multilayers showed that interfaces can effectively capture radiation induced defect clusters (*123*), and hence reduce the defect density in irradiated metallic multilayers. Similarly coherent Cu/Co layer interface may be as effective as incoherent interfaces.

Second, when h = 5 nm, clear alignment of He bubbles along interfaces was observed. Similar phenomena have been reported in He ion irradiated FCC/BCC systems, such as Cu/Nb and Cu/Mo (*106, 112, 127*). The Cu/Co interfaces clearly trap He efficiently and lead to the alignment of He bubbles along interfaces.

Third, further decrease of h from 5 to 1 nm does not lead to prominent benefit in reducing defect density. Similarly in immiscible incoherent metallic multilayers, size dependent reduction of He bubble density is insignificant when h is the range of several

nm (*104, 109, 122*). Radiation of immiscible incoherent multilayers, such as Cu/V (*104*) and Ag/Ni (*122*) to similar dose did not lead to destruction of layer interfaces when h is 2.5 nm or greater. Although layer interfaces in peak damage zone of irradiated Cu/Co 1 nm was invisible, this could be related to contrast variation compromised by He bubbles. Similar phenomena (disrupted layer interfaces) have been observed in other immiscible incoherent systems with h of 2.5 nm (*103, 110*). Meanwhile we notice that the SAD of peak damage zone in irradiated Cu/Co reveals single crystal like diffraction pattern (Fig. 80a). Furthermore XRD studies show the retention of single diffraction peak after radiation of Cu/Co 1 nm nanolayers, implying that coherency survived after such radiation (instead of forming semi-coherent interfaces). The survival of coherency implies that Cu and Co remain rigidly connected with corrugated coherent interface, which may continuously absorb radiation induced point defects. Finally, both XRD and TEM studies show no evidence of HCP Co after radiation, implying that FCC Co remains stable again He ion irradiation. This is an important observation as it simplifies our discussions on the influence of radiation on variation of strengthening mechanisms in irradiated Cu/Co nanolayers.

The position of peak He bubble density in irradiated Cu/Co 5 nm and Cu/Co 1 nm multilayers appears deeper (from surface) than that in irradiated Cu/Co 50 nm film. Such disparity may arise from ion channeling effect. During ion implantation of single crystals, channeling effect can occur, which may result in a deeper ion range than what is predicted by SRIM simulations (*82, 187, 197*). In FCC/FCC Cu/Co multilayers, the

system becomes increasingly coherent, when h is 5 nm or less, and hence the channeling effect may have become more prominent during ion irradiation.

6.5.2 Size dependent strengthening mechanisms in irradiated Cu/Co multilayers

Prior studies on immiscible multilayer systems, including Cu/V (*104*), Ag/V (*109*) and Ag/Ni (*122*), typically showed less radiation hardening at smaller h as shown in Fig. 82d. However, in Cu/Co multilayers, radiation hardening escalated with decreasing h, in drastic contrast to general trend in previous studies. The mechanisms behind such deviation will be discussed below.

(a) Strengthening mechanisms at small h (h < 10 nm): in as-deposited Cu/Ni (100) and Cu/Co (100) systems, the peak strength was determined by interface barrier strength of layer interfaces, and can be estimated by (*135*)

Equation 36 $$\tau^*_{barrier} = \tau^*_k + \tau^*_{ch} = \frac{\mu_1(\mu_2 - \mu_1)}{4\pi(\mu_2 + \mu_1)}\frac{b}{l} + \frac{\gamma_2 - \gamma_1}{b}$$

where τ^*_k is Koehler stress originating from modulus mismatch ($\mu_2 - \mu_1$), τ^*_{ch} is chemical interaction term related to SFE difference ($\gamma_2 - \gamma_1$) between layer constituents, b is Burgers vector. l is dislocation core size. τ^*_k for Cu/Co and Cu/Ni is close as they have similar magnitude of shear modulus mismatch (μ_{Co} = 82 GPa and μ_{Ni} = 76 GPa (*135*)). Thus, the major discrepancy of interface strength between Cu/Ni and Cu/Co ($\tau^*_{Cu/Ni} - \tau^*_{Cu/Co}$) mainly arises from the SFE difference. Given γ^{Co}_{SF} = 24 mJ/m^2 , γ^{Cu}_{SF} = 41

mJ/m^2, and γ_{SF}^{Ni} = 125 mJ/m^2, their difference in τ_{ch}^{*} amounts to ~ 0.19 GPa, corresponding to a hardness discrepancy by ~ 1.5 GPa (by estimating $H = 2.7\sigma$ (*206, 207*), where σ is the flow stress, and $\sigma = 3\tau^{*}$), close to the experimentally determined hardness difference, ~ 1.2 GPa. Physically this means that in Cu/Co multilayers, the peak strength is dominated by the interface barrier strength to transmission of partial dislocations, whereas in Cu/Ni system, it is the transmission of full dislocations that dictates the maximum strength of multilayers (*135*).

Fig. 83 schematically illustrates strengthening mechanisms in as-deposited and irradiated Cu/Co (100) multilayers at small h (using h of 5 nm as an example). The transmission of partial dislocations (Fig. 83a) dominates the strengthening mechanism in as-deposited Cu/Co system, as discussed previously (*135*). However, after radiation, He bubbles at layer interfaces (as observed experimentally) significantly interfere with the transmission of partials, as He bubbles are typically over pressurized (at the current high He concentration) and are strong obstacles (*103-105, 122*), as shown in Fig.83b.

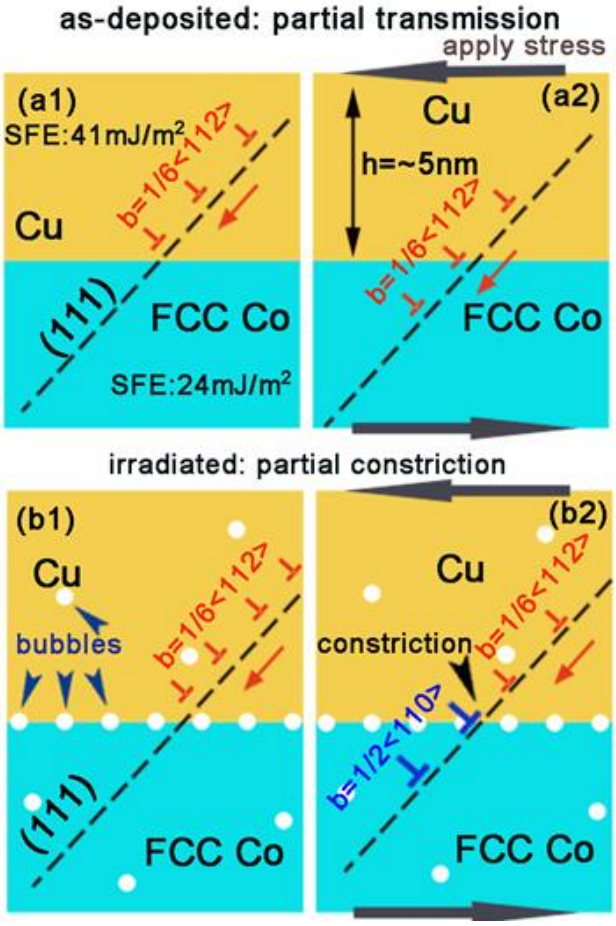

Figure 83 Hypothetical schematics illustrate strengthening mechanisms in as-deposited and irradiated Cu/Co (100) multilayers at small h (h = 5 nm). (a1-a2) In as-deposited films, partials can trespass layer interfaces due to low stacking fault energy of Cu and Co. (b1-b2) However, after radiation, bubbles at layer interface disrupt the transmission of partials. Consequently these partials may have to constrict to full dislocation before proceeding to the adjacent layers. Thus a stronger layer interface arising from He bubbles leads to prominently enhanced radiation hardening.

Consequently these partials may have to constrict to full dislocations (in Cu) before proceeding to the adjacent Co layers. In other words, He bubble decorated interface might become as strong as Cu/Ni interfaces, and only permit the transmission of full dislocations. Hence the interface barrier strength of irradiated Cu/Co should

include constriction stress $\tau^*_{constriction}$, and friction stress due to the bubble-dislocation interaction τ^*_{bubble}, in addition to τ^*_k and τ^*_{ch}, as described in the following equation

Equation 37 $$\tau^*_{barrier} = \tau^*_k + \tau^*_{ch} + \tau^*_{constriction} + \tau^*_{bubble}$$

First we estimate constriction stress arising from high-pressure He bubbles decorated layer interfaces. The equilibrium separation distance r_e between partials dissociated from a full dislocation inclined at an angle β to its Burgers vector can be estimated as (*208*)

Equation 38 $$r_e = \frac{\mu b^2}{8\pi\gamma}\frac{2-\nu}{1-\nu}\left(1-\frac{2\nu\cos 2\beta}{2-\nu}\right)$$

where ν is Poisson's ratio. Taking a full screw dislocation as an example, r_e can be estimated to be $9b$ (~ 2.2 nm for Cu). To avoid the cut-off problem in dislocation core in linear elasticity, MD simulation (*209*) was performed to investigate the dependence of constriction stress on partial separation distance in Cu, and the study showed a rapid increase of constriction stress with the decrease of partial separation distance. The equilibrium separation without stress from the simulation fits well to the value calculated by Eq. (38). With the increase of external applied stress to 0.0025-0.005μ, the partial separation distance reaches a separation of ~ $5b$ (~ 1 nm for Cu, referring to Fig. 2 in (*209*)), below which the partials could act as full dislocations. Using a lower bound estimation, the constriction stress could reach 0.0025μ, corresponding to hardening by

~ 1 GPa, comparable to the magnitude of radiation hardening observed in irradiated Cu/Co when h = 1 - 2.5 nm.

Next, besides the constriction, we also consider strengthening due to He bubble-dislocation interactions. The contribution of He bubbles to radiation hardening is negligible at low He concentration (< ~ 1%) and becomes significant with the increase of He concentration (*210*). He bubbles are generally treated as weak obstacles for dislocation migration (*104*). Friedel–Kroupa–Hirsch (FKH) model is widely used to describe weak obstacle induced strengthening ($\Delta\sigma$) (*104, 211*) by using

Equation 39 $$\Delta\sigma = \frac{1}{8} M \mu b d N^{2/3}$$

where M is the Taylor factor (~ 3.06), μ is the shear modulus (48 GPa for Cu), b is Burgers vector, d is the average bubble diameter (~1.2 nm), N is bubble density that can be obtained from TEM studies. Note that the average diameter of He bubbles has little dependence on irradiation depth for various irradiated Cu/Co multilayers. Using Eq. (39), we estimate the magnitude of He bubble induced yield strength increase to be ~ 0.05 GPa, corresponding to a hardness increase by ~ 0.15 GPa. Thus the magnitude of radiation hardening from partial constriction and He bubbles becomes ~ 1.2 GPa. Since the peak strength of as-deposited Cu/Ni is also controlled by constriction of dislocations (due to large SFE difference between Cu and Ni), the interface barrier strength of as-deposited Cu/Ni and irradiated Cu/Co becomes comparable.

(b) Strengthening mechanisms at large h (h = 50 – 200 nm): Fig. 84 schematically illustrates different strengthening mechanisms in as-deposited and irradiated Cu/Co (100) multilayers at large h (50-200 nm). In as-deposited state, as interface is a weak barrier to partial dislocation transmission, the mechanical strength of multilayers is determined primarily by high-density SFs in Co (with an average spacing of a few nm). The inset dark field TEM micrograph shows a typical Co layer with high-density SFs.

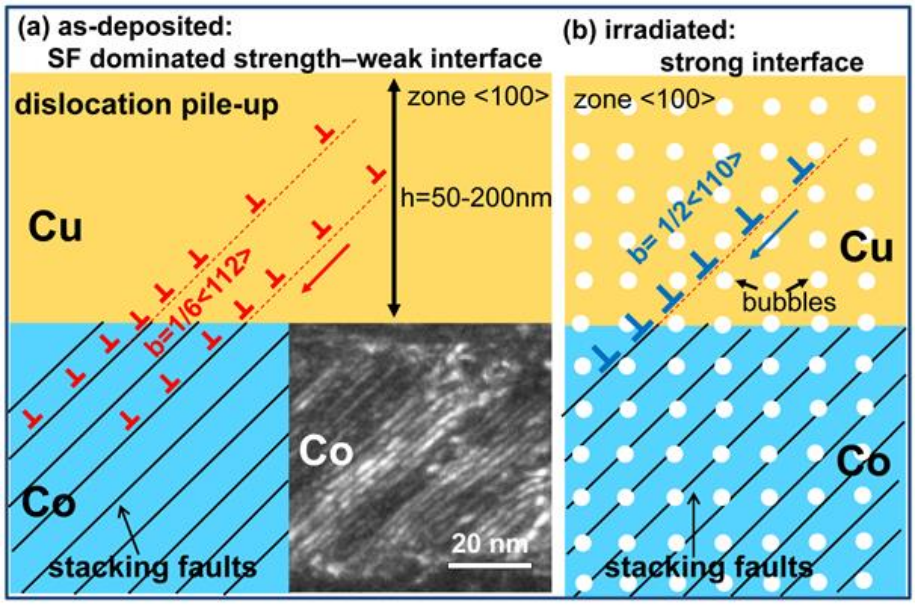

Figure 84 Hypothetical schematics illustrate different strengthening mechanisms in as-deposited and irradiated Cu/Co (100) multilayers at large h (h = 50-200 nm). (a) In as-deposited state, partial dislocations can transmit across the Cu/Co interface relatively easily, in other words, interface is a weak barrier for dislocation transmission. The mechanical strength of as-deposited multilayers with large h is determined primarily by high-density stacking faults in Co with an average spacing of a few nm. The inset TEM figure shows a typical Co layer with high-density stacking faults. (b) After radiation, high-density He bubbles are distributed both along the layer interface and within the layers. Consequently partials may be constricted into full dislocations within layers. The He bubble modified layer interface thus becomes stronger barrier against the pile-up of full dislocations.

After radiation, high-density He bubbles are distributed both along layer interfaces and within the layers as evidenced by extensive TEM studies. Furthermore XRD studies show that He bubbles clearly distorted crystal structures of irradiated multilayers as indicated by prominent reduction of peak intensity. The average bubble spacing (L) for Cu/Co 100 nm multilayer is ~ 9 nm ($L = 1/N^{1/3}$, where N is bubble density), larger than the average spacing between SFs. Hence SFs in Co remain the primary defects that determine the peak strength of multilayers. It follows that the magnitude of radiation hardening in Cu/Co 200 nm multilayers is insignificant. Our previous studies show that when h reduces to tens of nm or less, the density of SFs also reduces significantly (*135*). The magnitude of radiation hardening in Cu/Co 50 nm film is greater than that of Cu/Co 200 nm nanolayers, although the bubble density in Cu/Co 50 nm films is comparable to that of Cu/Co 200 nm. It is likely that He bubbles play increasing role in determining the strength of multilayers as the density of SFs reduces at smaller h. Consequently the magnitude of radiation hardening becomes prominent at smaller h.

Finally we notice that the Hall-Petch (H-P) slope (K_{HP}) of irradiated Cu/Co is similar to that of Cu/Ni, as He bubble decorated Cu/Co interfaces can effectively resist the pile-up of full dislocations. The H-P slope is related to the interface barrier strength (τ^*) via (*25*):

Equation 40 $$K_{HP} = \sqrt{\tau^* \mu b / [\pi(1-\nu)]}$$

For Cu, using μ = 48 GPa, b = 0.25 nm, and ν = 0.33, we obtain τ^* of 0.6 GPa. Correspondingly the peak hardness (H) can be estimated as ~ 4.9 GPa for both as-deposited Cu/Ni and irradiated Cu/Co, which is very close to the experimentally measured values of ~ 5 GPa for both systems.

It is worth emphasizing that the radiation hardening phenomenon in Cu/Co is very different from what have been reported before. Although radiation hardening increases at smaller h, it does not necessarily indicate a dramatic degradation of mechanical properties. The large hardening at smaller layer thickness is mainly a consequence of the surprisingly low initial hardness of as-deposited films, due to the partial dislocation dominated deformation mechanism. The layer interface in immiscible coherent Cu/Co system remain significant on alleviation of radiation damage as manifested by progressive reduction of He bubble density at smaller h.

Finally our previous dose dependent study on He ion irradiated incoherent Cu/V multilayers up to 18 dpa (*105*) shows superior stability of Cu/V interfaces and saturated radiation hardening at higher dose. The structural stability of interfaces and strengthening mechanisms in immiscible coherent Cu/Co multilayers subjected to much greater doses remain unclear and are interesting subjects for future studies.

6.6 Conclusions

We investigated He ion radiation response of immiscible coherent Cu/Co multilayer systems. Similar to incoherent interfaces in immiscible systems, the coherent interfaces can also effectively mitigate radiation damage in terms of reducing He bubble

density in nanolayers with smaller h. Layer interfaces in Cu/Co are in general resistant to radiation induced intermixing.

In contrast to the major reported trend of reduced radiation hardening at smaller h in immiscible incoherent multilayers, the size dependent strengthening behavior in Cu/Co system is just the opposite, although the density of He bubble density is indeed lower at smaller h. Such a surprising observation was explained by a transition from partial transmission dominated strengthening mechanisms (before radiation) to full dislocation transmission dictated deformation behavior in immiscible Cu/Co nanolayers due to decoration of pressurized He bubbles at layer interface in irradiated multilayers.

6.7 **Acknowledgements**

XZ acknowledge financial support by NSF DMR-1304101. This work was performed, in part, at the Center for Integrated Nanotechnologies, an Office of Science User Facility operated for the U.S. Department of Energy (DOE) Office of Science. Los Alamos National Laboratory, an affirmative action equal opportunity employer, is operated by Los Alamos National Security, LLC, for the National Nuclear Security Administration of the U.S. Department of Energy under contract DE-AC52-06NA25396. Access to microscopy and imaging center (MIC) at Texas A&M University is also acknowledged.

CHAPTER VII

DAMAGE TOLERANT NANOTWINNED METALS WITH NANOVOIDS UNDER RADIATION ENVIRONMENTS*

7.1 Overview

Material performance in extreme environments (e.g. high pressure, stress and radiation) is central to future energy technology. Radiation induces significant damage in form of dislocation loops and voids in irradiated materials and continuous radiation leads to void growth and subsequent void swelling. However, here by using *in situ* heavy ion irradiation in a transmission electron microscope we show that, pre-introduced nanovoids in nanotwinned Cu efficiently absorb radiation-induced defects accompanied by gradual elimination of nanovoids, enhancing radiation tolerance of Cu. *In situ* studies and atomistic simulations revealed that such remarkable self-healing capability stems from high density of coherent and incoherent twin boundaries that rapidly capture and transport point defects and dislocation loops to nanovoids, which act as storage bins for interstitial loops. This study describes a counterintuitive yet significant concept: deliberate introduction of nanovoids in conjunction with nanotwins enables unprecedented damage tolerance in metallic materials.

---

*This chapter reprinted with permission from "Damage-tolerant nanotwinned metals with nanovoids under radiation environments" by Y. Chen, K.Y. Yu, Y. Liu, S. Shao, H. Wang, M.A. Kirk, J.Wang X. Zhang; Nature Communications, Volume 6, article number 7036, Copyright 2015 by Nature Publishing Group.

7.2 Introduction

Materials that can sustain extreme environments, such as high stress and radiation, are constantly being sought for unprecedented performance. Nuclear energy currently accounts for more than 10% of electricity world wide and the discovery of advanced materials for extreme radiation environments resides at the center of the design of future nuclear reactors (*5, 72-76*). Irradiation of metals by neutrons or heavy ions results in a large number of point defects (*212-214*) and their clusters, including dislocation loops, voids and stacking fault tetrehedra (SFTs) (*83, 84, 215-218*), which cause severe void swelling, radiation hardening, embrittlement and creep (*86, 185, 186*). Interfacial defect sinks, such as grain boundaries (*10, 88, 90, 134, 136*), heterophase interfaces (*102, 104, 112, 128, 219*) and free surfaces (*202, 204, 220*), have proven to be effective in alleviating radiation damage. Grain size dependence of void swelling in stainless steel was observed previously (*88*) and recieved renewed intense interest as nanograins appear to drastically enhance radiation tolerence as shown experimentally (*10, 134*) and theoretically (*91, 136-139*). Howerver, nanograins tend to coarsen at elevated temperature and under irradiation (*74, 77*), compromising radiation tolerance. Recenty nanotwinned (nt) metals have been extensively studied, showing high strength and ductility (*31, 46-50*), outstanding microstructral stability under both radiation (*54*) and annealing conditions (*55, 56*), and twin boundaries (TBs) serve as defect sinks and destruct SFTs in nt metals (*57, 58*).

In general, continuous intense radiation leads to high-density voids with increasing void size and void swelling in irradiated metallic materials. However, here we show that by deliberate combination of nanovoids with nanotwins, unprecedented radiation tolerance could be achieved in irradiated nanovoid-nanotwinned (nv-nt) Cu. Using *in situ* radiation inside a transmission electron microscope, we observed self-healing of nanovoids. Atomistic simulations reveal that nanotwins are essential to achieve superior radiation tolerance as TB networks consisting of coherent and incoherent twin boundaries promote rapid migration of defect clusters to nanovoids, wherein they are annihilated. Nanovoids act as defect sinks to absorb radiation induced interstitial loops, as revealed by *in situ* radiation and confirmed by molecular dynamics simulations. This study provides a rejuvenating perspective on the design of metallic materials with extraordinary damage tolerance.

7.3 Experimental

Specimen preparation: Fully dense coarse-grained (cg) Cu foil with thickness of ~20 μm and nanotwinned Cu films with nanovoids (nv-nt) with thickness of 1.5 μm were prepared through magnetron sputtering by using 99.995% purity Cu target on HF etched Si(110) substrates. Subsequent annealing of free-standing cg Cu foil at 300^{o}C for 1 hour was performed to obtain large grain size. Prior to deposition, the chamber was evacuated to a base pressure of ~5 $\times 10^{-8}$ torr. Transmission electron microscopy (TEM) samples were prepared by dimpling, low energy (3.5 keV) Ar ion milling and subsequent ion polishing.

In situ Kr ion irradiation: In situ Kr^{++} ion irradiation at 1 MeV was performed for cg and nv-nt Cu at room temperature in the Intermediate Voltage Electron Microscope (IVEM) at Argonne National Laboratory, where an ion accelerator was attached to a HITACHI H-9000NAR microscope. The microscope was operated at 200 kV and kept on during radiation in order to record the microstructural evolution. The average dose rate was 1.8×10^{-3} dpa/s. A CCD camera was used to capture microstructural evolution during radiation at 15 frame/s. SRIM simulation was used to estimate the displacement damage profile and Kr^{++} ion distribution(*221*). The results (see Fig. 85) show that most of the Kr^{++} ions at 1 MeV will penetrate through TEM foils, which are ~ 100 nm in thickness, measured by using the Kossel-Mollenstedt fringes captured under two-beam conditions.

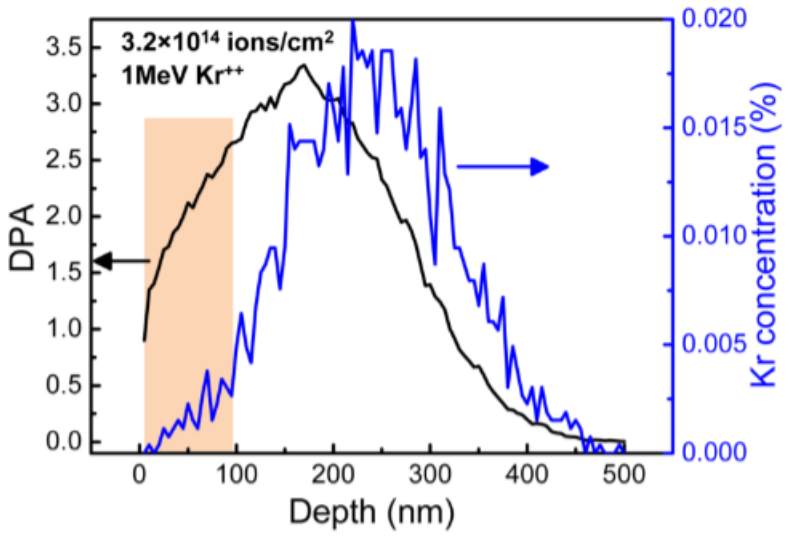

Figure 85 SRIM simulation showing the dpa and Kr concentration profiles along the ion penetration depth for 1 MeV Kr ions. The first 100 nm thick TEM foil was subjected to an average dose of ~ 1.56 dpa and most Kr ions penetrated through the TEM foil, leaving behind radiation damage and insignificant Kr concentration.

Molecular statics/dynamics simulations: Molecular statics with Nudged Elastic Band method (*222*) was used to calculate the formation/migration energy (E_f/E_m) for interstitials at twin boundaries and in the bulk, with the embedded atom method (EAM) interatomic potentials for Cu (*223*). Twinned structures were created by successively gliding Shockley partial dislocations on each (111) plane in a single crystal (*59, 140*). We introduced interstitials, one at a time, at all possible sites in the twinned structure and subsequently calculated the corresponding E_f and E_m with respect to migration path.

Molecular dynamics was used to study the void-Frank loop interaction under cascades. The box size is ~ 200×100×100 Å. A void was created in a shape of Wulff construction with a radius of ~1.5 nm. Frank loop takes a hexagonal shape with six <110> sides and radius of ~1.5 nm. EAM interatomic potential developed by Mishin *et al*. (*224*) was used to describe the interatomic interaction, splined to the ZBL repulsive potential for interatomic distances less than 0.5 Å. MD models were initially relaxed at 300 K. Cascade simulations were performed along different directions for primary knock-on atoms (PKA) with kinetic energy 5-8 keV. MD simulation stopped till the cascade cooled down without obvious rearrangement of atoms.

7.4 Results

Plan-view transmission electron microscopy (TEM) micrograph shows the as-prepared Cu contained abundant nanovoids primarily surrounding columnar domain boundaries (Fig. 86a-b). Fig. 86c shows high-density coherent twin boundaries (CTBs) with an average twin thickness of ~ 15 nm, and incoherent twin boundaries (ITBs) that

were decorated by a large number of nanovoids with an average diameter of ~ 10 nm. These 3 dimensional voids distributed at different depth in the film are introduced during magnetron sputtering process, void density can be controlled by tailoring deposition rate, substrate temperature as well as epitaxy between film and substrate. High-resolution TEM image in Fig. 86d shows atomic structure of CTBs and ITBs. Fig. 86e displays a conceptual schematic of nv-nt metals that contain ITB-CTB networks and nanovoids along ITBs. Fig. 86f shows diffusion channels associated with dislocations at CTBs and ITBs that could potentially transport interstitials and their clusters towards nanovoids. The significance of such ITB-CTB networks on radiation response of nt metals will be revisited later.

Radiation response of nv-nt Cu was investigated via *in situ* Kr ion irradiation studies. TEM snapshots compare the drastic difference in evolution of microstructure during irradiation of coarse grained (cg) (Fig. 87a) and nv-nt Cu (Fig. 87b). During initial radiation of cg Cu by 0.1 displacements-per-atom (dpa), there was a rapid, prominent increase in density of defect clusters; the density of dislocation loops increased monotonically with dose and a high density of dislocation segments were observed by 1.56 dpa. In contrast, in nv-nt Cu, the density of dislocation loops increased slightly with dose accompanied by a gradual elimination of nanovoids. By 0.56 dpa, a significant decrease of void density was observed. By 1.56 dpa, voids were mostly removed (Fig. 87c). However nanotwins retained after radiation (Fig. 88). A statistical study (Fig. 87d) shows that the defect density in cg Cu increased rapidly to a much greater saturation level than that in nv-nt Cu.

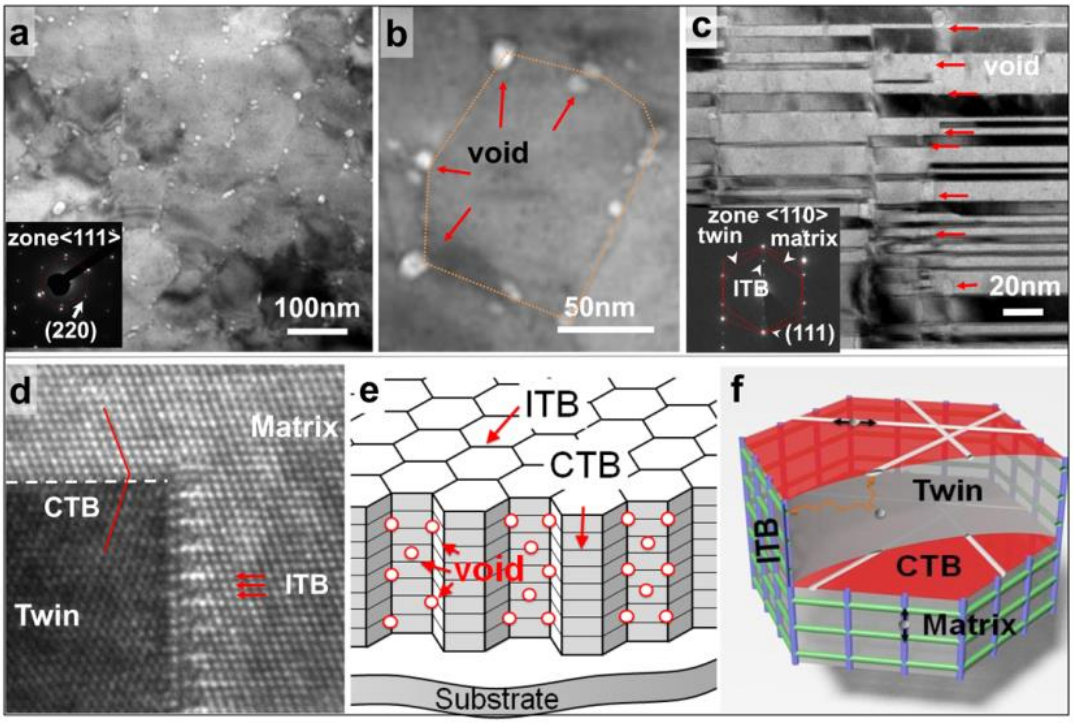

Figure 86 Deliberate introduction of nanovoids and nanotwins in Cu (nv-nt Cu). (a-b) Plan-view transmission electron microscopy (TEM) micrograph showing the as-prepared nv-nt Cu film containing abundant nanovoids primarily surrounding columnar domain boundaries. (c) Cross-section TEM micrograph shows high-density coherent Σ 3{111} twin boundaries (CTB) with an average twin thickness of ~ 15 nm, and Σ 3{112} incoherent twin boundaries (ITBs), which were decorated by a large number of nanovoids with an average diameter of ~ 10 nm. The inserted selected area diffraction (SAD) pattern confirms the formation of epitaxial nt Cu. (d) High-resolution TEM image of CTBs and ITBs. (e) A conceptual schematic of metals with CTB and ITB networks and nanovoids. (f) Inside a typical columnar grain radiation induced interstitials or their loops can rapidly migrate towards ITBs, where they can migrate rapidly to nanovoids.

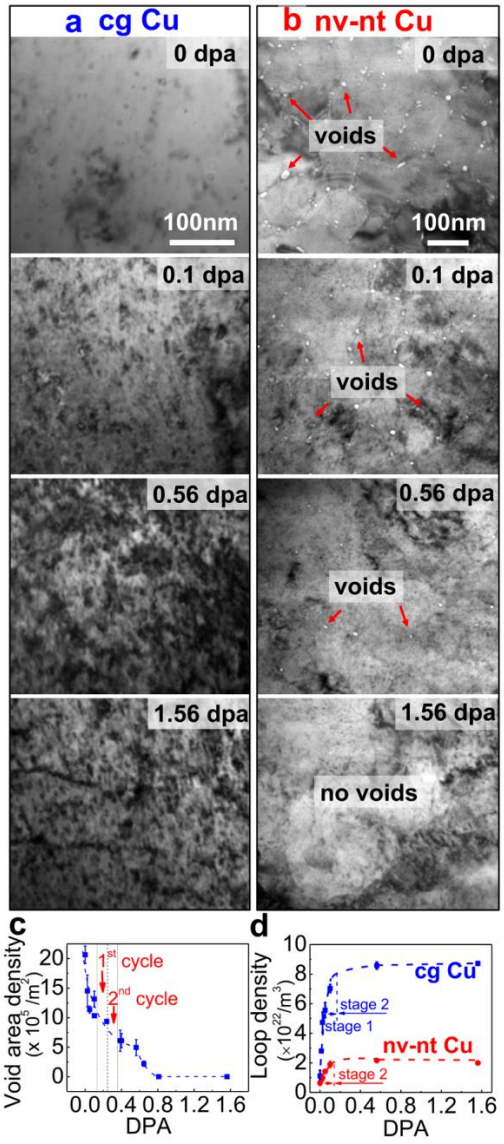

Figure 87 Superior radiation tolerance and void shrinkage in nv-nt Cu as evidenced by *in situ* Kr ion irradiation studies. TEM snapshots in (a) and (b) compare drastically different evolution of microstructure during *in situ* Kr ion irradiation of coarse grained (cg) and nv-nt Cu. (a) During initial radiation of cg Cu by 0.1 displacements-per-atom (dpa), there is a rapid and prominent increase in density of defect clusters, the density of dislocation loops increased monotonically with dose and high-density dislocation segments were observed by 1.56 dpa. (b) In contrast, in nv-nt Cu, the density of dislocation loops increased slightly with dose accompanied by a gradual elimination of nanovoids. (c) Up to 0.56 dpa, a significant decrease of area density of nanovoids was observed. By 1.56 dpa, nanovoids were mostly removed. (d) A statistical study shows that the defect density in cg Cu increased rapidly to a much greater saturation level than that in nv-nt Cu.

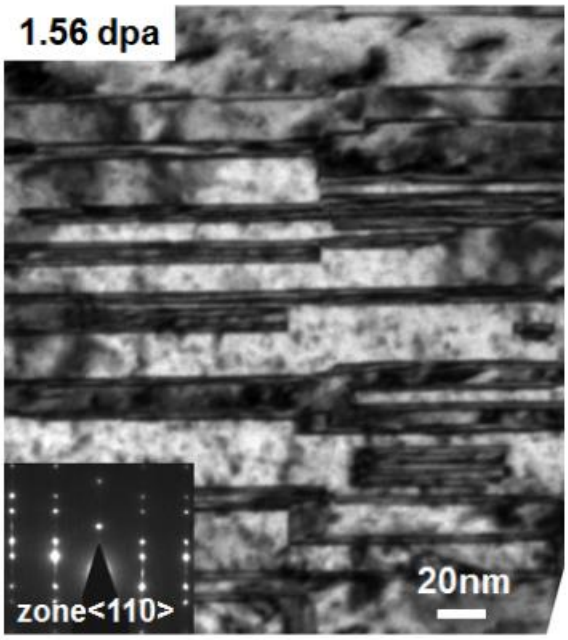

Figure 88 Cross-section TEM micrograph of irradiated nt Cu up to 1.56 dpa showing the remarkable retention of nanotwins after irradiation. The average twin thickness remained ~ 15 nm. The inset of SAD pattern confirms the retention of nt structure in the irradiated nt Cu.

Fig. 87c shows that the void density declined sharply with increasing radiation dose, and by ~ 0.7 dpa, nanovoids were barely detectable. The average diameter of nanovoids in as-fabricated nv-nt Cu was ~ 10 nm with frequent appearance of nanovoids as large as 20 nm. Radiation led to substantial shrinkage of nanovoids, and by 0.65 dpa, most of nanovoids were below 10 nm in diameter. Fig. 89a displays apparent shrinkage of nanovoids over 0.11 - 0.26 dpa. 3 voids with initial diameters of 5.9 nm (marked as V1), 7.2 nm (V2) and 7.4 nm (V3) were chosen to illustrate the shrinkage process. These voids reduced diameters continuously. At 82 s, V1 disappeared completely while V2 and V3 contracted to 2.3 and 4.6 nm, respectively.

Absorption of interstitial loops by nanovoids was frequently observed. A typical absorption event captured by *in situ* TEM experiments is shown in Fig. 89b. At 0 s, an interstitial loop with dimension of 15 nm in length and 7 nm in width impinged a nanovoid, ~ 6 nm in diameter. The loop shrank to 14 nm in length and 6 nm in width at 2.7 s, and was completely absorbed by the nanovoid by 4.1 s. Fig. 89c shows the variation of void size (d) with dose (time) for numerous nanovoids in nv-nt Cu. A majority of voids contracted continuously and gradually during radiation. When void diameter reduced to ~ 3 nm, there appeared to be an accelerated contraction of these tiny voids. Fig. 89d displays the reduction of void diameter, $\Delta d = d - d_o$, where d_o is the original diameter of voids. The greater shrinkage rate for the smaller voids than larger voids will be discussed later.

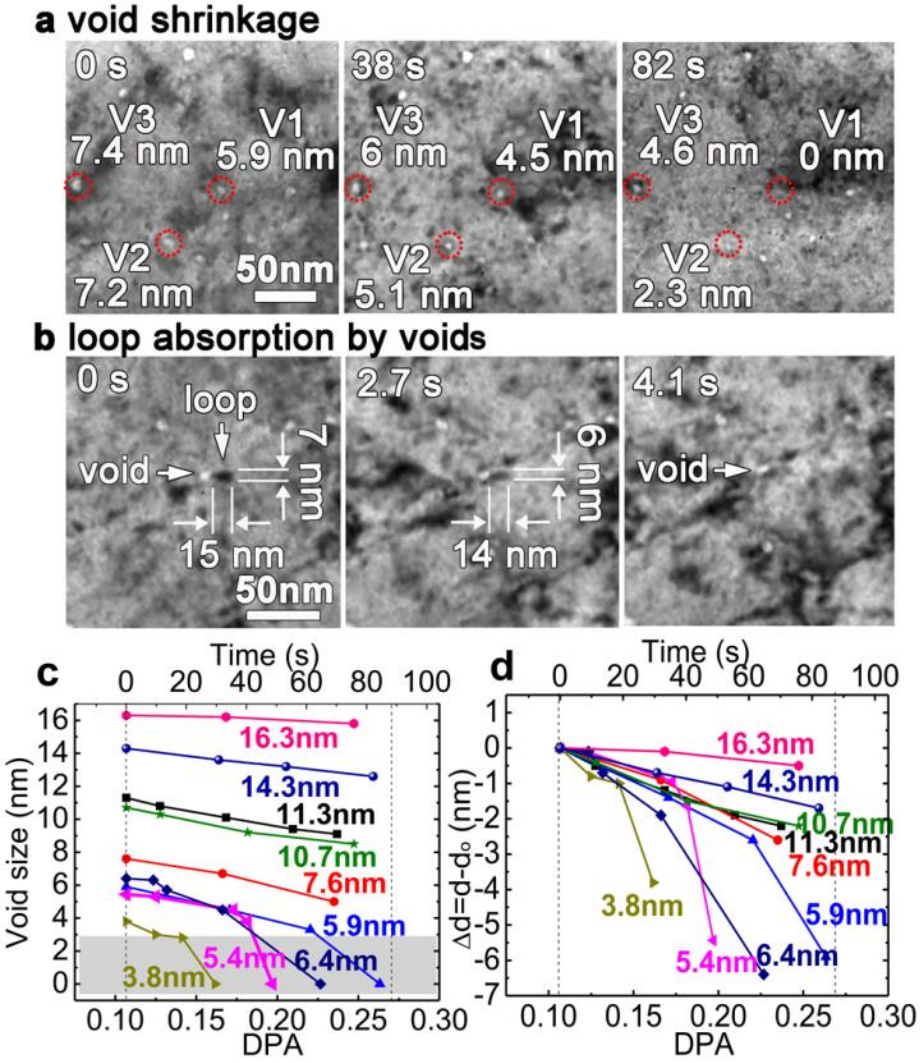

Figure 89 *In situ* Kr ion irradiation studies of nv-nt Cu unraveling continuous shrinkage of nanovoids and absorption of mobile dislocation loops by nanovoids. (a) *In situ* snapshots revealing shrinkage of numerous nanovoids over 0.11 - 0.26 dpa. At 0 s, 3 voids (V1-V3) with respective diameters of 5.9, 7.2 and 7.4 nm were tracked. At 82s, V1 disappeared completely, while V2 and V3 decreased to 2.3 and 4.6 nm, respectively. (b) Sequential snapshots capturing the absorption of dislocation loops by voids over 0.13-0.14 dpa. At 2.7 s, the loop was partially absorbed by the void. By 4.1 s a complete absorption of the dislocation loop was observed. (c) Compiled chart showing the shrinkage of nanovoids with different diameters during *in situ* radiation. While larger voids shrank continuously during radiation, the rate of shrinkage is clearly greater for smaller nanovoids. When void diameter reduced to ~ 3 nm (marked as grey band), there appeared to be an accelerated collapse of these tiny nanovoids, that is these voids vanished nearly instantaneously. (d) The evolution of reduction of void diameter $\Delta d=d-d_o$ with radiation dose, where d_o is the original void diameter.

In situ radiation of nv-nt Cu also reveals an unusual phenomenon: cyclic variation of mobile dislocation loop density (Fig. 90a1). Two short duration cycles were observed during radiation over 0.1-0.4 dpa, followed by a 3rd much longer cycle, whereas little mobile dislocations were observed in irradiated cg Cu. The first two prominent cycles had a similar period of ~75 s (Fig. 90a2), spanning across 0.11 - 0.34 dpa. Furthermore each cycle contained two maxima and an intermediate local minima state. *In situ* TEM snapshots were captured to investigate the two repetitive cycles. In the first cycle, the density of mobile dislocation loops increased rapidly and reached a maximum by 21.7 s at 0.15 dpa (Fig. 90b2); it decreased to an intermediate level at 27.1 s (Fig. 90b3); the population of dislocation loops then increased to a second maximum by 0.19 dpa (Fig. 90b4). This phenomenon repeated itself for a second cycle from 0.26 to 0.34 dpa as shown in Fig. 90c1-c4.

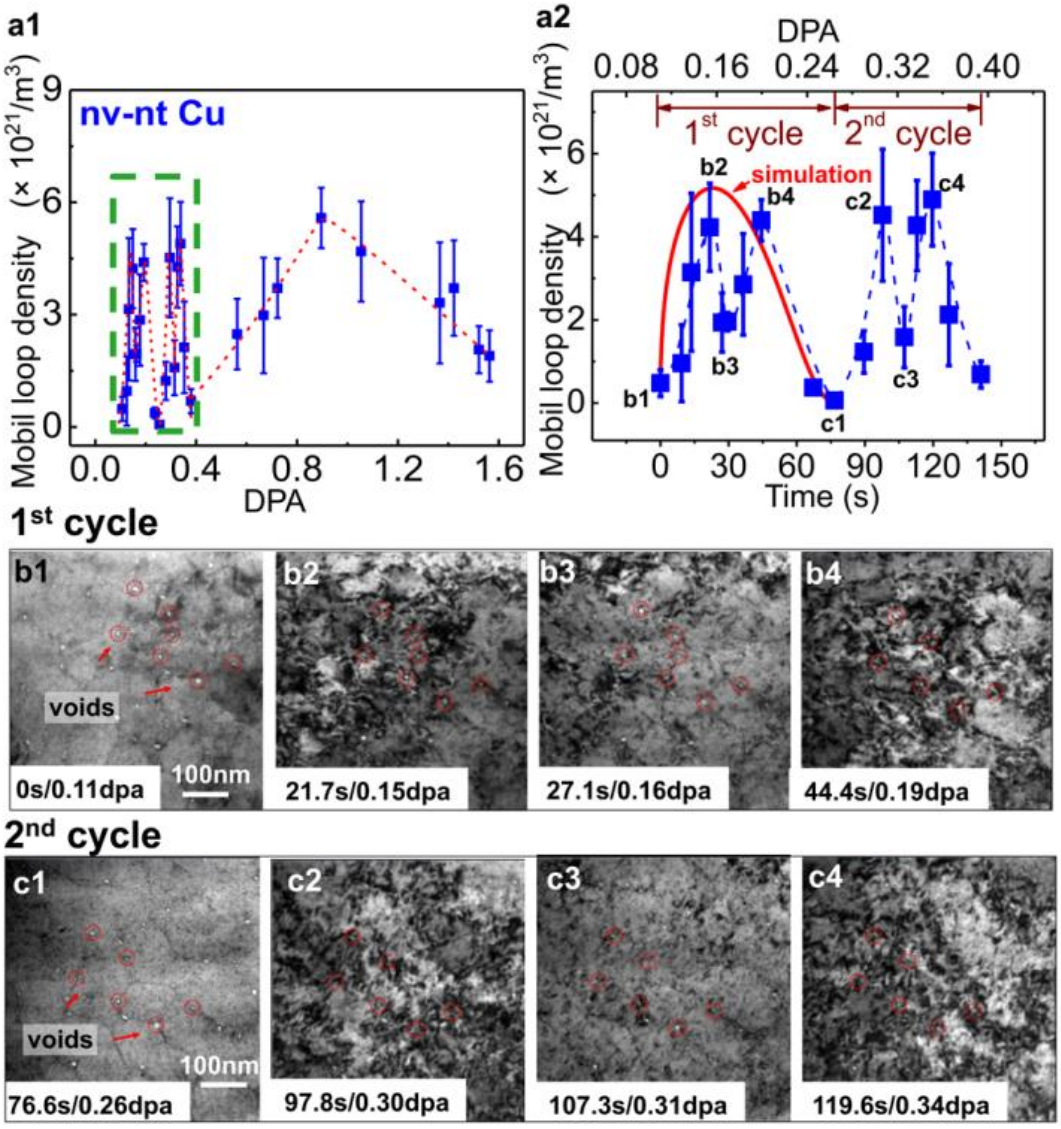

Figure 90 Significant cyclic variation of mobile loop density observed in nv-nt Cu subjected to *in situ* Kr ion irradiation within 0.4 dpa. (a1) Statistics studies show cyclic variation of mobile dislocation loop density, with two short cycles during 0.1-0.4 dpa (magnified in a2), a 3rd much longer cycle, while little mobile dislocation was observed in cg Cu. In each of the first 2 cycles, two peaks and an intermediate valley were observed. The simulation of the 1st cycle is shown as a red solid line. TEM micrographs in b1-b4 and c1-c4 show cyclic variation of mobile dislocation loop density in two cycles (0.11-0.19 dpa) and (0.26-0.34 dpa).

7.5 Discussion

Void swelling is widely observed in irradiated face-centered cubic (FCC) metals (*84*) , in particular in austenitic stainless steels (*86, 185, 225*), but the shrinkage of voids is rarely observed during radiation. The elimination of nanovoids in nv-nt Cu is thus unusual and must be related to the nv-nt microstructure.

TB networks enabled absorption and rapid transportation of defects/defect clusters**:** First, TBs are effective defect sinks. By using molecular statics simulations, we compared the formation and migration energies (E_f, E_m) of interstitials inside crystal and at ITB-CTB network (Fig. 91a). The formation energy for an interstitial within the crystal lattice is very large, ~ 3 eV, comparing to 1-2 eV on CTBs and ITBs (Fig. 91b), implying interstitials prefer to stay at TBs. Furthermore interstitials in grain interior experience very low migration energy (~0.11 eV), permitting their rapid migration to nearby CTBs or ITBs (marked as step 1 in Fig. 91a). Second, once arrived on ITB-CTB networks, defects or their clusters can be transported rapidly (similar to 1D diffusion) along fast diffusion channels to nanovoids (marked as step 2 in Fig. 91a). For regular ITBs consisting of sets of 3 adjacent Shockley partials (*140*), we characterized two fast diffusion paths along dislocation lines that experiences the kinetic barrier of 0.34 eV for channel 1 at tensile sites sandwiched by two partial dislocations (b_1 and b_3), and 0.01 eV for expeditious 1D crowdion diffusion in channel 2 (Fig. 91b) and the detailed diffusion mechanisms are displayed in Fig. 91c-d respectively. Third, although CTBs have low mobility, the capture of dislocation loops by CTBs can create abundant minuscule ITB

steps (*156*), that contain groups of highly mobile Shockley partials (*50*). *In situ* nanoindentation studies have shown that ITB steps in nt Cu can migrate rapidly during deformation at low stress (*226*). Hence the 3D ITB-CTB networks can transport defects and their clusters efficiently to nanovoids.

Void-loop interactions: forgoing discussion suggests that a large number of loops will be transported to voids via ITB-CTB networks whereby they are annihilated. Here we examine loop-void interaction mechanisms in detail. First, void size plays an important role in capturing and storing defects in nv-nt Cu. The analytical anisotropic solution of stress state between two voids calculated by using complex variable method indicates the existence of significant tensile stress surrounding voids. Smaller voids generate higher stress field near void surfaces, while larger voids introduce higher stress over a longer range. When a Frank loop approaches a nanovoid, the loop migration rate increases significantly as tensile stress induces a substantial reduction of formation and migration energies of the loop (Detailed calculation by molecular statics simulations is provided in Fig. 92).

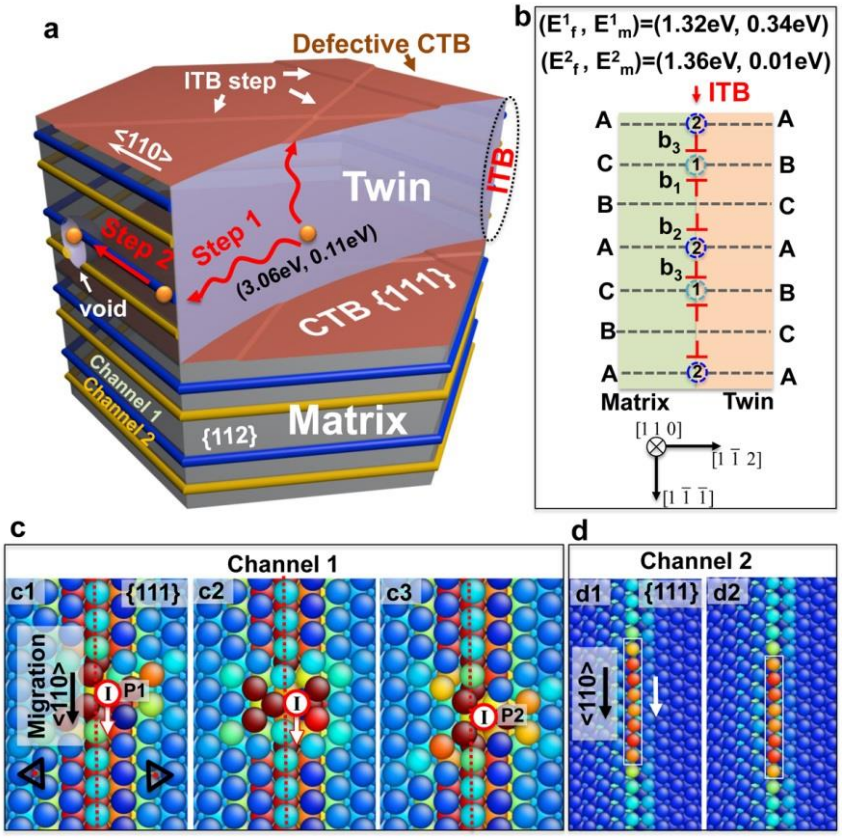

Figure 91 Absorption and diffusion of interstitials in nv-nt Cu. (a) Fast interstitial diffusion pipes enabled by ITB-CTB networks in nt Cu. (b) Two fast diffusion channels at ITBs and (c-d) the corresponding diffusion mechanisms. An interstitial created within the crystal will quickly migrate to ITBs or defective CTBs due to the low formation energy at these sites (labeled as step 1 in a). Once arrived at ITB-CTB networks, the interstitial can diffuse to a nanovoid at ITB via a rapid one-dimensional (1D) diffusion channel due to the low migration energy (step 2 in a), resulting in the shrinkage of the nanovoid. Topological model and atomistic simulations of ITB in an FCC structure, exploring that an ITB can be represented as an array of Shockley partial dislocations on each {111} plane as illustrated in the schematic (b), containing three repetitive partial dislocations (b_1, b_2 and b_3). Two fast diffusion channels along <110> dislocation lines are identified as channel 1 and channel 2. The migration paths with lowest energy barriers along the two channels are calculated by nudged elastic band (NEB) method as shown in (c) and (d), respectively. (c) For the channel 1, an interstitial initially stays at dislocation core in {111} layer sandwiched between b_1 and b_2. The interstitial then migrates downward to another low-energy site, with energy at the same level as its initial low-energy site. (d) For the channel 2, an interstitial has a spreading core associated with the distributed free volume along <110> dislocation line. The migration of the distributed interstitial requires a very low energy barrier (0.01eV) displaying a crowdion-type of behavior.

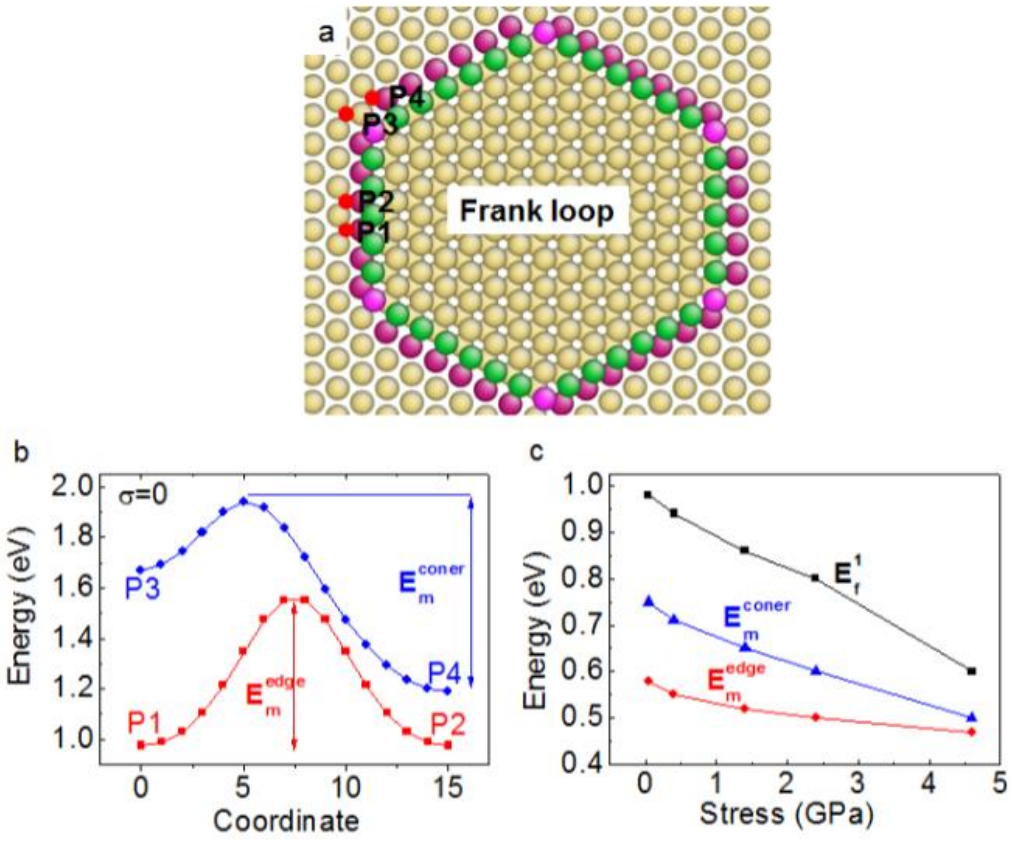

Figure 92 Interstitial formation and migration energies (E_f, E_m) along a Frank loop derived by molecular statics calculations. (a) Atomistic structure of a Frank loop. (b) The interstitial formation energy at different sites along the loop line under zero applied stress. The migration paths with lowest energy barriers at loop side and corner are provided by NEB method. (c) The interstitial formation and migration energies at different sites along the loop line under applied stress normal to Frank loop. With the increase of applied tensile stress, the interstitial formation and migration energies are significantly reduced.

Second, MD simulation reveals dynamic process through which a void absorbs a neighboring dislocation loop. Three scenarios subjected to self-ion irradiations, were compared, including a stand-alone Frank (interstitial) loop, a pair of nanovoid and Frank loop in immediate contact, and the similar pair that are separated by ~ 1 nm as shown in

Fig. 93a-c. During irradiation, the individual Frank loop was disturbed, but only slightly changes its shape after a cascade (Fig. 93a1-a3). In parallel the Frank loops immediately contacting the void (Fig. 93b1-b3) or slightly separated from the void (Fig. 93c1-c3) were prominently absorbed by the void after radiation.

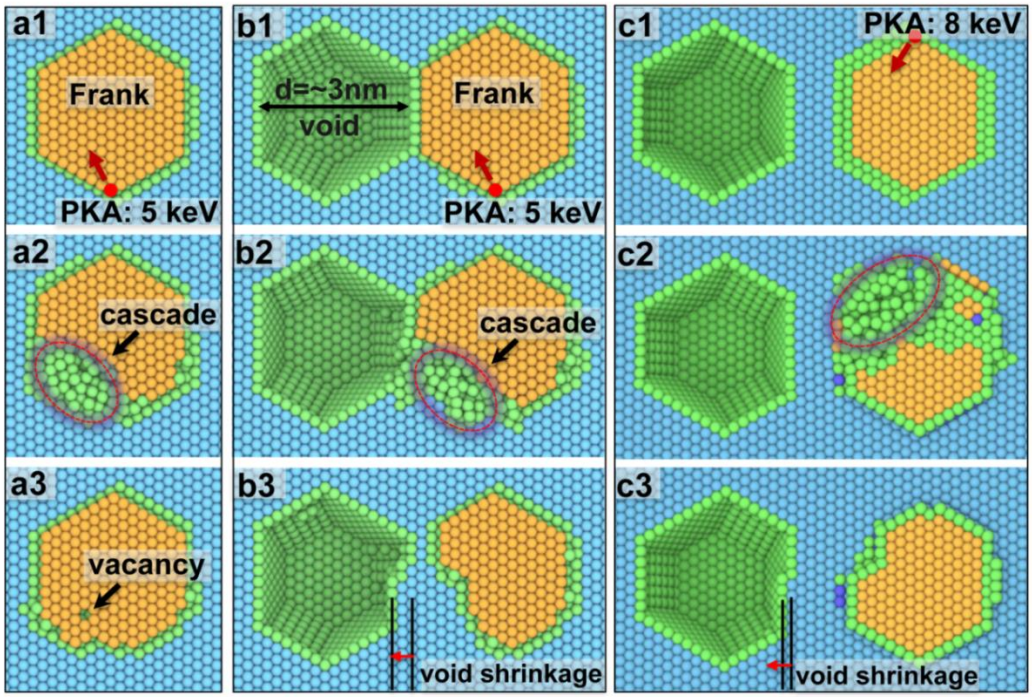

Figure 93 Two dimensional projected view of interstitial loop - nanovoid interactions. (a) For a stand-alone Frank loop, a 5 keV primary knock-on atom (PKA) generates a cascade at one corner of the loop (a2). During the quenching process, the cascade shrinks, accompanied by the recovery of the Frank loop. After the retreat of the cascade, the Frank loop evolves back to its original configuration, except a vacancy at the loop and an interstitial out of the loop (a Frenkel pair). (b1) For a Frank loop immediately next to a void (d = 3 nm), a similar cascade is performed. (b2) Accompanying by the retreat of the cascade, the interstitials are absorbed into the void (b3), leading to a shrinkage of the void and substantial removal of the Frank loop. No defects appear out of the Frank loop. (c1) For a Frank loop ~ 1 nm away from a void (d = 3 nm), a similar cascade generated by an 8 keV PKA is performed (c2). The interstitials of the Frank loop are attracted into the void (c3), leading to shrinkage of the void and Frank loop. No defects appear out of the Frank loop in cases b and c.

The amount of net interstitials (inside a Frank loop) absorbed by a void depends on the energy and fluence of primary knock-on atoms. Fig. 94 shows one of the cases wherein multiple cascades (3 incident ions) led to substantial absorption of a Frank loop and shrinkage of the void, leaving behind stacking faults, vacancies and a prismatic loop.

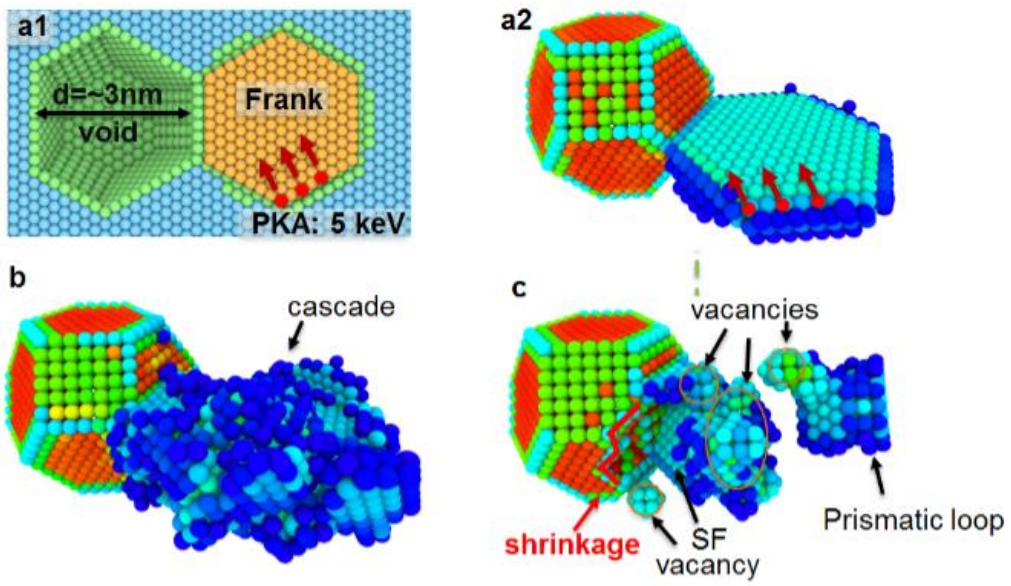

Figure 94 MD simulations of absorption of a Frank loop by a void under cascade. (a1-a2) 2D and 3D views of a Frank loop close to a void. (b) A snapshot of cascade structure when the Frank loop was bombarded by 5 keV primary knock-on atoms (PKA). (c) A cascade occurred over most of the loop and the void shank with the absorption of interstitials in the Frank loop. The Frank loop was destroyed by the cascade, generating other defects such as stacking faults, vacancies, and a prismatic loop

Cyclic variation of mobile dislocation loop density: *In situ* radiation studies show that cyclic variation in density of mobile dislocations is directly related to void shrinkage in nv-nt Cu. During radiation, the interaction of radiation induced defects and TBs provides a continuous source for mobile interstitial loops. In contrast, nanovoids are

sinks for these defects. The net accumulation of mobile loops is thus a competition between these two processes. The simulation developed from such concept (see Fig. 95 and Fig. 96 for details) yields time dependent evolution of mobile loop density (shown by solid red curve in Fig. 796a), in qualitative agreement with experimental observations.

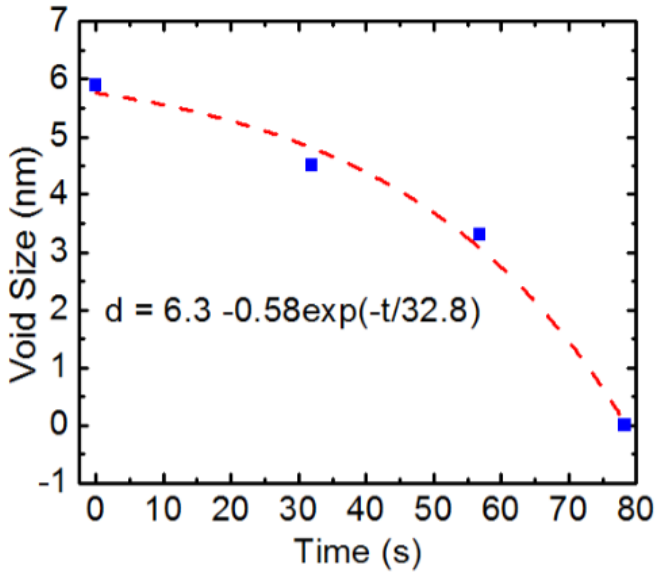

Figure 95 The evolution of void size with time for a typical nanovoid with initial diameter of ~ 6 nm. The time dependent reduction of void diameter is fitted as the red dash line using inserted analytical formula.

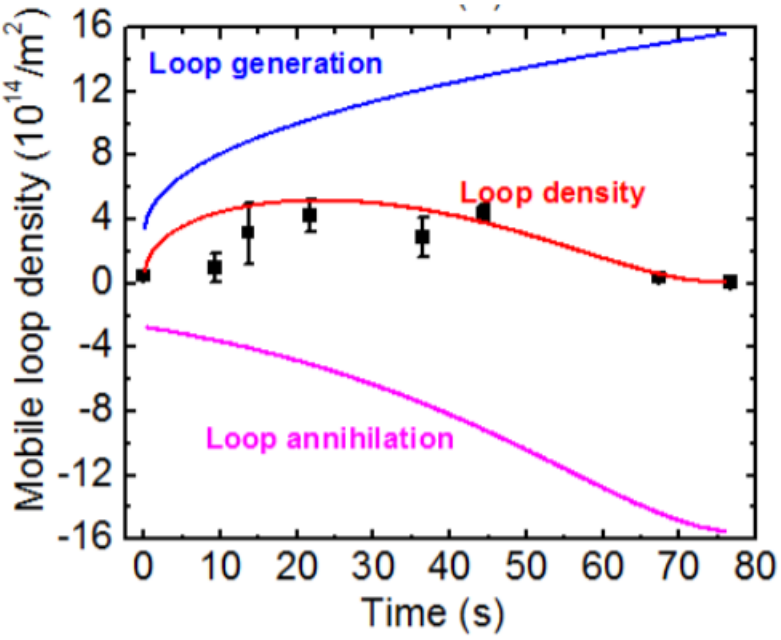

Figure 96 The evolution of dislocation density with time. Simulated evolution curve of dislocation density (red) is a summation of dislocation annihilation (pink) and dislocation generation (blue) curves. Please note that the pink line (due to loop induced annihilation of loops) was derived from empirical fitting of loop diameter. The blue line was obtained by using $\rho_{gen}(t) = a + bt^n$, where n = 0.43 from literature. Two fitting parameters, a and b, were thus used to obtain the red solid line to fit the experimentally determined time dependent variation of loop density (solid square data points).

Foregoing discussions highlight several uniqueness of nv-nt architecture in achieving unprecedented radiation tolerance. First, comparing to high angle grain boundaries in nanocrystalline metals, TBs are comparable defect sinks, but much more stable under radiation. Second, nt metals have extraordinary 3D ITB-CTB networks with rapid diffusion channels that act as highways to rapidly transport point defects and their clusters. The fast diffusion channels discovered in nt metals have one dimensional nature and are much more efficient than high angle grain boundaries to transport defect clusters to desirable destination (nanovoids). Third, abundant nanovoids at the end of these

highways have capacity to store and eliminate these defect clusters. In absence of nanovoids, even if TB networks remain actively transporting defects, there is no space to eliminate defect clusters in a timely manner and hence defect density will build up gradually.

7.6 Conclusion

In summary, we report on a new method beyond existing approaches (*3*) to achieve extraordinary radiation tolerance by using nv-nt architecture. The self-healing effect observed in this study shall not be interpreted as mitigation of void swelling only. Instead the proper insertion of nanovoids (along ITBs) ensures that mobile defect clusters can be 'stored', and consequently permits continuous and expeditious removal of mobile dislocation loops. The ITB-CTB networks in nt metals enable rapid transportation of radiation induced defect clusters to nanovoids and thus lead to their mutual recombination. The concept developed from this study - combination of nanovoids with nanotwin networks - not only helps us to understand defect mitigation mechanisms in irradiated materials, and but may also stimulate the design of damage tolerant materials in general that are subjected other extreme environments, such as high stress and high pressure impact.

7.7 **Acknowledgements**

We acknowledge financial support by NSF-DMR-Metallic Materials and Nanostructures Program under grant no. 1304101. Y. Liu who works on fabrication of nanotwinned metals is supported by DOE-OBES under grant no. DE-SC0010482. YC,

SS, and JW acknowledge the support provided by the US Department of Energy, Office of Science, Office of Basic Energy Sciences, and the Los Alamos National Laboratory Directed Research and Development (LDRD-ER20140450). We also thank Peter M. Baldo and Edward A. Ryan at Argonne National Laboratory and L. Jiao in Texas A&M University for their help during *in situ* irradiation experiments. The IVEM facility at Argonne National Laboratory is supported by DOE-BES. Access to the DOE - Center for Integrated Nanotechnologies (CINT) at Los Alamos and Sandia National Laboratories and Microscopy and Imaging Center at Texas A&M University is also acknowledged.

CHAPTER VIII

CONCLUSIONS AND FUTURE WORK

8.1 Conclusions

(1) Microstructure and strengthening mechanisms in Cu/Fe multilayers: We studied strengthening mechanisms of Cu/Fe multilayers with various individual layer thicknesses on Si (100) and Si (110) substrates. K-S and N-W orientation relationships were identified along layer interfaces. When h > 25 nm, the nanocolumn grain size in Fe is smaller than h, and is the primary parameter that dominates the strength of multilayers. A plateau of hardness is achieved when h = 2.5 - 25 nm, and can be explained by interface barrier strength model. Fully coherent interfaces were achieved at h of 0.75 nm in both sets of multilayers. The hardness of (111) textured Cu/Fe 0.75 nm multilayer remains high due to the formation of a large amount of nanotwins, wherein (100) textured Cu/Fe, significant softening was observed due to the formation of fully coherent layer interface and diminishing Koehler stress.

(2) Enhanced radiation tolerance in Cu/Fe multilayers: A systematic study on radiation response of immiscible Cu/Fe multilayers with incoherent and coherent layer interfaces was performed. At large layer thickness ($h \geq 5$ nm), incoherent Cu/Fe interface is stable and enables significant reduction of He bubble density. At smaller layer thickness ($h \leq 2.5$ nm) when coherency prevails, bubble density increases. However the average bubble size is substantially curtailed by fully coherent immiscible

interfaces, leading to reduced swelling. Therefore, this study suggests that coherent immsicible interfaces can also prominently alleviate radiaiton damage.

(3) Unusual size dependent radiation hardening in Cu/Co multilayers: We investigated He ion radiation response of immiscible coherent Cu/Co multilayer systems. Similar to incoherent interfaces in immiscible systems, the coherent interfaces can also effectively mitigate radiation damage in terms of reducing He bubble density in nanolayers with smaller h. Layer interfaces in Cu/Co are in general resistant to radiation induced intermixing. In contrast to the major reported trend of reduced radiation hardening at smaller h in immiscible incoherent multilayers, the size dependent strengthening behavior in Cu/Co system is just the opposite, although the density of He bubble density is indeed lower at smaller h. Such a surprising observation was explained by a transition from partial transmission dominated strengthening mechanisms (before radiation) to full dislocation transmission dictated deformation behavior in immiscible Cu/Co nanolayers due to decoration of pressurized He bubbles at layer interface in irradiated multilayers.

(4) In situ studies of heavy ion irradiation response of Cu/Fe multilayers: We studied monolithic Cu films and Cu/Fe multilayers with individual layer thickness of 100 and 5 nm, subjected to *in situ* Cu ion irradiation at room temperature to 1 displacements-per-atom, where a clear size effect in defect density and size was observed: in monolithic Cu, rapid propagation of defect clusters was observed, whereas fewer defects (less than 1/5 of defects in Cu) were generated in Cu/Fe 100 nm multilayer

and radiation induced defects in Cu/Fe 5 nm multilayer were barely observed. A statistical study in 100 nm thick Cu layers via *in situ* video reveals the existence of layer interface affected zone, that is the number of nucleation sites of loops declines when approaching Cu/Fe interfaces. Meanwhile, the defect growth in 5 nm thick Cu layers was suppressed (~ 3 nm) by Cu/Fe interfaces while the defect sizes in monolithic Cu (~ 7 nm) and Cu layers in Cu/Fe (~ 9 nm) 100 nm multilayer are close.

(5) Damage tolerant nanotwinned Cu with nanovoids under radiation environments: In this part, we report on a new method to achieve extraordinary radiation tolerance by using nv-nt architecture. The self-healing effect observed in this study shall not be interpreted as mitigation of void swelling only. Instead the proper insertion of nanovoids (along ITBs) ensures that mobile defect clusters can be 'stored', and consequently permits continuous and expeditious removal of mobile dislocation loops. The ITB-CTB networks in nt metals enable rapid transportation of radiation induced defect clusters to nanovoids and thus lead to their mutual recombination. The concept developed from this study - combination of nanovoids with nanotwin networks - not only helps us to understand defect mitigation mechanisms in irradiated materials, and but may also stimulate the design of damage tolerant materials in general that are subjected other extreme environments, such as high stress and high pressure impact.

8.2 Future work

This thesis covers certain enhanced radiation tolerant nanostructures, including Cu/Fe and Cu/Co multilayers and nanotwinned Cu with nanovoids. However, new-

generation nuclear reactors demand the application of nanostructured materials at elevated temperature as well as high radiation dose (200 dpa). Therefore, further studies are necessary to achieve a better understanding in radiation response of these nanostructures. (1) The thermal stability of layer interfaces: ex- and in-situ annealing experiments are required to examine thermal stability of layer interfaces in Cu/Fe and Cu/Co multilayers with different h at elevated temperature. (2) Radiation damage in multilayers subjected to high-dose radiation: radiation dose in Cu/Fe and Cu/Co multilayers needs be increased to high dpa (e.g., 200 dpa). Under high radiation dose, more aggressive interaction would occur between layer interface and radiation induced defects. It is necessary to examine the interface stability and its capability under high radiation dose. Defect migration kinetics and radiation induced intermixing of interfaces in multilayers with different h are the focus, assisted by *ex*- and *in-situ* radiation experiments.

Nanotwinned Cu with nanovoids has demonstrated superior radiation tolerance. However, this is just the first step to probe this unique design. In future, a systematic study on the effect of void size and density as well as twin spacing on radiation damage is required and would be fruitful. Meanwhile, follow-up study on radiation response at elevated temperature and high radiation dose is also interesting for the design of novel radiation tolerant materials in future.

REFERENCES

[1] Chu, S. & Majumdar, A., Opportunities and challenges for a sustainable energy future. *Nature* **488**, 294 (2012).

[2] Marquis, E. A. *et al.*, Nuclear reactor materials at the atomic scale. *Materials Today* **12**, 30 (2009).

[3] Zinkle, S. J. & Snead, L. L., Designing radiation resistance in materials for fusion energy. *Annu. Rev. Mater. Res.* **44**, 241 (2014).

[4] Odette, G. R. *et al.*, Recent developments in irradiation-resistant steels. *Annu. Rev. Mater. Res.* **38**, 471 (2008).

[5] Zinkle, S. J. & Was, G. S., Materials challenges in nuclear energy. *Acta Mater.* **61**, 735 (2013).

[6] Gleiter, H., Nanocrystalline materials. *Prog. Mater. Sci.* **33**, 223 (1989).

[7] Suryanarayana, C. & Koch, C. C., Nanocrystalline materials – Current research and future directions. *Hyperfine Interact.* **130**, 5 (2000).

[8] Baibich, M. N. *et al.*, Giant magnetoresistance of (001)Fe/(001)Cr magnetic superlattices. *Phys. Rev. Lett.* **61**, 2472 (1988).

[9] Clemens, B. M. *et al.*, Structure and strength of multilayers. *MRS Bull.* **24**, 20 (1999).

[10] Sun, C. *et al.*, In situ evidence of defect cluster absorption by grain boundaries in Kr Ion irradiated nanocrystalline Ni. *Metall. Mater. Trans. A* **44**, 1966 (2013).

[11] Anderoglu, O. *et al.*, Epitaxial nanotwinned Cu films with high strength and high conductivity. *Appl. Phys. Lett.* **93**, (2008).

[12] Misra, A. *et al.*, Length-scale-dependent deformation mechanisms in incoherent metallic multilayered composites. *Acta Mater.* **53**, 4817 (2005).

[13] Biener, J. *et al.*, Size Effects on the mechanical behavior of nanoporous Au. *Nano Lett.* **6**, 2379 (2006).

[14] Misra, A. & Krug, H., Deformation behavior of nanostructured metallic multilayers. *Adv. Eng. Mater.* **3**, 217 (2001).

[15] Kurdjumov, G. & Sachs, G., Over the mechanisms of steel hardening. *Z. Phys* **64**, 325 (1930).

[16] Wasermann, G., Orientation relationship between FCC and BCC. *Arch. Eisenhutt Wes.* **16**, 647 (1933).

[17] Nishiyama, Z., Growth Orientation between FCC and BCC, *Sci. Rep. Res. Insts.Tohoku Univ.* **23**, 638 (1934).

[18] Pitsch, W., The martensite transformation in thin foils of iron-nitrogen alloys. *Philos. Mag.* **4**, 577 (1959).

[19] Bain, E. C., A new orientation relationshp between FCC and BCC, *Trans. Metall. Soc. A.I.M.E.* **70**, 25 (1924).

[20] Wang, J. *et al.*, Interface dislocation patterns and dislocation nucleation in face-centered-cubic and body-centered-cubic bicrystal interfaces. *Int. J. Plast.* **53**, 40 (2014).

[21] Wang, J. *et al.*, Characterizing interface dislocations by atomically informed Frank-Bilby theory. *J. Mater. Res.* **28**, 1646 (2013).

[22] Hirth, J. P. *et al.*, Interface defects, reference spaces and the Frank–Bilby equation. *Prog. Mater. Sci.* **58**, 749 (2013).

[23] Wang, J. *et al.*, Modeling interface-dominated mechanical behavior of nanolayered crystalline composites. *JOM* **66**, 102 (2014).

[24] Embury, J. D. & Hirth, J. P., On dislocation storage and the mechanical response of fine scale microstructures. *Acta Metall.* **42**, 2051 (1994).

[25] Anderson, P. M. *et al.*, Dislocation-based deformation mechanisms in metallic nanolaminates. *MRS Bull.* **24**, 27 (1999).

[26] Misra, A. *et al.*, Structure and mechanical properties of Cu-X (X = Nb,Cr,Ni) nanolayered composites. *Scripta Mater.* **39**, 555 (1998).

[27] Liu, Y. *et al.*, Mechanical properties of highly textured Cu/Ni multilayers. *Acta Mater.* **59**, 1924 (2011).

[28] Wang, J. & Misra, A., An overview of interface-dominated deformation mechanisms in metallic multilayers. *Curr. Opin. Solid State Mater. Sci.* **15**, 20 (2011).

[29] Petch, N. J., The cleavage strength of polycrystals. *J Iron Steel Inst* **174**, 25 (1953).

[30] Zhang, X. *et al.*, Enhanced hardening in Cu/330 stainless steel multilayers by nanoscale twinning. *Acta Mater.* **52**, 995 (2004).

[31] Li, X. *et al.*, Dislocation nucleation governed softening and maximum strength in nano-twinned metals. *Nature* **464**, 877 (2010).

[32] Lu, K. *et al.*, Strengthening materials by engineering coherent internal boundaries at the nanoscale. *Science* **324**, 349 (2009).

[33] Zhu, Y. T. *et al.*, Dislocation–twin interactions in nanocrystalline fcc metals. *Acta Mater.* **59**, 812 (2011).

[34] Misra, A. *et al.*, Deformation mechanism maps for polycrystalline metallic multiplayers. *Scripta Mater.* **41**, 973 (1999).

[35] D. Nix, W., Elastic and plastic properties of thin films on substrates: nanoindentation techniques. *Mater Sci Eng A* **234–236**, 37 (1997).

[36] Koehler, J. S., Attempt to design a strong solid. *Phys. Rev. B* **2**, 547 (1970).

[37] Rao, S. I. & Hazzledine, P. M., Atomistic simulations of dislocation-interface interactions in the Cu-Ni multilayer system. *Philos. Mag. A* **80**, 2011 (2000).

[38] Zhu, X. F. *et al.*, Understanding nanoscale damage at a crack tip of multilayered metallic composites. *Appl. Phys. Lett.* **92**, 161905 (2008).

[39] Misra, A. *et al.*, Work hardening in rolled nanolayered metallic composites. *Acta Mater.* **53**, 221 (2005).

[40] Zhang, J. Y. *et al.*, Tailoring nanostructured Cu/Cr multilayer films with enhanced hardness and tunable modulus. *Mater. Sci. Eng., A* **543**, 139 (2012).

[41] Niu, J. J. *et al.*, Size-dependent deformation mechanisms and strain-rate sensitivity in nanostructured Cu/X multilayer films. *Acta Mater.* **60**, 3677 (2012).

[42] Fu, E. G. *et al.*, Mechanical properties of sputtered Cu/V and Al/Nb multilayer films. *Mater. Sci. Eng., A* **493**, 283 (2008).

[43] Wei, Q. & Misra, A., Transmission electron microscopy study of the microstructure and crystallographic orientation relationships in V/Ag multilayers. *Acta Mater.* **58**, 4871 (2010).

[44] Wang, J. *et al.*, Atomistic modeling of the interaction of glide dislocations with "weak" interfaces. *Acta Mater.* **56**, 5685 (2008).

[45] Hoagland, R. G. *et al.*, On the role of weak interfaces in blocking slip in nanoscale layered composites. *Philos. Mag.* **86**, 3537 (2006).

[46] Lu, L. *et al.*, Ultrahigh strength and high electrical conductivity in copper. *Science* **304**, 422 (2004).

[47] Lu, L. *et al.*, Revealing the maximum strength in nanotwinned copper. *Science* **323**, 607 (2009).

[48] Zhang, X. *et al.*, High-strength sputter-deposited Cu foils with preferred orientation of nanoscale growth twins. *Appl. Phys. Lett.* **88**, 173116 (2006).

[49] Jang, D. *et al.*, Deformation mechanisms in nanotwinned metal nanopillars. *Nature Nanotech.* **7**, 594 (2012).

[50] Wang, Y. M. *et al.*, Defective twin boundaries in nanotwinned metals. *Nature Mater.* **12**, 697 (2013).

[51] Bufford, D. *et al.*, High strength, epitaxial nanotwinned Ag films. *Acta Mater.* **59**, 93 (2011).

[52] Li, N. *et al.*, Influence of slip transmission on the migration of incoherent twin boundaries in epitaxial nanotwinned Cu. *Scripta Mater.* **64**, 149 (2011).

[53] Li, N. *et al.*, Twinning dislocation multiplication at a coherent twin boundary. *Acta Mater.* **59**, 5989 (2011).

[54] Demkowicz, M. J. *et al.*, The influence of Σ3 twin boundaries on the formation of radiation-induced defect clusters in nanotwinned Cu. *J. Mater. Res.* **26**, 1666 (2011).

[55] Zhang, X. & Misra, A., Superior thermal stability of coherent twin boundaries in nanotwinned metals. *Scripta Mater.* **66**, 860 (2012).

[56] Anderoglu, O. *et al.*, Thermal stability of sputtered Cu films with nanoscale growth twins. *J. Appl. Phys.* **103**, 094322 (2008).

[57] Yu, K. Y. *et al.*, Removal of stacking-fault tetrahedra by twin boundaries in nanotwinned metals. *Nat. Commun.* **4**, 1377 (2013).

[58] Niewczas, M. & Hoagland, R. G., Molecular dynamic studies of the interaction of a/6<112> Shockley dislocations with stacking fault tetrahedra in copper. Part II: Intersection of stacking fault tetrahedra by moving twin boundaries. *Philos. Mag.* **89**, 727 (2009).

[59] Wang, J. *et al.*, Dislocation structures of Σ3 {112} twin boundaries in face centered cubic metals. *Appl. Phys. Lett.* **95**, 021908 (2009).

[60] Murr, L. E., Interfacial phenomena in metals and alloys. (1975).

[61] Hirth, J. P. & Lothe, J., Theory of dislocations. (1982).

[62] Anderoglu, O. *et al.*, Plastic flow stability of nanotwinned Cu foils. *Int. J. Plast.* **26**, 875 (2010).

[63] Bufford, D. *et al.*, Thermal stability of twins and strengthening mechanisms in differently oriented epitaxial nanotwinned Ag films. *J. Mater. Res.* **28**, 1729 (2013).

[64] Zhang, X. *et al.*, Thermal stability of sputter-deposited 330 austenitic stainless-steel thin films with nanoscale growth twins. *Appl. Phys. Lett.* **87**, (2005).

[65] Yu, K. Y. *et al.*, Basic criteria for formation of growth twins in high stacking fault energy metals. *Appl. Phys. Lett.* **103**, (2013).

[66] Bufford, D. *et al.*, In situ nanoindentation study on plasticity and work hardening in aluminium with incoherent twin boundaries. *Nat Commun* **5**, (2014).

[67] Bufford, D. *et al.*, Formation Mechanisms of High-density Growth Twins in Aluminum with High Stacking-Fault Energy. *Mater. Res. Lett.* **1**, 51 (2013).

[68] Liu, Y. *et al.*, A formation mechanism for ultra-thin nanotwins in highly textured Cu/Ni multilayers. *J. Appl. Phys.* **111**, 073526 (2012).

[69] Yu, K. Y. *et al.*, Strengthening mechanisms of Ag/Ni immiscible multilayers with fcc/fcc interface. *Surf. Coat. Technol.* **237**, 269 (2013).

[70] Chen, Y. *et al.*, Microstructure and strengthening mechanisms in Cu/Fe multilayers. *Acta Mater.* **60**, 6312 (2012).

[71] Pande, C. S. *et al.*, Effect of annealing twins on Hall–Petch relation in polycrystalline materials. *Mater. Sci. Eng., A* **367**, 171 (2004).

[72] Grimes, R. W. *et al.*, Greater tolerance for nuclear materials. *Nature Mater.* **7**, 683 (2008).

[73] Was, G. S., Materials degradation in fission reactors: Lessons learned of relevance to fusion reactor systems. *J. Nucl. Mater.* **367–370, Part A**, 11 (2007).

[74] Ackland, G., Controlling Radiation Damage. *Science* **327**, 1587 (2010).

[75] Sickafus, K. E. *et al.*, Radiation-induced amorphization resistance and radiation tolerance in structurally related oxides. *Nature Mater.* **6**, 217 (2007).

[76] Sickafus, K. E. *et al.*, Radiation tolerance of complex oxides. *Science* **289**, 748 (2000).

[77] Kaoumi, D. *et al.*, A thermal spike model of grain growth under irradiation. *J. Appl. Phys.* **104**, (2008).

[78] Kinchin, G. & Pease, R., The displacement of atoms in solids by radiation. *Rep. Prog. Phys.* **18**, 1 (1955).

[79] Caturla, M. J. *et al.*, Comparative study of radiation damage accumulation in Cu and Fe. *J. Nucl. Mater.* **276**, 13 (2000).

[80] Olander, D. R., "Fundamental aspects of nuclear reactor fuel elements" (California Univ., Berkeley (USA). Dept. of Nuclear Engineering, 1976).

[81] King, W. E. *et al.*, Threshold energy surface and frenkel pair resistivity for Cu. *J. Nucl. Mater.* **117**, 12 (1983).

[82] Was, G. S., Fundamentals of radiation materials science: metals and alloys. (Berlin: Springer, 2007).

[83] Zinkle, S. J. *et al.*, I. Energy calculations for pure metals. *Philos. Mag. A* **55**, 111 (1987).

[84] Singh, B. N. & Zinkle, S. J., Defect accumulation in pure fcc metals in the transient regime: a review. *J. Nucl. Mater.* **206**, 212 (1993).

[85] Singh, B. N. *et al.*, Review: Evolution of stacking fault tetrahedra and its role in defect accumulation under cascade damage conditions. *J. Nucl. Mater.* **328**, 77 (2004).

[86] Mansur, L. K., Theory and experimental background on dimensional changes in irradiated alloys. *J. Nucl. Mater.* **216**, 97 (1994).

[87] Schäublin, R. *et al.*, Quantitative analysis of CTEM images of small dislocation loops in Al and stacking fault tetrahedra in Cu generated by molecular dynamics simulation. *J. Nucl. Mater.* **276**, 251 (2000).

[88] Singh, B. N., Effect of grain size on void formation during high-energy electron irradiation of austenitic stainless steel. *Philos. Mag.* **29**, 25 (1974).

[89] Singh, B. N. & Foreman, A. J. E., Calculated grain size-dependent vacancy supersaturation and its effect on void formation. *Philos. Mag.* **29**, 847 (1974).

[90] Han, W. Z. *et al.*, Effect of grain boundary character on sink efficiency. *Acta Mater.* **60**, 6341 (2012).

[91] Bai, X.-M. *et al.*, Efficient annealing of radiation damage near grain boundaries via interstitial emission. *Science* **327**, 1631 (2010).

[92] Chen, D. *et al.*, Defect annihilation at grain boundaries in alpha-Fe. *Sci. Rep.* **3**, (2013).

[93] Yu, K. Y. *et al.*, Radiation damage in helium ion irradiated nanocrystalline Fe. *J. Nucl. Mater.* **425**, 140 (2012).

[94] Serra, A. *et al.*, Strengthening and microstructure modification associated with moving twin boundaries in hcp metals. *Philosophical Magazine Letters* **87**, 451 (2007).

[95] Niewczas, M. & Hoagland, R. G., Molecular dynamic studies of the interaction of a/6⟨112⟩ Shockley dislocations with stacking fault tetrahedra in copper. Part II: Intersection of stacking fault tetrahedra by moving twin boundaries. *Philos. Mag.* **89**, 727 (2009).

[96] Segall, R., Coherent annealing twin boundaries as vacancy sinks. *Acta Metall.* **12**, 117 (1964).

[97] King, A. H. & Smith, D. A., On the mechanisms of point-defect absorption by grain and twin boundaries. *Philos. Mag. A* **42**, 495 (1980).

[98] Bailat, C. *et al.*, Deformation modes of proton and neutron irradiated stainless steels. *J. Nucl. Mater.* **276**, 283 (2000).

[99] Yu, K. *et al.*, Removal of stacking-fault tetrahedra by twin boundaries in nanotwinned metals. *Nat. Commun.* **4**, 1377 (2013).

[100] Heinisch, H. L. *et al.*, The effects of interfaces on radiation damage production in layered metal composites. *J. Nucl. Mater.* **329–333**, 924 (2004).

[101] Höchbauer, T. *et al.*, Influence of interfaces on the storage of ion-implanted He in multilayered metallic composites. *J. Appl. Phys.* **98**, (2005).

[102] Zhang, X. *et al.*, Nanostructured Cu/Nb multilayers subjected to helium ion-irradiation. *Nucl. Instrum. Methods Phys. Res., Sect. B* **261**, 1129 (2007).

[103] Fu, E. G. *et al.*, Size dependent enhancement of helium ion irradiation tolerance in sputtered Cu/V nanolaminates. *J. Nucl. Mater.* **385**, 629 (2009).

[104] Fu, E. G. *et al.*, Interface enabled defects reduction in helium ion irradiated Cu/V nanolayers. *J. Nucl. Mater.* **407**, 178 (2010).

[105] Fu, E. G. *et al.*, Fluence-dependent radiation damage in helium (He) ion-irradiated Cu/V multilayers. *Philos. Mag.* **93**, 883 (2013).

[106] Li, N. *et al.*, The influence of interfaces on the formation of bubbles in He-ion-irradiated Cu/Mo nanolayers. *Philos. Mag. Lett.* **91**, 18 (2010).

[107] Gao, Y. *et al.*, Radiation tolerance of Cu/W multilayered nanocomposites. *J. Nucl. Mater.* **413**, 11 (2011).

[108] Li, N. *et al.*, He ion irradiation damage to Al/Nb multilayers. *J. Appl. Phys.* **105**, 123522 (2009).

[109] Wei, Q. M. *et al.*, Suppression of irradiation hardening in nanoscale V/Ag multilayers. *Acta Mater.* **59**, 6331 (2011).

[110] Wei, Q. M. *et al.*, Nucleation and growth of bubbles in He ion-implanted V/Ag multilayers. *Philos. Mag.* **91**, 553 (2010).

[111] Demkowicz, M. & Hoagland, R., Simulations of collision cascades in Cu–Nb layered composites using an EAM interatomic potential. *Int. J. Appl. Mech.* **1**, 421 (2009).

[112] Misra, A. *et al.*, The radiation damage tolerance of ultra-high strength nanolayered composites. *JOM* **59**, 62 (2007).

[113] Wang, J. *et al.*, Room-temperature dislocation climb in metallic interfaces. *Appl. Phys. Lett.* **94**, (2009).

[114] Li, N. *et al.*, In situ TEM observations of room temperature dislocation climb at interfaces in nanolayered Al/Nb composites. *Scripta Mater.* **63**, 363 (2010).

[115] Demkowicz, M. J. *et al.*, Influence of interface sink strength on the reduction of radiation-induced defect concentrations and fluxes in materials with large interface area per unit volume. *Phys. Rev. B* **84**, 104102 (2011).

[116] Mansur, L. K. & Coghlan, W. A., Mechanisms of helium interaction with radiation effects in metals and alloys: A review. *J. Nucl. Mater.* **119**, 1 (1983).

[117] Stoller, R. E. & Odette, G. R., Analytical solutions for helium bubble and critical radius parameters using a hard sphere equation of state. *J. Nucl. Mater.* **131**, 118 (1985).

[118] Demkowicz, M. J. *et al.*, The effect of excess atomic volume on He bubble formation at fcc–bcc interfaces. *Appl. Phys. Lett.* **97**, (2010).

[119] Zhang, X. *et al.*, Design of Radiation Tolerant Nanostructured Metallic Multilayers. *J. Eng. Mater. Technol.-Trans. ASME* **134**, (2012).

[120] Kashinath, A. *et al.*, Stable Storage of Helium in Nanoscale Platelets at Semicoherent Interfaces. *Phys. Rev. Lett.* **110**, 086101 (2013).

[121] Beyerlein, I. J. *et al.*, Radiation damage tolerant nanomaterials. *Materials Today* **16**, 443 (2013).

[122] Yu, K. Y. *et al.*, Comparisons of radiation damage in He ion and proton irradiated immiscible Ag/Ni nanolayers. *J. Nucl. Mater.* **440**, 310 (2013).

[123] Yu, K. Y. *et al.*, Superior tolerance of Ag/Ni multilayers against Kr ion irradiation: an in situ study. *Philos. Mag.* **93**, 3547 (2013).

[124] Li, N. *et al.*, He ion irradiation damage in Fe/W nanolayer films. *J. Nucl. Mater.* **389**, 233 (2009).

[125] Zhang, X. *et al.*, Interface-enabled defect reduction in He ion irradiated metallic multilayers. *JOM* **62**, 75 (2010).

[126] Zhang, X. *et al.*, Design of Radiation Tolerant Nanostructured Metallic Multilayers. *J. Eng. Mater. Technol.* **134**, 041010 (2012).

[127] Li, N. *et al.*, Defect structures and hardening mechanisms in high dose helium ion implanted Cu and Cu/Nb multilayer thin films. *Int J. Plast.* **32**, 1 (2012).

[128] Demkowicz, M. J. *et al.*, The role of interface structure in controlling high helium concentrations. *Curr. Opin. Solid State Mater. Sci.* **16**, 101 (2012).

[129] Demkowicz, M. J. *et al.*, Interfaces between dissimilar crystalline solids. *Dislocations in solids* **14**, 141 (2008).

[130] Odette, G. R. *et al.*, Recent developments in irradiation-resistant steels. *Annu. Rev. Mater. Res.* **38**, 471 (2008).

[131] Klueh, R. L. *et al.*, Ferritic/martensitic steels – overview of recent results. *J. Nucl. Mater.* **307–311**, 455 (2002).

[132] Murty, K. L. & Charit, I., Structural materials for Gen-IV nuclear reactors: Challenges and opportunities. *J. Nucl. Mater.* **383**, 189 (2008).

[133] Schäublin, R. *et al.*, Microstructural development under irradiation in European ODS ferritic/martensitic steels. *J. Nucl. Mater.* **351**, 247 (2006).

[134] Ukai, S. & Fujiwara, M., Perspective of ODS alloys application in nuclear environments. *J. Nucl. Mater.* **307–311, Part 1**, 749 (2002).

[135] Liu, Y. *et al.*, Stacking fault and partial dislocation dominated strengthening mechanisms in highly textured Cu/Co multilayers. *Int. J. Plast.* **49**, 152 (2013).

[136] Singh, B. N. *et al.*, On grain-size-dependent void swelling in pure copper irradiated with fission neutrons. *Philos. Mag. A* **82**, 1137 (2002).

[137] Samaras, M. *et al.*, Computer simulation of displacement cascades in nanocrystalline Ni. *Phys. Rev. Lett.* **88**, 125505 (2002).

[138] Chen, D. *et al.*, Defect annihilation at grain boundaries in alpha-Fe. *Sci. Rep.* **3**, 1450 (2013).

[139] Millett, P. C. *et al.*, Phase-field simulation of irradiated metals: Part I: Void kinetics. *Comput. Mater. Sci.* **50**, 949 (2011).

[140] Wang, J. *et al.*, Detwinning mechanisms for growth twins in face-centered cubic metals. *Acta Mater.* **58**, 2262 (2010).

[141] ISO 14577-12002 Metallic materials --- Instrumented Indentation Test for Hardness, M. P., International Standard.

[142] Oliver, W. C. & Pharr, G. M., An improved technique for determining hardness and elastic modulus using load and displacement sensing indentation experiments. *J. Mater. Res.* **7**, 1564 (1992).

[143] Saha, R. & Nix, W. D., Effects of the substrate on the determination of thin film mechanical properties by nanoindentation. *Acta Mater.* **50**, 23 (2002).

[144] Ziegler, J. F. & Biersack, J. P., SRIM-2008, Stopping Power and Range of Ions in Matter. *Calculation using the Stopping and Range of Ions in Matter (SRIM) Code.* <http://www.srim.org/>. (2008).

[145] Stoller, R. E. *et al.*, On the use of SRIM for computing radiation damage exposure. *Nucl. Instrum. Methods Phys. Res., Sect. B* **310**, 75 (2013).

[146] Huang, B. *et al.*, Preparation of high strength bulk nano-scale Fe/Cu multilayers by repeated pressing-rolling. *J. Mater. Sci. Lett.* **20**, 1669 (2001).

[147] Gao, J. *et al.*, Evolution of nanoindentation Hardness of Fe/Cu nanometer-scale multilayers by magnetron sputtering. *Key Eng. Mater.* **373-374**, 104 (2008).

[148] Shamsutdinov, N. R. *et al.*, The effect of Cu interlayers on grain size and stress in sputtered Fe–Cu multilayered thin films. *Scripta Mater.* **54**, 1727 (2006).

[149] Lloyd, S. J., Strain in ferromagnetic face centred Fe–Cu multilayers examined using transmission electron microscopy. *J. Magn. Magn. Mater.* **198–199**, 671 (1999).

[150] Lee, D. W. *et al.*, Structural and magnetic properties of Cu/Fe multilayers. *Phys. Rev. B* **59**, 7001 (1999).

[151] Ernst, F. *et al.*, Theoretical prediction and direct observation of the 9R structure in Ag. *Phys. Rev. Lett.* **69**, 620 (1992).

[152] Wang, J. *et al.*, Dislocation structures of Sigma 3 {112} twin boundaries in face centered cubic metals. *Appl Phys Lett* **95**, 021908 (2009).

[153] Tu, K. N. *et al.*, *Electronic thin film science: for electrical engineers and materials scientists*. (Macmillan, New York, 1992).

[154] Lloyd, S. J. & Dunin-Borkowski, R. E., Electronic structure of face-centered-tetragonal iron in ferromagnetic iron-copper multilayers. *Phys. Rev. B* **59**, 2352 (1999).

[155] Lu, S. H. *et al.*, Structural properties of epitaxial films of Fe on Cu and Cu-based surface and bulk alloys. *Surf. Sci.* **209**, 364 (1989).

[156] Zhu, Y. T. *et al.*, Deformation twinning in nanocrystalline materials. *Prog. Mater. Sci.* **57**, 1 (2012).

[157] Li, B. Q. *et al.*, Twinnability Predication for fcc Metals. *J. Mater. Sci. Technol.* **27**, 97 (2011).

[158] Freund, L. B. & Suresh, S. (Cambridge University Press, Cambridge, 2004).

[159] Zhang, X. *et al.*, Strengthening mechanisms in nanostructured copper/304 stainless steel multilayers. *J. Mater. Res.* **18**, 1600 (2003).

[160] Reed, D., A review of recent theoretical developments in the understanding of the migration of helium in metals and its interaction with lattice defects. *Radiat Eff.* **31**, 129 (1977).

[161] Thomas, G., Experimental studies of helium in metals. *Radiat Eff.* **78**, 37 (1983).

[162] Lucas, A. A., Helium in metals. *Physica B+C* **127**, 225 (1984).

[163] Yu, K. Y. *et al.*, Removal of stacking-fault tetrahedra by twin boundaries in nanotwinned metals. *Nat. Commun.* **4**, 1377 (2013).

[164] Zhernenkov, M. *et al.*, Trapping of implanted He at Cu/Nb interfaces measured by neutron reflectometry. *Appl. Phys. Lett.* **98**, 241913 (2011).

[165] Kashinath, A. *et al.*, Stable Storage of Helium in Nanoscale Platelets at Semicoherent Interfaces. *Phys. Rev. Lett.* **110**, 086101 (2013).

[166] Song, M. *et al.*, Response of equal channel angular extrusion processed ultrafine-grained T91 steel subjected to high temperature heavy ion irradiation. *Acta Mater.* **74**, 285 (2014).

[167] Wang, H. *et al.*, Ion irradiation effects in nanocrystalline TiN coatings. *Nucl. Instrum. Methods Phys. Res., Sect. B* **261**, 1162 (2007).

[168] Shen, T. D. *et al.*, Enhanced radiation tolerance in nanocrystalline MgGa2O4. *Appl. Phys. Lett.* **90**, 263115 (2007).

[169] Hsiung, L. L. *et al.*, Formation mechanism and the role of nanoparticles in Fe-Cr ODS steels developed for radiation tolerance. *Phys. Rev. B* **82**, 184103 (2010).

[170] Jiao, L. *et al.*, Enhanced ion irradiation tolerance properties in TiN/MgO nanolayer films. *J. Nucl. Mater.* **434**, 217 (2013).

[171] Kim, I. *et al.*, Size-dependent radiation tolerance in ion irradiated TiN/AlN nanolayer films. *J. Nucl. Mater.* **441**, 47 (2013).

[172] Anderoglu, O. *et al.*, He+ ion irradiation response of Fe–TiO_2 multilayers. *J. Nucl. Mater.* **435**, 96 (2013).

[173] Chen, Y. *et al.*, In situ studies of radiation induced crystallization in Fe/a-Y_2O_3 nanolayers. *J. Nucl. Mater.* **452**, 321 (2014).

[174] Shao, S. *et al.*, spiral patterns of dislocations at nodes in (111) semi-coherent fcc interfaces. *Sci. Rep.* **3**, 2448 (2013).

[175] Hattar, K. *et al.*, Arrest of He bubble growth in Cu–Nb multilayer nanocomposites. *Scripta Mater.* **58**, 541 (2008).

[176] Chen, Y. *et al.*, Unusual size-dependent strengthening mechanisms in helium ion-irradiated immiscible coherent Cu/Co nanolayers. *Acta Mater.* **84**, 393 (2015).

[177] Chen, Y. *et al.*, Microstructure and strengthening mechanisms in Cu/Fe multilayers. *Acta Mater.* **60**, 6312 (2012).

[178] McPhie, M. G. *et al.*, Interfacial trapping mechanism of He in Cu-Nb multilayer materials. *J. Nucl. Mater.* **437**, 222 (2013).

[179] Trinkaus, H. & Singh, B. N., Helium accumulation in metals during irradiation – where do we stand? *J. Nucl. Mater.* **323**, 229 (2003).

[180] Tyson, W. R. & Miller, W. A., Surface free energies of solid metals: Estimation from liquid surface tension measurements. *Surf. Sci.* **62**, 267 (1977).

[181] Hough, R. R. & Rolls, R., Copper diffusion in iron during high-temperature tensile creep. *Metall. Trans.* **2**, 2471 (1971).

[182] Wonnell, S. K. *et al.*, Activation volume for the interdiffusion of Ag-Au multilayers. *J. Appl. Phys.* **72**, 5195 (1992).

[183] Bufford, D. *et al.*, Nanotwins and stacking faults in high-strength epitaxial Ag/Al multilayer films. *Appl. Phys. Lett.* **101**, 223112 (2012).

[184] Baibich, M. N. *et al.*, Giant magnetoresistance of (001)Fe/(001)Cr magnetic superlattices. *Phys. Rev. Lett.* **61**, 2472 (1988).

[185] Garner, F. A. *et al.*, Comparison of swelling and irradiation creep behavior of fcc-austenitic and bcc-ferritic/martensitic alloys at high neutron exposure. *J. Nucl. Mater.* **276**, 123 (2000).

[186] Kiener, D. *et al.*, In situ nanocompression testing of irradiated copper. *Nature Mater.* **10**, 608 (2011).

[187] Zinkle, S. J. & Snead, L., Designing radiation resistance in materials for fusion energy. *Annu. Rev. Mater. Res*, (2014).

[188] Saito, S., Role of nuclear energy to a future society of shortage of energy resources and global warming. *J. Nucl. Mater.* **398**, 1 (2010).

[189] Eldrup, M. *et al.*, Dose dependence of defect accumulation in neutron irradiated copper and iron. *J. Nucl. Mater.* **307–311, Part 2**, 912 (2002).

[190] Victoria, M. *et al.*, The microstructure and associated tensile properties of irradiated fcc and bcc metals. *J. Nucl. Mater.* **276**, 114 (2000).

[191] Bacon, D. J. *et al.*, The primary damage state in fcc, bcc and hcp metals as seen in molecular dynamics simulations. *J. Nucl. Mater.* **276**, 1 (2000).

[192] Yu, K. Y. *et al.*, In situ studies of irradiation-induced twin boundary migration in nanotwinned Ag. *Scripta Mater.* **69**, 385 (2013).

[193] Chen, Y. *et al.*, Unusual size-dependent strengthening mechanisms in helium ion-irradiated immiscible coherent Cu/Co nanolayers. *Acta Mater.* **84**, 393 (2015).

[194] Li, N. *et al.*, In situ probing of the evolution of irradiation-induced defects in copper. *J. Nucl. Mater.* **439**, 185 (2013).

[195] Chen, Y. *et al.*, Enhanced radiation tolerance in immiscible Cu/Fe multilayers with coherent and incoherent layer interfaces. *J. Mater. Res.* **(In press)**, (2015).

[196] Was, G. S., Fundamentals of radiation materials science: metals and alloys. (Springer, 2007).

[197] Averback, R. S., Atomic displacement processes in irradiated metals. *J. Nucl. Mater.* **216**, 49 (1994).

[198] Nastasi, M., Ion-solid interactions: Fundamentals and applications. (Cambridge University Press, 1996).

[199] Schäublin, R. *et al.*, Irradiation-induced stacking fault tetrahedra in fcc metals. *Philos. Mag.* **85**, 769 (2005).

[200] Wirth, B. D. *et al.*, Atomistic simulation of stacking fault tetrahedra formation in Cu. *J. Nucl. Mater.* **283–287, Part 2**, 773 (2000).

[201] Di, Z. *et al.*, Tunable helium bubble supperlattice ordered by screw dislocation network. *Phys. Rev. B* **85**, 052101 (2011).

[202] Bringa, E. M. *et al.*, Are Nanoporous Materials Radiation Resistant? *Nano Lett.* **12**, 3351 (2011).

[203] Fu, E. G. *et al.*, Surface effects on the radiation response of nanoporous Au foams. *Appl. Phys. Lett.* **101**, 191607 (2012).

[204] Sun, C. *et al.*, In situ study of defect migration kinetics in nanoporous Ag with enhanced radiation tolerance. *Sci. Rep.* **4**, 3737 (2014).

[205] Landau, P. *et al.*, Investigation Of Radiation Damage Tolerance In Cu/Fe Interface-Containing Nano-pillars. *Microsc. Microanal.* **18**, 730 (2012).

[206] Tabor, D., The hardness of metals. (Oxford university press, 2000).

[207] Mata, M. *et al.*, Contact deformation regimes around sharp indentations and the concept of the characteristic strain. *J. Mater. Res.* **17**, 964 (2002).

[208] Hirth, J. P. & Lothe, J., Theory of Dislocations. (Wiley, New York, 1982).

[209] Duesbery, M. S., Dislocation motion, constriction and cross-slip in fcc metals. *Modelling Simul. Mater. Sci. Eng.* **6**, 35 (1998).

[210] Ullmaier, H. & Camus, E., Low temperature mechanical properties of steels containing high concentrations of helium. *J. Nucl. Mater.* **251**, 262 (1997).

[211] Kroupa, F. & Hirsch, P. B., Elastic interaction betweeen prismatic dislocation loops and straight dislocations. *Discuss. Faraday Soc.* **38**, 49 (1964).

[212] Watkins, G. D., EPR observation of close Frenkel pairs in Irradiated ZnSe. *Phys. Rev. Lett.* **33**, 223 (1974).

[213] Wirth, B. D., How does radiation damage materials? *Science* **318**, 923 (2007).

[214] Fu, C.C. *et al.*, Multiscale modelling of defect kinetics in irradiated iron. *Nature Mater.* **4**, 68 (2005).

[215] Arakawa, K. *et al.*, Observation of the one-dimensional diffusion of nanometer-sized dislocation loops. *Science* **318**, 956 (2007).

[216] Matsukawa, Y. & Zinkle, S. J., One-dimensional fast migration of vacancy clusters in metals. *Science* **318**, 959 (2007).

[217] Cawthorne, C. & Fulton, E. J., Voids in Irradiated Stainless Steel. *Nature* **216**, 575 (1967).

[218] Osetsky, Y. N. *et al.*, Atomistic study of the generation, interaction, accumulation and annihilation of cascade-induced defect clusters. *J. Nucl. Mater.* **307–311, Part 2**, 852 (2002).

[219] Demkowicz, M. J. *et al.*, Interface structure and radiation damage resistance in Cu-Nb multilayer nanocomposites. *Phys. Rev. Lett.* **100**, 136102 (2008).

[220] Fu, E. *et al.*, Surface effects on the radiation response of nanoporous Au foams. *Appl. Phys. Lett.* **101**, 191607 (2012).

[221] Ziegler, J. F. & Biersack, J. P., SRIM-2008, Stopping Power and Range of Ions in Matter. (2008).

[222] Sorensen, M. R. & Voter, A. F., Temperature-accelerated dynamics for simulation of infrequent events. *J. Chem. Phys.* **112**, 9599 (2000).

[223] Mishin, Y. *et al.*, Structural stability and lattice defects in copper: Ab initio, tight-binding, and embedded-atom calculations. *Phys. Rev. B* **63**, 224106 (2001).

[224] Ziegler, J. F. *et al.*, The stopping and range of ions in matter, Vol. 1. (Pergamon, New York, 1985).

[225] Zinkle, S. J. *et al.*, Dose dependence of the microstructural evolution in neutron-irradiated austenitic stainless steel. *J. Nucl. Mater.* **206**, 266 (1993).

[226] Liu, Y. *et al.*, Plasticity and ultra-low stress induced twin boundary migration in nanotwinned Cu by in situ nanoindentation studies. *Appl. Phys. Lett.* **104**, 231910 (2014).